Sunlight variations under broken clouds

Wouter Mol

Propositions

1. Shallow cumulus unjustifiably overshadows all other clouds in solar radiation research
   (this thesis)

2. The relationship between clouds and surface solar irradiance is simple
   (this thesis)

3. Striving for perfectionism is essential to the creative process

4. Any organisation that claims to improve quality of life without having an ambitious carbon neutrality goal is greenwashing

5. Pretending that there is a social safety structure is harmful to social safety

6. Running is the best sport in a world of cognitively demanding desk jobs

Propositions belonging to the thesis, entitled

Sunlight variations under broken clouds

Wouter B. Mol
Wageningen, 27 September 2024

Sunlight variations under broken clouds

Wouter Mol

Thesis committee

Promotors
Dr C.C. van Heerwaarden
Associate Professor, Meteorology and Air Quality Group
Wageningen University & Research

Prof. Dr J. Vilà-Guerau de Arellano
Professor of Meteorology
Wageningen University & Research

Co-promotor
Dr B. G. Heusinkveld
Senior Scientist, Meteorology and Air Quality Group
Wageningen University & Research

Other members
Prof. Dr L. Kooistra, Wageningen University & Research
Prof. Dr R. Pincus, Columbia University, New York, United States of America
Dr F. Couvreux, Toulouse University, Météo-France, France
Prof. Dr P. Blanc, MINES ParisTech, PSL Research University, France

This research was conducted under the auspices of the Graduate School for Socio-Economic and Natural Sciences of the Environment (SENSE)

Sunlight variations under broken clouds

Wouter Mol

Thesis
submitted in fulfilment of the requirements for the degree of doctor at
at Wageningen University
by the authority of the Rector Magnificus,
Prof. Dr C. Kroeze,
in the presence of the
Thesis Committee appointed by the Academic Board
to be defended in public
on September 27, 2024
at 1 p.m. in the Omnia Auditorium.

Wouter Mol
Sunlight variations under broken clouds,
238 pages.

PhD thesis, Wageningen University, Wageningen, NL (2024)
With references, with summary in English and Dutch

DOI https://doi.org/10.18174/660879

Summary

Solar radiation is a fundamental driver of weather and climate on Earth. Much of the theory of radiative transfer is well-established and applied to weather and climate modelling. In recent years, however, with the increase in both model resolution and demand for accurate surface solar irradiance forecasts, it has become apparent that models do poorly at resolving solar radiation at the scale of clouds.

A significant amount of variability in solar irradiance occurs at the scale of clouds. This variability and its relationship to clouds is not well observed, characterised, or understood. This thesis focuses first on providing much needed observations of surface solar irradiance at the scale of clouds, i.e., from seconds to hours and meters to tens of kilometres. Second, we aim to understand the relationship between clouds and solar irradiance variability based on these observations.

The thesis is divided into three parts. In the first part, we introduce two observational techniques used in this thesis to observe solar radiation at the scale of clouds. In the second part, we provide a broader context for cloud-scale variability through a study on atmospheric cloud-scale variability, a description of long-term trends and synoptic scale extremes in irradiance in Europe, and an analysis of cloud-scale surface solar irradiance variability. Finally, with this context in mind, we explore the details of spatial and spectral measurements of solar irradiance and conclude by providing a foundational understanding of the key drivers of cloud-scale variability of surface solar irradiance.

Novel observational techniques and data

Chapter 2 describes a 10-year dataset of high-quality solar irradiance measurements from the Baseline Surface Radiation Network (BSRN) station in Cabauw, the Netherlands. This dataset contains measurements of global, direct, and diffuse solar irradiance at a 1-second resolution. Additional data such as clear-sky irradiance, wind speed, and solar zenith angle enables the classification of the time series into categories of solar irradiance variability, such as cloud shadows or irradiance enhancement above clear-sky values. An additional three years of satellite observations provide information on cloud type and cover. These data are analysed in Chapters 5, 6, and 8.

Chapter 3 introduces a novel instrument for spatial and spectral measurements of solar radiation, called FROST. Key features of FROST are its low cost and ease of use, which enable

scaling up fieldwork to a network of these instruments to gather spatial observations. In this technical description, we go into the details of how the instrument is made, both in terms of hardware and software, and provide extensive validation and testing of individual components. The instruments have been deployed in the Netherlands, Germany, Spain, the Amazon (Brazil), and Australia. Results of fieldwork in Germany (FESSTVaL campaign) and Spain (LIAISE campaign) are analysed in Chapters 7 and 8.

Large-scale perspectives

Variability of solar radiation and clouds is a core theme of this thesis. Chapter 4 is a great illustration of how variability is a fundamental characteristic of the atmosphere. In this chapter, we performed simulations of an idealised tropical atmosphere with a high resolution cloud-resolving model to understand the role of near-surface wind in heat exchange between ocean and atmosphere. Starting from a horizontally homogeneous and stable atmosphere, strong variability in cloudiness, wind speed, and temperature naturally emerges as deep convection forms. Deep convection forms as a result of the radiative cooling in the atmosphere balanced by surface heat exchange with the ocean. We find that coarse models (non-cloud-resolving) do not treat the surface heat exchange correctly and thereby affect the path to large-scale convective organisation.

As for variability on a longer time scale, Western Europe saw a period of record-high solar irradiance that coincided with COVID-19 lockdowns in 2020, exceeding the previous record by 11 %. Motivated by claims in the media about the lack of pollution from industry and (airplane) traffic being the cause, we investigated the irradiance extreme using observations (described in Chapter 2) and modelling in Chapter 5. While the air was indeed unusually clean and cloud-free for much of spring 2020, we found that the record-high solar irradiance was caused by anomalous synoptic scale weather patterns. Lockdown-related reductions in air pollution and contrail-cirrus only resulted in a small reduction in the amount of diffuse radiation.

In Chapter 6, we characterise 10 years of surface solar irradiance time series and link it to cloud sizes and types using the dataset of Chapter 2. Our main finding is that the size of cloud shadows follows a power law distribution that we can reproduce directly from cloud size distributions, thereby reconciling research on cloud and solar irradiance variability. Both distributions have a power law exponent of -5/3 (within the range of uncertainty), but the shadows of clouds are $\sim$ 50 m smaller due to the transparency of cloud edges to direct irradiance. Furthermore, we find irradiance enhancements above clear-sky and cloud shadows are equally common (each occurs $\sim$ 185,000 times in the 10 years of data). Lastly, we conclude from satellite observations that low, broken cloud fields are the main source of variability.

Spatial observations and analyses at cloud-scale

In Chapter 7, we present the key fieldwork activities of this thesis where we deployed 20 to 25 FROST instruments in Germany and Spain to gather spatial and spectral observations of

solar radiation at cloud-scale. With this study, we show that observing detailed spatiotemporal irradiance patterns is possible using a relatively small, low-cost sensor network. We find in case studies of cumulus, altocumulus, and cirrus clouds that these clouds generate large spatiotemporal variability in irradiance, but through different mechanisms and at spatial scales ranging from 50 m to 30 km. Spectral irradiance in the visible range varies at similar scales. Significant blue enrichment is found in cloud shadows, most strongly for cumulus. Red enrichment is found in irradiance peaks, particularly in the case of semi-transparent clouds or near cumulus cloud edges. In cloud-free conditions, solar irradiance varies significantly in water vapour absorption bands at the minute scale, due to variability in atmospheric moisture in the boundary layer.

The spatial patterns of SSI and shifts in spectral irradiance have led to the formation of hypotheses on the mechanisms driving cloud-scale variability. Combined with insights from previous chapters, we further formulate these hypotheses and test them in a modelling study presented in Chapter 8. Our main conclusion is that we can describe the essence of the formation of cloud-scale surface solar irradiance variability and their surface patterns with just four mechanisms: *forward escape*, *downward escape*, *side escape*, and *albedo enhancement*. The relative importance of each mechanism relates to cloud optical thickness, 3D cloud geometry, cloud altitude, and surface albedo. This result provides a framework for understanding the vast diversity and complexity found in surface solar irradiance and cloudiness.

In conclusion, this thesis gives a comprehensive description of surface solar irradiance variability in the presence of clouds based on novel observations, and provides a foundational understanding of the link between this variability and the clouds that drive it. One of the challenges of measuring or simulating surface solar irradiance variability is the wide range of spatiotemporal scales and diversity of optical properties with which clouds present themselves. In the concluding general discussion (Chapter 9), I elaborate further on the implications of these findings regarding the description of clouds and variability, model validation, and future fieldwork.

Samenvatting

Zonlicht, of preciezer, *zonnestraling*, is de basis van het weer en klimaat op Aarde. Er is al veel bekend over hoe deze vorm van energie zich gedraagt, en deze kennis is toegepast in rekenmodellen van het weer en klimaat. Deze modellen krijgen steeds meer detail, en in recente jaren is er een groeiende vraag naar nauwkeurige voorspellingen van zonnestraling op het aardoppervlak, bijvoorbeeld voor zonne-energie. Echter blijkt dat de modellen niet in de staat zijn het gedrag van zonnestraling nabij individuele wolken goed op te lossen. Dit terwijl de hoeveelheid zonnestraling op het aardoppervlak in de aanwezigheid van wolken extreem veel kan variëren.

Een van de oorzaken van dit probleem is dat men niet goed weet hoe zonnestraling varieert op de tijd- en ruimteschalen van individuele wolken. Dit proefschrift richt zich daarom op het verzamelen van observaties van zonnestraling onder wolken, en het begrijpen van de relatie tussen wolken en zonnestraling. In de introductie (Hoofdstuk 1) ga ik verder in op de motivatie en onderzoeksvragen van dit proefschrift.

In het eerste deel van dit proefschrift worden twee soorten observaties beschreven. De eerste, in Hoofdstuk 2, is een dataset van tien jaar aan hoogwaardige zonnestralingsmetingen van het meteorologisch observatorium in Cabauw, Nederland. Bijzonder aan deze dataset is dat er elke seconde een meting is. Er wordt tevens onderscheid gemaakt tussen straling die direct van de zon komt, of straling die via wolken of andere luchtdeeltjes op het aardoppervlak terecht komt, ook wel verstrooiing genoemd. In Hoofdstuk 3 wordt een nieuw instrument beschreven, die als deel van dit project ontwikkeld is. Met dit nieuwe instrument, goedkoop genoeg zodat we er 25 van hebben gemaakt, kunnen we een ruimtelijk netwerk uitzetten om zo patronen van zonlicht op het aardoppervlak te meten. Daarnaast meten we ook de variaties in de golflengtes van zonnestraling (de kleur van het licht), wat meer informatie geeft over de eigenschappen van de atmosfeer.

Voordat we in detail naar zonnestraling onder wolken kijken, wordt in het tweede deel van dit proefschrift een breder beeld gegeven van variaties op grotere tijd- en ruimteschalen. Allereerst, in Hoofdstuk 4, wordt een simulatie van een tropische atmosfeer boven een zeeoppervlak beschreven. Hierin ontstaat spontaan een grote diversiteit aan wolken en windpatronen, terwijl in eerste instantie de atmosfeer homogeen was. Hoewel het onderzoek in Hoofdstuk 4 zich richt op de invloed van wind laag bij de zee, is het een mooi voorbeeld van hoe variaties in de atmosfeer vanzelf ontstaan. In Hoofdstuk 5 wordt de recordhoeveelheid zonnestraling in west Europa in het voorjaar van 2020 besproken. Precies toen de COVID-19

pandemie uitbrak en er in allerlei landen gestopt werd met vliegen en autorijden, verdwenen de wolken en werd de lucht blauw. Dit bleek echter toeval: de recordhoeveelheid zonnestraling was vooral te wijten aan een geblokkeerd weerpatroon boven west Europa. Als laatste, in Hoofdstuk 6, wordt de tien jaar aan data beschreven in Hoofdstuk 2 geanalyseerd om de variaties in zonnestraling onder wolken algemeen te beschrijven. Uit de analyse blijkt dat er een nauw verband is tussen de grootte van wolken en de variaties in zonnestraling. Op basis van satellietwaarnemingen blijkt ook dat de meeste wolkenschaduwen en periodes met versterkte zonnestraling veroorzaakt worden door lage, gebroken wolken.

In het derde en laatste deel van dit proefschrift wordt de relatie tussen wolken en zonnestraling in detail onderzocht. Met de instrumenten beschreven in Hoofdstuk 3 zijn meerdere meetcampagnes uitgevoerd. Hoofdstuk 7 beschrijft de hoofdbevindingen van deze meetcampagnes. De ruimtelijke patronen van zonnestraling zijn sterk afhankelijk van het soort wolk, maar kunnen een groot contrast laten zien ongeacht of het lage, middelbare, of hoge wolken zijn. Ook is er op basis van de waarnemingen per golflengte te zien dat schaduwen over het algemeen blauwer zijn, en het door wolken versterkt zonlicht dicht bij de schaduwen iets roder. Tot slot komen alle inzichten uit de waarnemingen samen in Hoofdstuk 8, om te begrijpen hoe wolken de waargenomen patronen vormen. Op basis van experimenten met modelsimulaties, waarin waarnemingen nagebootst worden, concluderen we dat er tot 4 mechanismen zijn die de variaties in zonnestraling onder wolken verklaren. Voor dunne wolken, of kleine stukjes wolk, gaat de straling vooral recht door de wolk en vind er weinig verstrooiing plaats. Voor dikke wolken wordt het juist in alle richtingen naar het aardoppervlak verstrooid. Als een wolk verticaal ontwikkeld is wordt een deel van de straling diffuus uit de zijkant verstrooid, waarvan een deel ook op het aardoppervlak valt. Het vierde mechanisme is een versterking van straling door een verhoogd albedo van het aardoppervlak, vooral relevant als er sneeuw ligt. Tezamen verklaren deze mechanismen de variaties in zonnestraling onder wolken voor allerlei wolkenvelden.

Samengevat, dit proefschrift heeft nieuwe observaties van zonnestraling onder wolken geïntroduceerd, de relatie tussen wolken en zonnestraling op verschillende tijd- en ruimteschalen beschreven, en verklaard hoe de relatie tot stand komt. Hiermee is een stap gezet naar het bouwen en testen van allerlei modellen die op een snelle manier de waargenomen variaties in zonnestraling kunnen simuleren. In de einddiscussie van dit proefschrift (Hoofdstuk 9) wordt verder ingegaan op de implicaties van deze bevindingen voor het beschrijven van wolken en variaties in zonnestraling, modelvalidatie, en toekomstig veldwerk.

Contents

Chapter 1

General introduction

1.1 Variations in sunlight

The Sun emits roughly 3.8×10^{26} Joules of energy per second (W) in the form of electromagnetic radiation, in all directions. Only the tiniest amount of that energy, 0.000000045 %, reaches Earth – still roughly 10,000 times more than what humanity consumes globally (Ritchie et al., 2024). It emits this radiation across a spectrum of wavelengths ($\sim$250 to 4000 nm), of which we can see nearly half as visible light. When integrating along this spectrum of wavelengths, we find 1361 W m^{-2} of energy at the top of the atmosphere. Globally averaged, this amounts to 340 W m^{-2}, with the majority entering at the equator and much less so at the poles. It is this energy input that on daily time scales drives weather and, over many years, averages to what we define as climate.

The variations in the top of atmosphere solar spectral irradiance and uncertainty in the exact amount are so low ($\sim$0.1 %, Coddington et al., 2016) that in the context of atmospheric science, and this thesis, this is a solved problem. However, the closer we get to the surface, and the smaller the spatial and temporal scale we consider, the more this once constant energy input becomes highly variable and difficult to predict. On time scales shorter than one day (intra-day), clouds are the primary cause of variations in solar radiation. Figure 1.1 illustrates three examples of this variability.

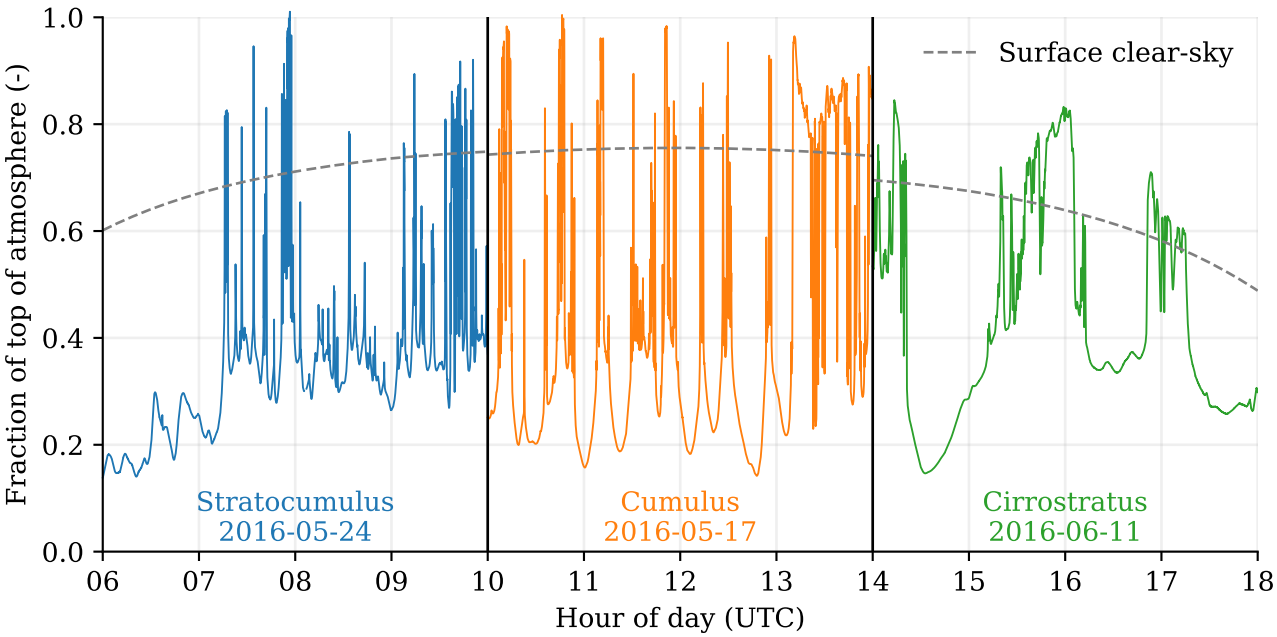

Figure 1.1: Constant input, variable result. Composite of time series of measured surface solar irradiance for three different cloud fields in Cabauw, the Netherlands. Local time is UTC+2. Data is plotted relative to the incoming solar radiation at the top of the atmosphere. The theoretical cloud-free reference (clear-sky) varies with the Sun's position in the sky and the amount of aerosol. The data source is introduced in Chapter 2.

There are many processes in the weather and climate system that are directly or indirectly driven by solar irradiance and its variations. On a broad scale, important direct ones are the heating of Earth's surface and evaporation of water (driving weather), photosynthesis (part of the carbon cycle), and photochemistry (relates to air quality). In addition to weather and climate, sunlight is essential for human health, but too much of it, especially ultraviolet, is hazardous. Solar energy, captured using photovoltaics (PV), is relatively new. This rapidly growing source of renewable energy is expected to play a key role in decarbonising society to mitigate climate change.

Zooming in on these processes, we find that many are non-linear and part of a complex system of feedbacks and interactions. Importantly, because of this complexity, it matters how solar irradiance is distributed over time, space, and wavelength. For example, boundary-layer cumulus clouds, formed as a result of a land surface heated through solar irradiance, change the amount and distribution of irradiance and thereby influence their own formation (Mayer, 2009; Veerman et al., 2022). Such a land surface may be full of vegetation doing photosynthesis in response to solar irradiance, taking up carbon and releasing moisture through stomata, small openings on the surface of leaves. Stomata, however, only slowly open and close in response to irradiance, thus photosynthesis depends on how much irradiance varies (Way & Pearcy, 2012). How vegetation responds to changes in the spectral composition of irradiance remains an open question (Durand et al., 2021; Huber et al., 2024).

Solar energy yield efficiency of PV panels depends on their temperature. Intermittent shading therefore affects efficiency compared to a constant exposure to the same amount of total irradiance. Also, PV technologies have their own specific wavelength response, further impacting efficiency relative to total solar irradiance (Dirnberger et al., 2015; Lindsay et al., 2020). However, the largest consequence of variable irradiance for solar energy is that historically, electricity grids have been designed for a constant and predictable energy supply. Increasing solar energy in the total mix of resources makes the energy supply less predictable, bringing operational problems to grid stability. This is a practical challenge in the transition towards renewable energy that needs to be overcome (Yang et al., 2022).

These are just a few examples in which solar spectral irradiance variability and its accurate simulation or forecasting are important. Simulations that are able to fully and accurately resolve observed irradiance variability at the cloud-scale remain non-existent, because, for starters, it would require resolving processes across scales ranging from meters to hundreds of kilometres. Being able to observe, describe, and explain irradiance variability at cloud-scale are necessary steps to improve simulation accuracy – easier said than done. Historically, the focus has been largely on the climate and global scale, and rightfully so. But now we are confronted with a lack of observations and understanding of irradiance and its impact on the surface at the scale of clouds. In this thesis, I aim to address the lack in observations and understanding of irradiance variability at cloud-scale, primarily through the collection of new spatially and spectrally resolved observations and analyses of both these new and existing observations. The overarching question of this endeavour is: How do clouds drive surface solar irradiance variability?

In the remainder of this introduction, I will give a brief overview of what we already know about the primary drivers of irradiance variability, how observations of irradiance are gathered, and why models struggle to accurately simulate what we observe. Lastly, I will lay out the structure of this thesis, in which we aim to contribute to this field of research through new (spatial) observations of irradiance variability and a better understanding of its drivers in a meteorological context.

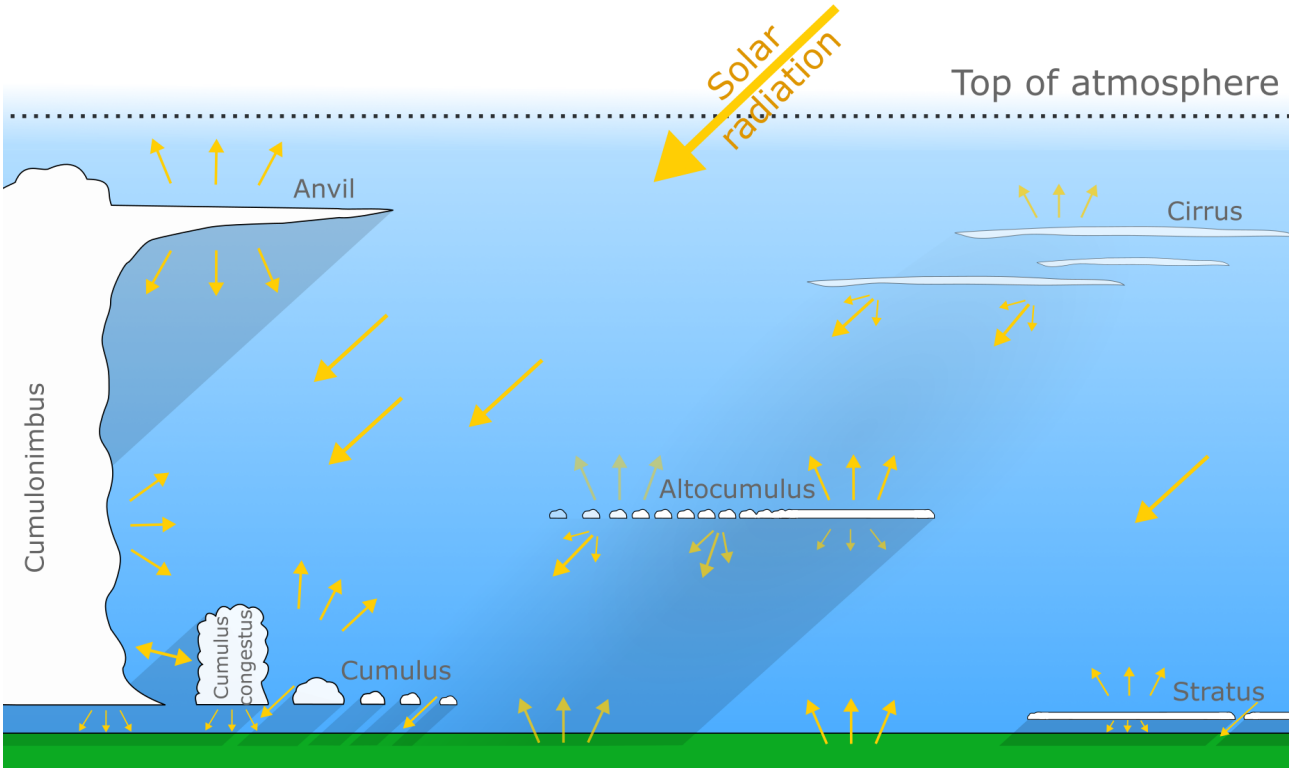

Figure 1.2: Schematic of a solar radiation travelling through a cloudy atmosphere. This sketch features some of the cloud types discussed in this thesis. Satellites can see the radiation that is scattered back to space, whereas I focus on the part that is able to reach the surface.

1.2 What drives surface irradiance variability?

1.2.1 Clouds

Clouds, whether made of water droplets, ice particles, or both, are highly effective scatterers of radiation. Physically, scattering means the ability of cloud particles to intercept photons and change their direction of travel. Only a small fraction of photons gets absorbed and warms up the cloud. In practice, this means that introducing a cloud in an otherwise homogeneous and cloud-free atmosphere will result primarily in a redistribution of the incoming solar radiation.

Part of the radiation is scattered back to space, another part finds a way to the surface that deviates from its original path (Figures 1.2 and 1.3). This horizontally redistributed irradiance brightens already fully sunlit areas and result in the total surface irradiance exceeding

that of cloud-free conditions, potentially even the top of atmosphere values (Yordanov et al., 2015; Gueymard, 2017; Cordero et al., 2023). This local enhancement of irradiance is an essential characteristic of surface solar irradiance in the presence of broken clouds. Figure 1.1 illustrates three such examples.

Often, this scattered radiation is called *diffuse*, as opposed to unscattered *direct* irradiance. Diffuse radiation may be more familiar to some as haze, you can see some of that haze in the top left cloud in Figure 1.3, and also *diffuse* commonly implies light comes from (or goes to) many directions. However, *diffuse* can mean different things in terms of the direction and spectral composition of light, and so to be specific and for sake of clarity, I will mostly use the term *scattering* when talking about the processes.

Cloud geometry, phase of its condensate, and altitude will all influence its scattering properties, and so clouds of various types make distinct and unique patterns in the surface solar irradiance field and affect the spectral composition of light. Falconer (1965) used this to broadly derive cloud type from observed time series of total irradiance, and Robinson (1977) went on to detail the distribution of surface irradiance caused by isolated shallow cumulus. For vertically structured clouds, Segal & Davis (1992) describe what they call *reflections* from the sides of (isolated) cumulonimbus clouds that cause enhanced irradiance on the surface at the sunlit side (such as on the left in Figure 1.2). These three studies may have been ahead of their time, given today's efforts and how well the results have held up.

Clouds are more often than not part of complex multi-layered and/or vertically structured cloud fields. This gives rise to a multitude of scattering phenomena that are best described as *entrapment* of radiation between clouds (and the Earth's surface) and *escape* from its sides, top, or bottom, as described within a top of atmosphere perspective by Várnai & Davies (1999) and Hogan et al. (2019). Figure 1.3 shows a (very incomplete) collection of cloud photos to illustrate some of the complexity that goes well beyond what satellites or models can resolve. This complexity has yet to be fully understood.

1.2.2 Other factors

While clouds are the primary source of variations in solar irradiance, we need to consider the following other factors.

Scattering and absorption by gases

In a cloud-free atmosphere, gases scatter and absorb light as a function of wavelength. Perhaps the two most well-known phenomena here are the absorption of ultraviolet (UV) radiation by ozone, which protects us from this high energy radiation, and the blue sky due to Rayleigh scattering. The latter is a scattering mode where the particle a photon interacts with, here a gas molecule, is much smaller than the wavelength (λ) of the photon. This scattering is proportional to λ^{-4}, meaning shorter wavelengths scatter significantly more than longer ones. Scattered sunlight thus appears blue to our eyes whereas the Sun itself is (bright) yellow, relative to white.

Figure 1.3: A collection of the visible effects of clouds. In the top left is a cumulus cloud about 10 times larger than the cumulus in the top center ($\sim$ 1 vs. 0.1 km across). The top right features various forms of cirrus and virga. The bottom left shows semi-transparent altocumulus, and the bottom right illustrates heterogeneous surface irradiance under a cumulus field.

Absorption of radiation results in warming and reduces the total solar irradiance at the surface. Scattering by gases also slightly reduces the surface irradiance, as part of the photons scatter back to space before reaching the surface. Absorption and scattering by atmospheric gases are one reason why the clear-sky surface solar irradiance is less than the top of atmosphere solar irradiance, as can be seen in Figure 1.1.

Aerosols

The other reason that surface irradiance is less than at the top of the atmosphere is aerosols. Aerosols are small particles (diameters typically between 10 nm and 10 μm) that are suspended in the atmosphere and can be of both anthropogenic and natural origin. For example, (Sahara) dust, black carbon, and sea salt. Each type has its own optical properties that are wavelength dependent, some even change with increased relative humidity, called hygroscopic growth. In addition to scattering and absorbing part of the solar radiation themselves, aerosols act as cloud condensation nuclei, enabling cloud formation. But they also influence cloud droplet size distributions, where more aerosols result in more but smaller

droplets, making clouds brighter (Twomey, 1974), at least initially (Feingold et al., 2024). It is clear that analyses of the effects of clouds on solar irradiance would be incomplete without factoring in the role of aerosols.

Surface albedo

This brings us to albedo, which is a quantity that indicates how much irradiance a surface or material reflects and is a function of wavelength. While initially albedo may only seem relevant for determining the net surface shortwave irradiance, the reflected light in fact partially scatters back against the overlying atmosphere. Incoming surface solar irradiance is thereby increased by a few per cent in cloud-free conditions. In the presence of clouds, back-scattering can have a significant effect over surfaces with high albedo, shown by e.g. Gueymard (2017) and Villefranque et al. (2023).

Vegetation

Those studying photosynthesis will notice that the swaying of branches or fluttering of leaves makes light vary more quickly than what clouds can achieve (Way & Pearcy, 2012). Analyses presented in this thesis are done with measurements or modelling away from the direct effects of vegetation, i.e., vegetation is not included beyond their effective albedo, hence *surface* irradiance refers to a location just above any vegetation (typically grass). Some campaigns in which we have participated by taking irradiance measurements were motivated by understanding the role of in-canopy processes, and you can find those observations in the open data section.

1.2.3 What remains?

Part of what makes understanding the visuals in Figure 1.3 so challenging is that the many processes just described happen simultaneously, and all contribute something. It is clear that we are not starting on this topic from scratch, but there remains much to be done. The processes and details of irradiance variability are mostly studied individually, only for specific cloud types, from a top of atmosphere (satellite) perspective rather than from the surface, or qualitatively.

Before getting lost in the complexity and detail, it is good to realise there are still basic questions about characterising what we see. For example, how often does cloud-induced enhancement in surface irradiance occur? How long do cloud shadows last and how big are they typically? What cloud types are good at creating irradiance extremes, and which are most diffusive? These questions bring us to the topic of observations.

1.3 Measuring variability

Part of understanding the processes and improving simulation accuracy starts with making observations. Firstly, observations allow us to characterise the phenomena and answer the questions I just posed, and secondly, they provide a ground-truth to validate models against.

Figure 1.4: Thermopile pyranometers to measure solar irradiance. On the right are two thermopile pyranometers, one facing up and one facing down, which together measure net solar irradiance. The bottom left is a zoom in on the black surface beneath a glass dome that heats up in response to radiation. This one could use cleaning. Out of focus in the top left are two instruments to measure incoming and outgoing long wave radiation.

Nowadays, the most accurate instruments can be found in stations that are part of the Baseline Surface Radiation Network (BSRN, Driemel et al., 2018). These instruments, called pyranometers and pyrheliometers, are thermopile-based instruments that measure integrated solar irradiance by means of an absorbing black surface that heats up in response to solar radiation, thereby changing the voltage across a thermocouple (Figure 1.4). This voltage is proportional to the solar irradiance in W m^{-2}. Mounted on a sun tracker, a pyrheliometer has an opening angle of 5° (or 10 times the apparent diameter of the Sun), and follows the Sun to measure what is called direct normal irradiance (DNI). A pyranometer mounted on the same sun tracker is shaded by a sphere that blocks direct sunlight (5° in apparent diameter), and measures what we call diffuse horizontal irradiance (DIF). In the context of measurements,

DNI refers to unscattered sunlight that reaches the surface directly, whereas DIF refers to scattered light, in this case light that reaches the surface indirectly. Technically, however, measured direct irradiance also includes a small amount of scattered light coming from the Sun's corona and any light that is scattered in the forward direction in the close vicinity of the Sun's disk (e.g., Blanc et al., 2014). Combined with the solar zenith angle θ, the total horizontal incoming solar irradiance, or global horizontal irradiance (GHI), then follows as $\text{GHI} = \text{DNI} \cdot \cos(\theta) + \text{DIF}$. A separate unshaded pyranometer measures GHI directly, like the one in Figure 1.4, and provides a good reference for quality control.

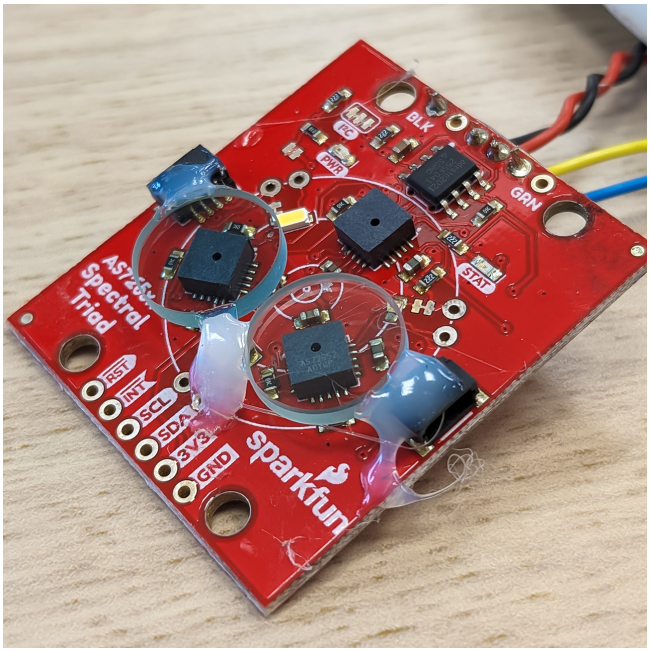

Figure 1.5: Photodiode spectrometer. This one features three subsensors in a triad of black squares, each with a tiny opening where light can enter. The circular glass pieces are additional band pass filters. The red printing plate is about the size of the glass dome of the pyranometer in Figure 1.4. More on this sensor and its measurements in Chapters 3, 7, and 8.

The advantage of BSRN stations is the high quality of measurements performed over long periods of time to enable climatological analyses and accurate quantification of the surface net radiation. On the other hand, these stations are very expensive (instrumentation alone costs over 10,000 euros), pyranometers have a response time of several seconds, and they only measure spectrally integrated solar irradiance. This means the fastest fluctuations at the scale of seconds are not well captured, and spectral information is lost. Perhaps more importantly, solar irradiance measurements have historically been nearly exclusively single-location time series, because spatial measurements at the scale of clouds are financially unfeasible.

This is changing with the onset of solar energy, bringing increased attention towards understanding variability of irradiance at cloud-scale, and new sensor techniques. Some PV parks have arrays of pyranometers that can be used to study irradiance variability spatially (e.g., Lappalainen & Valkealahti, 2016b; Järvelä et al., 2020). For larger and denser networks, scientists use photodiode-based instruments (e.g., Figure 1.5). These trade in some accuracy

due to a reduced spectral sensitivity, but they are cheaper and, importantly, photodiodes have a (practically) instant response time. One such network of 99 pyranometers was deployed in Germany during the HOPE campaign (Madhavan et al., 2016), while another network of 19 pyranometers was deployed in Hawaii (Tabar et al., 2014).

Ultimately, however, high-frequency spatial solar irradiance measurements at cloud-scale are far and few in between, and none have any spectral resolution. This is what has largely motivated us to develop a new sensor, using the photodiode spectrometer shown in Figure 1.5, with which we gather spatial observations of spectral surface solar irradiance variability at cloud-scale. This will be extensively discussed in Chapter 3.

1.4 Modelling variability

A model capable of fully and accurately resolving observed surface solar irradiance variability requires two main components. One is a detailed and accurate 3D description of the state of the atmosphere in terms of optical properties (cloud amount, cloud phase, aerosol type and amount, and gas concentrations) including surface properties (spectral albedo, orientation). The second component is a radiative transfer model that can resolve absorption and the scattering of radiation in all directions given this description of the atmospheric state.

In practice, for such a model to be useful in any kind of forecasting scenario, it should be able to run faster than real-time. This is not remotely possible to do. Even in academic setups, where we can afford to be slower, certain processes are missing or parameterised, and the atmospheric state is at best approximated. Fundamentally, the problem lies in a limit of available computing power and energy, information on the state of the atmosphere, knowledge of all processes involved, and stochastic nature of the atmosphere. Ensemble methods would help with the stochasticity, but are also constrained by computing power and energy.

I identify three main limitations in the accuracy of modelling surface solar irradiance. First, models do not fully resolve cloud fields. Models are discretised in space on a finite resolution grid, which means even state-of-the-art numerical weather prediction (NWP) models do not resolve clouds. Cloud-resolving models cannot be run on domains big enough to capture the full scale of variability (van Stratum et al., 2023), and it is debatable whether simulated clouds are realistic (e.g., Romps et al., 2021). Second, radiative transfer calculations are among the most computationally expensive components of a model, even after simplifications. To run them in operationally requires reduced dimensionality (independent-column approximation, so 1D instead of 3D), reduced spectral resolution, and reduced call frequency (Hogan & Bozzo, 2018). And third, the initial state of the atmosphere is uncertain. Even if we had enough computing power to globally resolve clouds and run full 3D radiative transfer calculations, we lack the observations to initialise a model at such detail.

These limitations are not easily overcome. It also comes down to the important question of what is accurate enough, and the answer will depend greatly on who you ask. I believe we

can, and should, improve the way solar radiation is treated in models, from which all related processes benefit. Computing power and energy constraints mean we need to be efficient with our resources. With a better quantification and understanding of irradiance variability, we can build, improve, and validate parameterisations, statistical methods, machine learning, and other techniques to forecast it or simulate its effects in models.

1.5 Goal and structure of this thesis

This thesis is primarily concerned with the question of characterising surface solar irradiance variability, both in time and space, and understanding the underlying causes of this variability. Observations are at the core of the question of characterisation, while we aim to gain understanding using a mixture of observations and modelling. The thesis is therefore largely structured in three content parts: observational techniques, large-scale perspectives, and observation and analyses at cloud-scale.

1.5.1 Novel observational techniques and data

The first part of this thesis, as mentioned before, further introduces the observational techniques that we have developed and used. In Chapter 2, we describe the gathering and classification of a 10-year dataset of high quality surface solar irradiance time series using conventional pyranometers sampled at 1 Hz. These measurements were taken at the Ruisdael Observatory in Cabauw, the Netherlands. We combine the irradiance measurements with the meteorological observations at this observatory and satellite-derived cloud properties at the same location. In Chapter 3, we introduce our new technique to measure the spectral surface solar irradiance using a cost-effective design. Here, we traded in absolute accuracy for a sensor that is small, affordable, and which can be deployed in a network to measure not only with high temporal resolution, but also in space.

1.5.2 Large-scale perspectives

Before moving on to detailed cloud-scale analyses, we touch upon three aspects of weather and climate in the context of radiation to provide a larger scale perspective. First, Chapter 4 demonstrates how homogeneous initial and boundary conditions, with uniform net cooling of the atmosphere due to longwave radiation as the only forcing, lead to an atmosphere that closely resembles that of the real-world tropics: heterogeneous cloud cover and deep moist convection. This study focuses on the role of surface fluxes in this process, but in the context of this thesis also serves to balance the otherwise lacking analyses of long-wave radiation as a driver of weather. Second, in Chapter 5 we discuss long-term trends in solar radiation as it relates to reduced cloudiness and aerosol amount in Europe, motivated by a record high amount of solar irradiance during the COVID-19 lockdowns in 2020. Third, in Chapter 6 we analyse the 10-year time series dataset of Chapter 2 to characterise irradiance variability, find the typical scales of cloud shadows and irradiance peaks (time, space, and intensity) and link it to the sizes of clouds. This chapter, I believe, comes closest to providing a universal

description of cloud-scale variability in solar irradiance.

1.5.3 Spatial observations and analyses at cloud-scale

In the final section, we explore the details of the spatial patterns of solar (spectral) irradiance for individual clouds. This involves results from spatial measurements performed during two field campaigns in 2021 using the instrument introduced in Chapter 3. Measurement strategy, results, and interpretation of the data are presented in Chapter 7. To conclude, in Chapter 8 we bring various observations and modelling together to attempt to get to the main mechanisms that drive the observed spatial variability in solar irradiance.

1.5.4 Closing words

A synthesis and broader discussion of all results and reflection on the motivation laid out in this Introduction are given in Chapter 9. An overview of all published datasets and articles can be found in the back of this thesis.

Finally, in between Chapters you will find photos I have taken of clouds interacting with solar radiation, similar to the examples shown in Figure 1.3. I hope these photos will help you, as they have helped me, reflect on what reality looks like while navigating the sometimes abstract scientific content.

Chapter 2

Ten years of 1 Hz solar irradiance observations at Cabauw, the Netherlands, with cloud observations, variability classifications, and statistics

This chapter is based on:

Mol, W. B., Knap, W. H., & van Heerwaarden, C. C. (2023). *Ten years of 1 Hz solar irradiance observations at Cabauw, the Netherlands, with cloud observations, variability classifications, and statistics*. In Earth System Science Data. Copernicus GmbH. https://doi.org/10.5194/essd-15-2139-2023

Abstract

Surface solar irradiance varies on scales down to seconds, of which detailed, long-term observational datasets are rare but in high demand. Here, we present an observational dataset of global, direct, and diffuse solar irradiance sampled at 1 Hz, and fully resolved variability until at least 0.1 Hz, over a period of 10 years, from the Baseline Surface Radiation Network (BSRN) station at Cabauw, the Netherlands. The dataset is complemented with irradiance variability classifications, clear-sky irradiance and aerosol reanalysis, information about the solar position, observations of clouds and sky type, and wind measurements up to 200 meters above ground level. Statistics of variability derived from all time series include approximately 185,000 detected events of both cloud enhancement and cloud shadows. The Cabauw measurement site has additional observations freely available at the open data platform of the Royal Netherlands Meteorological Institute. This paper describes the observational site, quality control, classification algorithm with validation, and the processing method of complementary products. Additionally, we discuss and showcase (potential) applications, including limitations due to sensor response time. These observations and derived statistics provide detailed information to aid research into how clouds and atmospheric composition influence solar irradiance variability, and to help validate models that are starting to resolve variability at higher fidelity. The main datasets are available at `https://doi.org/10.5281/zenodo.7093164` (Knap & Mol, 2022) and `https://doi.org/10.5281/zenodo.7092058` (Mol et al., 2022), see the data availability section for the complete list.

2.1 Introduction

Clouds generate large intra-day surface solar irradiance variability, the spatiotemporal scales of which reach down to seconds or less (Yordanov et al., 2013; Tabar et al., 2014; Gueymard, 2017; Kivalov & Fitzjarrald, 2018), or tens of meters (Lohmann et al., 2016, Chapter 6). Observing, understanding, and forecasting irradiance variability at these scales is important for a range of applications. Solar energy production and electricity grid stability is negatively affected by fast and local irradiance variability (Liang, 2017; Yang et al., 2022). Numerical weather prediction models are incapable of forecasting variability at these short scales, but as their resolution keeps increasing and sub-grid scale irradiance variability parameterizations are developed, they require more detailed observations for validation. Cloud resolving models and the development of more accurate 3D radiative transfer calculations in academic setups (e.g. Jakub & Mayer, 2015; Gristey et al., 2020b; Veerman et al., 2022), likewise require detailed and accurate observations of solar irradiance. Heterogeneity of solar irradiance and resulting surface fluxes is also an increasingly important topic in the field of land-atmosphere interaction (Helbig et al., 2021), with a non-linear response of vegetation's photosynthesis to varying light intensities (Pearcy & Way, 2012) or diffuse irradiance penetration into canopies (Mercado et al., 2009; Durand et al., 2021).

Existing observational datasets of surface solar irradiance at the sub-minute scale are rare, in particular for multiple years or longer and with separate direct and diffuse irradiance measurements. Notable examples of such datasets include those used in previously mentioned studies (Tabar et al., 2014; Gueymard, 2017; Kivalov & Fitzjarrald, 2018; Lohmann, 2018; Gristey et al., 2020b). In this work, we present such a dataset, which consists of 10 years of 1 Hz resolution global, direct, and diffuse irradiance, supplemented with meteorological observations for interpretation and data analysis. To the best of our knowledge, this is a unique observational dataset given its time span, temporal resolution, and multi-component measurements. The separation of global horizontal irradiance (GHI) into direct and diffuse components is important for distinguishing and characterizing the different types of atmospheric conditions and specific conditions under which irradiance variability is generated. Most notably, the phenomenon of cloud enhancement, where clouds scatter additional sunlight to cloud-free spots on the surface to significantly increase total irradiance (Yordanov, 2015; Gueymard, 2017, Chapter 6), is by definition a combination of direct and diffuse irradiance and cannot be understood with only GHI observations.

In this work, we will describe the 10-year observational dataset of solar irradiance, all supplementary meteorological observations and related processing, the time series variability classification algorithm, statistical datasets derived from all time series and classifications, and examples of how the data can be used. Sections 2.2 and 2.3 are a complete and more elaborate version of the condensed dataset description published in Chapter 6.

2.2 Observational data description

All in-situ observations in this dataset are taken at the Ruisdael Observatory in Cabauw (previously known as CESAR, `https://ruisdael-observatory.nl/cabauw/`) of the Royal Netherlands Meteorological Institute (KNMI). The observatory, hereafter referred to as Cabauw, is located in a rural area in the south-west of the Netherlands at 51.97°N, 4.92°E (Figure 2.1a). The climate in the Netherlands is a typical ocean-influenced west coast climate, with relative mild and wet winters despite its high latitude, and milder summers than further inland. KNMI provides an overview of the current Dutch climate and trends on their website (`https://www.knmi.nl/klimaat`), including the long term increasing trend of incoming solar radiation and recent extremes (e.g., that of spring 2020, Chapter 5). The following section describes all the observational data we use from Cabauw, the supplementary modeled clear-sky irradiance, atmospheric composition re-analysis, calculated solar positions, satellite-derived cloud types, and ground based cloud cover.

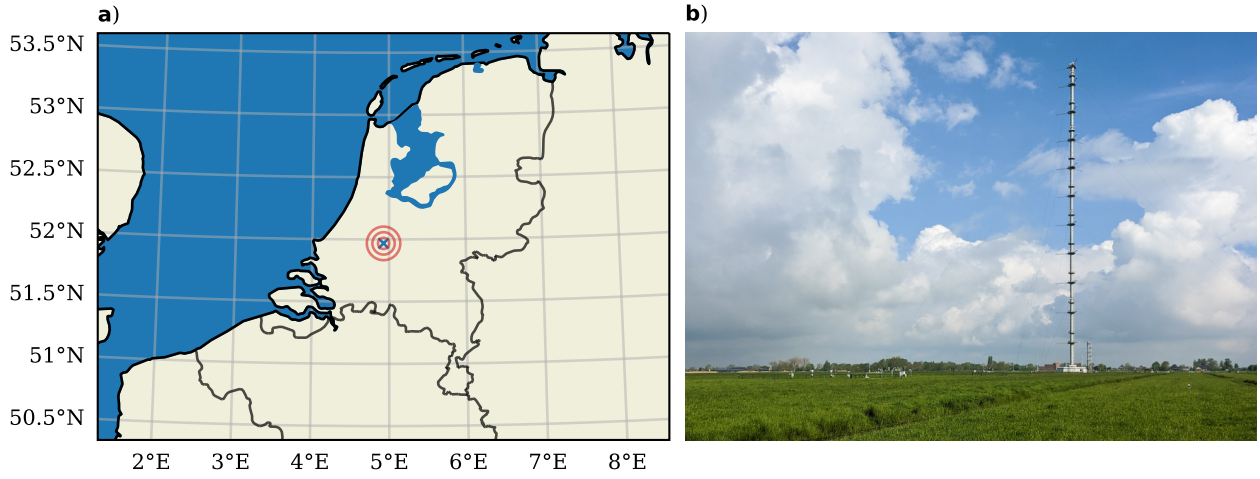

Figure 2.1: Ruisdael Observatory Cabauw, the Netherlands, where all observations in our dataset are located. The geographical location is marked in **(a)** with a cross, the circles are the 5 to 15 km radii for satellite cloud type extraction. A photograph of the 213-meter-high tower at the Cabauw site, with the BSRN station among other instruments in the bottom left, is shown in **(b)**.

2.2.1 Surface solar irradiance observations

The surface solar irradiance station at Cabauw is part of the Baseline Surface Radiation Network (BSRN, Driemel et al., 2018), operational since 2005. The BSRN station measures all components of the surface radiation balance. Observations are logged at a 1 Hz frequency, reprocessed to 1 minute quality controlled and validated data, made available publicly at the PANGAEA data repository (Knap, 2022) with instrument metadata, maintained by station scientist Wouter Knap (KNMI). While 1 minute resolution is enough for many applications, in particular those concerned with the surface net radiation balance at longer time scales, much of the cloud driven irradiance variability occurs at sub-minute scales. For the purpose

of research into cloud-driven irradiance variability at these short time scales, a separate 10-year subset of solar irradiance at 1 Hz resolution has been released (Knap & Mol, 2022), and is described in here. This subset spans from 2011-02 until 2020-12. The three components are global horizontal irradiance (GHI) and diffuse irradiance (DIF), measured with Kipp & Zonen CM22 pyranometers, and direct normal irradiance (DNI), measured with a Kipp & Zonen CH1 pyrheliometer.

Sensor response time and resolved variability

The pyranometer and pyrheliometer instruments are thermopiles, meaning there is a non-zero response time to variations in incoming radiation, i.e. the time it takes for the thermopile to adjust to changes in irradiance signal. Thus, the true resolved resolution is not 1 Hz, though it depends on the magnitude and rate of change of irradiance variability whether this impact is noticeable. According to manufacturer's specifications, the CH1 pyrheliometer has a 7 second (95%) or 10 second (99%) response time (Kipp & Zonen, 2001), and 1.66 seconds (66%) or 5 seconds (95%) for the CM22 pyranometers (Kipp & Zonen, 2004). This results in a likely underestimation of variability at 1 Hz, but the exact extent to which that happens is hard to quantify given the absence of solar irradiance measurements with fast responding sensors at a similar location, and for long enough to sample diverse weather conditions. Figure 2.2 illustrates the power spectral density (PSD) of a year of BSRN 1 Hz data. Tabar et al. (2014) present spectra (their Figure 2) for one year of data from a semiconductor pyranometer, thus with a $>$ 1 Hz response time, which shows an order of magnitude higher PSD at 1 Hz compared to 0.1 Hz as in our Figure 2.2. However, these data were collected in Hawaii, which is a very different geographical location and climate than Cabauw. Alternatively, two weeks of summer time 10 Hz irradiance observations from fast radiometers (Mol et al., 2023a) show a steeper decline between 0.1 and 1 Hz than the BSRN data. This supports the idea that the true cloud-driven irradiance variability does not always extend towards 1 Hz and higher frequencies, and that often the slow response time has no noticeable effect.

Based on the technical specifications of the pyranometer and pyrheliometer, we are at least confident that variability is resolved up to 0.1 Hz (10 seconds). This is also supported by van Stratum et al. (2023), where they show agreement between the BSRN dataset presented in this paper and irradiance spectra from semi-realistic large-eddy simulation up to 0.1 Hz (their Figure 6). Given the uncertainty of how much of the true variability is resolved between 0.1 and 1 Hz, we advise analyses at 1 Hz only in combination with additional constraints, such as knowledge of cloud properties and their velocity to estimate the fastest possible changes in irradiance. For example, in Chapter 6, knowledge of wind speed, cloud size distributions, and cloud edge transparency were combined to utilize the data down to 1 Hz.

One last implication is that the slow response time slightly reduces the contrast in data. Ehrlich & Wendisch (2015) demonstrate a reconstruction technique of the true 1 Hz signal through deconvolution, essentially a sharpening technique, which is not a trivial exercise. We have not applied this here, as we cannot validate whether it works reliably for our dataset,

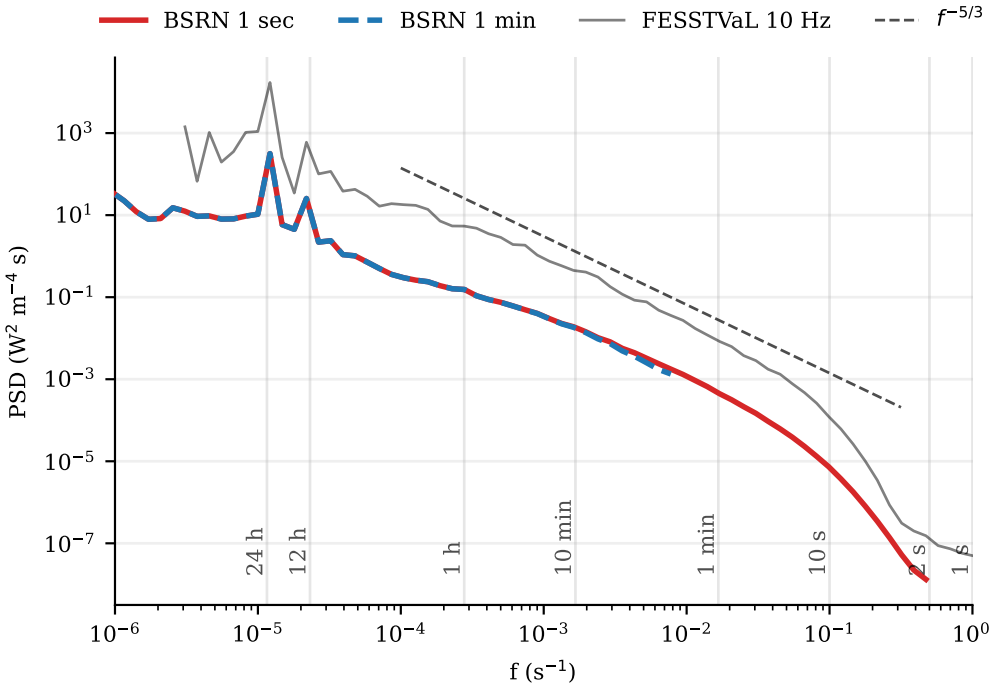

Figure 2.2: Power spectral density of one year (2016) of 1 Hz BSRN data (GHI component). The one minute spectrum is based on resampled 1 Hz data. As a reference, $f^{-5/3}$ scaling is added to emphasize the steep decline after 0.1 Hz towards 1 Hz. An additional comparison is the spectrum from a semiconductor radiometer deployed during the FESSTVaL field campaign from June 14 to 30, 2021 near Berlin, Germany.

but we mention it as an option to anyone who might want to attempt to apply the method despite its challenges. The only pre-processing we apply to the data, namely gap filling and quality control, is discussed in Section 2.3.1.

2.2.2 Supplementary irradiance data

Solar position and direct horizontal irradiance

Information about the sun's position is important for quality control, data analysis, and interpretation of results. Calculations of the sun's position (elevation and azimuth angle) are done using the python package PySolar (`https://github.com/pingswept/pysolar`) at a 1-minute resolution, linearly interpolated to 1 second. The calculations are for the purposes of this research area indistinguishable from highly accurate peer reviewed code such as the Solar Position Algorithm (SPA, `https://midcdmz.nrel.gov/spa/`). Using the solar elevation angle α (degrees above horizon, or as zenith angle $\theta = 90 - \alpha$), we calculate the horizontal component of direct irradiance: DHI = DNI $\cdot$ sin(α). An alternative calculation is DHI = GHI $-$ DIF, which in the case of a good measurement setup should be equal to DNI $\cdot$ sin(α), and is the basis for one of the checks in data quality control (discussed in Section 2.3.1).

Clear-sky irradiance and atmospheric composition

Clear-sky global horizontal irradiance (GHI_{cs}) is the total downwelling horizontal solar irradiance in the absence of clouds. We use CAMS McClear version 3.5 (Gschwind et al., 2019) as the GHI_{cs} reference for our dataset, released in September 2022. CAMS McClear includes corrections based on atmospheric composition re-analysis, such as aerosols and total column atmospheric water vapour. This allows us to define times when GHI exceeds GHI_{cs} as those purely driven by clouds as accurately as possible, as opposed to definitions based on simpler models, which is necessary for the irradiance classification algorithm described in Section 2.3.3. Atmospheric composition input for McClear is included in their publicly available dataset (`https://www.soda-pro.com/web-services/radiation/cams-mcclear`), which we add to our dataset for context. The only further processing applied to this data is linear interpolation from 1 minute to 1 second to match the irradiance observations.

2.2.3 Additional in-situ measurements

Wind profiles from Cabauw

A 213-meter-high tower provides wind speed and direction measurements at 2, 10, 20, 40, 80, 140 and 200 meters above ground level at a 10-minute interval (Wauben et al., 2010). Figure 2.1b shows the tower with respect to the BSRN site, which is a few hundred meters to the south. We apply no further processing to this data, apart from creating daily files from the monthly files. The original tower data (including temperature, visibility, and humidity) is shared publicly by the KNMI on their open data platform: `https://dataplatform.knmi.nl/dataset/cesar-tower-meteo-lb1-t10-v1-2`.

Nubiscope

Detailed cloud cover observations, for analysis, validation of satellite observations (Section 2.2.4), and irradiance based sky type classification (Section 2.3.3), we use the observations from a nubiscope located within a few meters from the BSRN instrumentation (Wauben et al., 2010). In 10 minutes, this instruments makes a hemispherical scan of the sky using infrared sensors to determine cloud fraction and sky type of various categories. We subset the nubiscope to three years (2014 to 2016) for validation and analyses purposes. If necessary, additional data (2008-05 to 2017-04) is publicly available at `https://dataplatform.knmi.nl/dataset/cesar-nubiscope-cldcov-la1-t10-v1-0`. Again, no further processing is applied by us, apart from turning monthly files into daily files.

2.2.4 Satellite observations

The satellite product CLAAS2 (Benas et al., 2017) provides cloud cover, cloud top pressure (CTP), and cloud optical thickness (COT), available every 15 minutes during daytime at an approximate spatial resolution of 20 km^2 over Cabauw. We provide three years of satellite data (2014-2016) for both validation and cloud type analyses, and describe the post-processing steps in Section 2.3.2.

2.3 Processing and methods

2.3.1 Quality control and completeness of irradiance data

One of the first steps in the processing is constructing daily files from the raw instrument data, which occasionally misses a few seconds of data. In such cases, we apply linear gap filling between measurement points, after which we apply quality control and derive all other variables. Gap filled data points are not flagged. Data quality control for the irradiance measurements is necessary to mask out station maintenance, malfunctioning instruments, or other cases of bad data like those caused by precipitation. Maintenance happens on a semi-daily basis (Monday, Wednesday, Friday) to ensure the high BSRN quality standards are met, and is the most common source of anomalous measurements. It is typically brief and only involves sensor cleaning, though sometimes instrumentation is disabled or replaced due to quality issues such that there are gaps of hours up to a few days. For the official 1-minute BSRN dataset (Knap, 2022), all measurements during such periods are filtered. The 1 Hz version includes quality flags ('good' or 'bad' data) derived from the official dataset, where 'good' means all three components (GHI, DNI, DIF) are valid. The 1 Hz version includes the original measurements, and quality flags have to be applied to filter bad data, such that the user can decide on the strictness of filtering themselves. We independently determined data quality at the 1 Hz level by performing the following checks, which is a result of a trial and error process through manual data inspection:

1. The absolute rate of change of the DIF and DNI components with respect to clear-sky between two seconds has to be below 5% and 20%, respectively.
2. The same for GHI, except the limit is 5% for cloudy conditions and 20% for sunny conditions. This leads to some false positives, which are reset if GHI and DHI changes are well-correlated.
3. Invalid measurements are padded by 180 seconds before and after to be on the safe side.
4. The residuals ΔQ_{abs} = |GHI - (DHI + DIF)| and ΔQ_{rel} = |GHI / (DHI + DIF) · 100 – 100| have to be below 10% and 20 W m^{-2} for a 15-minute time frame, respectively. This time frame is necessary, because the instruments are a few meters apart, which leads to decorrelation of the individual components and larger residuals the shorter the time scale.
5. For 'good' quality, all three components have to pass the tests. If one or more components include missing or bad data, the data for that time if flagged as 'bad'.

The implementation of these rules are in the published processing code (see Section 2.6), and can be modified to adjust the strictness of quality control. There are only minor differences between these custom 1 Hz based quality flags and the official 1-min BSRN dataset flags. For all data during day time (solar elevation angle above 0 degrees), 97.98% of the flags are similar, 1.26% are bad for custom flags and good in official, and 0.77% are good in custom but

bad in official. Most of these mismatches originate from just a few days and resulting data is otherwise in very close agreement, with the vast majority of data being of good quality. Figure 2.3 illustrates for the whole 1 Hz dataset the data availability after (custom) quality control, and shows that most months and years have near 100% complete and good data for all three measured irradiance components. Figure 2.9 illustrates that after quality control, DIF + DHI = GHI for every month of the year, as a proof data quality. The minor negative bias of DIF+DIR that is visible for some months is within 0.3 to 0.6%, which far exceeds constraints imposed by the official BSRN standard. These residuals are deemed insignificant and have no implications for the use cases of this dataset, as these concern irradiance variability.

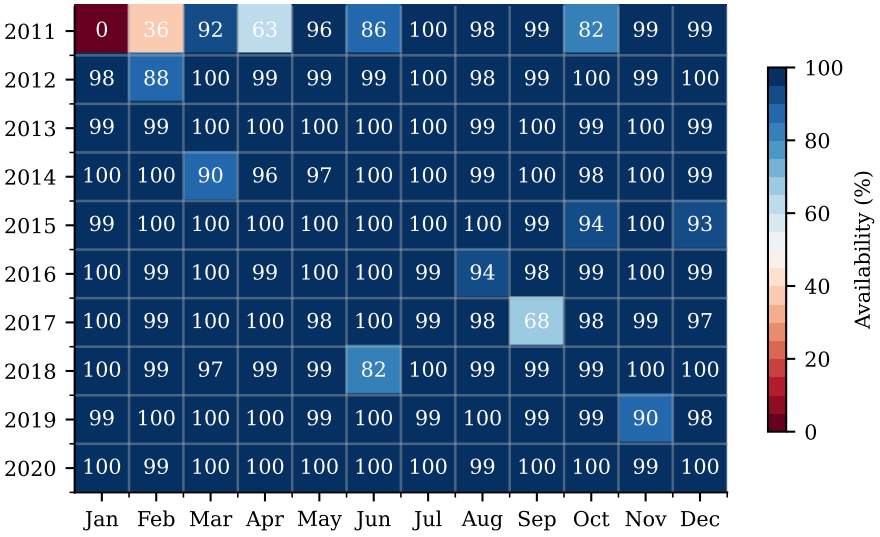

Figure 2.3: BSRN Cabauw 1 Hz data availability per month of available years, during daylight (solar elevation angle above 0 degrees), after custom quality control. Numbers are rounded off percentages.

2.3.2 Nubiscope and satellite processing

The nubiscope and satellite data are used both as a validation dataset for irradiance derived sky types (described in Section 2.3.3), and to provide observations of clouds and sky type for data analysis. Here, we describe the processing applied to the cloud observations, and how the validation dataset is created.

Satellite processing

We classify cloud types using a simple cloud top pressure (CTP) and cloud optical thickness (COT) categorization (see Rossow (2022) ISCCP algorithm description, their Figure 20). The 9 types are cumulus (Cu), stratocumulus (Sc), stratus (St) for low clouds; altocumulus (Ac), altostratus (As), and nimbostratus (Ns) for middle clouds; cirrus (Ci), cirrostratus (Cs), and cumulonimbus (Cb) for high clouds. Cu, Ac, and Ci are the optically thinnest clouds for each altitude, and St, Ns, and Cb the thickest, where Cb spans from low to high altitude as the only exception in this list. In this study, we use it to group together cloud conditions of various

altitudes and optical thicknesses in a more intuitive way, though analyses can be done on the input COT and CTP data rather than derived cloud types. The main limitations are that both the cloud fraction and actual cloud optical thickness contribute to a higher reported optical thickness in a satellite pixel, which is a result of limited spatial resolution, and higher clouds can obscure lower clouds. The spatial satellite product is converted to a time series representative for the BSRN station by determining the most common cloud class within a 5, 10, or 15 km radius around Cabauw, illustrated by the circles in Figure 2.1a. A smaller radius is not possible due to satellite resolution (pixel area $\approx$ 20 km^2) and larger radii become unrepresentative for Cabauw. Cloud cover is derived by calculating the fraction of pixels with clouds within a given radius, which is likely an overestimation due to sub-pixel cloud fractions not always being 1. Overall agreement with the nubiscope is not bad, however, as illustrated by the similar probability densities in Figure 2.4. Correlation coefficients between the two only show marginal improvement between 10 and 15 km. The satellite derived cloud cover overestimates the extremes at [0.0-0.1) and [0.9-1.0] compared to values bins [0.1-0.2) and [0.8-0.9), and does not have the nuances the nubiscope can resolve. For r = 5 km, there are only 4 pixels, so cloud cover from this is too coarse for most applications, but the dominant cloud type derived from this narrow area around Cabauw is expected to be most representative. This might change for high altitude clouds at low solar elevation angles for example, requiring perhaps more sophisticated approaches, and therefore we have included the original spatial satellite fields in our dataset.

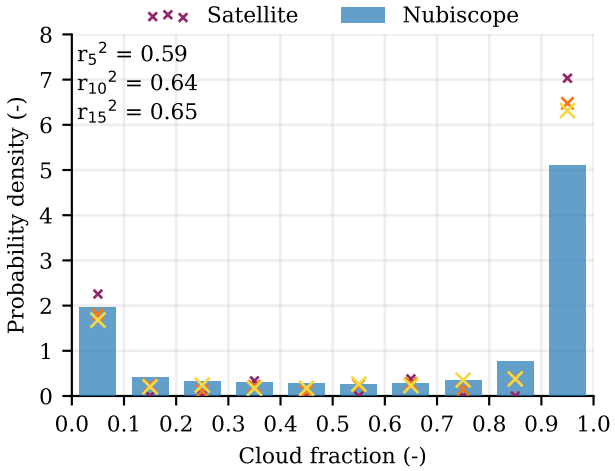

Figure 2.4: Comparison of cloud fraction derived from satellite to the ground-based nubiscope. The analysis is done for radii 5, 10, and 15 km, and show the probability density for 10 bins between 0 and 1 cloud fraction. Satellite radii go from 5 km (dark, small) to 15 km (light, large) cross markers. Correlation coefficients are shown in the top left for each radius. Data ranges from 2014-01 to 2016-12, and is interpolated (nearest-neighbour) to a common 5-minute time axis.

Validation dataset

We derive a validation dataset with clear-sky and overcast classifications based on a combination of the nubiscope and satellite data, to be used for statistical verification of sky types

based on irradiance observations (Section 2.3.3). Because both instruments have their limitations, the idea is to only identify a situation as clear-sky or overcast if both datasets are in agreement. The rest of the preprocessing involves interpolation to a common 1-minute resolution grid, and masking out any data if either of the two products is missing for given a given time. The validation dataset is provided in Mol et al. (2022) for all three radii, though we mostly use r = 10 km, for years 2014 until 2016. Disagreement between the two observational datasets is common, with the nubiscope being roughly 3 or 1.5 times more conservative with classifying a sky type as clear or overcast, respectively. This likely has to do not only with the difference in type of observation (ground-based versus remote sensing), but also in that the nubiscope is a more sensitive instrument, as we illustrated in Figure 2.4 and discussed in Section 2.3.2. In most cases, the nubiscope is more conservative, such that both clear-sky and overcast conditions are mostly controlled by what the nubiscope sees. Figure 2.8 illustrates this best, with the satellite and nubiscope differing in seasonal cycle for clear-sky conditions and in yearly averages for both clear-sky and overcast.

2.3.3 Irradiance classifications

The main addition to the core 1 Hz irradiance time series is the classification of measurements into various categories that describe the type of irradiance variability. We calculate two sets of classification types, one being an instantaneous classification to give a qualification to single measurement point, and the other a more indirect qualification of sky type based on longer time frames. First we describe what the classifications represent and how they are calculated, and then how they are further processed to derive a wide range of interesting statistics about irradiance variability. Examples are shown in Figures 2.5, 2.6, and 2.7, and the public dataset (Mol et al., 2022) includes similar quicklooks for all 10 years of time series.

Cloud shadow and enhancement

One of the most noticeable drivers of intra-day irradiance variability are broken cloud fields making patterns of cloud shadows and cloud enhancements (e.g. Yordanov et al., 2015; Gueymard, 2017; Veerman et al., 2022). Cloud shadows are where (most) direct irradiance is blocked, and cloud enhancement where light scattered by clouds locally coincides with direct irradiance to increase global horizontal irradiance above clear-sky values. We define a shadow where direct normal irradiance (DNI) is below 120 W m^{-2}, which is the inverse of what the World Meteorological Organization defines as sunshine (DNI $\geq$ 120 W m^{-2}, WMO (2014)), and a straightforward implementation. Cloud enhancement requires a more careful approach. We define cloud enhancement as a single measurement where global horizontal irradiance (GHI) exceeds the reference clear-sky (GHI_{cs}). In reality, observed GHI can still fluctuate noticeably in cloud-free conditions, and the GHI_{cs} reference may not be perfect, such that there is some uncertainty in the detection for weak cases of cloud enhancement. To prevent false positives in the detection algorithm, we first apply an activation threshold of GHI exceeding GHI_{cs} by 1% and 10 W m^{-2}. Both a relative and absolute threshold are used, as clear-sky irradiance ranges from 10^0 to 10^3 W m^{-2} as function of the solar elevation angle (i.e., time of day). 10 W m^{-2} is based on 1% of the typical order of magnitude for clear-sky

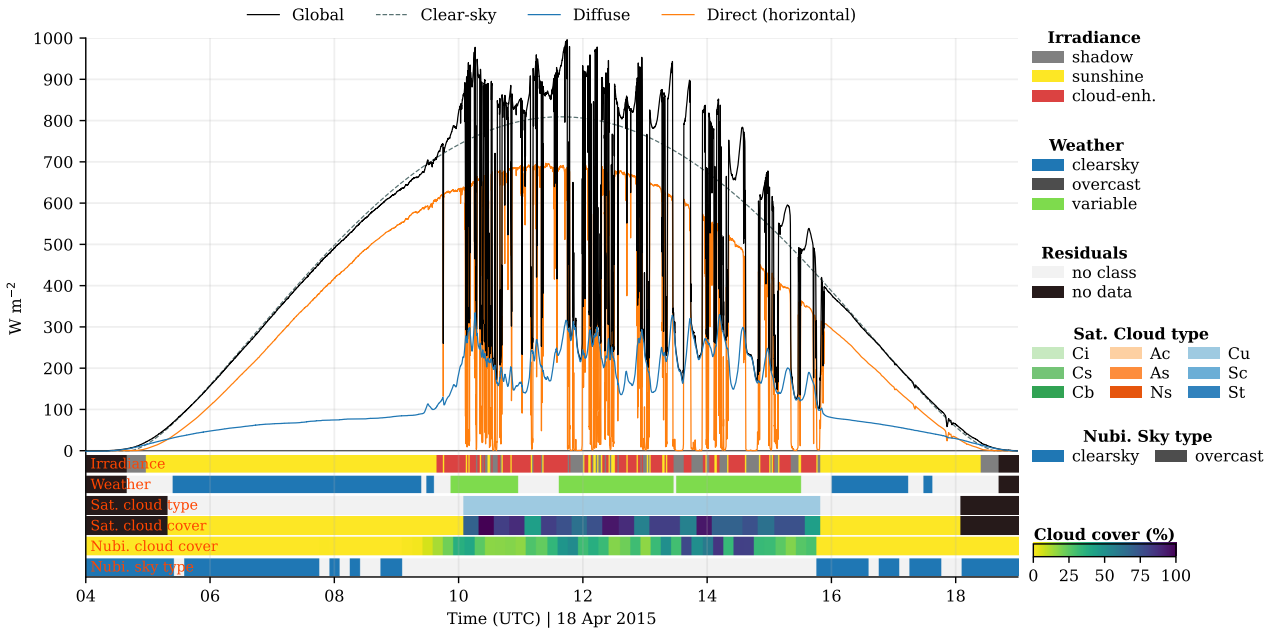

Figure 2.5: Surface solar irradiance time series at 1 Hz, irradiance classifications, and cloud observations for 18 April 2015. It starts with clear-sky conditions and turns into highly variable surface irradiance thanks to scattered boundary layer clouds. The three measured irradiance components, global, diffuse, and direct horizontal irradiance are shown together with modeled (CAMS McClear) clear-sky irradiance.

irradiance around noon for Cabauw. When the threshold is reached, adjacent measurements are also marked as cloud enhancement so long as they exceed GHI_{cs} by 0.1%. Edge cases at low solar elevation angles are removed by requiring DNI to be at least 10 W m^{-2}. All of these thresholds are chosen to enable us to capture all but the weakest of cloud enhancements, which arguably are not important. The residual third class is called 'sunshine', which is the WMO definition of sunshine minus cloud enhancement. Detection criteria can be adjusted in the code and recalculated, or another level of filtering can be applied after classification through the derived event statistics (discussed in Section 2.3.4). Examples of the classifications are shown in the top color-coded bar beneath the time series in Figures 2.5, 2.6, and 2.7.

Overcast, clear-sky, and variable irradiance

The second group of classifications represents irradiance 'weather' type, or sky type, based on irradiance data only. The weather types are clear-sky and overcast for smooth and predictable surface irradiance, and a third class of 'variable' irradiance representing pronounced and unpredictable 3D radiative effects to contrast the former two. The way these classifications are derived is partially based on subjective thresholds and assumes good quality clear-sky data, and thus we validate against satellite and ground-based cloud cover observations.

We classify as clear-sky those points in the time series for which, in a 15-minute centered moving window, GHI stays within 3% or 5 W m^{-2} of GHI_{cs} with a maximum standard de-

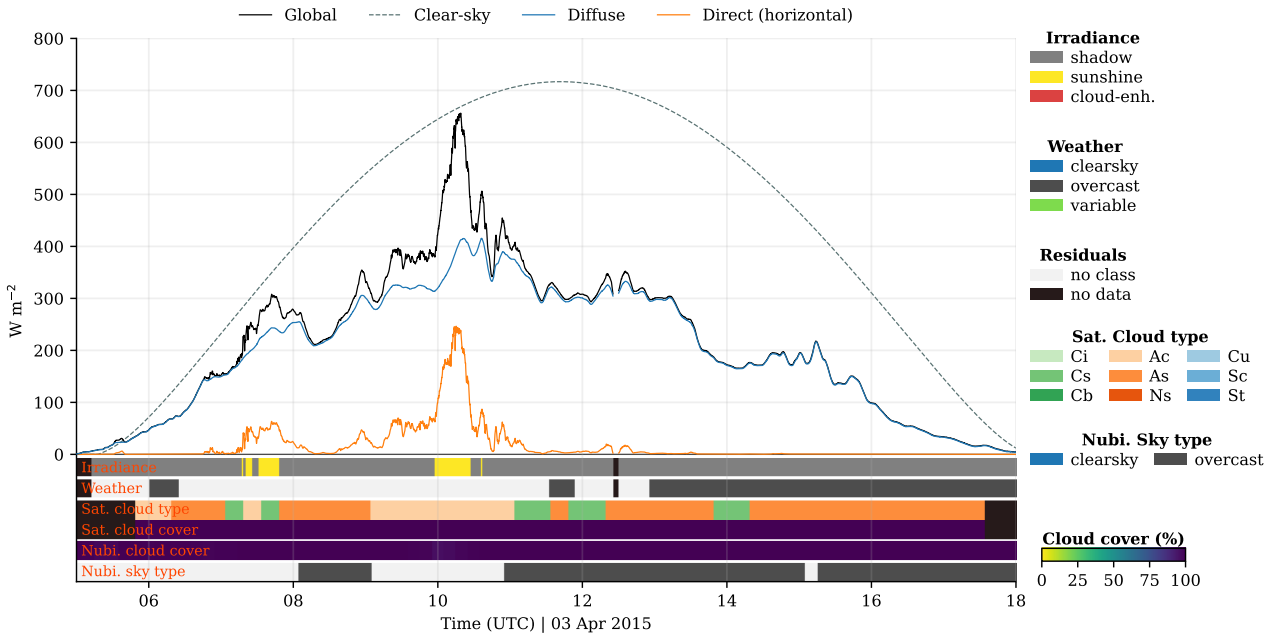

Figure 2.6: Surface solar irradiance observations of a mostly overcast day (3 April 2015), similar layout as Figure 2.5. The satellite and nubiscope observations indicate overcast conditions of mostly opaque mid to high level clouds (altostratus (As) or cirrostratus (Cs)), though there are brief periods of partially transparent clouds (altocumulus (Ac)).

viation of the ratio GHI/GHI$_{cs}$ = 0.01 within that window. This irradiance based algorithm emphasizes smoothness, and thus predictability, more than exactly matching GHI$_{cs}$, so as to not rely too much on CAMS McClear being perfectly accurate. Clear-sky conditions are uncommon, occurring between 5 to 15% of the time depending on observational method (Figure 2.8). Skill scores indicate that the irradiance based classification misses almost half the cases (probability of detection close to 50%), and is generally too conservative (bias < 1) with respect to the validation dataset (see Table 2.1). The negative bias against the validation dataset, which is not what Figure 2.8 shows, is due to the skill scores being calculated for cases only when there is agreement between the satellite and nubiscope, rather than for all available data in Figure 2.8. The order of magnitude of occurrence is similar to what the validation dataset suggests, but the seasonal cycle is not reproduced, though seasonality between the irradiance classification and satellite alone are similar. For 2014 and 2015, the seasonal correlation to the nubiscope is also much better, but in 2016 there were many cases where the nubiscope saw thin cirrus (cloud cover $< 5\%$, August 17, 18, 23, 24, and 25) rather than clear-sky. In all these cases, GHI $<$ GHI$_{cs}$, consistent with thin cirrus attenuating incoming solar radiation slightly, and not part of the validation set because of disagreement between satellite and nubiscope. It appears (from Table 2.1 and Figure 2.10) that there is poor skill in the irradiance-based classification, though manual inspection of quicklooks gives a different impression and most of the bias shown in Figure 2.10 appears to stem from cases with thin cirrus. If one wants to filter out the thin cirrus cases, the classification threshold can be set more strict and thereby limit cases to more true clear-sky. Figure 2.6 shows a case with overall agreement between the nubiscope, satellite, and irradiance based clear-sky classification.

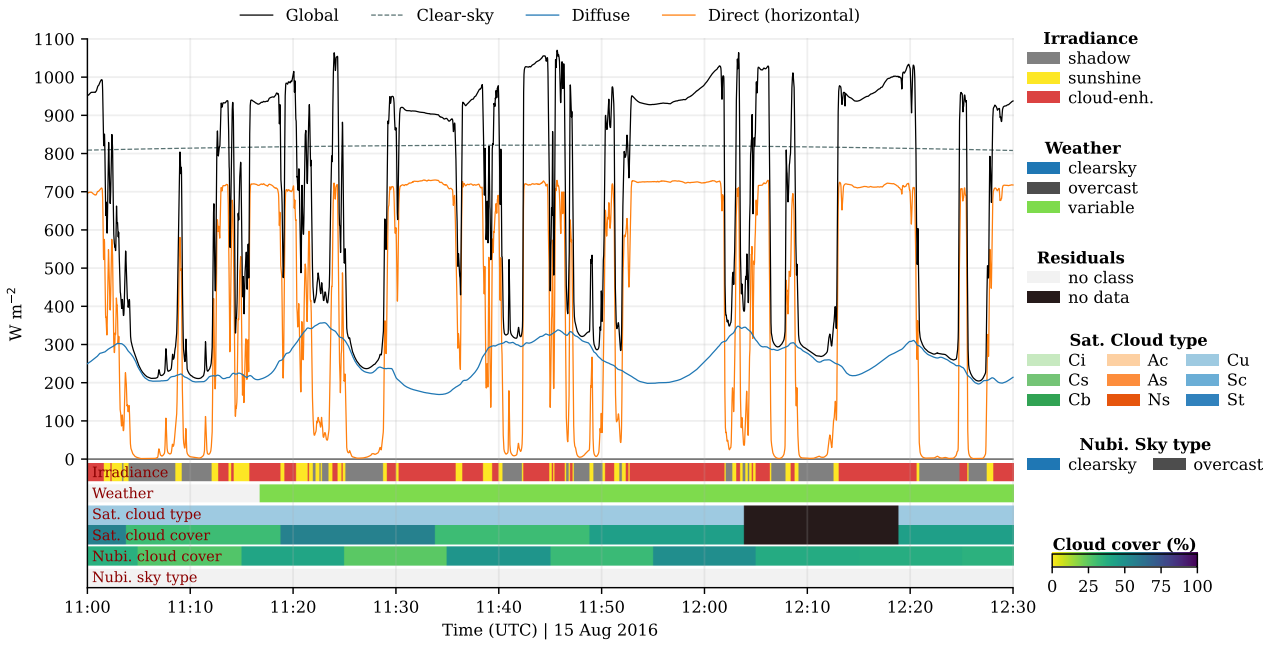

Figure 2.7: Detailed example of cloud-driven irradiance variability. Similar to Figure 2.5, but for 90 minutes of 15 August 2016.

We refer the reader to the public dataset (Mol et al., 2022) with time series quicklooks for many more examples.

We define overcast weather as a period of 45 minutes for which the sum of DNI is below 1% of GHI_{cs}, and the average below 10 W m^{-2} to catch rare edge cases. This class is indicative of continuous, optically thick and persistent cloud cover, which is a common occurrence in the Netherlands (20 to 50% of the time depending on the season) and does well against the validation dataset. Probability of detection is high (92%), with 6% false alarms and only a slight negative bias of -1.7%. Scores slightly move toward positive (+2.6%) or negative (-5.1%) bias when shortening or lengthening the moving window to 15 minutes and 60 minutes, respectively. Although a cloud cover of 100% as seen by the nubiscope and satellite is classified as overcast in the validation dataset, cloud cover does not imply the optical thickness is high enough to block all direct irradiance. This distinction is illustrated in Figure 2.6, which show good agreement for overcast conditions overall, but there is still some irradiance variability with 100% cloud cover around 10 UTC. This example emphasizes our definition of overcast as smooth and predictable diffuse irradiance weather as opposed to a sky type with 100% cloud cover. The seasonal cycle between the irradiance based sky type and nubiscope correlate well (Figure 2.10), whereas the satellite yearly cycle is less pronounced.

Finally, the variable weather class is defined as any 60-minute window in which 10 transitions from a shadow to cloud enhancement or vice versa occur, built upon the instantaneous classifications defined in Section 2.3.3. It is indicative of weather associated with a characteristic bi-modal distribution of irradiance, cloud enhancements, and at least a handful of large fluctuations in a short time frame, all of which current numerical weather prediction

Table 2.1: Skill scores for irradiance based sky type classifications compared to the validation dataset (satellite + nubiscope). Scores are based on a contingency table approach. POD is Probability Of Detection, FAR means False Alarm Ratio.

Year	Accuracy	Bias	POD	FAR	Samples (hours)
Clear-sky					
2014	0.969	0.624	0.478	0.233	3346
2015	0.962	0.610	0.494	0.191	3311
2016	0.968	0.666	0.486	0.271	3244
Overcast					
2014	0.951	0.979	0.912	0.068	2914
2015	0.954	0.971	0.914	0.059	2946
2016	0.956	0.980	0.923	0.058	2872

models cannot reproduce. This classification does well in locating highly variable irradiance conditions, of which examples are shown in Figure 2.5 and 2.7, and can for example be used to find case studies.

2.3.4 Event statistics

Within the classified irradiance time series, we call sections of cloud enhancements or shadows 'events'. The 10 years of irradiance time series contain 184,447 cloud shadows and 186,685 cloud enhancement events. For every event, the start and end time are used to select complementary radiation and meteorological data, such that every cloud enhancement and shadow event can be characterized. Notable examples are statistics of event duration, maximum cloud enhancement strength, minimum direct irradiance 'min(DNI)', mean 200 meter wind speed, dominant cloud type, maximum cloud top height, and mean solar elevation angle. Event statistics such as these allow for filtering of events according to additional criteria, e.g. for comparing events of different magnitudes or finding the most extreme cases of cloud enhancement for a given cloud type. Event statistics for cloud shadows and enhancements for are included in the public dataset (Mol et al., 2022).

2.3.5 Daily statistics

For case study selection or climatological overviews, we calculate daily statistics, which are mostly aggregates of irradiance and classification data. This statistic file is included in the public dataset. We use this to create figures such as Figures 2.3, 2.9, and 2.10, and to find specific case studies as detailed in Table 2.2.

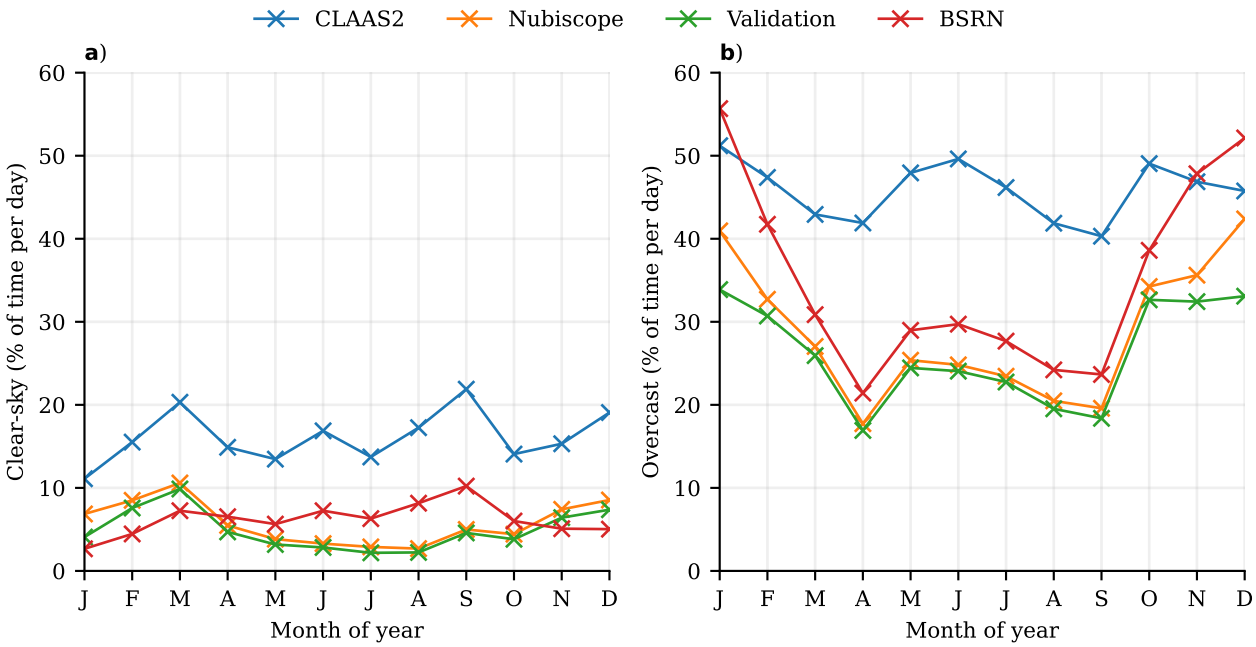

Figure 2.8: Comparison of sky type classifications based on satellite time series (r = 10 km), nubiscope, and 1 Hz irradiance observations. The validation period is from 2014 until 2016, in units relative to available data during daylight (solar elevation angle $\alpha > 0$ degrees).

2.4 Examples and use cases

The following section provides some examples and (potential) use cases of the dataset, including previously completed work. Veerman et al. (2022) and Tijhuis et al. (2023) research 3D radiative transfer modelling approaches for cumulus case studies, where 1 Hz irradiance time series and statistics are used as validation. In Chapter 6, we show how the spatiotemporal scales of cloud shadows and enhancements are described by power laws and driven by cloud size distributions, using the event statistics as described in Section 2.3.4.

Figures 2.9 and 2.10 give an overview of the seasonal and yearly variability of solar irradiance and its classifications that characterize the mid latitude climate of Cabauw. Figure 2.9 also partially serves as validation of the BSRN instrumentation, with the direct and diffuse components adding up to GHI as should be the case. Figure 2.10 illustrates the typically overcast conditions during winter, and highly variable irradiance conditions during summer with significant year to year variability.

In order to find specific types of case studies for analysis, you can use either the event statistics or daily statistics to query and filter specific conditions. As an example, we use the daily statistics file and Python's Xarray to find case studies of the most variable irradiance throughout the day or specific cases where overcast conditions transition to clear-sky (or vice versa), which have a potential for brief periods of strong variability and cloud enhancement. These examples are shown in Table 2.2, and the code is publicly available (Section 2.6).

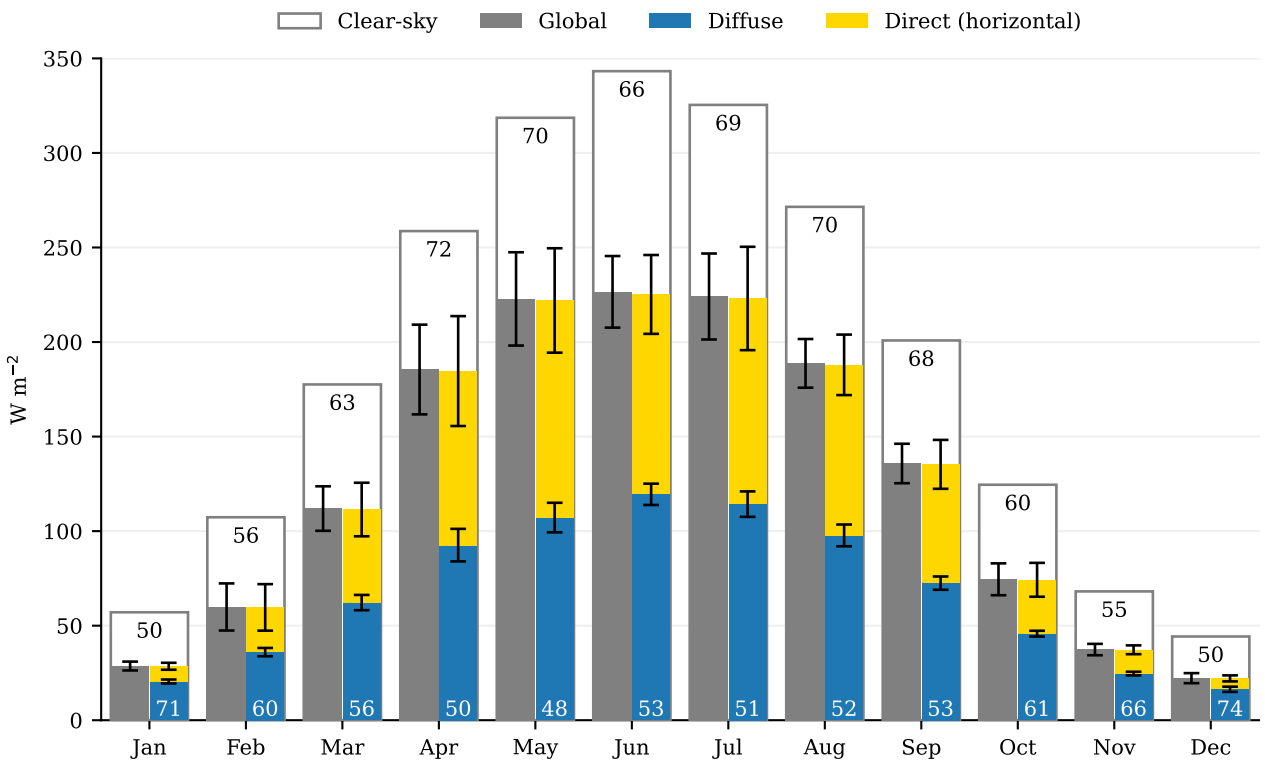

Figure 2.9: Surface irradiance climate for period 2011-02 until 2020-12 based on the 1 Hz dataset of all three components. The numbers in the bottom indicate the percentage of diffuse irradiance (DIF) to global horizontal irradiance (GHI). The error bars indicate, for each component, the year-to-year standard deviation. The white bars encompassing the three components is the clear-sky irradiance (GHI_{cs}) for each month, based CAMS McClear, where the numbers in the top are the percentage of GHI compared to GHI_{cs}. Only days with $>$ 95% of data completeness are included.

Table 2.2: Examples of finding case studies using daily statistics. The table shows for a custom period (2014-2016) the top 5 cases for two example queries. The first is the absolute most variable irradiance weather. The second are cases with at least 5% overcast, variable and clear-sky, sorted by those with the most variability, which is a way to find case studies with overcast to clear-sky transitions.

Top cases	Most variable	Overcast ↔ clear-sky
1	2015-07-22	2015-04-30
2	2015-07-17	2016-05-17
3	2016-07-02	2015-05-12
4	2014-08-09	2016-08-06
5	2015-06-18	2016-04-19

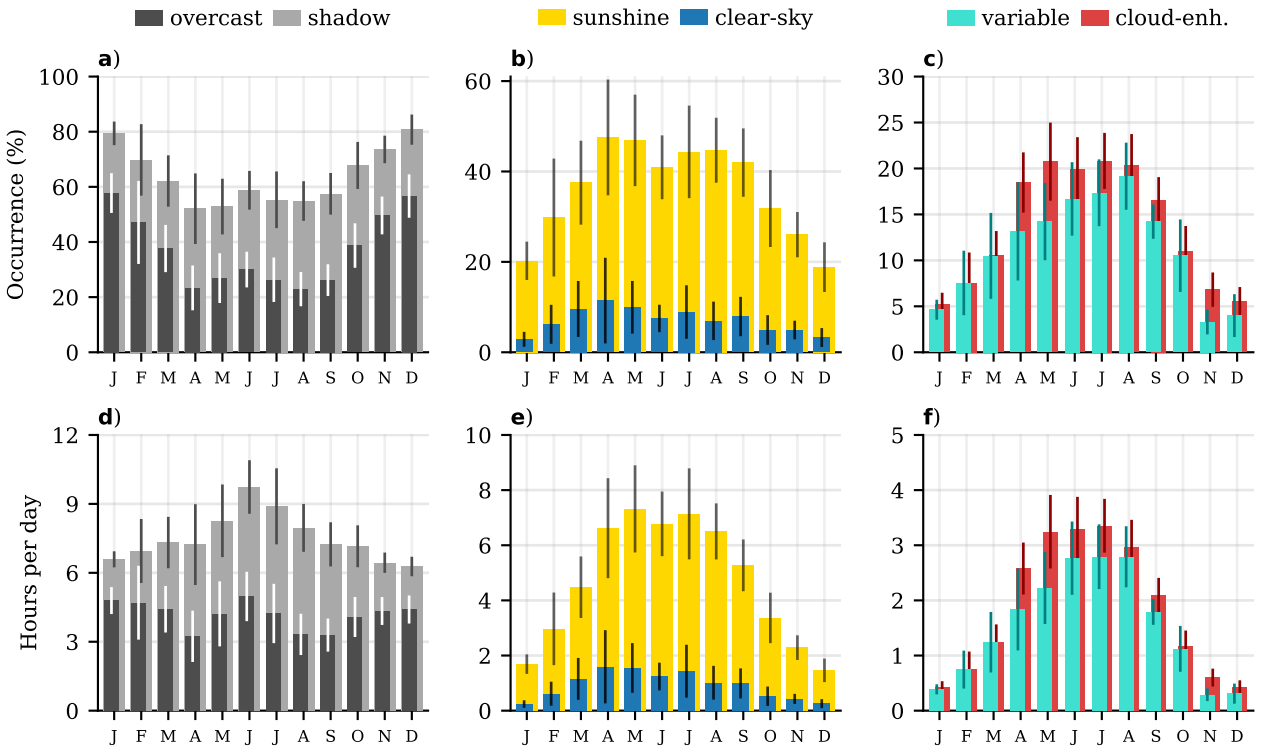

Figure 2.10: Instantaneous and weather classification occurrence per month, showing the relative (top row) and absolute (bottom row) climatology of each classification throughout the year for all available data (2011-02 to 2020-12). Here, sunshine, also includes the portion marked as cloud enhancement, such that shadow + sunshine = 100%. See Section 2.3.3 for the six classification definitions shown here. The relative occurrence is expressed as a percentage of daylight (solar elevation angle $> 0°$), absolute occurrence is expressed in average hours per day. Error bars indicate the year-to-year standard deviation.

2.5 Conclusions

In this paper, we describe a high resolution, 10-year long observational dataset of detailed surface solar irradiance, complemented with meteorological data. Using time series classification algorithms, we derive statistics about sky type and irradiance variability. We provide examples and use cases of this dataset to illustrate its potential, ranging from case study selection and model validation to fundamental insight into drivers of irradiance variability. With all data and processing code publicly available, the user is free to modify our classification algorithm to their liking and validate against independent observations, or expand upon the large set of statistics already provided. Quicklooks for all available days from 2011-02 until 2020-12 are provided to get familiar with the dataset contents and get an impression of the many different types of weather conditions at Cabauw. We believe this dataset is of great use in research into cloud driven irradiance variability, and it provides a necessary validation reference for models that are starting to resolve the full spectrum of variability.

2.6 Open data

1 Hz GHI, DIF and DNI observations of the BSRN station at Cabauw are published on Zenodo (Knap & Mol, 2022), Irradiance time series classifications, supplementary data, quality control, event and daily statistics, and satellite data are published as a separate, complementary dataset on Zenodo (Mol et al., 2022). Satellite data for an area around Cabauw is taken from the CLAAS2 open access dataset described in Benas et al. (2017), and included in the previous dataset for 2014 to 2016. Also included there is the nubiscope data (Wauben et al., 2010), taken from the KNMI Data Platform (`https://dataplatform.knmi.nl/dataset/cesar-nubiscope-cldcov-la1-t10-v1-0`) for years 2014 to 2016. All code to reproduce the classifications from the irradiance observations, event and daily statistics, and figures presented in this paper is archived at `https://zenodo.org/record/7851741`.

Chapter 3

A new accurate low-cost instrument for fast synchronized spatial measurements of light spectra

This chapter is based on:

Heusinkveld, B. G., Mol, W. B., & van Heerwaarden, C. C. (2023). *A new accurate low-cost instrument for fast synchronized spatial measurements of light spectra*. In Atmospheric Measurement Techniques. Copernicus GmbH. https://doi.org/10.5194/amt-16-3767-2023

Abstract

We developed a cost-effective Fast-Response Optical Spectroscopy Time-synchronized instrument (FROST). FROST can measure light spectra in 18 wavebands ranging from 400 to 950 nm with a 20 nm full-width half-maximum bandwidth. The FROST 10 Hz measurement frequency is time-synchronized by a global navigation satellite system (GNSS) timing pulse, and therefore multiple instruments can be deployed to measure spatial variation in solar radiation in perfect synchronization. We show that FROST is capable of measuring global horizontal irradiance (GHI) despite its limited spectral range.

It is very capable of measuring photosynthetic active radiation (PAR) because 11 of its 18 wavebands are situated within the 400-to-700 nm range. A digital filter can be applied to these 11 wavebands to derive the photosynthetic photon flux density (PPFD) and retain information on the spectral composition of PAR. The 940 nm waveband can be used to derive information about atmospheric moisture.

We showed that the silicon sensor has undetectable zero offsets for solar irradiance settings and that the temperature dependency as tested in an oven between 15 and 46 °C appears very low (-250 ppm K^{-1}). For solar irradiance applications, the main uncertainty is caused by our polytetrafluoroethylene (PTFE) diffuser (Teflon), a common type of diffuser material for cosine-corrected spectral measurements. The oven experiments showed a significant jump in PTFE transmission of 2 % when increasing its temperature beyond 21 °C.

The FROST total cost ($<$ €200) is much lower than that of current field spectroradiometers, PAR sensors, or pyranometers, and includes a mounting tripod, solar power supply, data logger and GNSS, and waterproof housing. FROST is a fully standalone measurement solution. It can be deployed anywhere with its own power supply and can be installed in vertical in-canopy profiles as well. This low cost makes it feasible to study spatial variation in solar irradiance using large-grid high-density sensor setups or to use FROST to replace existing PAR sensors for detailed spectral information.

3.1 Introduction

Understanding solar irradiance and its interaction with clouds and vegetation is of utmost importance in unraveling the complexity of feedback systems that determine our weather and climate. Cloud-shading dynamics of irradiance are highly dynamic (Lohmann, 2018), and cloud-resolving models (CRMs) are unable to resolve short time intervals and small spatial scales. At grid scales below 1 km, 3-D radiative transfer models can greatly improve the 3-D surface and atmosphere heating rates in atmospheric models (Cahalan et al., 2005; Jakub & Mayer, 2015). A good example is the complexity of the radiative effects of shallow cumulus clouds and their interactions with a vegetated surface. Traditional 1-D radiation models produce unrealistic surface radiation fields, but Veerman et al. (2020) showed that a 3D radiation transfer model could greatly improve the coupling mechanisms between clouds and the land surface. The small circulations, turbulence, and combined cloud micro-

physics in convective boundary layers are all highly nonlinear and complex. CRMs are crucial for improving weather forecasting models and for the energy meteorology sector. Kreuwel et al. (2020) showed that solar-powered grid loading is highly dynamic and especially so for smaller household photovoltaic (PV) systems, leading to grid overload challenges at very short time intervals of seconds. High-quality observations, both in high resolutions spatially and with a high temporal resolution, are required to test such models, but so far observations are lacking (Guichard & Couvreux, 2017).

Yordanov et al. (2013) showed that cloud enhancements can significantly increase solar irradiance levels ($>$ 1.5 times), which result in peak irradiance levels well exceeding extraterrestrial levels even at high altitudes and latitudes (Yordanov et al., 2015). They used fast-response silicon sensors, and their highest detected irradiance bursts lasted about 1 s, which led them to believe that the required light sensor response time should be at least 0.15 s, much faster than traditional thermopile pyranometers with a response time of several seconds. The slow response time of those thermopile sensors is related to the thermal mass of the thermopile sensor. Semiconductor light sensors respond faster because photons directly mobilize electrons that can be measured directly. The downside of semiconductor light sensors is their limited and non-flat spectral response and temperature sensitivity. Thermopile-based pyranometers are also expensive as compared to a silicon-based solution, which limits their large-scale use in meteorological measurement networks. Martínez et al. (2009) showed that a factor-of-10 reduction in pyranometer costs as compared to a thermopile sensor is possible with the use of a silicon photodiode; however, their spectral response is limited (400 to 750 nm) and it has non-flat spectral response. A major solar spectral change occurs in the infrared due to water absorptions bands, which leads to an overestimation for clear-sky conditions and an underestimation for overcast skies when calibrated for average weather conditions.

The spectral-response limitations of the photodiode used by Martínez et al. (2009) can be improved with a wider spectral-response silicon-type pyranometer such as applied in the LI-COR LI-200SZ as demonstrated by Michalsky et al. (1991). They compared the LI-COR LI-200SZ with a thermomopile pyranometer (Kipp & Zonen CM 11). The CM 11 has a flat spectral response (300 to 2500 nm), whereas the LICOR LI-200SZ exhibits a very non-linear and limited spectral response starting at 400 nm, increasing 5-fold in sensitivity towards its peak at around 1000 nm, and then sharply dropping off to zero at 1100 nm (Alados-Arboledas et al., 1995). Their main uncertainty is related to the temperature dependence of silicon sensors. After a temperature correction, these performed similarly to thermopile pyranometers (11.4 $\mathrm{W\,m^{-2}}$ RMSEs) under clear- and cloudy-sky conditions. This is surprisingly accurate because LI-COR calibrates their pyranometer against a reference thermopile pyranometer, and therefore a change in the solar spectrum may affect its accuracy. Michalsky et al. (1991) argued that the clear- or cloudy-sky global horizontal irradiance (GHI) spectra are similar because of clouds mixing the direct and blue skylight. This, however, is contradicted by a recent study by Durand et al. (2021), where they investigated the spectral differences between clear and overcast skies. They showed that clouds, in relative terms, enrich GHI spectra in wavelengths $<$ 465 nm and deplete them in wavelengths $>$ 465 nm. This may well ex-

plain why the LI-COR sensor performed so well because its main sensitivity is in wavelengths $>$ 465 nm, thus indirectly correcting for the reduced infrared in the major water absorption bands beyond its spectral range.

Optoelectronics are evolving rapidly, and innovations in semiconductor integration with optical components and microprocessors are paving the way for cost-effective spectrometers that can provide even temperature-compensated spectral details about solar radiation. A leading manufacturer in this field is Austria Micro Systems (AMS), which offers various intelligent light-sensing products that are capable of measuring light intensity within multiple optical wavebands. These sensors are mass-produced, resulting in low-cost sensors. Tran & Fukuzawa (2020) tested such a cost-effective 18-band multi-spectral sensor (AS7265x, AMS) for spectroscopy of fruit (between 400 and 950 nm), and useful information could be derived. Such filter spectroscopy sensors would be very interesting for solar global horizontal irradiance (GHI) measurements. Quantifying the spectral signature of radiation is very relevant, since clouds and air pollution modify the solar light spectrum and light scattering. Additionally, multiple reflections between various ground and water surfaces and clouds will further influence the light spectral composition. This is especially relevant in the photosynthetic active radiation (PAR) wavelengths for vegetation cloud feedbacks, since PAR affects photosynthesis and evapotranspiration Durand et al. (2021).

Here we present the development of a cost-effective fast-response solar light sensor grid for spatially and temporally high resolution multiple-light-waveband-resolved GHI measurements. The required large number of sensors necessitates cost-effective design optimization.

Additionally, we tested these sensors for meteorological, photosynthesis, and remote sensing applications as well as performance both in the lab and in field experiments.

3.2 Instrument design and measurement method

The measurement system we developed is depicted in Figure 3.1 (Fast-Response Optical Spectroscopy Time-synchronized instrument - FROST) and consists of a silicon light sensor chipset (AMS AS7265x), a global navigation satellite system (GNSS) for time synchronization, a cosine corrector light-diffusing input port, and a microcomputer. See Table 3.1 for a list of components.

Time-synchronized measurements are achieved using a hardware GNSS receiver timing pulse (PPS) to trigger each measurement, and time-stamped data are processed and collected by a microcomputer board (Figure 3.1, Table 3.1).

The light sensors are mounted on camera tripods, which makes leveling easy (Figure 3.2). A camera metal shoe mount adapter was glued under the polycarbonate housing for fast mounting. For winds $>$ 6 m s^{-1} it is advised to use tent herrings to fix the tripod to the ground. The power consumption is 0.5 W, and a 6 Ah LiPo battery will last for 40 h without sunshine. Battery capacity is reduced at lower temperatures. The 4.2 W polycrystalline solar

Table 3.1: List of components for the waterproof solar-powered spectrometer.

Component	Manufacturer and model	Price (EUR)
Spectroscopy chipset	AS7265x spectral sensors, triple (AMS, Austria) with interfacing logic mounted on a printed circuitboard (PCB) by SparkFun (USA)	70.00
Optical filter	Schott heat-absorbing colored glass filter KG3 or KG1, 2 mm (Germany)	11.00
UV sensor	GUVA-S12SD (optional, with a second thin PTFE diffuser)	1.70
PTFE diffuser	32 mm diameter, cut from a plate (S-Polytec GmbH, Germany)	3.00
GNSS receiver	TOPGNSS GN-901, China; GPS and GLONASS receiver	6.00
Microcomputer	Arduino MKR Zero	23.00
Memory card	Kingston Canvas Select Plus microSDHC 32 GB	4.00
Breadboard	Solderless PCB breadboard mini protoboard	0.90
Solar panel	First Solar, China; CNC165x165-5, polycrystalline, 4.2 W, 5 V, 840 mA, 165 $\times$ 165 mm	7.00
Battery	Li-ion battery LP906090JH, Jauch, Germany	30.00
Charger controller	Mini solar LiPo charger board CN3065	1.40
Box	Outdoor junction box 100 $\times$ 150 $\times$ 70 mm waterproof IP65, shockproof ABS plastic; Manhua, China (AliExpress)	9.00
Tripod mount adapter	Camera metal shoe mount adapter 1/4 in. thread	0.75
Tripod	König KN-TRIPOD21/4 camera tripod, pan and tilt 130 cm	12.00
Ground anchor	Tent herring	1.00
Adhesive sealant	Permatex 81158 or Bison black silicone adhesive	1.00

panel together with a LiPo charge regulator is a reliable power supply solution for continuous operation in the Dutch climate from April to September. The solar panel is glued on a specially shaped wooden frame that slides over the tripod center tube, with the solar panel sides resting against the two outer tripod legs (Figure 3.2). It is fixed to the rear leg with a thin metal wire. Hot glue appeared unsuitable for the panels, and it is advised to use epoxy glue.

The polytetrafluoroethylene (PTFE) diffuser was glued to the box by roughening the surfaces and using a black silicone adhesive around the diffuser edges.

The correct synchronization of the sensor grid measurements is essential, and several options were considered, such as a network configuration with synchronized triggering at fixed time intervals. Wires in the field were not an option due to logistic challenges, and radio communication is possible but adds to the cost with reduced reliability due to radio interference. As a robust option, a GNSS receiver was chosen that constantly synchronizes its internal time to an international clock standard. Similar timing synchronizations are used for sensors grids in seismic activity monitoring of volcanos where timing is essential to determine seismic propagation and where synchronization accuracy of 50 ns could be achieved (Lopes Pereira et al., 2014)

3.2.1 Light sensor

The light-sensing element is the AMS AS7265x, a smart spectrometer sensor capable of measuring light at 18-channel 20 nm full-width half-maximum (FWHM) bandwidth from visi-

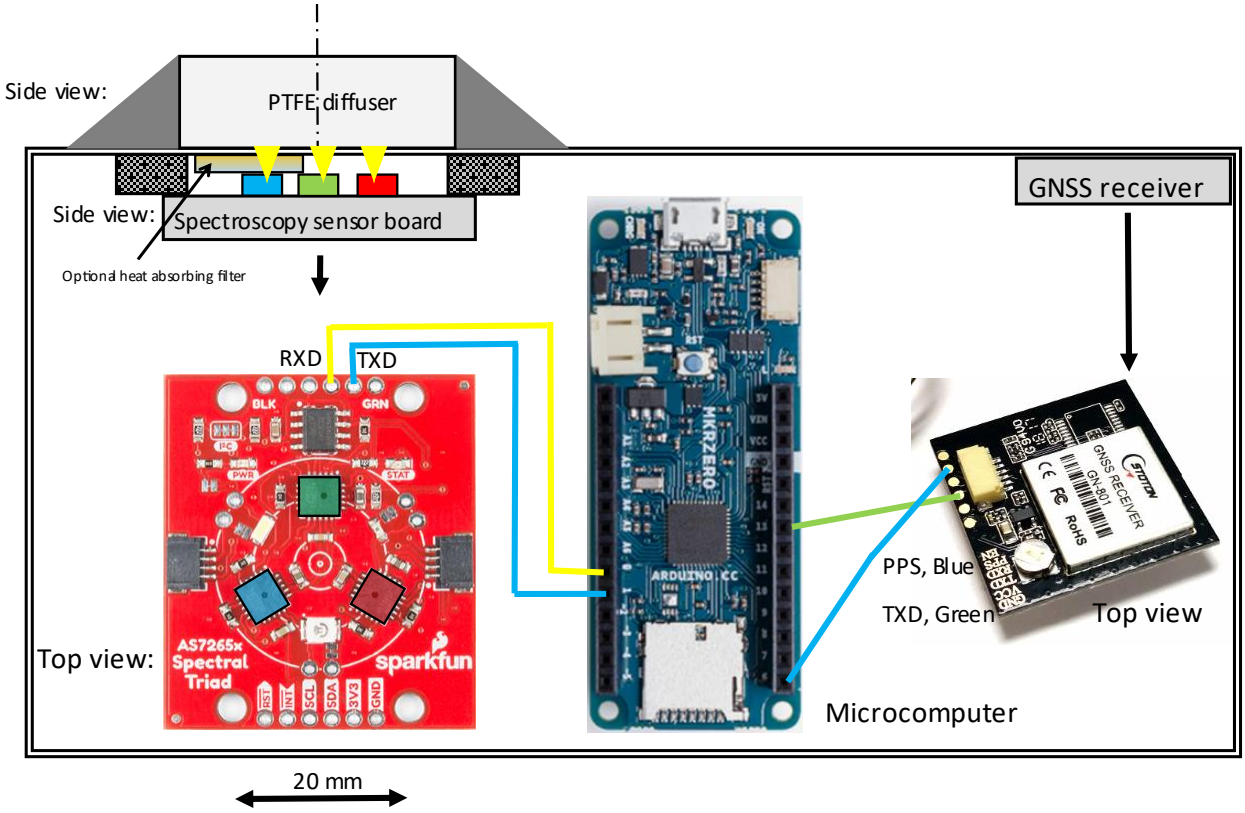

Figure 3.1: Mechanical layout and wiring diagram of the FROST spectrometer (sensor: 3.2 mm below a Teflon filter with radius of 32 mm). For easy identification, we color-coded the three light sensors (blue, green, and red), each measuring six channels. RXD stands for received data and TXD stands for transmitted data.

ble and near-infrared spectral bands (410 to 940 nm) with an electronic shutter (manufacturer: AMS, Australia). It has a broad operational temperature range from -40 to 85 °C. The spectrometer consists of three separate integrated circuits with each including six silicon-based photodiodes with integrated optical bandpass interference filters, micro-lenses, a programmable analog amplifier, an analog-to-digital converter, and a microprocessor. We identify the AS72651, AS72652, and AS72653 as the blue, red, and green sensors, as indicated in Figure 3.1. The integrated light interference filters are directly deposited onto the silicon. Factory calibration values are stored inside the internal memory. Two serial communication options are available for interfacing with a microcomputer: a universal asynchronous transmission (UART) and a synchronous serial transmission (I2C) port. The three light sensor view angles are limited by the chip-housing light input port to 41°, which ensures that the optical interference band filters stay within the 20 nm FWHM and ± 10 nm center-wavelength specifications. AMS state that their filter stability (in time and against temperature) is not detectable but do not provide further specifications. They do mention that the wavelength accuracy is within ± 10 nm.

The AS7265x triple set of light sensor chips, each capturing six light wavebands, poses a challenge to couple optically all three to the same sensing area and to assure a good cosine

Figure 3.2: FROST with solar panel mounted on a camera tripod.

response needed for the accurate measurement of GHI. The limited opening angle poses an additional challenge for GHI measurements, since they require a viewing angle of 180°; therefore, an achromatic cosine-corrected diffuser is required.

3.2.2 Diffuser material

Teflon (PTFE) material is commonly used as an effective light diffuser, with a large spectral transmission range starting below 300 nm, and is available from various manufacturers. However, PTFE light transmittance exhibits a temperature dependency caused by a major phase change in its crystalline structure at 19 °C. The phase change can cause a significant change in transmittance. Ylianttila & Schreder (2005), tested three commercially available PTFE diffusers and found transmission changes between 1 % and 4 % at the phase change temperature. By comparison, they also showed a quartz diffuser with a linear response to temperature (0.035 % $°C^{-1}$) without the sudden transmission jump as found in the PTFE diffusers. Despite this, PTFE was chosen for FROST as a cost-effective diffuser to maximize the amount of sensors.

The diffusers were cut from PTFE plates (S-Polytec GmbH, Goch, Germany) using a vice and a hole punch to press round diffusers. Diffusers 10.6 and 2.0 mm were tested. The transmission temperature dependency of our PTFE diffusers was tested in a temperature-controlled oven with a cooler (WTB Binder, Germany, with forced convection and Eurotherm temperature controller). The oven is equipped with a glass front door, and the lowest possible temperature setting was kept above the dew point temperature of the laboratory to avoid

moisture condensation issues. An LED light source (LCS, 17 W, 2500 lm) was chosen for its high output and limited thermal infrared and was powered by a stabilized voltage power supply. The LED was placed outside the oven in front of the oven's glass door about 1 m away to minimize lamp heating. A second light sensor was placed outside the oven next to the lamp to monitor its output. Diffuser light transmission measurements were corrected for variation in lamp output. Subsequently, the light sensor without a diffuser was tested. Temperature sensitivity measurement results are presented in Section 3.3.2.

The spectrometer performance was also tested at the DWD (German Weather Service) radiation calibration facility in Lindenberg, Germany. The spectrometer output was compared against a calibrated xenon light source, and the intensity was adjusted by varying the lamp sensor distance between 0.5 and 0.7 m. The possible spectral crosstalk of infrared light was tested by placing a very steep long-pass interference filter with a cut-on wavelength of 1000 ± 9 nm (dielectric-coated long-pass filter, 25.4 mm diameter, 1.1 mm thick, transmission > 95,%, OD5 blocking, Edmund Optics, stock no., 15-463) in front of the sensor. The long-pass filter blocks all sensor wavebands, and any remaining signal is then considered infrared crosstalk. The position of the optical waveband filters was tested using a Cary 4000 (Agilent, USA) UV-Vis-NIR spectrophotometer at Wageningen University, the Netherlands. Results are presented in Section 3.3.1.

3.2.3 Cosine response

The cosine response was determined by placing an LED light source (LED light bulb 2500 lm, diameter 0.1 m) and our light sensor 5 m apart, both on tripods at 1 m height. Since a darkroom was not available, the measurements were performed outdoors at night to avoid reflection from ceilings and walls. A night with low humidity was chosen to minimize aerosol light scattering. The direction of the light sensor was adjusted from 0° (viewing the light source) to 90° (perpendicular to the light beam). To keep the distance between the sensor and light source constant during rotation, the plane of rotation was located exactly at the diffuser surface. A shading screen was placed between the light source and sensor to shade the ground surface to avoid any light reflection into the sensor. Results are presented in 3.3.3.

3.2.4 Time synchronization

Instead of using a GNSS for synchronizing an internal clock or using the serial date and time output, we use the very precise ($<$ 100 ns accuracy) hardware timing pulse of a GNSS module to trigger each measurement directly (at 10 Hz.). The data are time-stamped with the GNSS date and time output. A special GNSS receiver was selected that also outputs a programmable timing pulse for synchronization purposes (better than 50 ns). As a bonus, it also provides location data within a few meters. These receivers can be purchased for less than €6 (Table 3.1). The time synchronization analysis can be found in Section 3.2.4.

3.2.5 Data logging

The data logging of the GNSS date, time, latitude, longitude, and the 18-channel spectroscopy measurements at 10 Hz results in a dataflow of $>$ 100 MB of data per day. The spectroscopy sensor outputs ASCII data, and the bandwidth of the I2C interface on the spectroscopy side was insufficient; thus the UART serial interface was selected. The sensor can be triggered by serial command to do a measurement, and this command in turn is triggered by the hardware timing pulse of the GNSS.

For data logging, the MKR Zero of the Arduino family microprocessor platforms was chosen. It is a cost-effective and low-power data-logging solution using a 48 MHz SAM D21 Cortex 32 bit low-power ARM MCU and a built-in microSD card holder (max 32 GB). A consumer-grade 32 GB SD card was selected, data rates are low ($< 5\,\mathrm{kB\,s^{-1}}$), and the large size ensures that the card does not wear down fast ($<$ 4 GB per month). The challenge with this data-logging solution is that the default operating system cannot handle sustained data writing to an SD card at 10 Hz using linear programming (despite a low data rate of $<$ 5 kB $\mathrm{s^{-1}}$). In fact, the SD card would regularly delay the measurements by an estimated 200 ms, resulting in a loss of data (tested with a new, fast SD card with 85 MB $\mathrm{s^{-1}}$ max write speed). Thus, a microcontroller multitasking real-time operating system is needed, and FreeRTOS (`https://freertos.org`, last access: 27 July 2023, FreeRTOS_SAM21 by BriscoeTech, version 2.3.0) was chosen to overcome this challenge. Two tasks that run semi-parallel on the single-core CPU were defined. The first task with the highest priority will initiate a measurement cycle at the falling edge of the hardware timing signal of the GNSS. Task 2 will be triggered each second and writes the 10 Hz buffered data to the SD card (Figure 3.3).

3.2.6 Field experiments

The field experiments were conducted at various locations. At the Veenkampen weather station, Wageningen, the Netherlands (lat 51.981°, long 5.620°), sensor performance was tested against GHI measurements and a spectrophotometer. Although GHI is directly measured with a pyranometer, it was decided to use the pyrheliometer and diffuse radiation sum to reduce cosine response errors. The instruments consist of a Kipp & Zonen pyrheliometer CHP1 with a calibration accuracy of $\pm$ 0.5 % and a first-class pyranometer CM 21 for diffuse radiation measurements with a time constant of 5 s, directional error $< \pm$ 10 W $\mathrm{m^{-2}}$, tilt error $\pm$ 0.2 %, zero-offset due to T change $<$ 2 W $\mathrm{m^{-2}}$ at 5 K $\mathrm{h^{-1}}$, and cosine response error max $\pm$ 2 % at 60° and max $\pm$ 6 % at 80°. Both instruments were mounted on a sun tracker (EKO Instruments, Japan, STR-21 with shading disk). On selected days the solar spectrum was measured with an ASD FieldSpec (USA) field spectroradiometer with a cosine collector and with a factory recalibration performed in 2021.

Additionally, a set 25 sensors was deployed during the FESSTVaL campaign (`https://fesstval.de/`, last access: 08 April 2024) at the German Weather Service (DWD) in Falkenberg, Germany, to study the spatial variation in solar irradiance (June 2021). For that campaign, it was crucial to obtain fast and time-synchronized spatial solar irradiance measurements. Their Baseline Surface Radiation Network (BSRN) location at Lin-

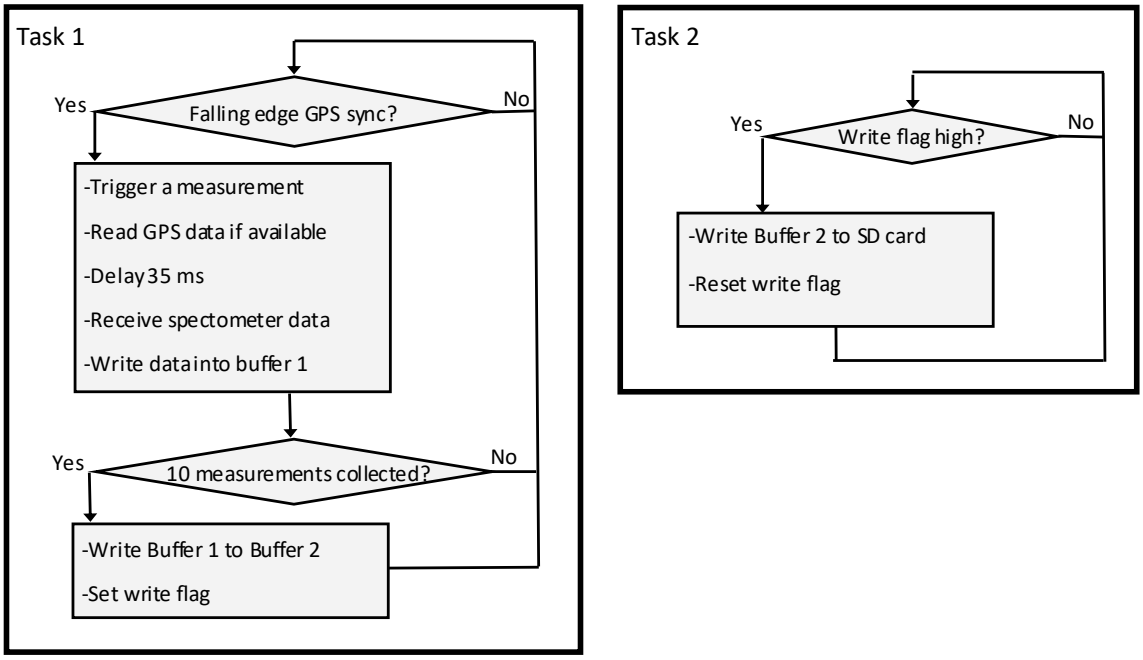

Figure 3.3: Multitasking software implementation for synchronized measurements and data storage. Each buffer can contain 10 rows of data. The program is available at Zenodo (`https://doi.org/10.5281/zenodo.6945812`)

denberg (Driemel et al., 2018) was used to test long-term stability from 22 June to 31 August 2021. A FROST network was also deployed in La Cendrosa, Spain (lat 41.692537°, long 0.931540°) from 14 to 29 July 2021, during the LIAISE campaign (`https://liaise.aeris-data.fr/`, last access 10 June 2024). It was used, among other things, to study crop growth. Chapter 7 describes the campaigns and our results relating to solar irradiance variability in detail.

3.3 Performance and applications

The performance of the sensor, the temperature dependency and cosine response of the diffuser, and the time synchronization are presented below. The infrared crosstalk is analysed by measuring signal response with all light below 1000 nm blocked using a low-pass infrared filter. Subsequently a correction method using heat-absorbing infrared filters (referred to as "correction filters") is introduced and tested. This results in three versions of FROST: one with a 10.6 mm diffuser, one with a 2 mm diffuser including a correction filter on the blue sensor, and one with a 2 mm diffuser with two correction filters (on the blue and red sensor).

3.3.1 Spectral response and calibration

According to the manufacturer specifications, the normalized (at peak wavelength) responsivity of their spectroradiometer has a good narrow-band response (20 nm FWHM) and limited overlap for the 18 channels. Wavelength accuracy is within $\pm$ 10 nm, and this was confirmed

by testing the sensor inside a Cary 4000 UV-Vis spectrophotometer equipped with a universal attachment accessory. Unfortunately, the Cary spectrophotometer had a limited spectral range; thus, we were unable to test the crosstalk in the near infrared or test the 940 nm band (Figure 3.6).

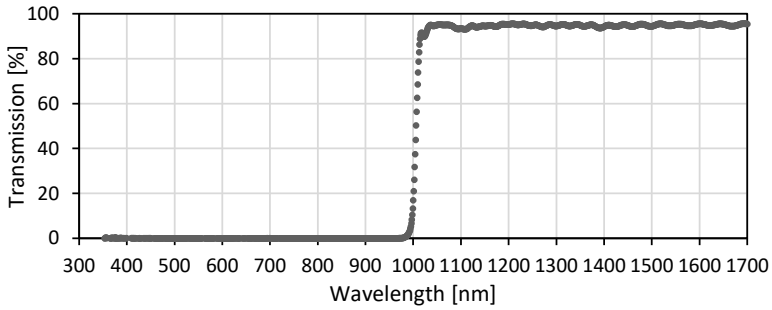

Figure 3.4: Transmission of the optical LP filter measured with a Cary 5000 UV–Vis–NIR spectrophotometer equipped with a universal measurement accessory at the DWD, Lindenberg, Germany.

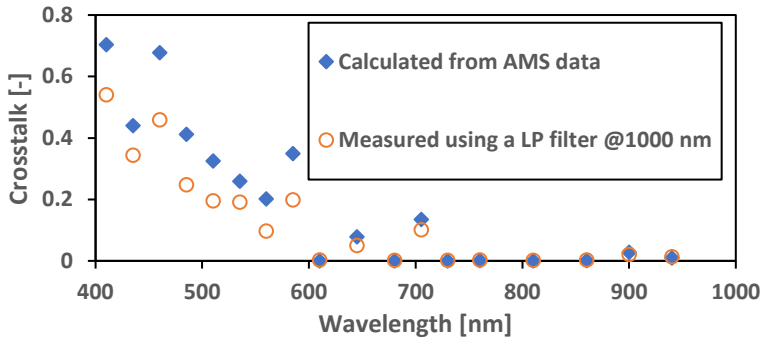

Figure 3.5: Measured spectroscopy sensor infrared crosstalk from wavelengths $>$ 1000 nm, tested with a xenon lamp and an optical long-pass filter (LP at 1000 nm) and calculated from spectral response data as supplied by the manufacturer (AMS). Crosstalk is defined as the fraction of light wavelengths $>$ 1000 nm that the sensor is responding to; for example at 410 nm, 55 % of the measured signal actually originates from wavelengths $>$ 1000 nm

Linearity was tested by comparing the spectroradiometer against a reference thermopile pyranometer CM 21 (Kipp & Zonen, the Netherlands) and a stabilized halogen light source in a darkroom. The intensity was adjusted by changing the lamp distance. The FROST non-linearity was at least as good as the CM 21, which has a non-linearity of $< \pm$ 0.2 %. The factory-calibrated accuracy is $\pm$ 12 % according to the manufacturer specifications (35 counts μW^{-1} cm^2). After initial testing using solar radiation as a light source for reflectance measurements of lawn grass, we were confronted with unusual data. The PAR region clearly showed very high reflection values, more than 5 times what is typical of such a surface.

After consultation with the manufacturer (AMS), they clarified that the AS72653 sensor has a strong crosstalk in the near infrared. The sensor was meant to be used with LED light for spectral reflectance measurement applications, which would not produce light $>$ 1000 nm. They recommend a specific LED for each sensor, and therefore each reflectance measurement

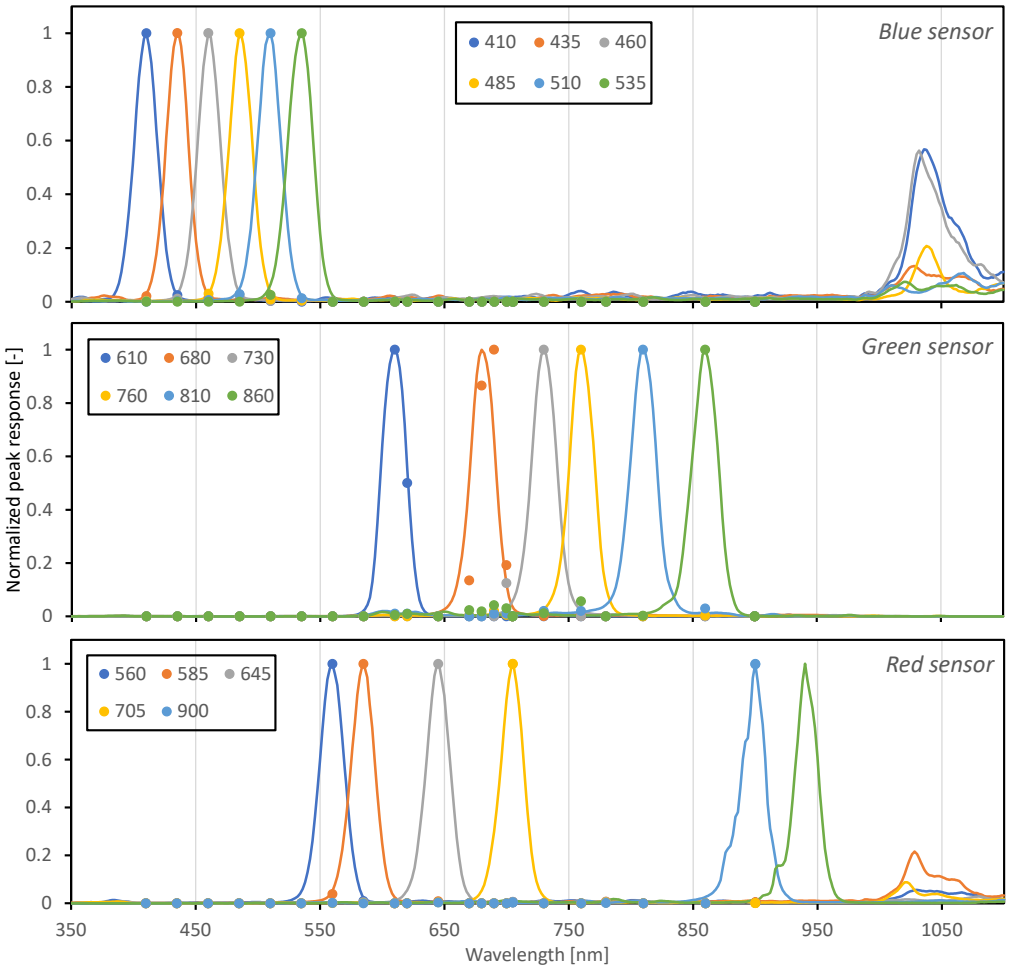

Figure 3.6: Normalized peak spectral response of the triple AMS sensor (denoted as blue, green, and red sensor); data provided by manufacturer after consultation (solid lines) and our measured response up to 900 nm (dots) as measured with a sensor placed inside a Cary 4000 UV–Vis spectrophotometer equipped with a universal measurement accessory.

would consist of three separate measurements, with each using one sensor and with one specific LED at a time.

We tested the sensor at the DWD radiation calibration facility in Lindenberg using a calibrated light source. The crosstalk caused by light wavelengths beyond 1000 nm was measured by using an optical long-pass (LP) interference filter that blocks all light below 1000 nm. Thus, the remaining signal on all 18 channels can be attributed to crosstalk from wavelengths >1000 nm. The blocking filter characteristics were tested in a Cary 5000 UV-Vis-NIR spectrophotometer equipped with a universal attachment accessory (Figure 3.4).

Figure 3.5 shows the fraction of infrared light (>1000 nm) within the sensor output for each of the 18 channels. The sensor output was corrected for the LP filter transmission loss (about 5 %; see Figure 3.4). Note that the crosstalk is larger than during solar radiation measurements because a xenon light source contains a higher amount of infrared radiation. Cloudy conditions would further reduce crosstalk. For clearsky conditions, the crosstalk would be

about half of the xenon light. The blue diamonds in Figure 3.5 show the calculated crosstalk using the AMS sensor spectral filter response data obtained through personal communication (Kumud Dey, personal communication, 2020) with the manufacturer (Figure 3.6). The measured crosstalk on the blue sensor appears to be slightly better. The crosstalk is very large in the visible light range and confirms the provided filter transmission curves from AMS (Kumud Dey, personal communication, 2020). Note that those transmission curves (Figure 3.6) are not available on the publicly available datasheet. Figure 3.5 shows that only half of the channels provide the correct spectral information (if calibrated correctly using the data from Figure 3.6). However, there are enough channels to measure the so-called red edge around 700 nm in vegetation light transmission and reflection. This opens up applications for vegetation growth measurements without further modifications.

All channels in the blue sensor and some of the channels (650 and 685 nm) in the red sensor have very high crosstalk from the 1000-to-1100 nm range, but the crosstalk makes the sensor cover a larger range of the solar spectrum. It is therefore still usable if this can be quantified.

In Figure 3.7, the right panels show that the crosstalk for a flat spectrum, defined as the signal above or below 3×0.5 FWHM from the center wavelength, is large (up to 60 %) in the PAR range for the blue sensor and mainly from the infrared beyond 1000 nm. The green sensor performs much better and exhibits minimal infrared crosstalk (< 5 %). The red sensor has an issue, mainly with the first two channels.

To remove infrared crosstalk, an optical short-pass filter is required. However, a filter with a sharp cutoff at 1000 nm is, to our knowledge, not available or probably very expensive and sensitive to the angle of incidence. Cost-effective shortpass filters are made from heat-absorbing glass and have a dye added to the glass that absorbs infrared radiation (Figure 3.8). However, these heat-absorbing filters do not have a steep filter response and therefore are ineffective at correcting the red sensor without attenuating the 900 and 940 nm channels too much. The Schott heat-absorbing filters KG3 and KG1 appear to offer a good solution for the blue sensor (Figure 3.9, second-row panels). The remaining crosstalk is mainly related to the slightly broader filter response. The first four channels of the red sensor (Figure 3.7, lower panels) can also be improved. However, such a correction filter for the red sensor would increase crosstalk from shorter wavelengths for the 900 and 940 nm wavebands (see lower-right panel in Figure 3.9) and greatly reduce signal strength. For accurate PAR measurements and when the 900 and 940 nm channels are not needed, using the weaker KG1 filter for the red sensor is recommended.

Because of the limited view angle of the spectroscopy sensors (40°), it is crucial to add a light diffuser. Two light-diffusing materials were tested, PTFE and opal cast acrylic sheet glass, and the transmission measurements are shown in Figure 3.10 (measured with the ASD FieldSpec).

The reduced transmittance of the PTFE diffusers in the shorter wavelengths (Figure 3.10) enhances the near-infrared crosstalk (compare Figure 3.9 top-right panel with Figure 3.7

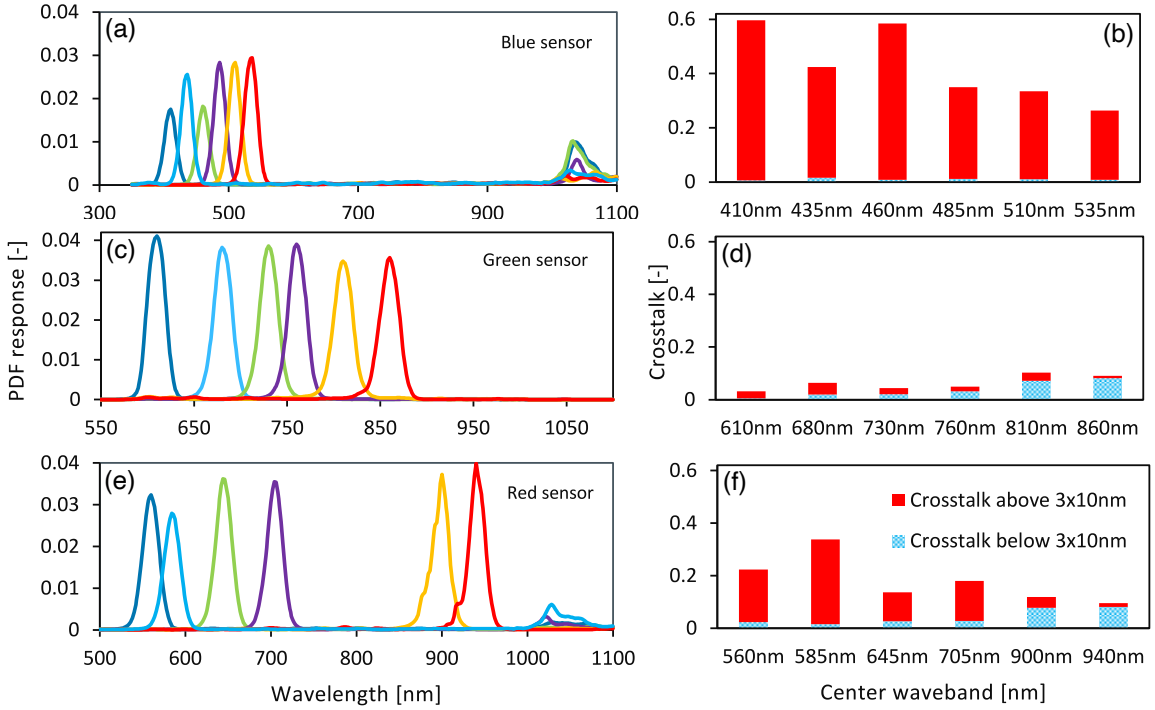

Figure 3.7: (a, c, e) Spectral response of the triple AMS sensor (denoted as blue, green, and red sensor), Probability density functions (PDFs) calculated from data provided by the manufacturer AMS (Kumud Dey, personal communication, 2020). **(b, d, f)** The crosstalk for each channel is presented as two values: signal originating from > (center wavelength + 30 nm) divided by total signal of a channel (red) and signal < (center wavelength - 30 nm) divided by total signal of a channel (blue) (sensor only, without diffuser)

top-right panel). The combined effect of sensor and PTFE spectral response with or without correction filters is shown in Figure 3.11. Three versions of the spectrophotometer were developed: one with a 10.6 mm PTFE diffuser to improve cosine response (FROST1), a second version with a 2 mm PTFE diffuser and a correction filter on the blue sensor (FROST2), and a third version with a 2 mm PTFE diffuser and correction filters on the blue and red sensor (FROST3). The spectral selective quality on real-world measurements (Figure 3.11) was calculated from the combined effect of the spectrophotometer filter characteristics (Figures 3.7 and 3.8), diffuser (Figure 3.10), and Schott correction filters (Figure 3.8).

Figure 3.11 shows that the first 8 channels, if uncorrected with a heat-absorbing filter, underestimate the irradiance levels at the expected wavebands because these bands are very sensitive to the infrared region between 1000 and 1100 nm. At this infrared region, the solar radiation intensity is lower than what the blue sensor is supposed to see and thus leads to an underestimation of the blue sensor for the visible channels. The heat-absorbing filters effectively remove this crosstalk. It also shows that the red sensor benefits from a heat-absorbing filter for the wavebands 560 and 585 nm, but it greatly reduces the sensitivity of the 900 and 940 nm wavebands, which makes the contribution of crosstalk from short wavebands too high (large positive deviation). Therefore, the red sensor should not be equipped with such a filter if the 900 and 940 nm wavebands are important, for example to estimate column

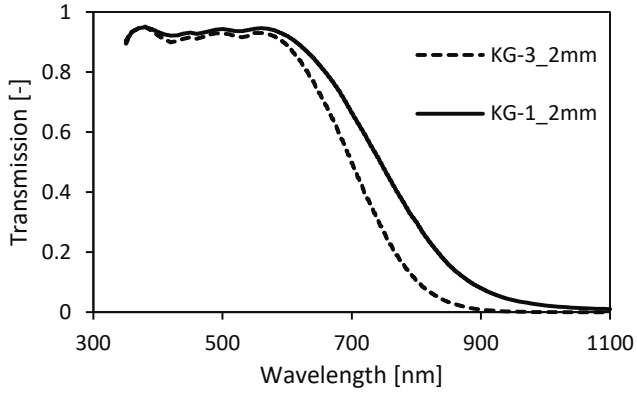

Figure 3.8: Correction filters for the infrared crosstalk: Schott heat-absorbing filters (adapted from Schott AG manufacturer data)

atmospheric moisture (see Figure 3.17).

The procedure to calibrate each waveband of FROST would require an accurate spectrophotometer and a clear day. First, each of the 18 PDF band responses of the sensor (with or without a correction filter!) and diffuser combinations is multiplied with the known solar spectrum for a very clear day or measured with a calibrated spectrophotometer. This gives the nW m^{-2} reference value that the FROST sensor should produce for each waveband. Subsequently, the 18 raw FROST wavebands' outputs are multiplied by the AMS calibration factors (since we use the uncalibrated output for fast measurement) and divided by the reference values. The AMS spectroscopy sensor factory calibration values are written to the SD card at the very start of the measurements. The derivation of the calibration values for each FROST channel i in counts W^{-1} m^2 can be written as

$$\mathrm{Cal}_{\mathrm{FROST},i} = \frac{\mathrm{Counts}_i \cdot \mathrm{Cal}_{\mathrm{manufacturer},i}}{\sum_{\lambda_1}^{\lambda_2} \left[\frac{R_{\mathrm{sensor}_{i,\lambda}} \cdot T_{\mathrm{diffuser}_\lambda} \cdot T_{\mathrm{filter}_\lambda}}{\sum_{\lambda_1}^{\lambda_2} R_{\mathrm{sensor}_{i,\lambda}} \cdot T_{\mathrm{diffuser}_\lambda} \cdot T_{\mathrm{filter}_\lambda}} \cdot \mathrm{Source}_\lambda \right]} \tag{3.1}$$

where Counts_i is the signal output of a FROST channel i, from 1 to 18 (-); $\mathrm{Cal}_{\mathrm{manufacturer},i}$ is the manufacturer calibration factor (-) for channel i; $R_{\mathrm{sensor}_{i,\lambda}}$ is the normalized peak spectral response of channel i at wavelength λ (nm); $T_{\mathrm{diffuser}_\lambda}$ is the spectral transmission of the diffuser (-) at wavelength λ (nm); $T_{\mathrm{filter}_\lambda}$ is the transmission of the (optional) crosstalk correction filter (-) at wavelength λ (nm); Source_λ (W m^{-2}) is the output of the reference light source at wavelength λ (nm) (preferably the Sun); and λ_1 and λ_2 are the lower and upper boundaries of the spectral sensitivity range (including crosstalk) of FROST. Note that the denominator is the spectrally weighted source signal strength.

The sensor output sensitivity is then expressed as counts W^{-1} m^2. The normalized sensor response is provided in Figures 3.7 and 3.9 and in the online Supplementary data. An example of sensitivity values is presented in Table 3.2. These values were derived on 11 March 2022 at 13:35 UTC for the 10.6 mm diffuser version and the 2 mm diffuser + one filter version. The 2 mm diffuser with two correction filters was measured on 15 May 2022 (Figure 3.11).

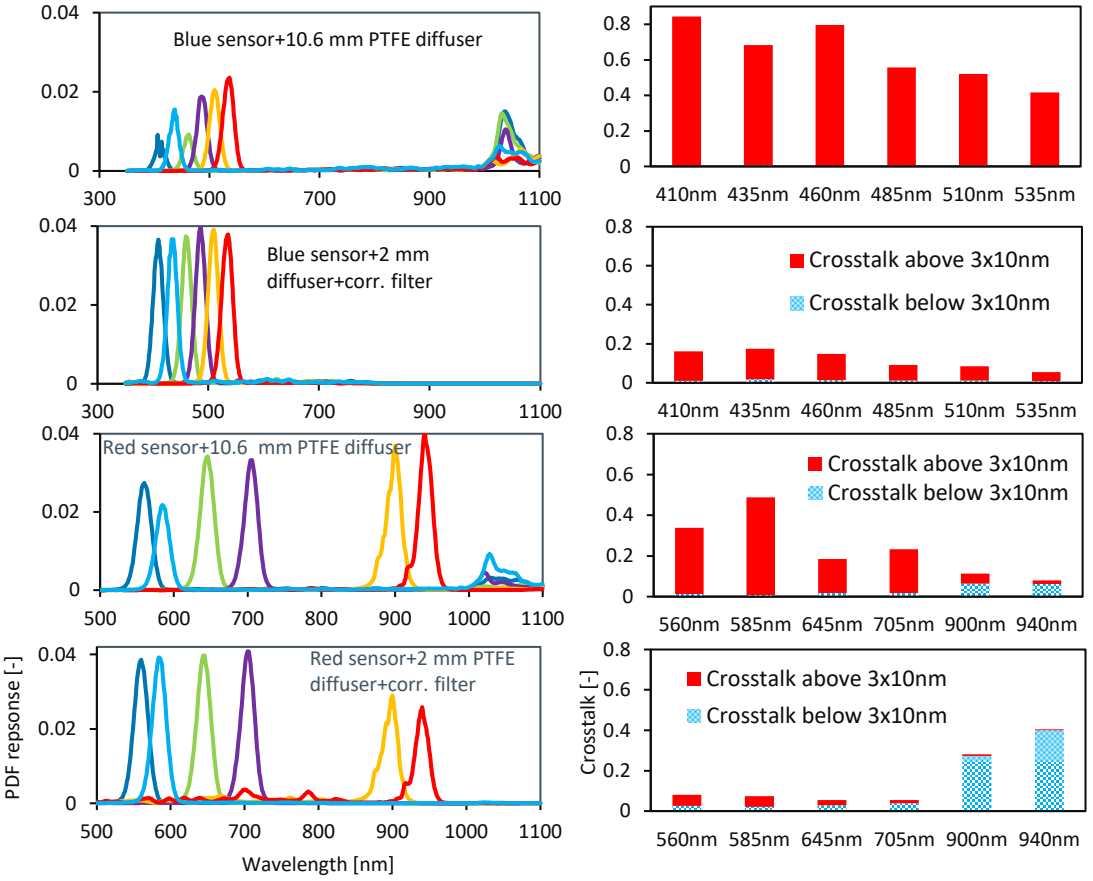

Figure 3.9: Spectral response and crosstalk (for a flat spectrum) of the blue and red sensor, without or with correction filter. First row: blue sensor with 10.6 mm PTFE diffuser. Second row: blue sensor with 2 mm PTFE diffuser including a heat-absorbing filter (Schott KG3). Third row: red sensor with 10.6 mm PTFE diffuser. Fourth row: red sensor with 2 mm PTFE diffuser and heat-absorbing filter (Schott KG1), calculated from manufacturer data of sensor spectral response, transmission data of the Schott optical correction filter, and measured transmission of PTFE diffusers.

Note that these values are only valid for an integration value of 13.9 ms and a gain of 16. We do not recommend using channels with Flag 2 or 3 if spectral accuracy is required.

3.3.2 Temperature sensitivity and drift

The diffuser and sensor were both tested for temperature effects. The measurements were corrected for sensor temperature drift or drift in lamp output by measuring the lamp output with an extra sensor outside the oven. The oven has an internal fan to assure a homogeneous temperature within the oven chamber. The PTFE filter shows a significant jump in transmission around 21 °C; then it reaches a plateau and slowly declines past 35 °C (Figure 3.12, upper panel). The temperature was slowly increased and stabilized for 30 min at each measurement point to minimize thermal delays in the PTFE material.

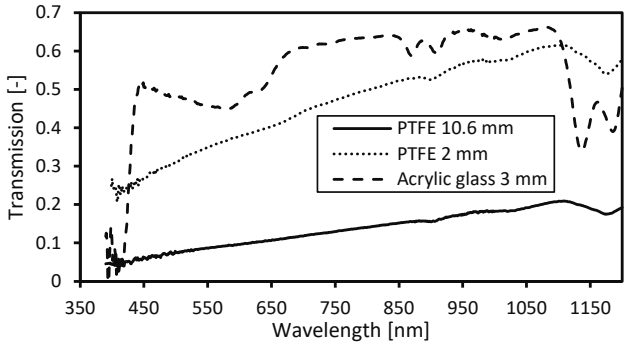

Figure 3.10: Transmission of PTFE diffusers and an opal cast acrylic sheet glass diffuser measured with an ASD FieldSpec spectroradiometer.

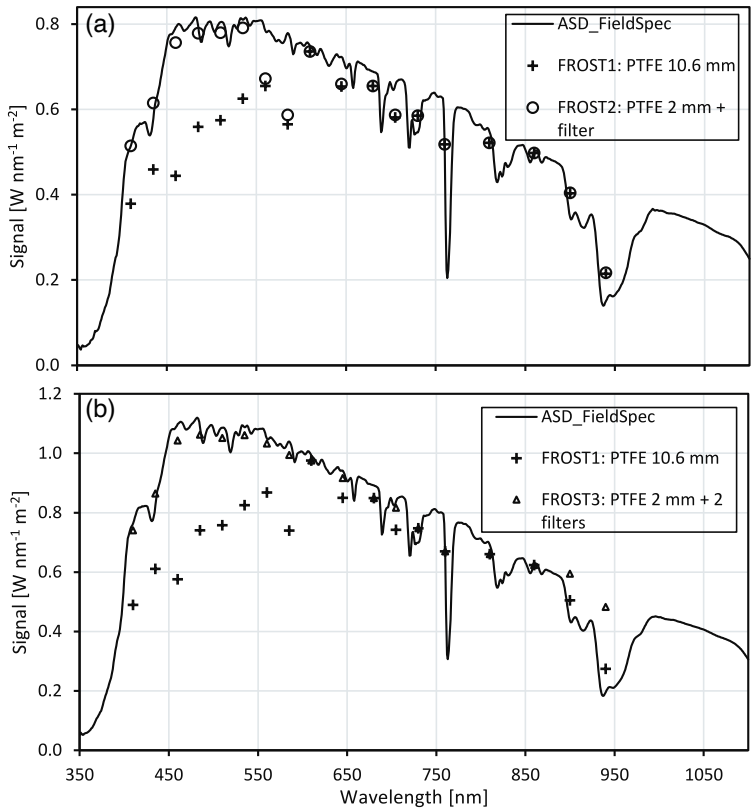

Figure 3.11: Outdoor measurements (ASD FieldSpec) with calculated response of three FROST versions: FROST1 with a 10.6 mm diffuser, FROST2 with a 2 mm PTFE diffuser and a correction filter on the blue sensor, and FROST3 with a 2 mm PTFE diffuser and a correction filter on the blue and red sensor, considering sensor spectral response and transmission of diffuser and correction filter, during clear-sky conditions, Wageningen: **(b)** 15 May 2022, 14:24 UTC; **(a)** 11 March 2022, 13:35 UTC.

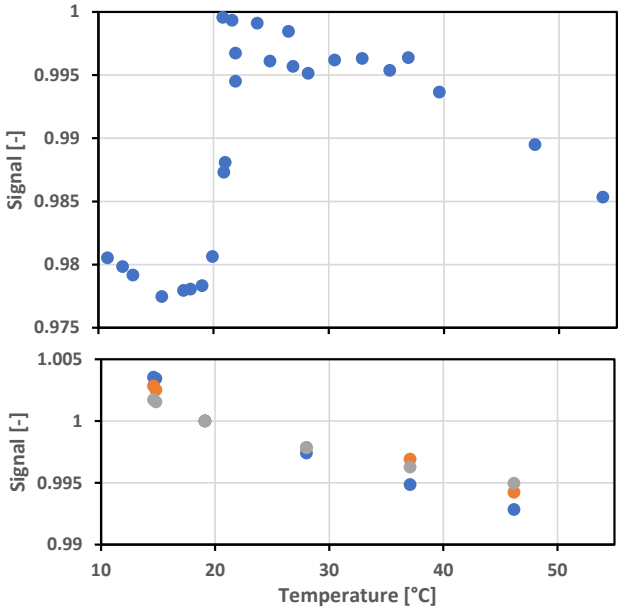

Figure 3.12: Temperature response of the PTFE diffuser (top) and three random light sensors (bottom) (-250 ppm).

Three spectroscopy sensor chipsets (3 × 18 wavebands) were oven-tested for temperature sensitivity between 16 and 46 °C. Overall temperature sensitivity is -250 ppm K^{-1} with a small variation among the three sensors. Lower temperatures were not possible due to condensation issues when reaching the dew point temperature of the laboratory (Figure 3.12).

3.3.3 Cosine response and GHI

The cosine response measurements (outside, LED lamp) had a better performance for the 10 mm diffuser, but nevertheless had some inconsistencies among the three sensors. We tried to improve the cosine response by leaving part of the sides uncovered, but this caused a very high asymmetry among the three sensors. The explanation is that the three sensors do not have the same viewing angle location under the diffuser; thus some will see more from the side than the other sensors. The side sensitivity is greatly reduced with a thinner filter but at the expense of a reduced cosine response (Figure 3.13).

We found that most of the cosine response errors can be corrected afterward and is demonstrated for the 2 mm filter, which had the largest cosine response error but less transmission loss. The accurate measurement of GHI can be achieved by first correcting for the zenith angle response (see Figure 3.13, lower-middle panel) and subsequently applying a second-order linear regression against a reference pyranometer on 1 clear day (19 March 2021). Additionally, a correction for the limited spectral response is needed. We tested this calibration method for the average signal of all 18 wavebands and on single wavebands. The dataset contains clear-sky days (Figure 3.14), overcast days (Figure 3.15), and rainy weather (Figure 3.16). The best overall results were achieved with either channel 645 or channel 705 nm, with residual errors mainly below 10 W m^{-2} during contrasting weather conditions. Due to the spatial separation of 156 m between our sensors and the reference solar radi-

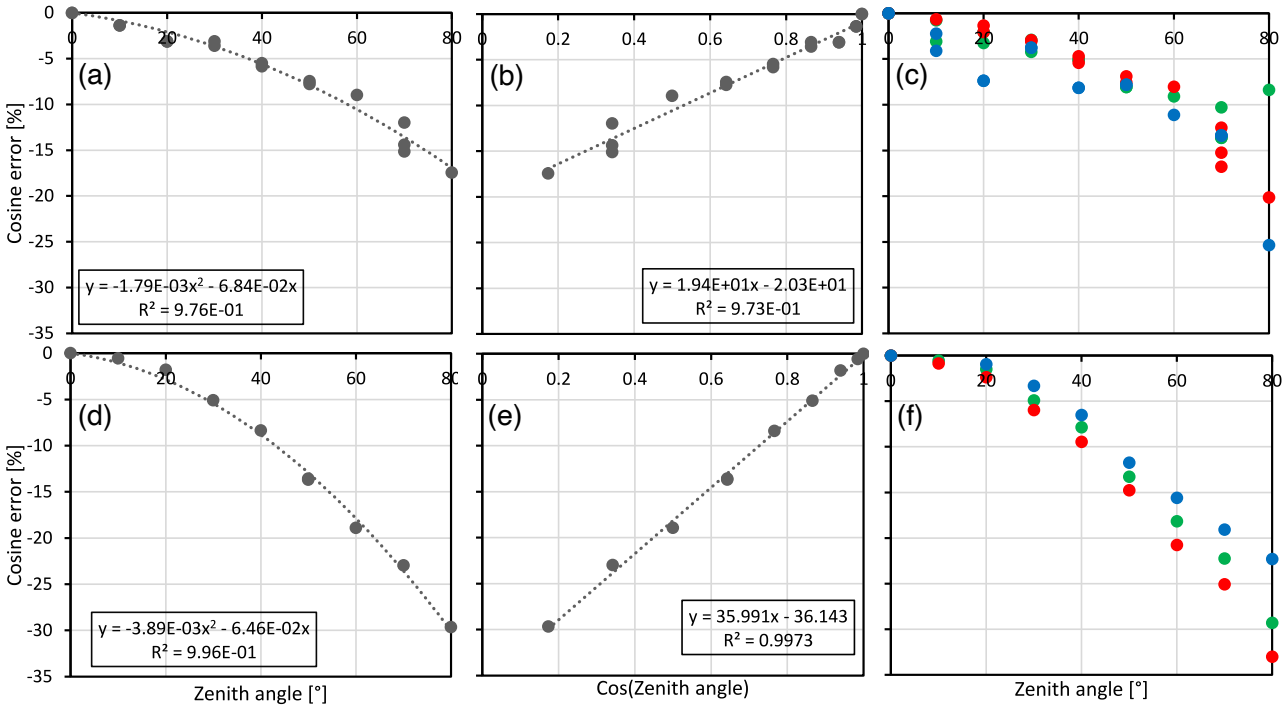

Figure 3.13: **(a-c)** The 10.6 mm diffuser (black sides). **(d-f)** The 2 mm diffuser (sides painted black). Panels **(c)** and **(f)** are color-coded for each sensor integrated circuit.

ation measurements and the differences in response speed, we rejected the cloud passage time intervals. The 645 and 705 nm wavebands seem to correct cloud effects on the GHI where irradiance is enhanced below 500 nm and reduced due to water absorption bands at wavebands $>$ 1000 nm.

The remaining uncertainty in the clear-day calibration (up to 10 W m^{-2} or 5 %) is mainly related to small leveling uncertainties or tolerances in input optics of both the reference and our sensors. This is visible as a shift from a negative to a positive bias around 12:00 UTC (Figure 3.14).

The instruments were not dried during the precipitation event (Figures 3.16 and 3.17). Water droplets on the diffuser may affect light transmission and diffuser optical properties. Note that in Figures 3.14 to 3.16, the nocturnal offsets are zero.

Next, we investigated how the light spectra are modified by clouds or rain. The two instruments, one with a 10 mm diffuser (FROST1) and the second version with a 2 mm diffuser and crosstalk correction filter on the blue sensor (FROST2), were used to calculate the spectral change due to cloudy or rainy weather conditions (Eq. 3.2).

$$\text{Spectral\_range}_i = \frac{\dfrac{\text{Counts}_{i,\text{clouds\_rain}}}{\frac{1}{18}\sum_{i=1}^{18}\text{Counts}_{i,\text{clouds\_rain}}}}{\dfrac{\text{Counts}_{i,\text{clear}}}{\frac{1}{18}\sum_{i=1}^{18}\text{Counts}_{i,\text{clear}}}} \tag{3.2}$$

Table 3.2: Sensitivity, or counts (C) W^{-1} m^2 of FROST1, FROST2, and FROST3 with different configurations; offsets are always zero. Every sensor uses a gain of 16 and an integration time of 13.9 ms. The flags denote quality of measurement (waveband accuracy). Flag 0: low crosstalk; Flag 1: crosstalk $< 20\,\%$; Flag 2: $20\,\% <$ crosstalk $< 35\,\%$; Flag 3: crosstalk $> 35\,\%$. The colors in the first column indicate each of the three sensors in FROST. The final column shows the improvement factor for sensitivity when using a 3 mm white acrylic glass diffuser instead of a 2 mm PTFE diffuser.

	FROST1		FROST2		FROST3		FROST_AG
Diffuser:	PTFE 10.6 mm		PTFE, 2 mm		PTFE, 2 mm		Acrylic glass, 3 mm
Filter:	no		on blue sensor		on blue and red sensor		Sensitivity increase
Waveband	Sensitivity		Sensitivity		Sensitivity		$\frac{T_{Acrylic\ glass_{3mm}}}{T_{PTFE_{2mm}}}$
[nm]	[C W^{-1} m^2]	Flag	[C W^{-1} m^2]	Flag	[C W^{-1} m^2]	Flag	
610	116	0	474	0	494	0	1.61
680	132	0	503	0	436	0	1.49
730	156	0	549	0	554	0	1.39
760	156	0	413	0	387	0	1.36
810	188	0	673	0	651	0	1.31
860	194	0	760	0	649	0	1.25
560	51	2	253	2	186	0	1.70
585	70	2	333	2	195	0	1.65
645	55	1	256	1	168	0	1.56
705	70	1	295	1	117	0	1.43
900	90	0	348	0	19	3	1.12
940	107	0	395	0	25	3	1.20
410	94	3	153	0	157	0	1.55
435	100	3	200	0	206	0	2.38
460	144	3	211	0	218	0	2.08
485	96	3	209	0	217	0	1.94
510	94	3	213	0	221	0	1.85
535	84	3	204	0	213	0	1.76

Data from the experiments shown in Figures 3.14 to 3.16 were used, and, of the 3 contrasting days, the 11:00-12:00 UTC intervals were averaged and normalized for the average spectral signal of the 18 wavebands. Figure 3.16 shows that the 940 nm waveband is very sensitive to moisture, with a reduction of more than 20 % as compared to its nearest waveband. Accordingly, it can be used to derive information about atmospheric moisture, such as column water vapor. Both cloudy and rainy conditions appear to modify the spectra in a similar way (Figure 3.17). The low enhancement in the first four wavebands of the instrument with the 10 mm diffuser version (FROST1) is related to the strong crosstalk in the near infrared. The corrected version with the 2 mm diffuser (FROST2), which contains the crosstalk correction filter, shows an enhancement due to clouds and is in line with the findings by Durand et al. (2021), who had an enhancement below 465 nm. The 645 or 705 nm waveband as shown in 3.14 to 3.16 appears to have the right amount of sensitivity reduction due to clouds and rain (slightly stronger) to be used for GHI measurements. It is, however, recommended to use all 18 bands and use a proper weighting function that reduces sensitivity in the visible region. We currently have no explanation for the enhancements between 750 and 860 nm.

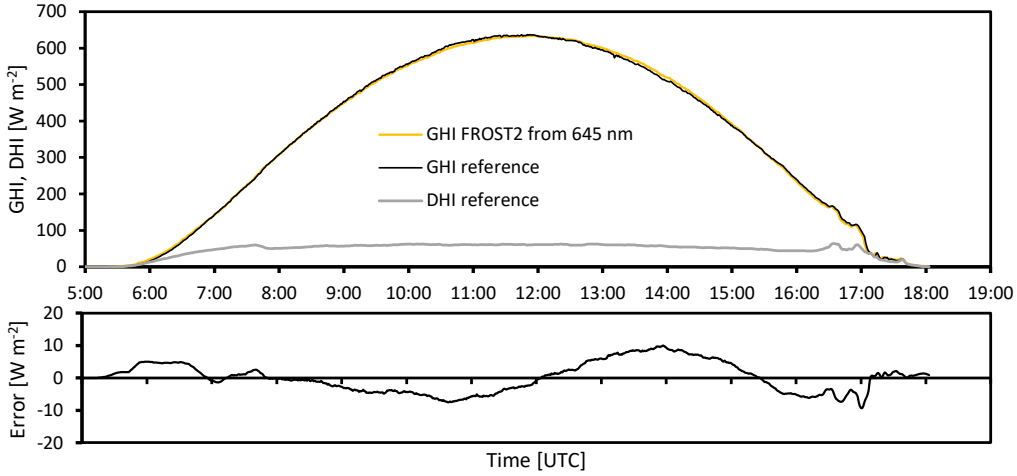

Figure 3.14: Comparison between GHI measured using a pyrheliometer and diffuse radiation sum (on a sun tracker and correcting for zenith angle) and a calibrated FROST2 with a 2 mm PTFE diffuser and one correction filter; diffuse horizontal irradiance (DHI) measured with a pyranometer mounted on a sun tracker with a shading ball, Veenkampen weather station, 19 March 2022. Relative errors at GHI $>$ 200 W m^{-2} are $<$ 2 % and mainly related to horizontal misalignment causing an asymmetric error before/after noon UTC.

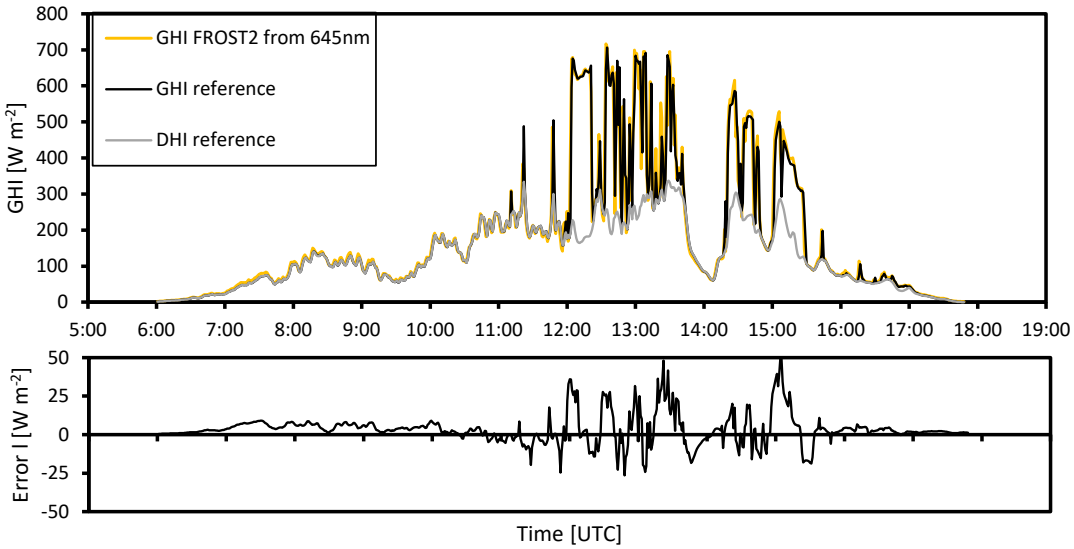

Figure 3.15: Calibrated FROST2 GHI from 645 nm (calibrated on a clear day, 19 March; see Figure 3.14); calibration tested with cloudy weather conditions - cloudy weather conditions in the morning, some clearing in the afternoon, 1 min averaged data, error plot 10 min running mean to suppress differences due to spatial separation of FROST and reference (145 m apart), Veenkampen weather station, 14 March 2022. Relative errors at GHI $>$ 100 W m^{-2} are $<$ 7 % and mainly related to spatial separation between FROST and reference.

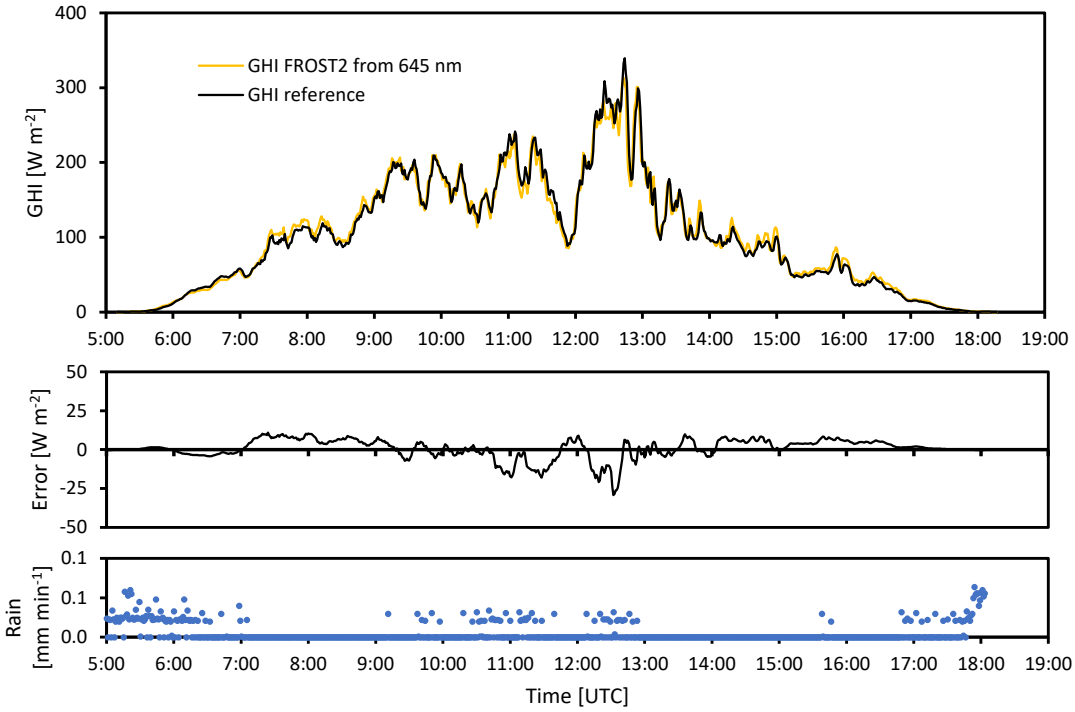

Figure 3.16: Calibrated FROST2 GHI from 645 nm (calibrated on a clear day, 19 March; see Figure 3.14); calibration tested under rainy weather conditions, 1 min averaged data, error plot 10 min running mean to suppress differences due to spatial separation of FROST and reference (145 m apart), Veenkampen weather station, 31 March 2022. Relative errors at GHI $>$ 100 W m^{-2} are $<$ 7 % and mainly related to spatial separation between FROST and reference.

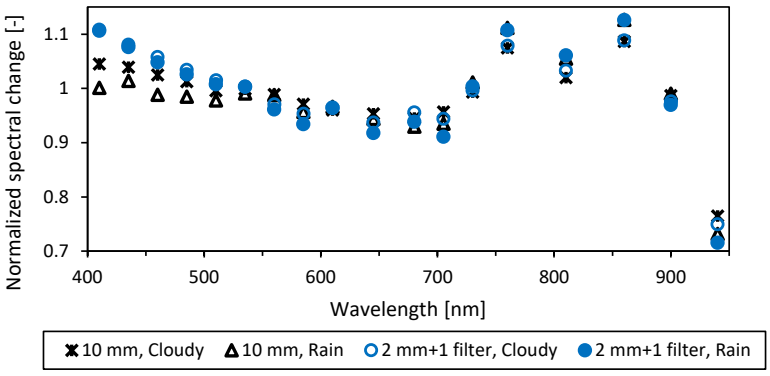

Figure 3.17: Two FROST instruments, one with a 10 mm diffuser (FROST1) and one with a 2 mm diffuser and correction filter (FROST2). The normalized spectral cloud modification factor is the spectral change in cloudy (14 March 2022) and rainy weather (31 March 2022) compared to a cloud-free day (19 March 2022), Veenkampen weather station, data averaged between 11:00 and 12:00 UTC for each day.

The long-term drift was tested at the Lindenberg rooftop observatory. One instrument was measuring from 22 June to 31 August 2021 (without any missing 0.1 s measurements). These data from 2.5 months were converted to GHI values by using only 1 relatively clear day (13 August) and compared with their reference pyranometer. The GHI standard error was 2.5 W m^{-2} for daily averages with a diffuser temperature correction obtained by increasing sensor values by 2 % at temperatures below 21 °C according to Figure 3.12 and cosine response correction according to Figure 3.13b (for daily errors see Figure 3.18, upper panel). Additionally, the GHI deviations in percentage between 12:00 and 13:00 UTC were averaged to reveal possible sensor drift in time. The diffuser temperature correction practically removed all long-term drift (Figure 3.18, middle panel).

3.3.4 Spatial measurements and synchronization

For spatial measurements, exact synchronization is essential. Our GNSS solution uses the hardware timing pulse of the GNSS to trigger a measurement. To illustrate the synchronization performance, we set up three standalone FROST sensors and let them run for 1 h outdoors. We then placed them in a darkroom, and at 12:00:45.6 UTC, a LED light source was switched on for 0.3 s. Figure 3.19 shows 1.1 s of collected 10 Hz data of the 610 nm waveband. The response appears instantaneous and perfectly synchronized. There is still an integration time for each measurement, and this was set at 13.9 ms for FROST s16 and s20 and, for testing purposes, twice as long for the experimental version with a less transparent diffuser to get more signal. This instrument is denoted with “Exp” in Figure 3.19. Therefore, the “Exp” FROST occasionally showed a small delay and illustrates the importance of configuring all sensors with the same integration time. Figure 3.19 also shows that the instruments have no zero-offset (no dark current) errors.

The full sensor readout requires two integration cycles, with each cycle measuring 12 channels (see Table 3.3). As a result, there is a maximum of one integration cycle delay between certain channels (with our default settings: maximum 28 ms). Six channels are measured twice within one default measurement cycle (Table 3.3). For critical synchronization applications, it is possible to measure only 12 of the 18 channels during each measurement cycle.

Table 3.3: Readout order during one full measurement cycle.

R	S	T	U	V	W	G	H	I	J	K	L	A	B	C	D	E	F
610nm	680nm	730nm	760nm	810nm	860nm	560nm	585nm	645nm	705nm	900nm	940nm	410nm	435nm	460nm	485nm	510nm	535nm
	1	1	1	1		1	1	1		1		1	1	1		1	
2		2	2		2	2	2		2		2	2	2		2		2

The downside of a fast integration cycle is a smaller output signal. The 10.6 mm diffuser reduces the light onto the detector significantly, approximately 120 to 30 counts per channel at 650 W m^{-2}. The 2 mm diffuser increases the signal by a factor of 4. Longer integration times are considered, but should be less than 50 ms to assure a sustained 10 Hz output (two integration cycles $<$ 100 ms). Additional time is needed for data communication. The AMS

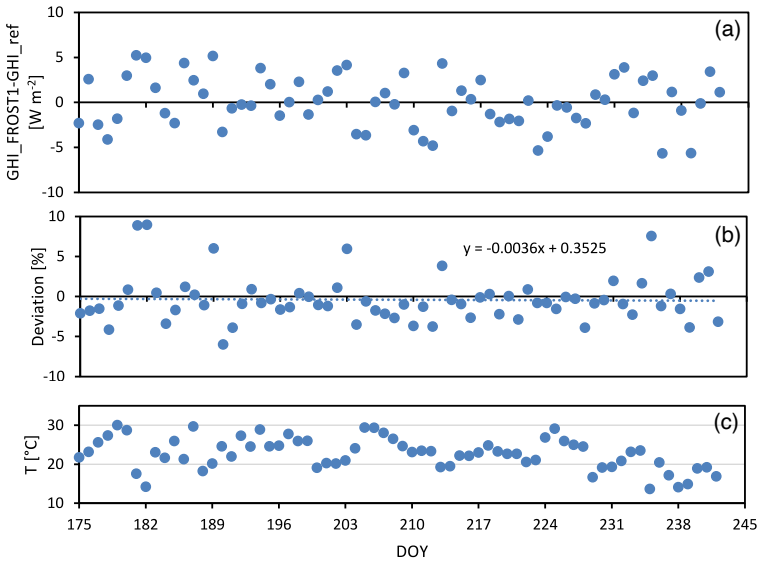

Figure 3.18: Long-term stability of FROST1 GHI measurements (using the 645 nm channel and calibrated with day of year (DOY) 226, 14 August 2021 data). **(a)** Daily average FROST GHI deviation from reference GHI. **(b)** FROST1 GHI deviation from averaged data between 12:00 and 13:00 UTC. **(c)** Average air temperature between 12:00 and 13:00 UTC, during a 2.5-month comparison experiment at Lindenberg. Measurements corrected for PTFE diffuser transmission change at 21 °C.

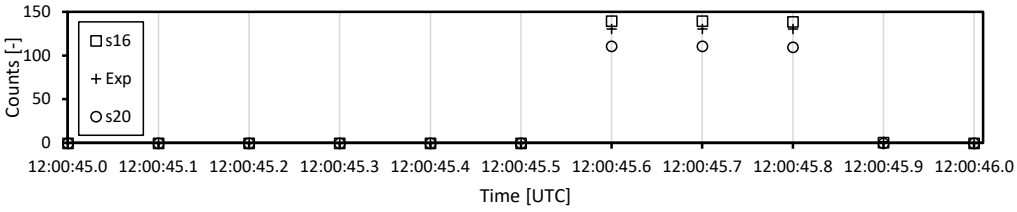

Figure 3.19: Example of synchronization, response speed, and zero offsets of three standalone instruments (uncalibrated). All three use their own GNSS for synchronization. Light pulse of 0.3 s generated by an LED lamp.

spectroscopy sensor output is in ASCII format, and therefore more digits require more time to transmit.

For the measurement campaign in Falkenberg, a large 2D sensor grid was deployed with 50 m grid spacing. It is a good illustration of the spatial dynamics of GHI during partly cloudy conditions. The 1 min averaged data at one point show the cloud enhancements, and the 10 Hz measurements show the high dynamics and spatial variation along a 150 m transect (Figure 3.20).

3.3.5 Other applications

For more use cases, related to photosynthetic active radiation, vegetation development, and surface albedo, refer to the full publication: Heusinkveld et al. (2023).

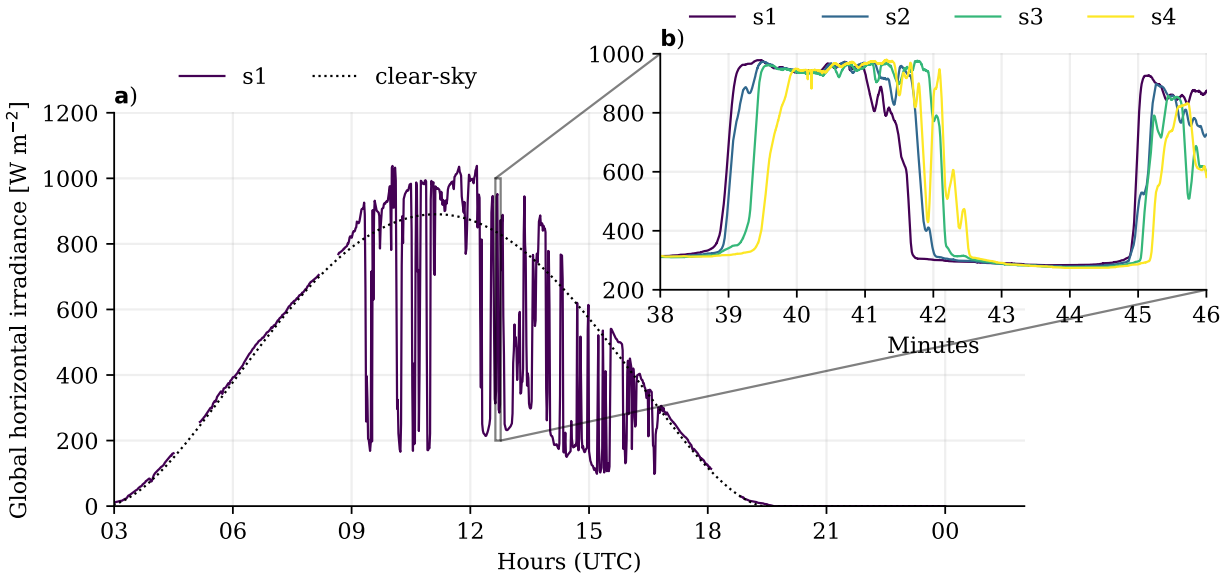

Figure 3.20: Measurements at 10 Hz of spatial variation in GHI at four locations along a 150 m west-east transect **(b)** compared to one location **(a)** at 1 min averages. The dashed line shows the CAMS McClear clear-sky product. Falkenberg, 27 June 2021.

3.4 Concluding remarks

We have introduced FROST: a new instrument for measuring surface solar spectral irradiance. Importantly, the low cost and standalone deployment enables spatial observations using a network of these instruments. Response time related to a change in irradiance is within 1 μs, synchronized in time using onboard GPS clocks. Temperature sensitivity is low (-250 ppm K^{-1}) and the response to radiation is linear ($<$ 0.2 %).

The main sources of measurement error come from a bias in the cosine response and spectral crosstalk. The cosine response can be corrected for by calibrating against high-quality reference instruments or using the experiment results shown in Figure 3.13. Crosstalk corrections require bandpass filters, meaning instruments without these filters have limited spectral accuracy, in particular in the shorter wavelength bands. In this thesis, FROST data is used extensively in Chapter 7, in which spatial data from the FESSTVaL and LIAISE field campaigns is analyzed. More details on instrument calibration and (spectral) accuracy in the practical context of these field campaigns are provided in that chapter.

FROST has also been deployed in-canopy in the Amazon rain forest in August 2022 as part of the CloudRoots-Amazon22 campaign (Vilà-Guerau de Arellano et al., 2024). Another in-canopy experiment was carried out with these instruments by Dr Hugo de Boer in Australia in November 2023. All published datasets of FROST measurements, as of the time of this writing, can be found in the publication list at the end of this thesis.

Chapter 4

Surface moisture exchange under vanishing wind in simulations of idealized tropical convection

This chapter is based on:

Mol, W. B., van Heerwaarden, C. C., & Schlemmer, L. (2019). *Surface Moisture Exchange Under Vanishing Wind in Simulations of Idealized Tropical Convection*. In Geophysical Research Letters. American Geophysical Union (AGU). https://doi.org/10.1029/2019gl085047

Abstract

Under radiative-convective equilibrium (RCE), surface moisture fluxes drive convection, while convection-driven winds regulate surface fluxes. Most simulations of RCE do not resolve the boundary-layer turbulence that drives near-surface winds due to too coarse grid spacing, and instead parameterize its effects by enforcing a minimum wind speed in the computation of the ocean-atmosphere exchange. We show from RCE simulations with fully-resolved boundary-layer turbulence that capturing wind dynamics at low speeds impacts the spatially-averaged surface moisture flux, as well as its spatial distribution. A minimum wind speed constraint of only 1 $\mathrm{m\,s^{-1}}$ leads to $\sim$10 % increase in spatially-averaged surface flux in the evolution towards RCE and reduces the surface flux differences between windy and calm regions with more than a factor of two. Hence, the ability of simulations to let wind vanish is key in representing the wind-induced surface heat exchange feedback and is potentially important in convective self-aggregation.

4.1 Introduction

Radiative-convective equilibrium (RCE) is an idealized representation of the tropical atmosphere in which cooling due to radiation is balanced by heating through convection. Simulation of RCE is often used to study the tropical climate and to assess the impact of climate change therein (e.g., Manabe & Strickler, 1964; Held et al., 1993; Tompkins & Craig, 1998a; Bretherton et al., 2005; Popke et al., 2013). Spontaneous self-aggregation of convection can occur in such simulations (Held et al., 1993) leading to a drastic decrease in the radiative forcing due to clouds (Tobin et al., 2013; Wing & Cronin, 2016) as large cloud free regions effectively emit radiation back to space. While self-aggregation is a potentially important negative feedback mechanism in global warming, understanding the underlying physics of its onset (Muller & Held, 2012; Coppin & Bony, 2015) and development (Muller & Bony, 2015; Holloway & Woolnough, 2016; Wing & Emanuel, 2014) remains challenging.

The surface-flux feedback has been introduced as a potential enhancer of self-aggregation (Wing & Emanuel, 2014). In RCE, surface moisture fluxes are the source of water and energy for deep convection, and in turn the convection driven winds, either as part of overturning cells (Coppin & Bony, 2015) or cold pools, (Schlemmer & Hohenegger, 2014; Zuidema et al., 2017) control the surface fluxes. In regions of strong convective activity the enhancement of surface moisture fluxes due to increased wind speed outweighs a possible reduction in fluxes as an effect of the decrease in the atmosphere-ocean specific humidity gradient due to additional moistening (Wing et al., 2017). Hence, the surface-flux feedback acts as a positive feedback in the development of self-aggregation.

The sea-surface temperature plays a major role in the presence, speed, and intensity of self-aggregation in simulations (Bretherton et al., 2005; Reed et al., 2015; Hohenegger & Stevens, 2016), but it remains unclear whether the simulations capture ocean-atmosphere exchange with sufficient detail. This is partially the effect of the horizontal resolution of typical RCE simulations ($\Delta x \sim 1\,\text{km}$) being sufficient to capture the circulation due to the largest clouds, but insufficient to resolve boundary-layer turbulence and shallow circulation (Naumann et al., 2017). In the absence of (fully) resolved boundary-layer turbulence, cloud-resolving and large-scale models parameterize its effects by introducing a minimum wind speed in the surface-exchange formulation. This added wind speed permits the widely used Monin-Obukhov similarity theory-based surface exchange formulations to be applied under conditions of free convection (Beljaars, 1995), such as RCE (Section 4.2).

The aim of this research is to study the influence of ocean-atmosphere exchange at very low wind speeds on the magnitude and spatial structure of the surface moisture fluxes in RCE simulations. We do this through large-eddy simulations following the RCEMIP case description (Wing et al., 2018), but with an increased spatial resolution ($\Delta x = 100\,\text{m}$) in order to fully resolve the boundary-layer turbulence at the expense of the domain size. Although the chosen domain size ($\sim$ 150 km) prevents self-aggregation from occurring, it permits us to study the subtle details of ocean-atmosphere exchange at wind speeds close to vanishing. We study to what extent RCE simulations are sensitive to imposing a minimum wind speed in

the surface-flux formulation. Our main hypothesis is that not allowing wind to vanish could result in an underestimation of the surface-flux feedback strength, as latent heat fluxes are increased in calm regions, thus reducing this flux contrast between calm and convective regions. It is likely that this effect is stronger in idealized setups such as RCEMIP than over the actual ocean, where large-scale disturbances in the ocean and atmosphere are additional drivers of horizontal wind.

We have set up a simulation experiment in order to test this hypothesis (Section 4.3). Based on the results of the experiment (Section 4.4), we discuss the implications for RCE simulations and studies to convective self-aggregation (Section 4.5).

4.2 Computation of surface fluxes under vanishing wind

The exchange of heat, water, and momentum between surface and atmosphere is commonly parameterized using Monin-Obukhov Similarity Theory (MOST) in atmospheric models (Chapter 10, Wyngaard (2010)). MOST predicts surface fluxes of moisture, temperature, and momentum from their respective near-surface gradients using empirical functions fitted to observational data. The surface latent heat flux is formulated as

$$\text{LHF} = -\rho_0 L_v u_* q_* \tag{4.1}$$

where ρ_0 is the reference density, L_v the latent heat of vaporization and u_* and q_* are the friction velocity and the moisture scale. MOST provides the framework to relate u_* and q_* to the values of wind speed and specific humidity at the first model level. We show u_* as an example, q_* is defined analogously, with its own roughness length and MOST functions:

$$u_* = \kappa \left(U_1 - U_{\text{SS}}\right) \left[\log\left(\frac{z_1}{z_{0m}}\right) - \Psi_m\left(\frac{z_1}{L}\right) + \Psi_m\left(\frac{z_{0m}}{L}\right)\right]^{-1}, \tag{4.2}$$

where κ is the Von Kármán constant, $U_1 - U_{\text{SS}}$ is the wind speed difference between atmosphere and ocean, z_1 is the height of the first model level, z_{0m} is the roughness length for momentum and L the Obukhov length, which is a measure of the stability of the near-surface atmosphere. The function Ψ_m is the integrated form of the empirical MOST relationship that relates the near-surface dimensionless vertical wind gradient to the surface momentum flux. Throughout the years, many studies have presented best fits of the MOST relationships to observational data (e.g. Högström, 1988), but most have the wrong asymptotic limit under free convective conditions with vanishing winds. More recently, Wilson (2001) provided alternative fits that have an overall good match with observational data, and in addition have the correct asymptotic behaviour, which is a key quality for RCE simulations.

The common approach to deal with free convection is to prevent U_1 in Eq. 4.2 from approaching zero by introducing convection-driven winds into its definition. The most basic method is

application of a minimum wind speed U_1 at height z_1:

$$U_1 = \max(U_1, U_{\min}), \tag{4.3}$$

which is the proposed method in the RCEMIP specification with $U_{\min} = 1\,\mathrm{m\,s^{-1}}$ (Wing et al., 2018). Large-scale models often use the method proposed by Beljaars (1995), in which the Deardorff free convective velocity scale w_* is added to the calculation of U_1:

$$U_1^2 = u_1^2 + v_1^2 + (\beta w_*)^2\,. \tag{4.4}$$

This extra term represents wind induced by convective eddies, where constant β is fitted on LES data. This method is, however, questionable for LES as the turbulence is resolved explicitly and adding a convective velocity to the total wind speed leads to (partial) double counting of convection-driven winds.

4.3 Methods

We perform large-eddy simulations using MicroHH (van Heerwaarden et al., 2017). Time integration is done with a fourth-order Runge-Kutta scheme, scalars are advected with a third-order near-monotonic scheme, referred to as `2i3`. A fourth-order variant, `2i4`, is used in a sensitivity experiment. Subgrid-scale turbulent transport is handled by a Smagorinsky scheme. We use a two-moment microphysics scheme (Seifert & Beheng, 2006). As discussed in Section 4.2, surface fluxes are calculated using a MOST-based parametrization with a correct free convection limit (Wilson, 2001). The ocean has a constant sea surface temperature with specific humidity at saturation at the sea surface. A sponge layer is applied above the troposphere.

The simulation setup follows the case description given by RCEMIP for an SST of 300 K. Rotation and large-scale forcings are absent. Initial random noise is applied to the θ_l field in the lowest model levels with a maximum amplitude of 0.1 K. As the cost of radiation computations would render this study impossible, we use a prescribed radiative cooling profile. This profile is based on the mean net radiative cooling rate over days 70-100 in a preliminary System for Atmospheric Modelling (Khairoutdinov & Randall, 2003) simulation of the 300 K RCEMIP case (courtesy of Allison Wing). Our results therefore describe the convective adjustment towards radiative cooling.

A series of simulations (Table 4.1) is set up that capture the initial stage of convection development under radiative cooling with a total duration varying between 20 and 30 days. A reference simulation (`ldr_reference`) is performed on a domain of size $153.6^2\,\mathrm{km}^2$ by 19.1 km, which is sufficiently large to capture the convective cells that are typical for the early RCE development. The minimum wind speed input for the surface layer formulation, $U_{\min}$, is set to $0.1\,\mathrm{m\,s^{-1}}$ in this reference run. A horizontal resolution of 100 m is combined with a vertical grid that stretches from $\Delta z = 30\,\mathrm{m}$ at the lowest level to $\Delta \mathrm{z} \approx 350\,\mathrm{m}$ at

Table 4.1: An overview of all the simulations. All simulations are performed using the SST=300 K case setup. The horizontal resolution of the additional sensitivity runs is halved, but the vertical resolution remains unchanged at $\Delta z = 30$ m for the lowest level.

simulation	U_{min} (m s^{-1})	length (d)	comments
large domain run			153.6^2 km^2 $\times$ 19.1 km, $\Delta x = 100$ m
`ldr_reference`	0.1	20	-
small domain runs			38.4^2 km^2 $\times$ 18.7 km, $\Delta x = 100$ m
`sdr_reference`	0.1	30	-
`sdr_forced`	1	30	-
sensitivity runs			38.4^2 km^2 $\times$ 18.7 km, $\Delta x = 200$ m
`sr_reference`	0.1	20	-
`sr_forced`	1	20	-
`sr_2i4_reference`	0.1	20	`2i4` advection scheme
`sr_2i4_forced`	1	20	`2i4` advection scheme

19 km. In our setup, the lowest level z_1 of the u and v horizontal wind components is at a height of 15 m. The high spatial resolution results in a large increase of the computational costs in comparison to the RCEMIP specification. Furthermore, a set of runs is performed on a smaller domain of 38.4^2 km^2 by 18.7 km in order to study the effect of $U_{\min}$ and test the importance of domain size for our results. This set features a reference (`sdr_reference`) and forced (`sdr_forced`) simulation, which are run with $U_{\min} = 0.1$ m s^{-1} and 1 m s^{-1} respectively, for 30 days. Additional runs are performed on a small domain at $\Delta x = 200$ m (Table 4.1) to test the sensitivity to horizontal resolution and advection scheme.

4.4 Results

4.4.1 The spatial characteristics of surface fluxes and near-surface wind

The cross section of the equivalent potential temperature (θ_e) combined with the near-surface wind speed mask (Figure 4.1) provides insight in the structure and magnitude of the convection-driven winds. The main structure is determined by cold pools, recognizable by low values of θ_e that mark the mid-tropospheric air that has been transported towards the surface by the downdrafts. The presence of the cold pools is in line with observations suggesting that cold pools form when rain rates exceed approximately 2 mm h^{-1} (Zuidema et al., 2017). The high spatial resolution of our simulations also reveals the structure of the shallow circulation that is the precursor of new rain cells to be formed in the near future. For example in the region surrounding $(x, y) = (25, 20)$ thin warm and moist bands of high θ_e mark the new convection.

The superimposed masks of regions with wind below 0.1 m s^{-1} (2.1 % of domain in Figure 4.1a) and 1 m s^{-1} (77 % of domain in Figure 4.1b) show that three quarters of the domain has near-surface wind speeds below 1 m s^{-1}. Only in the vicinity of cold pools centers (light colors in Figure 4.1) the 1 m s^{-1} threshold is exceeded. These regions correspond to the

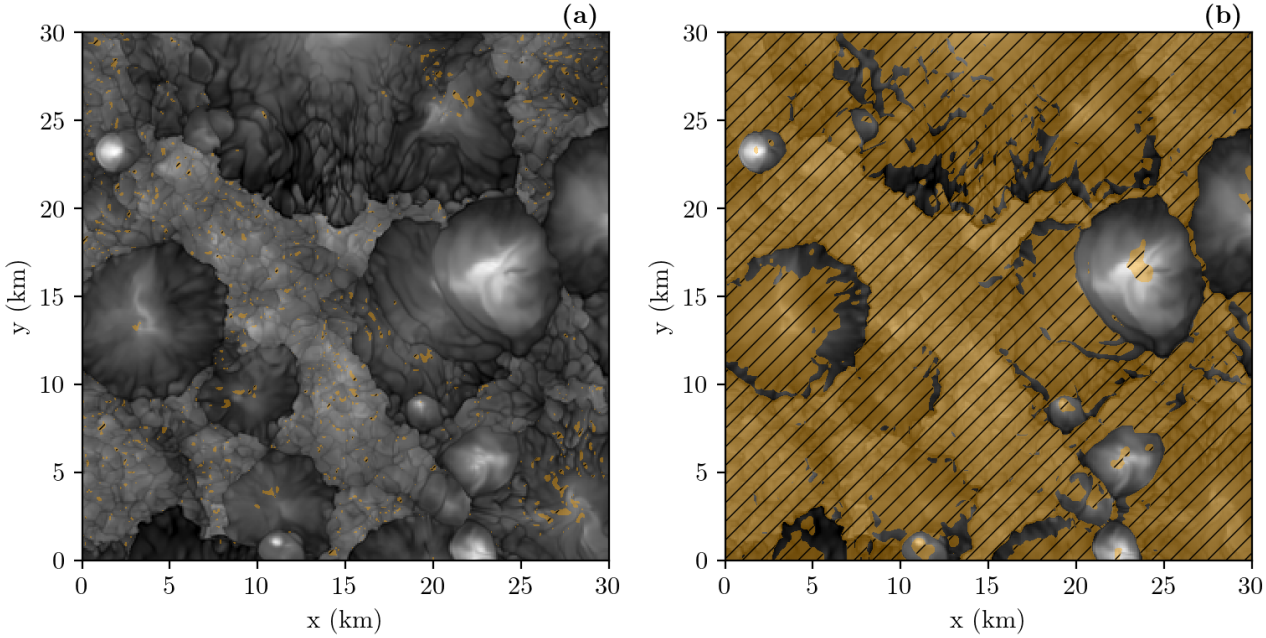

Figure 4.1: Example horizontal cross sections of θ_e at z_1 (= 15 m) for a 30 km by 30 km subsection of `ldr_reference`. θ_e is coloured in grey scale linearly from white (339 K) to black (346 K). This cross section is taken at t=8.8 days. The hatched, transparent light orange overlay marks the grid points where U_1 is below either 0.1 or 1 m s^{-1} for **(a)** and **(b)** respectively. The fraction of the domain covered by these masks is 2.1 % for **(a)** and 77 % for **(b)**.

leading edges, or gust fronts, of actively spreading cold pools. Increased latent heat fluxes and moisture convergence make these gust front regions both favourable for new convection to form and are also the main driver of the horizontal redistribution of moisture (Schlemmer & Hohenegger, 2014, 2016). The threshold of 0.1 m s^{-1} is exceeded in nearly the entire domain due to the wind speeds generated by boundary-layer turbulence and shallow convection in our simulations. Setting a minimum wind speed value of 1 m s^{-1} in the computation of the surface fluxes thus constrains the interaction between boundary-layer turbulence and surface fluxes and consequently narrows the range of wind speeds over which the surface-flux feedback can be active.

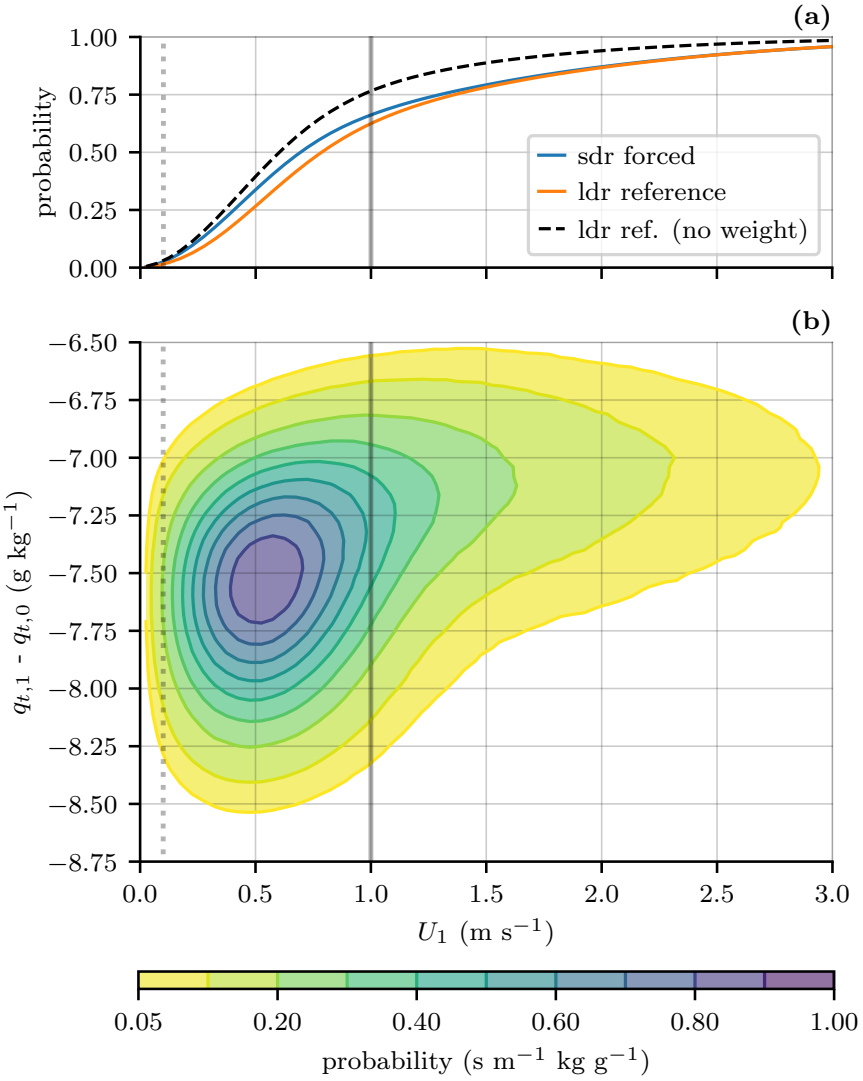

Figure 4.2: 2D PDF of U_1 versus the difference in q_t between z_1 and z_0 **(b)**. The PDF is weighted by the surface latent heat flux and is based on data of days 12 to 20 of `ldr_reference`, sampled every 2 hours. **(a)** features a 1D CDF version of the same data as a function of U_1 and a comparison with `sdr_forced`, also based on data between days 12 and 20. An additional unweighted CDF is also included. The solid vertical line is positioned at 1 m s^{-1}, the dotted line at 0.1 m s^{-1}.

While suppressing surface-flux feedback dynamics in such a large part of the domain is cause for concern, its impact can only be assessed through a quantitative analysis. MOST dictates that the surface flux is proportional to the wind speed and the moisture difference between atmosphere and ocean. Therefore, we have constructed the joint probability density function (PDF) of these two quantities based on data from days 12 to 20 of our reference simulation `ldr_reference` and combined it with cumulative density functions of the wind speed in the `ldr_reference` and `sdr_forced` simulations (Figure 4.2). In order to relate the occurrence of combinations of wind speed and moisture differences to the flux they produce together, a weighting of the probability by the surface moisture flux is applied. The CDFs show that approximately two-thirds of the surface moisture flux is generated in regions where surface wind speeds are below $1\,\mathrm{m\,s^{-1}}$, whereas the unweighted line shows that 76 % of the total surface area has a wind speed below $1\,\mathrm{m\,s^{-1}}$. Furthermore, the peak in the PDF is well-defined and located at a wind speed of $0.5\,\mathrm{m\,s^{-1}}$, indicating that the variability in this range needs to be well-resolved in order to capture the surface-flux feedback in all its detail. The structure of the PDF is indicative of a positive surface-flux feedback, because the loss of moisture difference between ocean and atmosphere is small for increasing wind speed. For instance, a five-fold increase in wind speed from the center of the PDF ($0.5\,\mathrm{m\,s^{-1}}$) to its tail ($2.5\,\mathrm{m\,s^{-1}}$) leads to a less than 10 % ($0.5\,\mathrm{g\,kg^{-1}}$) moisture difference reduction. Therefore, new convection is likely to form nearby an already active region.

To elaborate the impact of boundary-layer turbulence on the spatial structure of the surface moisture flux, we have quantified its partitioning between calm ($U_1 < 1\ \mathrm{s^{-1}}$) and convective ($U_1 \geq 1\,\mathrm{m\,s^{-1}}$) regions based on 4 days of data for all experiments in Table 4.1 (Figure 4.3). Each experiment contains a reference and a forced simulation. The forced simulations display significant differences in surface moisture flux between calm and convective regions as well as in the domain mean compared to the reference simulations. In forced simulations, the mean flux in calm regions is approximately $10\,\mathrm{W\,m^{-2}}$ (25 %) higher than in reference simulations and covers a slightly smaller area (2 to 4 percentage points). This relationship is reversed in the convective region of the domain, due to the decreased near-surface moisture gradient. Here, the mean flux is approximately $10\,\mathrm{W\,m^{-2}}$ (15 %) lower in forced simulations. Since this area is also three times smaller than the calm region, the total effect is a significant net increase in total surface latent heat flux of $\sim$10% and a shift of flux towards the calm region throughout the transition towards RCE. The results are robust under a reduction of the horizontal grid spacing to 200 m (`sr_200_`) as well as under a change in advection scheme (`sr_2i4_`).

4.4.2 The temporal evolution of convection

We now study the time evolution of convection, because idealized studies of convection over a constant temperature surface have shown a strong coupling between the rate of change of most of the bulk boundary-layer properties to the magnitude of the surface fluxes (Heerwaarden & Mellado, 2016). Figure 4.4 shows the temporal evolution towards RCE, the Bowen ratio, u_* and the specific humidity at the lowest model level for reference and forced simulations on a small and large domain (Table 4.1). The first strong cold pools form after

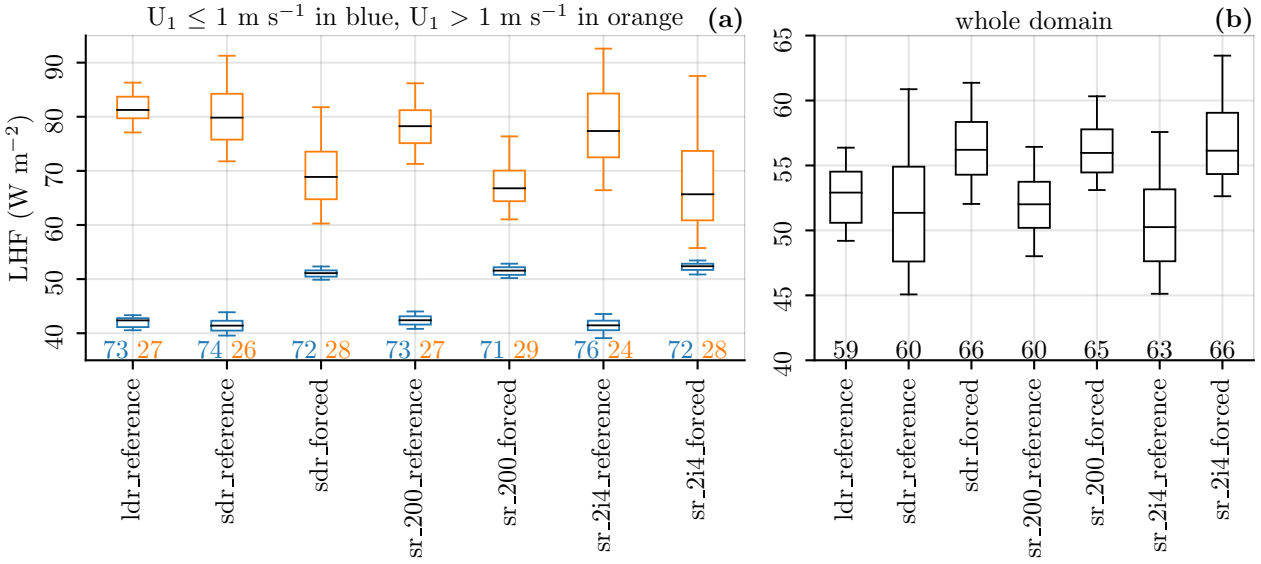

Figure 4.3: Box plots of the surface latent heat flux based on days 16 to 20, sampled every 360 seconds. **(a)** shows box plots based on the mean value for the area of the domain where U_1 is $\leq$ or $>$ than $1\,\mathrm{m\,s^{-1}}$, in blue and orange, respectively. The numbers at the bottom represent the percentage of the area of the domain where the U_1 condition is valid, color-coded according to the corresponding box plot. For **(b)**, the total domain mean values are used to create the box plot. Here, however, the values at the bottom indicate the percentage of the total flux that comes from the area where $U_1 \leq 1\,\mathrm{m\,s^{-1}}$. The black horizontal lines represent the median. The whiskers in each box plot delineate the 5-95 percentiles of the data.

$\sim$48 h, resulting in cascading release of convective available potential energy, which is particularly evident in `ldr_reference`. The surface enthalpy flux is consistently higher in the forced simulation for at least the first 25 days, after which it starts to converge with the reference simulation. Most of the enthalpy flux comes from the latent heat flux, given the low Bowen ratio throughout the simulations (Figure 4.4b), resulting in a marginal increase in precipitation in the forced simulation (Figure 4.4c). The convergence of the surface fluxes is a direct consequence of our experimental setup, as we are simulating adjustment to a prescribed radiative cooling profile in order to keep the simulation computationally affordable. This means that the sensible heat flux is decreased in the forced simulation compared to the reference (Figure 4.4b). Nonetheless, our simulations demonstrate that forced simulations consistently have a higher u_* for the same flux, and consequently a lower moisture difference between ocean and atmosphere. Therefore, there is a moister atmosphere, with the strongest moistening in the boundary layer (Figure 4.4f), caused by the enhanced surface moisture fluxes over the calm regions (Section 4.4.1). The potential for radiative cooling over dry areas is thus suppressed in the forced simulation. This most likely lowers the potential for self-aggregation, because the radiative cooling differences between dry and wet areas drive up-gradient moist static energy transport by shallow circulation (Naumann et al., 2019). In addition, the forced simulation adjusts faster to the radiative forcing, as is indicated by its higher surface enthalpy flux (Figure 4.4a). This is in line with earlier findings that the time

scale of convective adjustment is inversely proportional to the magnitude of the surface fluxes (Tompkins & Craig (1998b), their Eq. 12, Cronin & Emanuel (2013), their Eq. 7, and Heerwaarden & Mellado (2016), their Eq. 6). The faster adjustment makes radiative cooling a relatively less powerful mechanism to enhance contrasts between dry and moist areas.

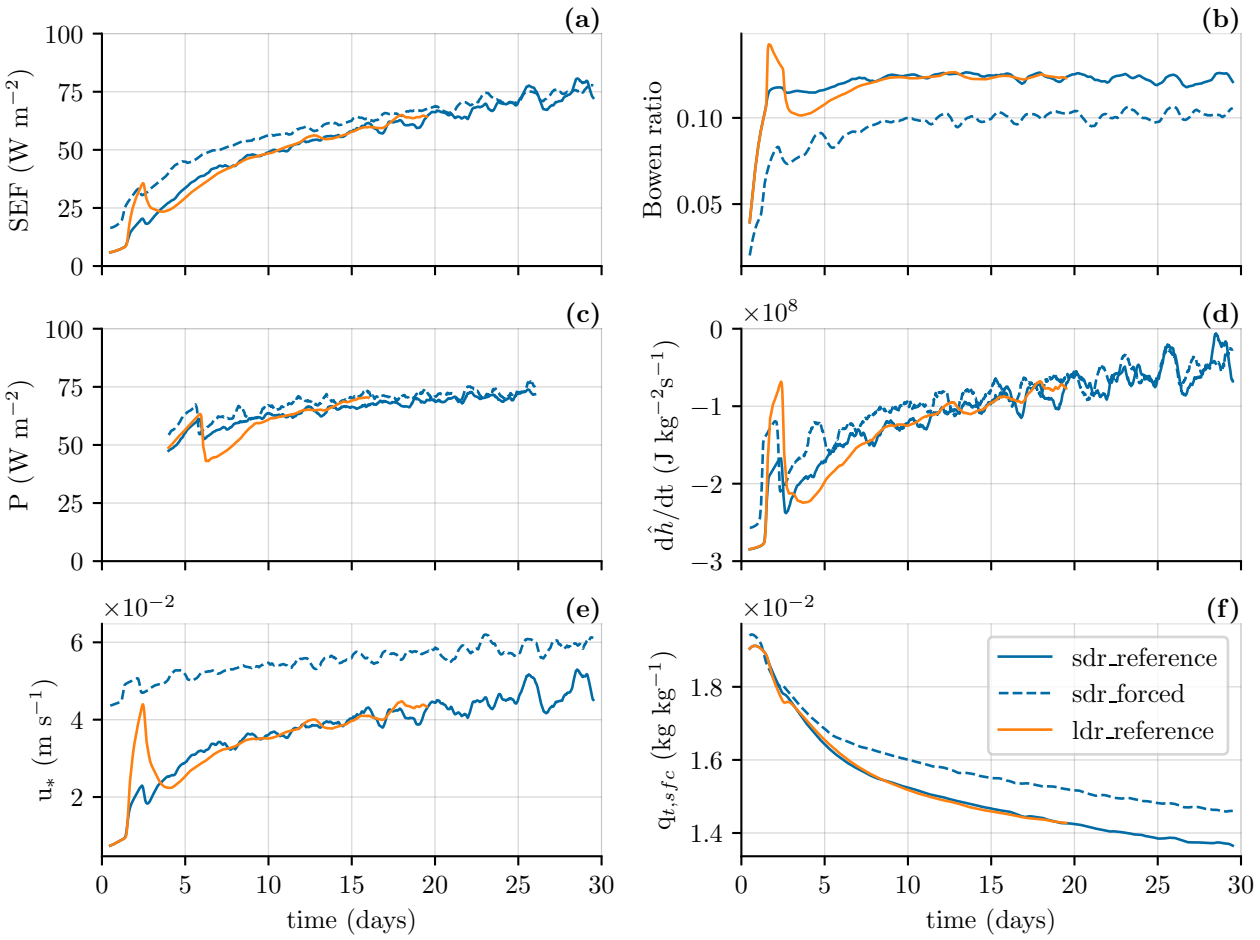

Figure 4.4: Time series of six domain-mean variables: **(a)** surface enthalpy flux (SEF), **(b)** Bowen ratio, **(c)** precipitation expressed in W m^{-2}, **(d)** rate of change of the vertically integrated moist static energy $\hat{h}$, **(e)** surface friction velocity and **(f)** specific humidity at the lowest model level. A 24-hour centered moving average is applied to all time series, except rain rate is averaged with a 8-day window. This is done to more clearly see differences between simulations.

4.5 Summary and perspective

In this study we demonstrate the importance of ocean-atmosphere moisture exchange at vanishing wind in simulations of idealized tropical convection. We have performed a series of high-resolution large-eddy simulations based on the Radiative Convective Equilibrium Model Intercomparison Project (RCEMIP, Wing et al., 2018), but with an increased spatial resolution in order to resolve boundary-layer turbulence. Our results show that enforcing a minimum wind speed to account for boundary-layer turbulence and shallow circulation, which is the

common practice in large-scale and cloud-resolving models, has a profound influence on the ocean-atmosphere moisture exchange. Imposing a minimum wind speed of $1\,\mathrm{m\,s^{-1}}$ enhances the mean surface latent heat flux with more than 10 % compared to a simulation in which the wind can vanish in the surface-flux computation. Furthermore, as the flux enhancement mostly happens in calm regions at the expense of the surface flux in the convective regions, the contrast in latent heat flux magnitude between calm regions and convective regions loses more than half of its magnitude if a $1\,\mathrm{m\,s^{-1}}$ minimum wind speed is imposed.

Our simulations give therefore a new perspective on the wind-induced surface heat exchange (WISHE) feedback. In our simulation setup, the ability of the model to reduce surface fluxes under vanishing wind is more important than the enhancement of fluxes in regions of high wind speeds. Furthermore, the simulations in which the wind can vanish have lower surface moisture fluxes, hence the ability of radiation to enhance contrasts between moist convective regions and dry calm regions is expected to be larger. Consequently, the surface-flux feedback in self-aggregation is potentially stronger than assumed until now. This conjecture can only be confirmed or rejected after performing RCE simulations on large domains with fully resolved boundary-layer turbulence and interactive radiation, but this will remain a computational challenge for the foreseeable future.

Chapter 5

Record high solar irradiance in Western Europe during first COVID-19 lockdown largely due to unusual weather

This chapter is based on:

van Heerwaarden, C. C., Mol, W. B., Veerman, M. A., Benedict, I., Heusinkveld, B. G., Knap, W. H., Kazadzis, S., Kouremeti, N., & Fiedler, S. (2021). *Record high solar irradiance in Western Europe during first COVID-19 lockdown largely due to unusual weather*. In Communications Earth & Environment. Springer. https://doi.org/10.1038/s43247-021-00110-0

Abstract

Spring 2020 broke sunshine duration records across Western Europe. The Netherlands recorded the highest surface irradiance since 1928, exceeding the previous extreme of 2011 by 13 %, and the diffuse fraction of the irradiance measured a record low percentage (38 %). The coinciding irradiance extreme and a reduction in anthropogenic pollution due to COVID-19 measures triggered the hypothesis that cleaner-than-usual air contributed to the record. Based on analyses of ground-based and satellite observations and experiments with a radiative transfer model, we estimate a 1.3 % (2.3 W m^{-2}) increase in surface irradiance with respect to the 2010-2019 mean due to a low median aerosol optical depth, and a 17.6 % (30.7 W m^{-2}) increase due to several exceptionally dry days and a very low cloud fraction overall. Our analyses show that the reduced aerosols and contrails due to the COVID-19 measures are far less important in the irradiance record than the dry and particularly cloud-free weather.

5.1 Introduction

A large part of Western Europe (Figure 5.1a, hatched area) experienced exceptionally sunny and dry weather from March 23 to the end of May 2020. Sunshine duration extremes were reported in the United Kingdom, Belgium, Germany, and The Netherlands (Madge, 2020; DWD, 2020; KNMI, 2020; KMI, 2020) paired with exceptionally deep blue skies (Knap & Meirink, 2020; Meirink et al., in press). For instance, The Netherlands reported 805 h of sunshine, compared to 517 h normally and 62 h more than the previous record of 2011 (KNMI, 2020). This resulted in a time-integrated surface solar irradiance for spring (March, April, May) that was the largest ever observed at the Veenkampen station (The Netherlands) since 1928 (Figure 5.1b). The daily mean irradiance sum of 206 W m^{-2} exceeded the previous record of 2011 by 25 W m^{-2}. The diffuse radiation reaching the surface was only 38 % of the total solar irradiance in the period, compared to 49–58 % in the other top-ten springs with high irradiance (Figure 5.1). Clouds reduced daily solar irradiance on average by 22 % in spring 2020 with respect to clear-sky conditions, 3σ less than the 2004-2020 mean reduction of 36 %, as computed from the observations of solar irradiance from Veenkampen station and clear-sky surface solar irradiance taken from McClear (Gschwind et al., 2019).

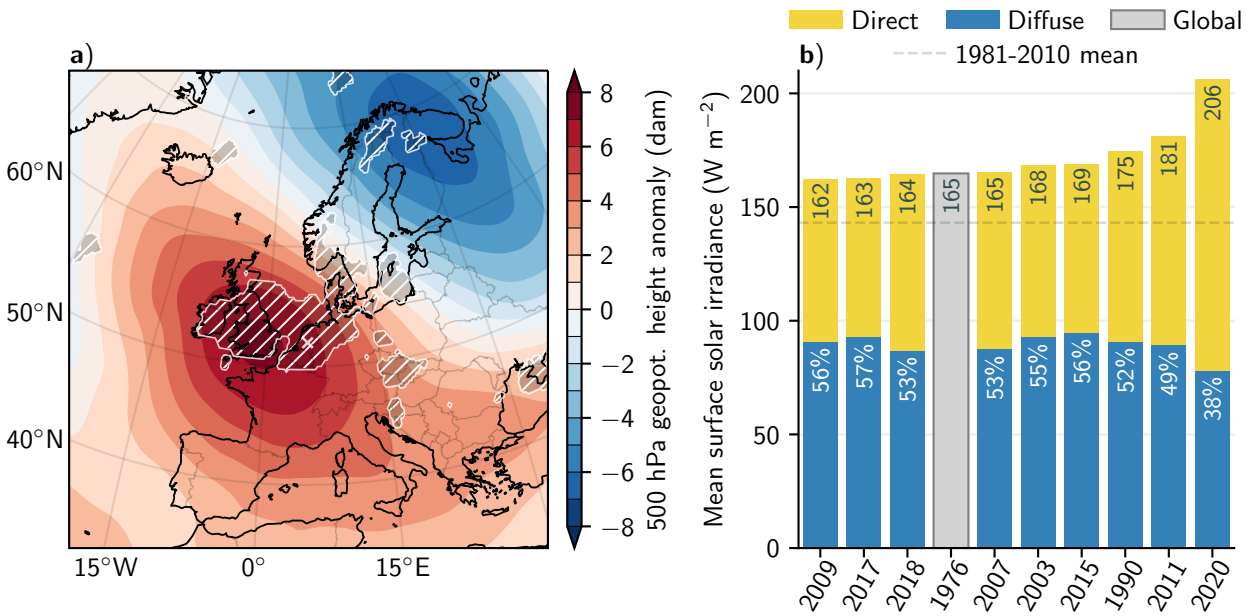

Figure 5.1: Surface irradiance in spring 2020 relative to earlier years. Figure shows **a)** 500 hPa geopotential height anomaly of 2020 spring (March, April, May) with respect to the 1981–2010 climatology, based on ERA5 reanalysis (Hersbach et al., 2020), hatched area indicate locations where the global irradiance (sum of direct and diffuse) in ERA5 exceeds the 1979–2019 maximum by more than 1 %, and **b)** top-10 years of daily mean integrated global horizontal irradiance (GHI) since 1928 for the Veenkampen station (white cross in panel a) from March 1 until May 31, partitioned into direct and diffuse. The percentages show the diffuse portion of GHI where such measurements are available. Veenkampen station was moved over a distance of 2 km in 2012, 1989 is missing from the record.

These records all happened amid the first European wave of the COVID-19 pandemic (JHU, 2020; ECDW, 2020), during which many countries went into lockdown, leading to a global reduction in anthropogenic pollution (Muhammad et al., 2020). Less traffic and industrial activity led to losses in NO_x, SO_2, and CO_2 emissions of tens of percents (Bauwens et al., 2020; Forster et al., 2020; Quéré et al., 2020), with consequent changes to the atmospheric composition (Le et al., 2020; Kroll et al., 2020) and the radiation balance (Forster et al., 2020). The large leap with which the irradiance records were broken made us hypothesize that the reduction in anthropogenic aerosols and contrails related to the COVID-19 lockdown are a secondary driving force behind the observed irradiance extremes next to the exceptionally cloud-free weather. This study aims to quantify the individual contributions of weather and aerosols to the extreme irradiance of 2020. With the already relatively clean air of Western Europe without the COVID-19 lockdown, we expect the contribution of weather to exceed that of aerosols. Nonetheless, an exact quantification of the contribution will provide useful insight in the lockdown effects, as well as in the extremity of the weather and future surface irradiance extremes.

5.2 Results

5.2.1 Time evolution of spring 2020

To test our hypothesis that COVID-19 lockdowns have contributed to the irradiance extreme, we first analysed data (Knap, 2022) from the Baseline Surface Radiation Network's (BSRN, Driemel et al., 2018) measurement station in Cabauw, The Netherlands. This station is located in the center of the regions that reported sunshine duration records, and has already available observations of irradiance and aerosol optical depth (AOD) for spring 2020 (Figure 5.2). The onset of the prolonged time period of fair weather on March 21, as identified by the moment where the global irradiance starts approximating the clear-sky radiation, coincides with the strong drop in flight activity that marked the onset of the COVID-19 lockdown in many European countries (Figure 5.2). The fair weather is reflected by the large amounts of global irradiance, i.e., direct and diffuse irradiance taken together in the observations (Figure 5.2), and the large contribution of direct solar irradiance therein. Until May 31, there were only three overcast days. The surface irradiance is gradually increasing over time towards the end of May, hence the sunny days later in the period weigh more heavily in the mean shown in Figure 5.1. To enable comparison among days without the yearly cycle, Figure S5.1 contains a normalized version of Figure 5.2.

Especially the period of 21 to 31 March was remarkably cloud free, e.g., seen by the global irradiance equal to the clear-sky radiation, and values for diffuse irradiance are the smallest in the period. These days recorded the lowest AOD of the entire period and the lowest precipitable water in the atmosphere (Figure 5.2), underlining the cleanliness and dryness of the air. Radiosonde observations of De Bilt showed strikingly low amounts of precipitable water (Figure S5.3). Based on ERA5 Reanalysis at a similar location, March 22 to 26 had on average 4.0 $\pm$ 1.2 kg m^{-2} precipitable water, far below the 1981–2019 mean of 11.5 $\pm$ 4.2

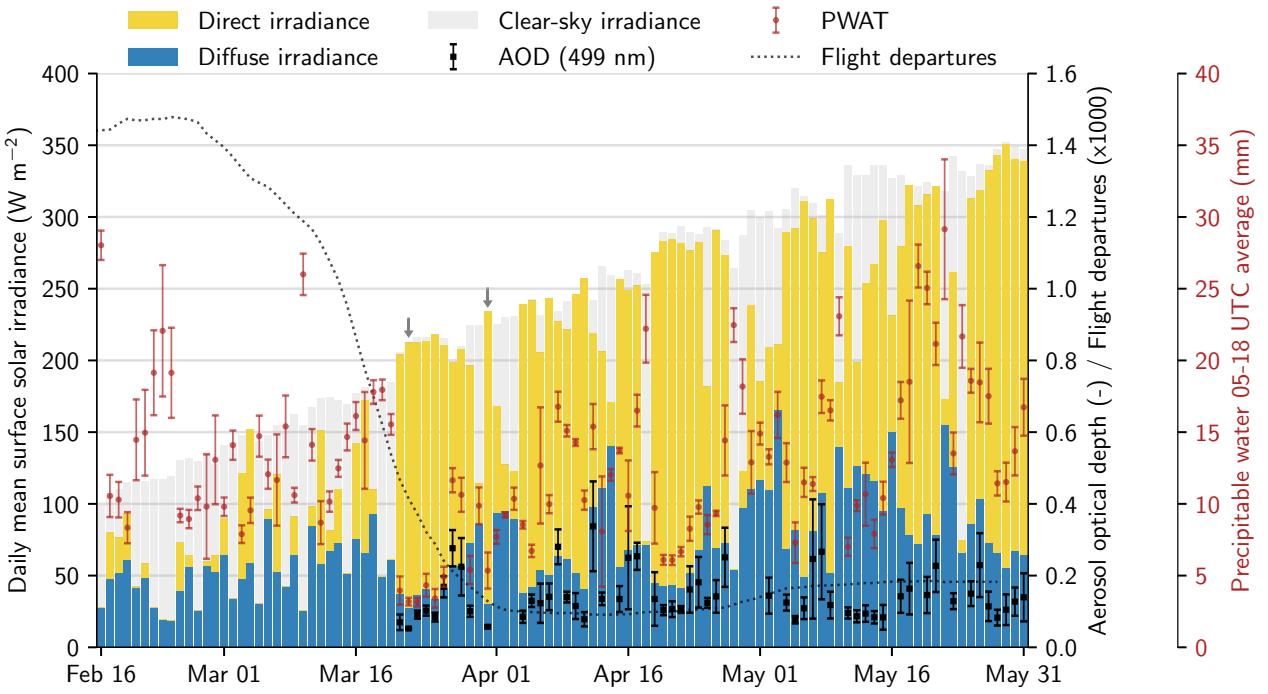

Figure 5.2: Time series of relevant variables in spring 2020 in Cabauw, NL. These include time series of measured direct and diffuse irradiance (BSRN Cabauw, NL), clear-sky global horizontal irradiance (Copernicus Atm. Monitoring Service (CAMS) McClear dataset for Cabauw), 499 nm aerosol optical depth (AOD) at Cabauw measured using a precision filter radiometer and processed at PMOD/WRC (Kazadzis et al., 2018), daytime precipitable water at the grid point closest to Cabauw based on ERA5 reanalysis (Hersbach et al., 2020) and the weekly moving average of flight departures at (major) Western Europe airports (OpenSkyNetwork COVID-19 dataset (Schafer et al., 2014)). Error bars indicate daily variability ($\pm\sigma$). Arrows point to 22 and 31 March. Instrument maintenance and cloud-contamination prevented ground-based AOD observations before 21 March. Complementary AOD data combined with normalized irradiance and a cross-validation of the complementary AOD data are found in Figs. S5.1 and S5.2.

kg m^{-2} for the same period. Later, in May, multiple days had a very low AOD (below 0.1), including days with partial cloudiness, e.g., May 11 to 15.

5.2.2 Anomalies in weather patterns, aerosols, and contrails

In order to assess the potential impact of the COVID-19 lockdown on the irradiance extremes, and to evaluate extremes in weather versus human activity, we discuss the anomalies in atmospheric circulation (Figure 5.1a), in precipitable water, cloud cover, and AOD (Figure 5.3), and in contrail formation with respect to their climatology.

Spring 2020 had recurring weather patterns favorable for sunshine, with persistent north- to easterly flow over Western Europe or weak winds in the centre of high pressure systems. These conditions are reflected by a positive anomaly in the 500-hPa geopotential height in the lockdown period centered over the south of the United Kingdom and a negative anomaly in

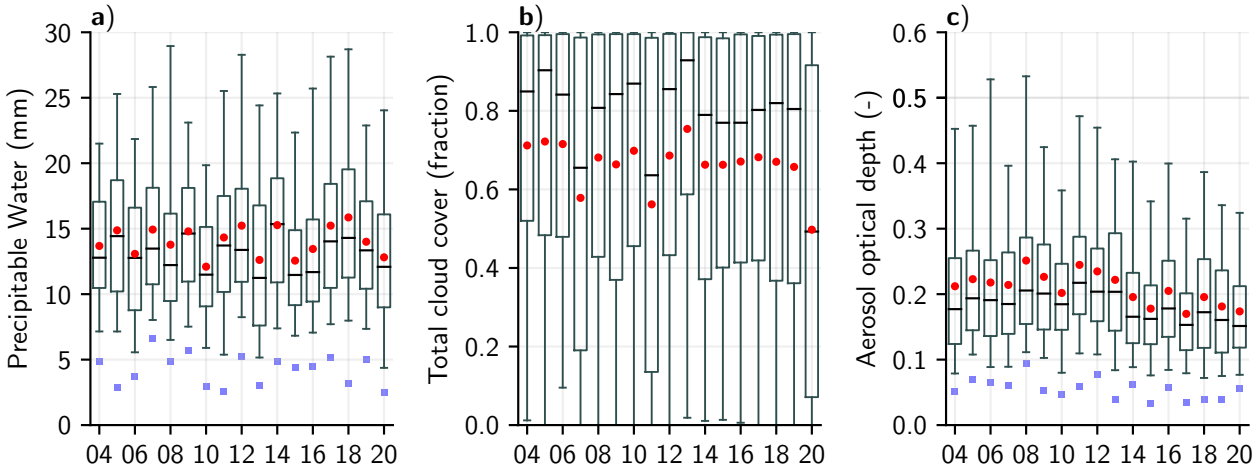

Figure 5.3: Box plots of values during spring of variables affecting surface solar irradiance. Figure shows **a)** ERA5 precipitable water, **b)** ERA5 total cloud cover, and **c)** CAMS aerosol optical depth at 550 nm. Box plots are based on hourly values for March, April and May, between 5 and 18 UTC (approximate mean day time) at the location or grid point closest to Cabauw, NL. Red circles indicate mean values, blue squares are minima, and whiskers represent 5th and 95th percentiles. Data spans years 2004 to 2020.

northern Scandinavia and Russia (Figure 5.1a). This pattern is typical for atmospheric blocking conditions (Folland et al., 2009), which are often drivers of heatwaves in summer and cold spells in winter (Pfahl & Wernli, 2012). In absence of temperature extremes, springtime blocking conditions attract relatively less interest (Woollings et al., 2018), despite regular occurrence (Brunner et al., 2017). They are, as this study shows, a contributor to surface irradiance extremes due to their related cloud-free skies, caused by its dry and sinking air masses. To further elaborate the weather patterns, the German objective weather type classification (Bissolli & Dittmann, 2001), which contains The Netherlands within its domain, showed that 2020 had approximately ten more spring days in dry and anticyclonic regimes compared to its 1980-2019 mean (Figure S5.4), confirming favorable synoptic conditions for sunshine.

Also the precipitable water and total cloud cover (Figure 5.3a and Figure 5.3b) display the exceptional weather. The box plot of hourly values of precipitable water (Figure 5.3a), which measures the vertical integral of water in the atmosphere, shows that 2020 was among the drier years in the record (2004-2020) with the lowest 5th-percentile and minimum value corresponding to the very dry period starting March 21 (Figure 5.2). The exceptional conditions of 2020 are most prominently reflected in the box plot of hourly values of total cloud cover (Figure 5.3b), with the 95th-percentile, mean, median, and 5th-percentile being by far the lowest on record. The mean cloud cover of 0.5 is more than 0.16 less than the mean over 2004-2020 (0.66) and also 0.05 lower than 2011, the year of the previous record.

Within cloud-free conditions, irradiance increases with decreasing AOD. We documented many days in spring 2020 with exceptionally low humidity and a low AOD (Figure 5.2).

To appreciate the AOD observations, we have to acknowledge the challenge in separating aerosols from homogeneous, optically thin cirrus in observations using sun photometers (Chew et al., 2011) or satellite products (Kaufman et al., 2005), which can result in a positively biased AOD. To avoid this difficulty and to assess a longer statistic of AOD, we use here the hourly AOD values from the CAMS aerosol product (Figure 5.3c, Figure S5.1), which compares well against ground-based observations over Europe (Gueymard & Yang, 2020) (Figure S5.2). Our analysis highlights that spring 2020 had the lowest median in hourly AOD since 2004. Spring 2020 was also among the springs with the lowest mean AOD, with only 2015 and 2017 being lower, but its minimum and 5th percentile values did not stand out from the statistics of hourly AODs. Therefore, the reduction in anthropogenic aerosol pollution due to the lockdowns did not lead to new extremely low hourly values of AOD, but rather to frequent hours with low AODs.

A reduction in contrail-cirrus due to the drop in flight activity (Figure 5.2) is another pathway for the lockdowns to enhance surface irradiance. This is particularly true in Western Europe, which is a hot spot for contrail-cirrus, owing to a combination of high aviation activity, and suitable meteorological conditions. To obtain a rough estimate of the effect, we compared spring 2020 to 2011 and 2015, which are both among the top-five years in terms of surface irradiance (Figure 5.1b), while having contrasting AODs. Year 2011 had the highest median AOD in recent years, whereas 2015 had an AOD statistic comparable to 2020 (Figure 5.3). The meteorological conditions for persistent contrail formation at 250 hPa, close to the typical flight level of 230 hPa (Burkhardt & Kärcher, 2011; Lee et al., 2009; Jensen et al., 1998), are slightly less favourable (see Table S5.1 and Figure S5.5), thus we expect to observe less contrail-cirrus in 2020. Manual inspection of cirrus and contrail occurrence (see Methods and Figure S5.6 for an example) in NASA Worldview (NASA, 2024) imagery for The Netherlands gives results consistent with our expectation. The images showed that 2011 and 2015 had about twice as much cirrus, but with 50 % more contrail contamination, compared to 2020. Given that contrail-cirrus has a net shortwave radiative forcing in the order of -1 W m^{-2} over Western Europe (Stuber et al., 2006), but can enhance diffuse irradiance with tens of percents (Feister & Shields, 2005; Gueymard, 2012; Weihs et al., 2015), we conjecture that the low presence of contrails contributed to the extremely low diffuse fraction that was observed in 2020. To illustrate this further, we selected three pairs of consecutive days with a clear sky on the first day and cirrus clouds on the second. Clear-sky days March 23, April 22, and May 6 had diffuse fractions of respectively 17, 14, and 16 %, whereas days with cirrus March 24, April 23, and May 7 showed diffuse fractions of 19, 24, and 27 %. In each of the three pairs, the irradiance relative to clear-sky dropped at most a percent on the day with cirrus, indicating that cirrus clouds mainly caused downward scattering. This provides further evidence that, despite its large influence on diffuse irradiance, the reduced aviation is likely to play a minor role in the global surface irradiance extreme.

5.2.3 Radiative transfer modelling for interpretation of extremes

We present here estimations of i) the relative importance of different contributing factors to the extreme in surface irradiance, and ii) the anomalies in cloud radiative forcing and the

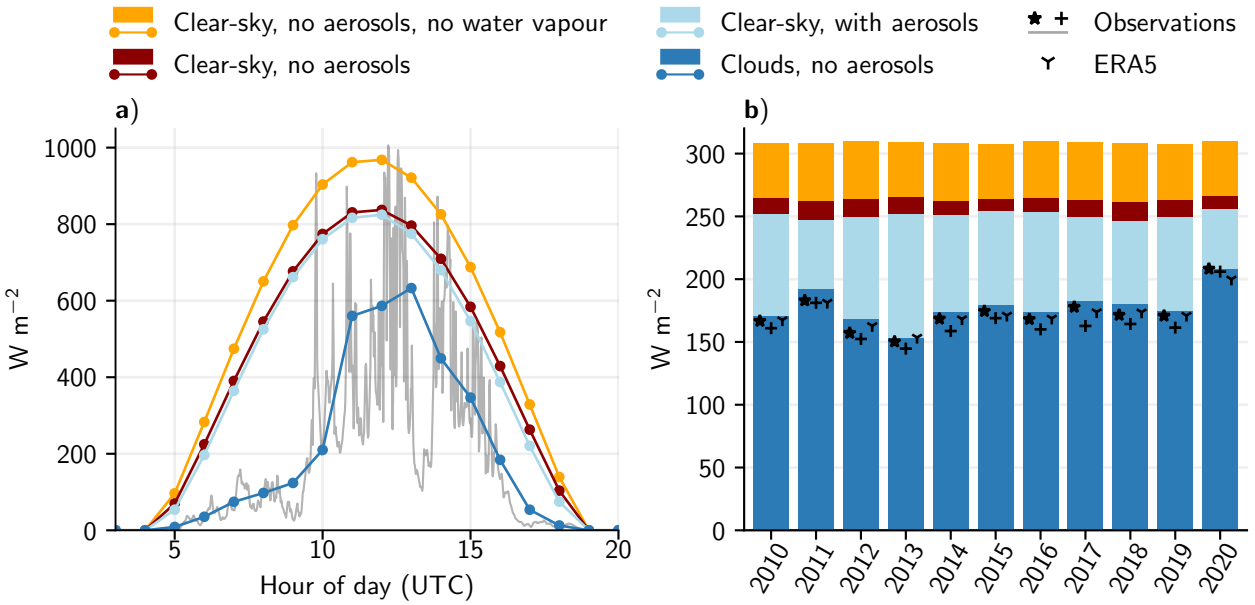

Figure 5.4: Modelled surface irradiance with a radiative transfer model. Irradiance is shown for **a)** an illustrative case study of 29 April 2020 compared against Cabauw observations, and **b)** averaged over the months March, April, and May compared against Cabauw ($\star$) and Veenkampen ($+$) observations and against the surface irradiance of ERA5. See Table S5.2 for exact values corresponding to bars.

direct aerosol effects. To this end, we used a contemporary radiative transfer model (Pincus et al., 2019) to first reproduce the observed surface irradiance, and subsequently repeat the calculation without individual components to assess their quantitative contribution to the surface irradiance. We used the McClear clear-sky radiation product to infer the aerosol contribution (Gschwind et al., 2019) (see Figure S5.7 for a validation of the direct aerosol effect as a function of AOD). Further details are given in the Methods section. The combination of the experiments with the radiative transfer model and the clear-sky data provides surface irradiance under four conditions, compared against the observations in Figure 5.4: i) experiment `dark blue` resembles the reality, but without aerosols in the atmosphere, ii) experiment `red` additionally removes the clouds, iii) experiment `orange` additionally removes the water vapour, and iv) experiment `light blue` is the clear-sky product, thus without clouds but with aerosols.

We first show the modelled surface solar irradiance for a single day on 29 April in Figure 5.4a for illustrating the transient behaviour of the radiative transfer model results. The experiment `dark blue` with clouds, but without aerosols closely follows the observed slowly increasing irradiance due to vanishing clouds. It confirms the ability of the model to reproduce the time series of surface irradiance (see Figure S5.8 for validation). At noon, removal of clouds (`red`) increases the irradiance by 250.7 W m^{-2}, and removing water vapour (`orange`) increases irradiance by a further 130.8 W m^{-2}, whereas the presence of aerosols (`light blue`) lowers the irradiance only by 12.5 W m^{-2}. Both the removal of water vapour and clouds have a larger effect on the irradiance than removing aerosols, due to the typically larger optical

depth of clouds than of aerosols.

We expand our analysis to the entire spring period for each of the past 10 years in Figure 5.4b. Here, the top of each bar segment indicates the global surface irradiance for the situation indicated by its color. If clouds, aerosols, and water vapour are removed, all years have a bar of approximately equal depth, indicating that our experiment captures the essence and that leap years and year-to-year variability in atmospheric pressure, ozone, and temperature are of minor importance to the irradiance extremes in 2020. The variation over the years is comparable between the two measurement stations and is closely following the radiative transfer computations with clouds (`dark blue`), but without aerosols. The observations are consistently lower than the model simulation, consistent with the here removed aerosols. Furthermore, the Cabauw station has a consistently higher irradiance than Veenkampen, due to its closer proximity to the coast, where clouds are less common (KNMI, 2024).

We quantify the cloud radiative effect at the surface as the difference between the experiment with clouds and the clear-sky experiment without aerosols (`dark blue` minus `red`). The irradiance increase due to the reduction in clouds is +30.7 W m^{-2} in spring 2020 with respect to the 2010–2019 mean cloud radiative effect of -88.6 W m^{-2}. Similarly, we quantify the aerosol effect from the difference between the clear-sky experiment without aerosols and the McClear data (`light blue` minus `red`). This indicates an increase in irradiance of +2.3 W m^{-2}, with respect to the 2010–2019 mean aerosol effect of -13.0 W m^{-2}. The water vapour effect is quantified as the clear-sky experiment minus the dry experiment (`red` minus `orange`) and gives an enhancement of only +1.5 W m^{-2} with respect to the 2010–2019 mean water vapour effect of -45.4 W m^{-2}. The vapour enhancement is only the contribution to the optical properties of the clear-sky radiation, and that the most important signal of the atmospheric moisture anomaly of 2020 is tightly linked with the low magnitude of the cloud cover. The low humidity also affects the aerosol optical depth in the sense that less water vapour is available for condensation on the aerosol surface keeping the aerosol optical depth smaller than in moist conditions. The quantification of the three effects highlights the relative importance of variations in cloud cover over the years in explaining the surface irradiance. It emphasizes that the sunny weather played the most important role in setting the 2020 record in surface irradiance, while the reduced emission of anthropogenic aerosols is of smaller importance to the extent that even without the reduction the irradiance record had occurred.

5.3 Discussion

During the exceptionally sunny spring in Western Europe amid the COVID-19 pandemic in 2020, The Netherlands received the most solar radiation at the surface since the start of the measurements in 1928 and never experienced so little scattering of light (Figure 5.1b). The particularly dry atmosphere (Figure 5.2) and weather patterns favouring sunny weather (Figure 5.1a) led to fewer clouds than in previous years. Based on radiative transfer calculations, we estimated the relative contributions of clouds, water vapour, and aerosols and argue that

the former is the dominant contributor to the new irradiance extreme (Figs. 5.3 and 5.4), while the impact of COVID-19 measures via aerosols is an order of magnitude less.

With all but two of the top-10 spring irradiance years since 1928 observed in the two most recent decades (Figure 5.1), it has become clear that conditions are now more favorable for sunshine than in the past. This is partially explained by a well-documented downward trend in aerosol concentrations over Western Europe, leading to a large-scale upward trend in surface solar irradiance, often referred to as brightening (Wild et al., 2004, 2005; Wild, 2012). Our data fits into that picture as, measured by the median, spring 2020 was the cleanest on record in The Netherlands since 2004 (Figure 5.3b) and the data shows an ongoing downward AOD trend (-3.5 $\cdot$ 10^{-3} y^{-1}, as derived from Figure 5.3b). With exceptional weather conditions emerging as the main contributor to the 2020 extreme, the question arises if weather patterns are also showing a trend that is more favorable for sunshine. There is a clear link between weather patterns and surface irradiance, as has been shown for Northern Europe (Parding et al., 2016). At the same time, there is an extensive debate on the existence of trends in weather patterns in Europe in recent decades, mainly due to their strong sensitivity to the chosen classification method and domain location and size (Kučerová et al., 2017). To illustrate, an increase in spring blocking highs over Europe and a drop in cyclonic activity in Scandinavia has been reported (Philipp et al., 2007), in line with more general claims that anthropogenic influence on the jet stream makes weather more persistent (Francis & Vavrus, 2012; Coumou et al., 2018). At the same time, recent studies show an absence of trends in the frequency and the persistence of blocking events in spring (Brunner et al., 2017; Huguenin et al., 2020). With the above-mentioned uncertainty in trends, we cannot confirm nor rule out the influence of changing weather patterns on the frequency of cloud-free and exceptionally dry skies. The still uncertain response of clouds and circulation to warming (Woollings et al., 2018; Bony et al., 2015) prevents a conclusion on their future contribution to the frequency and strength of new seasonal extremes in irradiance.

Further effects of the aerosol removal are possible, including rapid adjustments of clouds to associated temperature changes and aerosol effects on cloud microphysical processes, but these can not be quantitatively assessed with the model used here. Furthermore, given the worldwide impact of COVID-19 lockdown on emissions of anthropogenic aerosols and greenhouse gases (Forster et al., 2020), there exists a possibility of a response of the global circulation to the perturbed radiation balance. With the inherent variability of the weather, proving such a response is challenging based on a single spring, yet studies with global models have shown interactions between aerosols, clouds, and circulation based on longer time scales (Liepert et al., 2004; Liu et al., 2019; Wilcox et al., 2019; Fiedler & Putrasahan, 2020). To conclude, if we account for additional aerosol effects, the impact of the reduced anthropogenic aerosols due to the lockdown is potentially larger than our estimate of the instantaneous clear-sky radiative effects of the aerosol removal.

With the prospect of anthropogenic aerosol emissions in Europe to stay small or even decrease further in the future (Fiedler et al., 2019), weather will be the most relevant factor in establishing new spring irradiance records. At the moment, however, many regions of

the world are more strongly polluted than Western Europe, and larger regional effects of aerosol reductions on irradiance from COVID-19 lockdowns are already being documented (Peters et al., 2020). With the pandemic still going on, more data to test our expectation will become available in the near future.

5.4 Methods

5.4.1 Cirrus and contrail-contamination estimation

Effects of aviation are estimated by comparing two top-5 irradiance years with relatively high and low AOD with 2020, hence the choice of 2011 and 2015. Environmental conditions favourable for persistent contrails, namely low air temperature at flight level (Jensen et al., 1998), and often occurring supersaturation with respect to ice (Burkhardt & Kärcher, 2011; Lee et al., 2009), are quantified using ERA5 reanalysis for a domain covering approximately The Netherlands at 250 hPa.

Cirrus occurrence and whether it is contaminated by contrails is manually counted by looking at high resolution satellite images from Terra and Aqua MODIS, available on the NASA Worldview website (NASA, 2024). The inspected area covers The Netherlands and closely neighbouring regions (Belgium, western Germany and part of the North Sea). This area is part of the irradiance extreme coverage (Figure 5.3 and helps offset the fact only two images close to noon per day are available. Only cirrus and contrails optically thick enough to be detectable by eye can be counted, anything that is too thin to detect is assumed to have only a very small impact on irradiance. Contrail-contamination is counted when there is cirrus with five or more linear (typically overlapping) or unnatural looking (dispersed) condensation trails present. See Figure S5.6 for a clear example.

5.4.2 Radiative transfer modelling

We used the Radiative Transfer for Energetics and RRTM for General circulation model applications—Parallel (RTE+RRTMGP) (Pincus et al., 2019) to reproduce the surface irradiance observations at Cabauw, The Netherlands for spring 2020 (March, April, May) in order to construct Figure 5.4. The computation requires hourly atmospheric profiles of pressure, temperature, water vapour, liquid water, ice, cloud cover, cloud liquid water, cloud ice, and ozone at a $0.25 \times 0.25^\circ$ grid resolution taken from the ERA5 reanalysis (Hersbach et al., 2020). We used the data on 37 pressure levels instead of the 137 native model levels, but the vertical integrals are approximately conserved. We assume i) clouds to be horizontally homogeneous within one grid cell, ii) that adjacent cloud layers have overlap, iii) that the spatial correlation between two clouds layers decreases exponentially (using a decorrelation length of 2 km) with increasing vertical distance between the layers, and iv) that separated cloud layers have random overlap. To obtain a statistical distribution of the cloud fields, we sampled 100 vertical profiles, calculated radiative fluxes for each profile and subsequently averaged the surface irradiance. To infer the effect of aerosols, we used the surface irradiance product of the Copernicus Atmosphere Monitoring service (CAMS) McClear Clear-Sky Irradiating

service (Gschwind et al., 2019).

5.5 Open data

All data used in this manuscript is either available from public sources or included with this manuscript. The ERA5 data is available from the Copernicus Climate Data Store: https://cds.climate.copernicus.eu/cdsapp#!/dataset/reanalysis-era5-pressure-levels-monthly-means?tab=overview and https://cds.climate.copernicus.eu/cdsapp#!/dataset/reanalysis-era5-pressure-levels?tab=overview. CAMS McClear and AOD data is available from http://www.soda-pro.com/web-services/radiation/cams-mcclear. OpenSkyNetwork flight activity data is available from https://zenodo.org/record/3928550. Solar irradiance observations and ground-based AOD observations are available from https://doi.org/10.5281/zenodo.4455892.

Supporting information

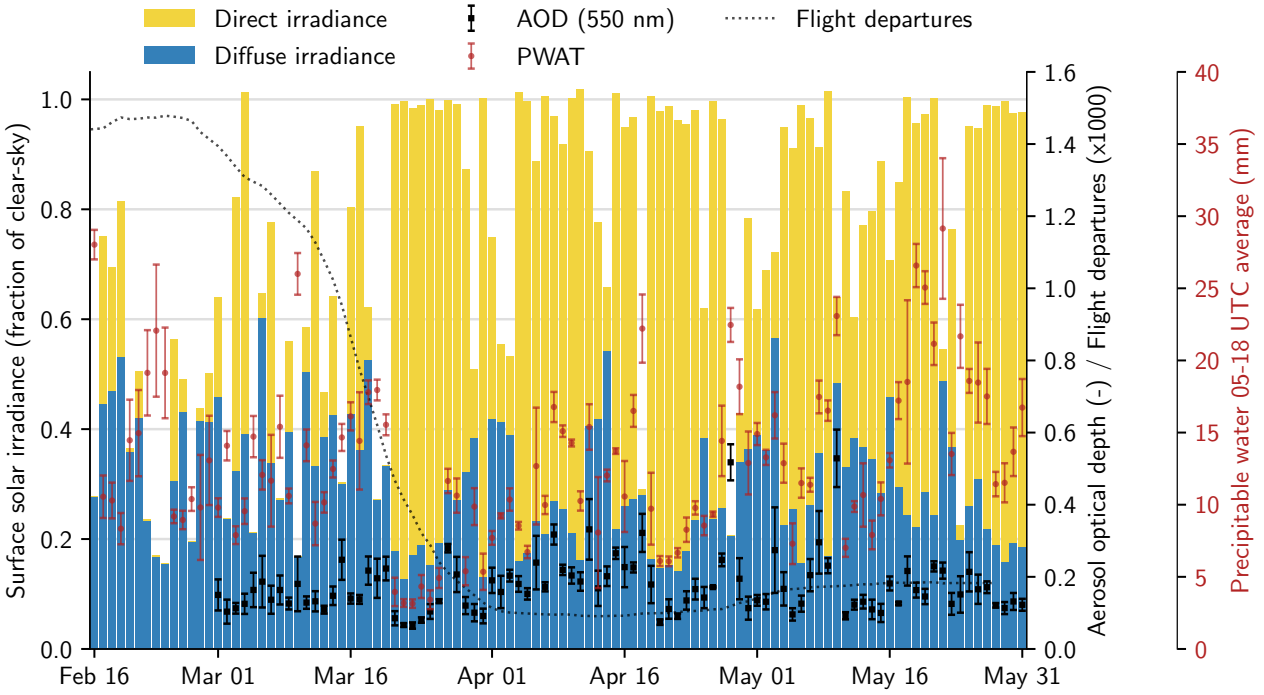

Figure S5.1: Alternative version of Figure 5.2, where measured AOD has been replaced by CAMS McClear AOD (7 to 17 UTC mean + standard deviation) and solar irradiance measurements have been normalized by the CAMS McClear clear-sky global horizontal irradiance.

Table S5.1: Percentage of days in March, April and May with visible cirrus and the percentage those days which are visibly contaminated with contrails. Based on Terra and Aqua MODIS imagery on NASA Worldview (NASA, 2024).

	2011	2015	2020
Cirrus	51	60	30
Contrail contaminated	62	59	42

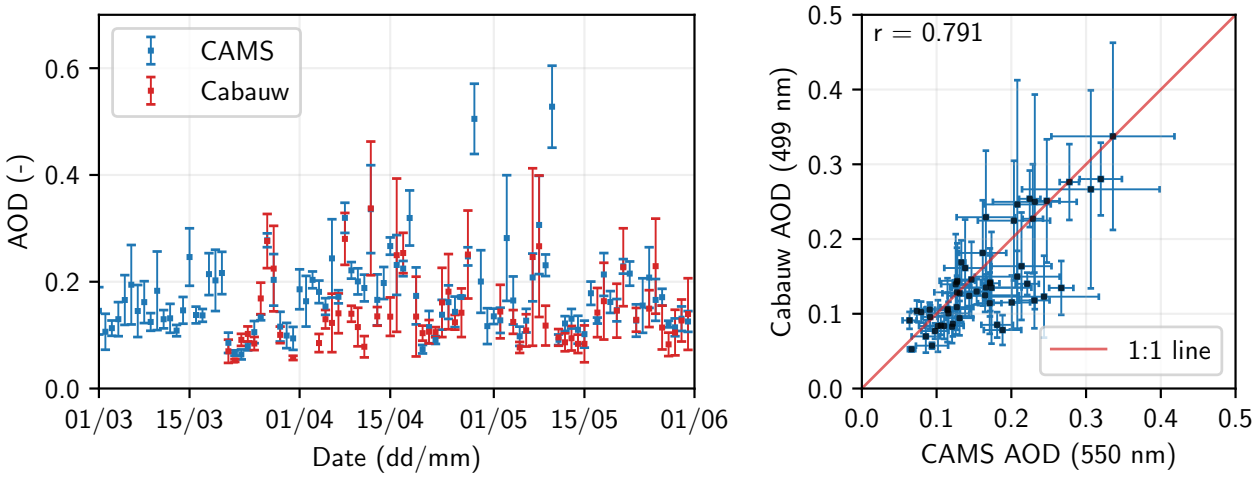

Figure S5.2: Comparison of measured aerosol optical depth (AOD) of Cabauw and modelled AOD from CAMS for the same location during Spring 2020. Note Cabauw has missing data on cloudy days and for the first weeks of March. Errorbars indicate daily (daytime) variability in the data for each dataset. Correlation coefficient is 0.791 based on daily means for all days where both data sources have data available. Note Cabauw and CAMS AOD are at different wavelengths (499 vs. 550 nm), and daytime averages of Cabauw are based on a variable amount of samples due to irregular data availability (cloud contamination).

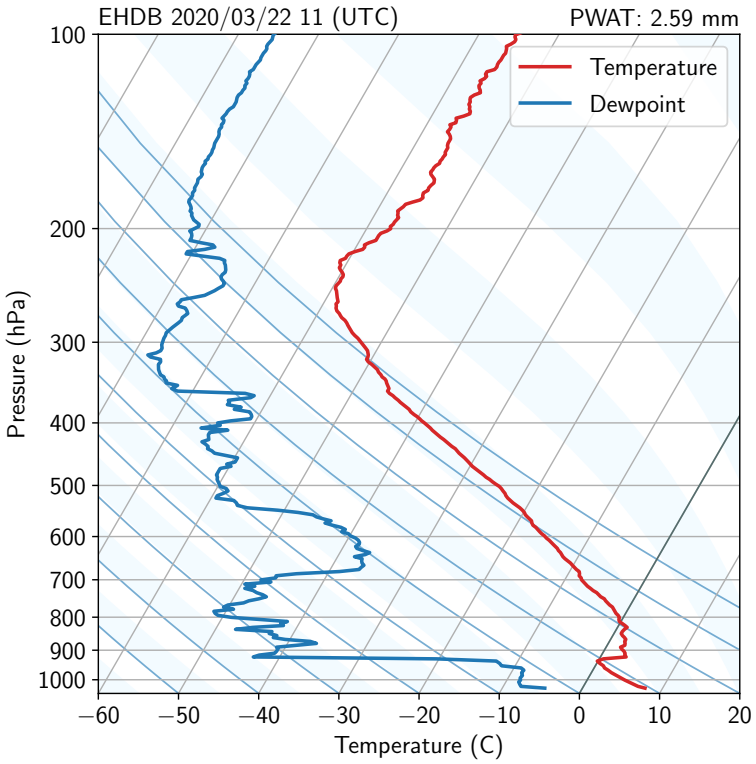

Figure S5.3: Measured atmospheric profile on 22 March 2020 at 11 UTC, De Bilt, The Netherlands. Vertically integrated moisture amounts to 2.59 mm. Data provided by the KNMI.

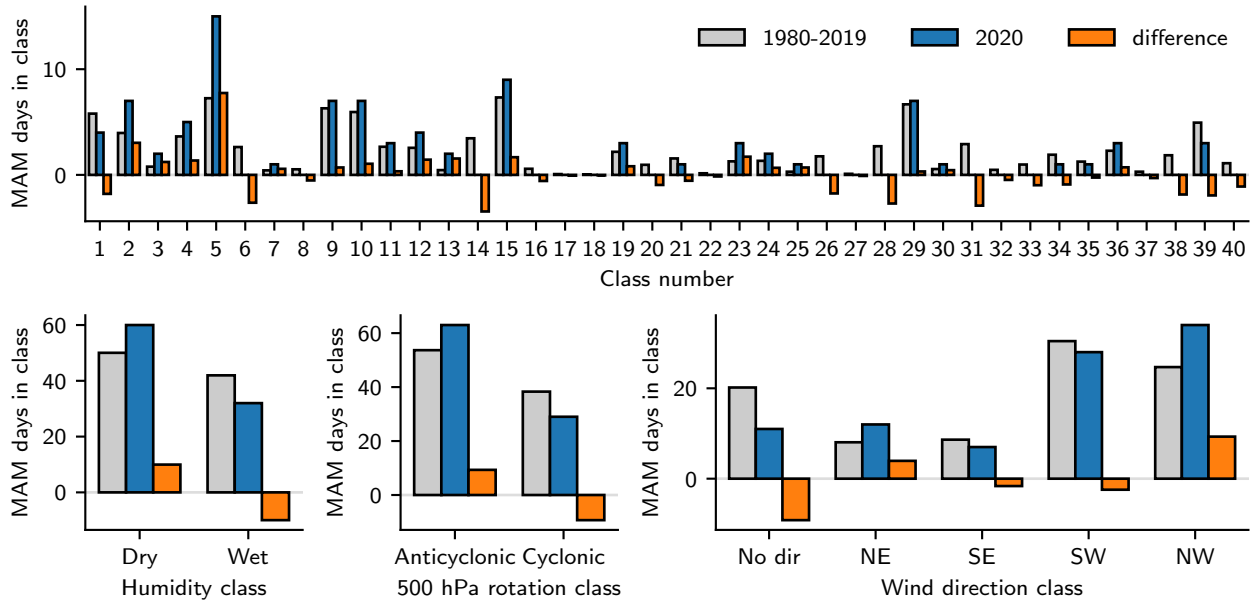

Figure S5.4: Weather type classification of spring 2020 using the 40 groups of the German objective classification system (Bissolli & Dittmann, 2001) compared against the 1980-2019 climatology of March, April, and May (MAM). Bottom row contains aggregated data from top row based on humidity, rotation at the 500 hPa level, or wind direction. See `https://www.dwd.de/EN/ourservices/wetterlagenklassifikation/kennzahlen_kennungen.html` for a description of the classes.

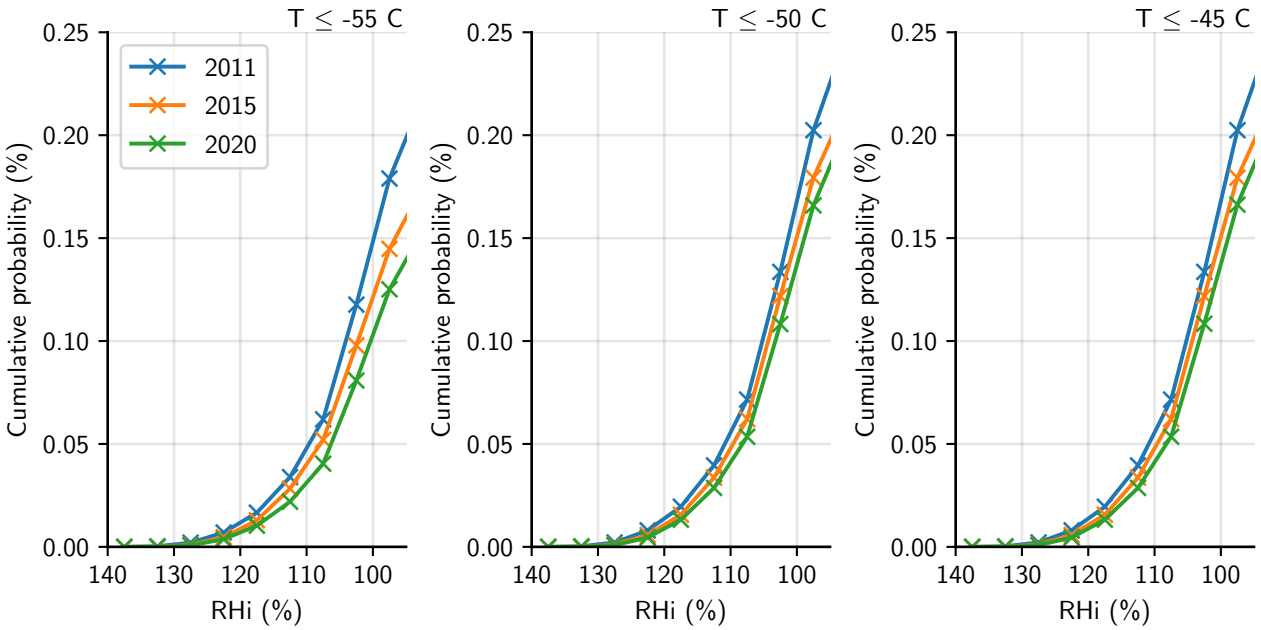

Figure S5.5: Cumulative probability of relative humidity over ice (RHi) based on ERA5 Reanalysis data for three different temperature thresholds. Data is taken at 250 hPa from 50 to 55 degrees latitude and 3 to 7 degrees longitude and compares years 2020 to 2011 and 2015.

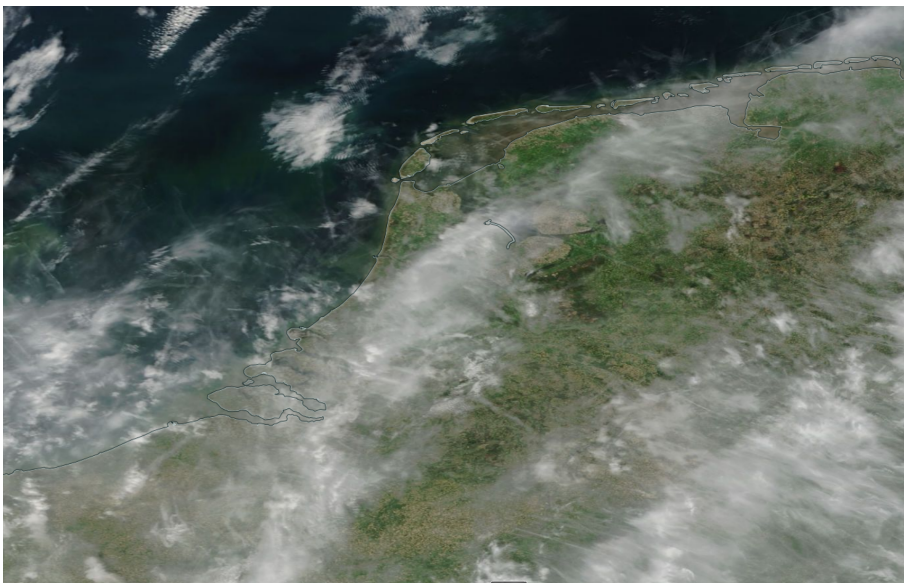

Figure S5.6: Example of cirrus that contains (and is therefore enhanced in coverage and optical thickness) contrails, from narrow and straight ones to older and more dispersed. The date of this image is 11 May 2015. We acknowledge the use of imagery from the NASA Worldview application (`https://worldview.earthdata.nasa.gov`), part of the NASA Earth Observing System Data and Information System (EOSDIS).

Table S5.2: Surface irradiance per experiment in units of W m^{-2} for the period March, April, May for each of the years 2010–2020.

	2010	2011	2012	2013	2014	2015	2016
Dry (`orange`)	308.2	308.1	310.0	309.1	308.6	307.7	309.9
Clear (`red`)	264.6	262.4	263.4	265.3	261.9	263.8	264.8
McClear (`light blue`)	252.1	247.1	249.0	251.6	250.7	254.3	253.2
Clouds (`dark blue`)	170.5	191.9	168.5	153.4	173.5	179.6	173.6

	2017	2018	2019	2020
Dry (`orange`)	309.4	308.5	307.8	310.1
Clear (`red`)	262.9	261.4	262.6	266.2
McClear (`light blue`)	249.2	246.6	249.3	255.4
Clouds (`dark blue`)	182.1	179.9	174.2	208.3

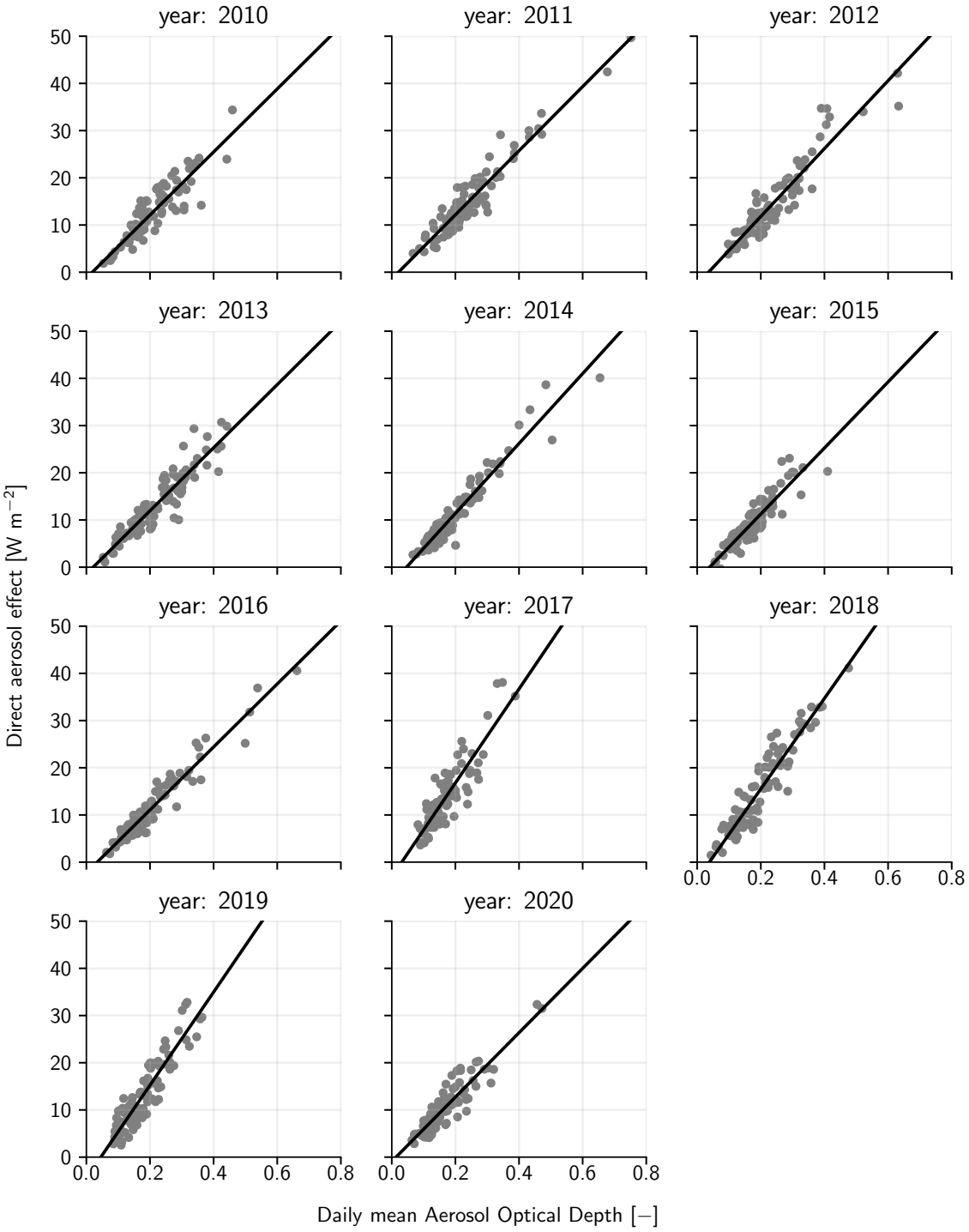

Figure S5.7: Daily mean direct aerosol effect, computed as the difference between the clear-sky RTE+RRTMGP simulation with water vapor but without clouds and aerosols and the McClear clear-sky product, against daily mean aerosol optical depth. Each year is shown in a single panel and the data points represent all individual days in March, April, and May. The black lines indicate the linear trend.

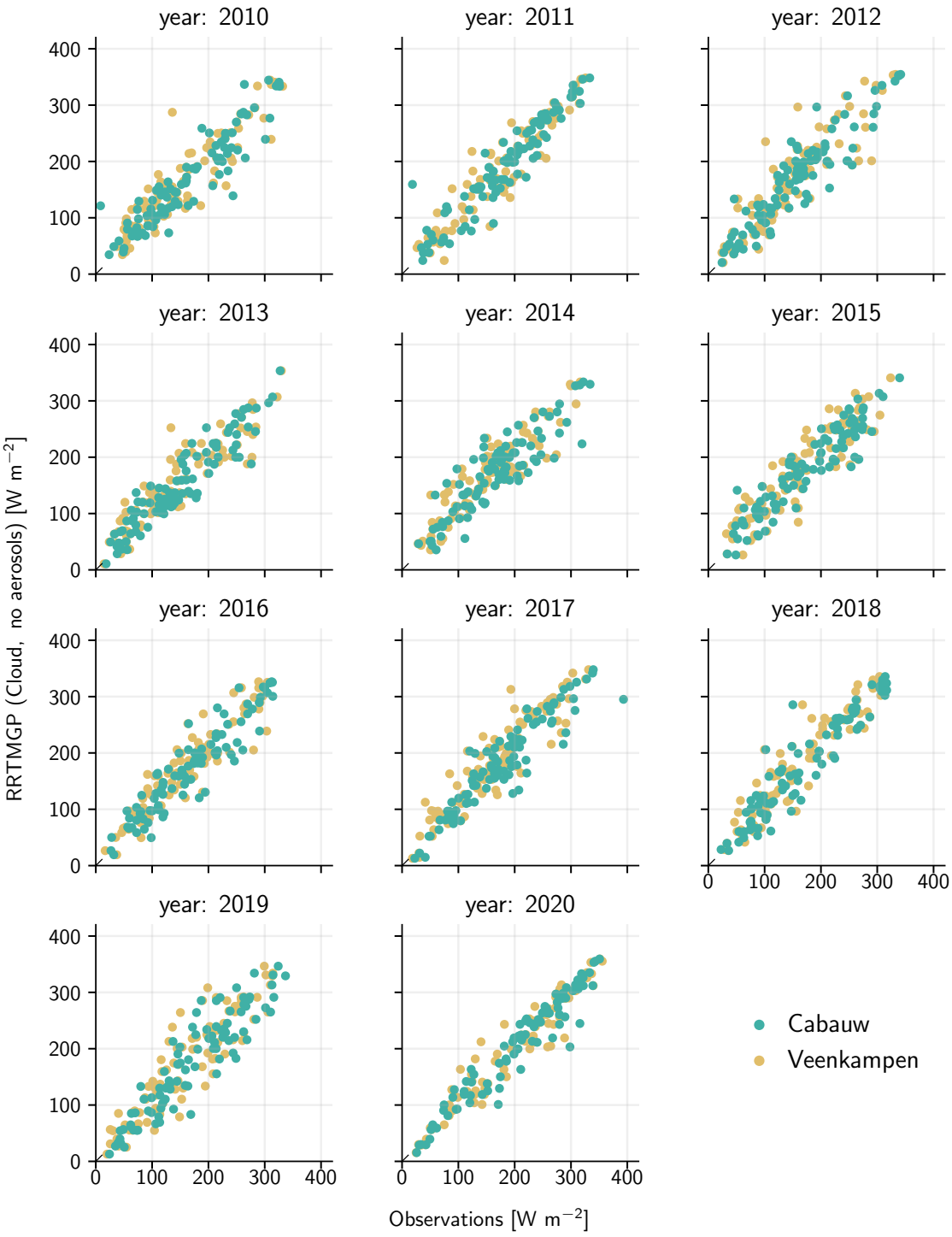

Figure S5.8: Daily mean surface irradiances based on RTE+RRTMGP simulation with clouds but without aerosols against daily mean surface irradiances based on observations at Cabauw and at Veenkampen. Each year is shown in a single panel and the data points represent all individual days in March, April, and May.

Chapter 6

Reconciling observations of solar irradiance variability with cloud size distributions

This chapter is based on:

Mol, W. B., van Stratum, B. J. H., Knap, W. H., & van Heerwaarden, C. C. (2023). *Reconciling Observations of Solar Irradiance Variability With Cloud Size Distributions*. In Journal of Geophysical Research: Atmospheres. American Geophysical Union (AGU). https://doi.org/10.1029/2022jd037894

Abstract

Clouds cast shadows on the surface and locally enhance solar irradiance by absorbing and scattering sunlight, resulting in fast and large solar irradiance fluctuations on the surface. Typical spatiotemporal scales and driving mechanisms of this intra-day irradiance variability are not well known, hence even one day ahead forecasts of variability are inaccurate. Here we use long term, high frequency solar irradiance observations combined with satellite imagery, numerical simulations, and conceptual modelling to show how irradiance variability is linked to the cloud size distribution. Cloud shadow sizes are distributed according to a power law over multiple orders of magnitude, deviating only from the cloud size distribution due to cloud edge transparency at scales below $\approx$ 750 meters. Locally cloud-enhanced irradiance occurs as frequently as shadows, and is similarly driven mostly by boundary layer clouds, but distributed over a smaller range of scales. We reconcile studies of solar irradiance variability with those on clouds, which brings fundamental understanding to what drives irradiance variability. Our findings have implications for not only for weather and climate modelling, but also for solar energy and photosynthesis by vegetation, where detailed knowledge of surface solar irradiance is essential.

6.1 Introduction

Surface solar irradiance can exceed clear-sky, even extraterrestrial irradiance (e.g. Yordanov et al., 2015; Gueymard, 2017), caused by the scattering of radiation by broken clouds, referred to as cloud enhancement. Simultaneously these clouds cast shadows, creating ever changing and moving patterns of alternating high and low irradiance at the surface, resulting in high ramp rates and heterogeneity in surface heat fluxes. The resulting spatiotemporal variability on the intra-day and local scale poses a challenge for stable integration of solar energy in the electricity grid by being unpredictable (Liang, 2017; Yang et al., 2022), while society will increasingly depend on solar energy in mitigating climate change (Clarke et al., 2022). Furthermore, the global carbon, water, and energy cycles are affected by heterogeneous distribution of solar irradiance caused by clouds (Mercado et al., 2009; Lohou & Patton, 2014; Keenan et al., 2019; Humphrey et al., 2021; Hogan et al., 2019). Radiative transfer is well-described in theory, yet necessarily simplified in model implementations due to its high computational demand (e.g. Hogan & Bozzo, 2018). One such simplification is the two-stream approach, which calculates radiative transfer in only the up and downward direction, whereas in reality, photons travel in all directions. This means that even atmospheric models with fully resolved cloud fields are unable to resolve realistic surface irradiance variability. Apart from directly negative consequences for solar energy applications, these errors become more pronounced the better such models resolve individual clouds, and can feed back to other components of the model. Most notably, heterogeneity in surface irradiance can feed back through surface heat fluxes to alter the cloud field and domain-mean irradiance (Lohou & Patton, 2014; Jakub & Mayer, 2017; Veerman et al., 2022). Given the aforementioned importance of accurately resolved or forecast irradiance variability, it is imperative to understand on more fundamental level how irradiance variability is characterized and where it originates from.

Previous analyses of cloud shadow and enhancement duration have shown various statistical distributions that suggest irradiance variability occurs over a wide range of scales (Gu et al., 2001; Tomson, 2010; Tabar et al., 2014; Lappalainen & Valkealahti, 2016a; Madhavan et al., 2017; Kivalov & Fitzjarrald, 2018; Järvelä et al., 2020), but there is no consensus on how to characterise the distributions. This, in part, is owed to the studies focusing on different aspects of surface irradiance, using different instrumental setups, and sampling in different climatological regions and times of year. The debate has also been limited by the often lacking multi-year irradiance observations (for statistical convergence) sampled with at least 1 Hz temporal resolution, necessary to capture the details of the fast fluctuations (Yordanov et al., 2013). Examples most relevant to this study include Gu et al. (2001), who identify a 5/3 power law slope in irradiance power spectra below 10 minutes as turbulence-like, based on three weeks of 1-minute resolution observations. Based on a year of 1 Hz resolution data, this was also shown by Tabar et al. (2014) for a range of 10 to 1000 seconds, and they suggest this is rooted in the cloud size distribution, which similarly scales with $\approx 5/3$ (Wood & Field, 2011). Based on a dense spatial network of 99 pyranometers sampling at 1 Hz, Madhavan et al. (2017) find for overcast cases similar scaling in spatial power spectra between 50 and

1500 meters, but exponents vary for larger spatial scales or different cloud cover types. Evidence for a link to cloud size distributions in these studies is empirical and limited by the data resolution or temporal range of their observations, or the connection between temporal irradiance data and spatial cloud sizes is not made. However, the irradiance variability power law scaling and link to cloud sizes is certainly an appealing idea that deserves a more thorough analysis, which we will provide with a more robust dataset in the present study.

The Baseline Surface Radiation Network (BSRN, Driemel et al., 2018) station of the meteorological observatory in Cabauw, the Netherlands, has been measuring solar irradiance every second since 2005, with high standards of maintenance and quality control. The long measurement record, resolution, and multi-component properties of this dataset enable the analysis of the climatology of intra-day irradiance variability in meteorological context. Details of the data and methodology are described further in Section 6.2. From these observations, we describe the typical spatiotemporal scales of surface irradiance variability, how these vary by cloud type, and how variability is linked to cloud size distributions (Sections 6.3.1 to 6.3.3). We furthermore provide an interpretation of this link by doing an sensitivity analysis (Section 6.3.4), and by running a cloud resolving model that is able to reproduce observations (Section 6.3.5).

6.2 Data and methods

Our analysis makes extensive use of observational data, which is described in Section 6.2.1 and in more detail in Chapter 2. The analysis itself starts with irradiance time series classification into cloud shadow and enhancement categories, the methodology of which is described in Section 6.2.2. From these processed time series, we construct distributions of the spatiotemporal scales of cloud shadows and enhancements, and are further interpreted using cloud observations. In order to make the link between these distributions and cloud sizes, we make use of distribution fitting and a conceptual model, laid out in Section 6.2.3. For further interpretation, we use a cloud resolving model and an idealized cloud model, both explained in Section 6.2.4.

6.2.1 Observational data

The BSRN station of the atmospheric observation site in Cabauw, the Netherlands (`https://ruisdael-observatory.nl/cabauw/`) has logged irradiance measurements at a resolution of 1 second from 2005 onward. Direct, diffuse, and global horizontal irradiance for a subset of 10 years (2011-02 until 2020-12) are used in this study. The official 1-minute BSRN dataset, which covers the whole temporal range and additional variables, is described by Knap (2022). Direct irradiance is measured by a CH-1 pyrheliometer, which has a response time of 95 % in 7 seconds and 99 % in 10 seconds (Kipp & Zonen, 2001). Diffuse and global irradiance are measured by the CM-22 pyranometer, which is slightly faster (Kipp & Zonen, 2004). This means that while the sampling rate is 1 Hz, the resolved resolution is slightly lower, the implications of which are discussed in Section 6.3.3. Quality control is optimised

for the 1 Hz dataset in this study. Anomalous data, e.g. due to maintenance, is filtered out, but decorrelation at short time scales between the instruments, because they are a few meters apart, is kept in. Solar elevation angles (α) are calculated using PySolar (Pingswept, 2022) at a 1 minute resolution for Cabauw (51.968 N, 4.927 E), and linearly interpolated down to 1 second. Direct horizontal irradiance is calculated by multiplying direct irradiance with $sin(\alpha)$. CAMS McClear version 3.5 (Gschwind et al., 2019) is our source dataset for clear sky irradiance (GHI_{cs}), which takes into account the effect of aerosols and atmospheric gases. This is a model, rather than an observation, though similar to solar elevation angles it provides essential context for irradiance measurements, discussed further in Section 6.2.2. It is available at a 1 minute resolution, which we linearly interpolate to 1 second for direct comparison to observations. An example time series of the irradiance data is shown in Figure 6.1.

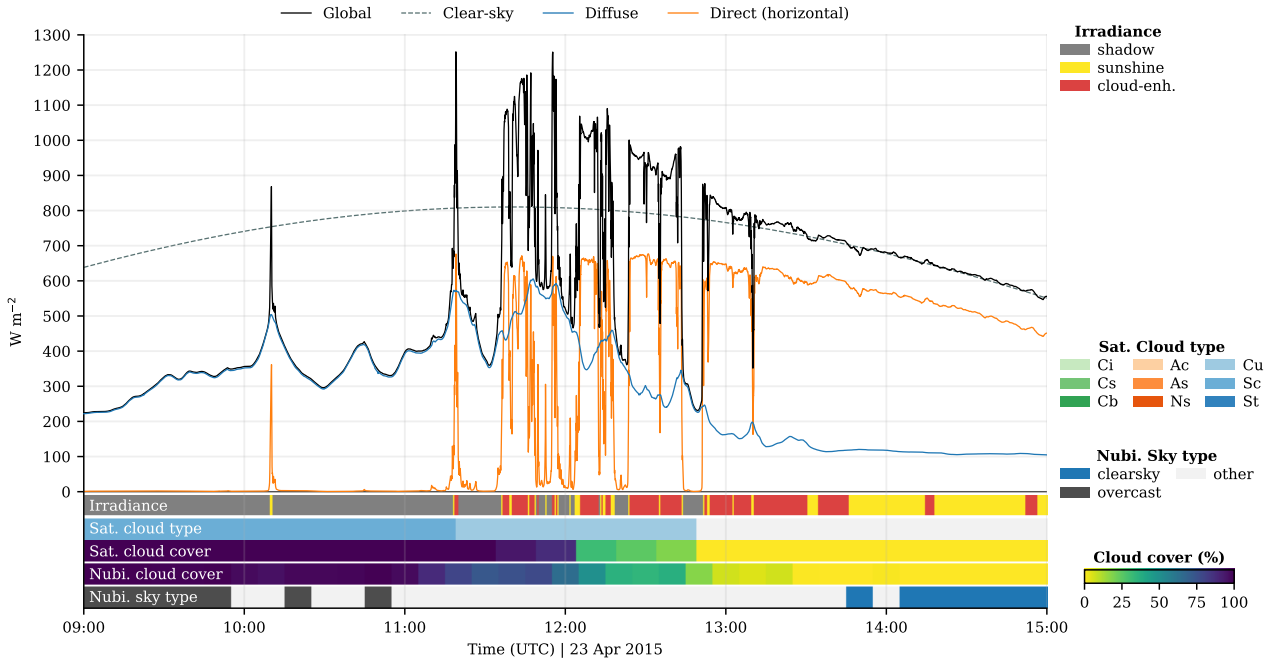

Figure 6.1: Cabauw BSRN time series, irradiance classifications, and cloud observations for part of 23 April 2015, which features a weather transition from overcast to clear-sky via a period of frequent and strong cloud enhancements. The three measured irradiance components, global, diffuse, and direct horizontal irradiance are shown together with modelled (CAMS McClear) clear-sky irradiance. The satellite and nubiscope observations show an overcast stratocumulus (Sc) field dissolving via cumulus (Cu) into to clear-sky conditions.

Meteorological context for the irradiance measurements is provided by the following datasets. From the Cabauw site, wind measurements at 200 meters are publicly available at a 10 minute resolution for our selected period of 2011 until 2020 (Bosveld, 2020). The CLAAS2 satellite product (Benas et al., 2017) provides cloud cover, cloud top pressure (CTP), and cloud optical thickness (COT), available every 15 minutes during day time at an approximate spatial resolution of 20 km^2 over Cabauw. Cloud top pressure and optical thickness from this product were validated against various other measurement techniques, by which the authors

confirmed the reliability of the satellite-derived cloud physical properties (Benas et al., 2017). Cloud type classifications are based on a simple cloud top pressure and optical thickness categorization (see Rossow (2022) ISCCP algorithm description, their Figure 20). The 9 types are cumulus (Cu), stratocumulus (Sc), stratus (St) for low clouds; altocumulus (Ac), altostratus (As), and nimbostratus (Ns) for middle clouds; cirrus (Ci), cirrostratus (Cs), and cumulonimbus (Cb) for high clouds. Cu, Ac, and Ci are the optically thinnest clouds for each altitude, and St, Ns, and Cb the thickest, where Cb spans from low to high altitude as the only exception in this list. This 9-type CTP vs. COT classification an oversimplification of reality, and there are alternative ways to set thresholds (e.g. Hahn et al., 2001). However, in this study we only use it to group together clouds conditions of various altitudes and optical thicknesses in a more intuitive way, rather than make strong claims for specific cloud types. The main limitations are that both the cloud fraction and actual cloud optical thickness contribute to a higher reported optical thickness in a satellite pixel, which is a result of limited spatial resolution, and higher clouds can obscure lower clouds, the implications of which are discussed further in Section 6.3.2.

The spatial satellite product is converted to a time series representative for the BSRN station by determining the most common cloud class within a 10 km radius around Cabauw. Results are similar for 5 or 15 km radii (Figure 6.5). A smaller radius is not possible due to satellite resolution (pixel area ≈ 20 km^2) and larger radii become unrepresentative for Cabauw. A few meters next to the BSRN station is a nubiscope (Wauben et al., 2010), which measures cloud cover at a 10 minute interval, and is used here only to visually validate our satellite time series processing. Cloud type and cover from the satellite, and the nubiscope as a reference, are included in Figure 6.1. Although the nubiscope would be a more reliable instrument for getting representative cloud cover for Cabauw, it cannot classify cloud types like the satellite product.

6.2.2 Time series classification

Deriving cloud enhancement (CE) and cloud shadow statistics starts with classifying all irradiance time series data. We define a shadow where direct normal irradiance (DNI) is below 120 W m^{-2}, which is the inverse of what the World Meteorological Organization defines as sunshine (DNI $\geq$ 120 W m^{-2}, WMO (2014)). Cloud enhancement refers to a situation where global horizontal irradiance (GHI) exceeds the reference clear-sky (GHI$_{cs}$) due to cloud radiative effects, though the exact definition and interpretation varies in literature. (Gueymard, 2017) discusses various such definitions, and favours fixed values such as 1000 W m^{-2} or a fraction of extraterrestrial irradiance as a reference, though this is within the context of photovoltaic applications. In our study, however, we aim to study the effect of clouds, and therefore we use a reference model (CAMS McClear) that calculates clear-sky irradiance for a geographical location, including the effect of aerosols and atmospheric composition such as water vapour and ozone. Using a model introduces some uncertainty, and in reality observed GHI still fluctuates slightly in cloud-free conditions (see e.g. 14-15 UTC in Figure 6.1), both of which make the detection of cloud enhancement tricky for the weakest cases. To prevent false positives in the detection of cloud enhancements, we first apply an activation threshold

of GHI exceeding GHI_{cs} by 1 % and 10 W m^{-2}. Both a relative and absolute threshold are used to deal with high and low solar zenith angles, where 10 W m^{-2} is based on 1 % of the typical order of magnitude for clear-sky irradiance around noon for Cabauw. When the threshold is reached, adjacent measurements are also marked as cloud enhancement so long as they exceed GHI_{cs} by 0.1 %. Edge cases at low solar elevation angles are removed by requiring DNI to be at least 10 W m^{-2}. All of these thresholds are subjective to some extent, but chosen to enable us to capture all but the weakest of cloud enhancements. The residual third class is simply 'sunshine', and an example of all three are illustrated in Figure 6.1.

Within the classified irradiance time series, we call sections of cloud enhancements or shadows 'events'. For every event, the start and end time are used to subset radiation and meteorological data, such that every cloud enhancement and shadow event can be characterized. These include statistics of event duration, maximum cloud enhancement strength 'max(CE)', minimum direct irradiance 'min(DNI)', mean 200 meter wind speed, dominant cloud type, maximum cloud top height, and mean solar elevation angle. Event statistics such as these allows for filtering of events according to additional criteria, e.g. for comparing events of different magnitudes. Events at the start or end of daylight are ignored in the analyses, because it is not possible to determine their true duration and other event statistics. Only events with a solar elevation angle above 5 degrees are included, to filter out small absolute errors in irradiance observations that become relatively big at sunrise or sunset.

6.2.3 Distribution fitting and conceptual model

A common way to analyse irradiance variability is by finding a best fit for the distribution of certain quantities of variability, which in this work are the spatiotemporal scales of cloud shadows and enhancements. The probability density function of cloud shadow sizes we present in Section 6.3.1b is analysed with the help of the Powerlaw package (Alstott et al., 2014), which takes care of the non-trivial fitting of heavy-tailed distributions. For a power law $f(x) = x^{\alpha}e^{x\lambda}$ this package automatically finds the start of the power law scaling range, x_{min}, where x is the shadow size and $f(x)$ is the according probability density. It does so by creating power law fits starting from every value possible for x_{min}, and finding the one that has the smallest Kolmogorov-Smirnov distance between the data and the fit (Alstott et al., 2014). An optional upper end of the scaling range, x_{max}, can be manually set to the highest possible expected value or a theoretical limit. In the case of this study, the maximum expected shadow size is the duration of daylight with a solar elevation angle above 5 degrees multiplied by the mean 200 meter wind speed for that part of the day. We find this to be 296 km, which is an average over all months in 2012 until 2020. Similarly, shadow sizes approaching the observational limit x_{max} are undersampled, because they are ignored when they overlap with sunset or sunrise as mentioned in the previous section. The exponential term $e^{x\lambda}$ in the power law $f(x)$ corrects for effect. The same procedure applies to summer (May to August) and winter (November to February) subsets of the data for sensitivity analyses. Additional sensitivity tests (yearly variability, solar elevation angle) are done using the $[x_{min}, x_{max}]$ range found for the whole dataset, because the reduction in amount of samples leads to a noisier distribution and less robust values for x_{min}.

6.2.4 Numerical modelling

The large-eddy simulations (LES) are performed with MicroHH (van Heerwaarden et al., 2017). Several new physics options were recently implemented to allow simulations with the complexity of realistic weather: the RTE-RRTMGP radiative transfer solver which calculates radiative transfer in 2D for each model column (Pincus et al., 2019), an interactive land-surface model closely following HTESSEL (Balsamo et al., 2009), and a single moment ice microphysics scheme (Tomita, 2008). In order to facilitate LES simulations of real-life weather, MicroHH was initialised and coupled to ERA5 (Hersbach et al., 2020) using a similar method as described by Neggers et al. (2012); Schalkwijk et al. (2015); Heinze et al. (2017). In this coupling the atmosphere and soil are initialized from ERA5, and the influence of spatial and temporal variability in the large-scale weather are imposed on the LES as time and height varying external forcings. These forcings include the large-scale advective tendencies of temperature, moisture, and momentum, the geostrophic wind components, and the subsidence velocity.

Three different LES experiments are performed over Cabauw, running from 01-08-2016 00 UTC to 01-09-2016 00 UTC, with horizontal domain sizes (grid spacing Δx) of 12.8 km (Δx = 50 m), 25.6 km (Δx = 100 m), and 51.2 km (Δx = 100 m). All simulations use the same stretched vertical grid with 192 levels, starting with a vertical grid spacing of Δz = 20 m at the surface, and a total vertical extent of 18.1 km.

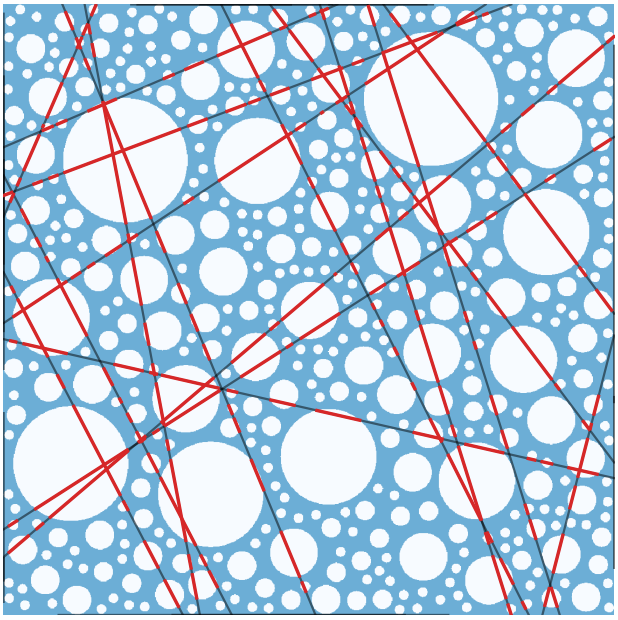

Figure 6.2: Top view of an idealised cloud field and the random line sampling technique. This example contains 765 'clouds', has a 'cloud' cover of 53.6 %, and features horizontal grey lines that represent random sampling transacts with the red sections the measured 'cloud' chord lengths. The size distribution is described by a power law, horizontal units are arbitrary.

The shadow lengths from LES are obtained using the surface irradiance extracted from an individual model column, sampled at a 5 second frequency. Shadows are determined using the

same definition as used for the BSRN observations, i.e. DNI $\leq$ 120 W m^{-2}, with an additional GHI$_{cs}$ $>$ 10 W m^{-2} constraint to filter out nights. The cloud size distributions from the LES simulations are obtained using the cloud tracking method of Heus & Seifert (2013), which identifies individual clouds as spatially continuous areas with a liquid water path (LWP) over a threshold of 5 g kg^{-1}. From these 2D cloud masks, the cloud sizes are either determined as $\sqrt{A}$ of each cloud area A, or by randomly sampling lines through each 2D cloud mask, determining the cloud sizes as the mask-line intersection lengths (or 'chord lengths'). The same methodology is used for the idealised circle model, only with the realistic 2D cloud masks replaced by a numerically generated 'cloud' field consisting of circles. This field is generated by randomly placing 10^5 circles, sampled from a power law distribution with a -2.7 slope, inside a domain of 500 $\times$ 500 km^2. The circles are placed ensuring that the individual circles do not overlap, resulting in a circle cover of 40.7 %. The resulting field is finally analysed using the same methods as used for the realistic 2D cloud masks from LES, with the circle sizes determined from either the circle area, or the intersection between the circles and randomly drawn lines. Figure 6.2 shows conceptually what such an idealised cloud field would look like, with 765 circles covering 53.6 % of a smaller domain. The horizontal lines represent random cross sections through this idealised cloud field, mimicking a situation where a cloud fields moves over a single measurement point. A similar technique for interpreting measurements is applied in Rodts et al. (2003), we further discuss the implications in our results Section 6.3.5.

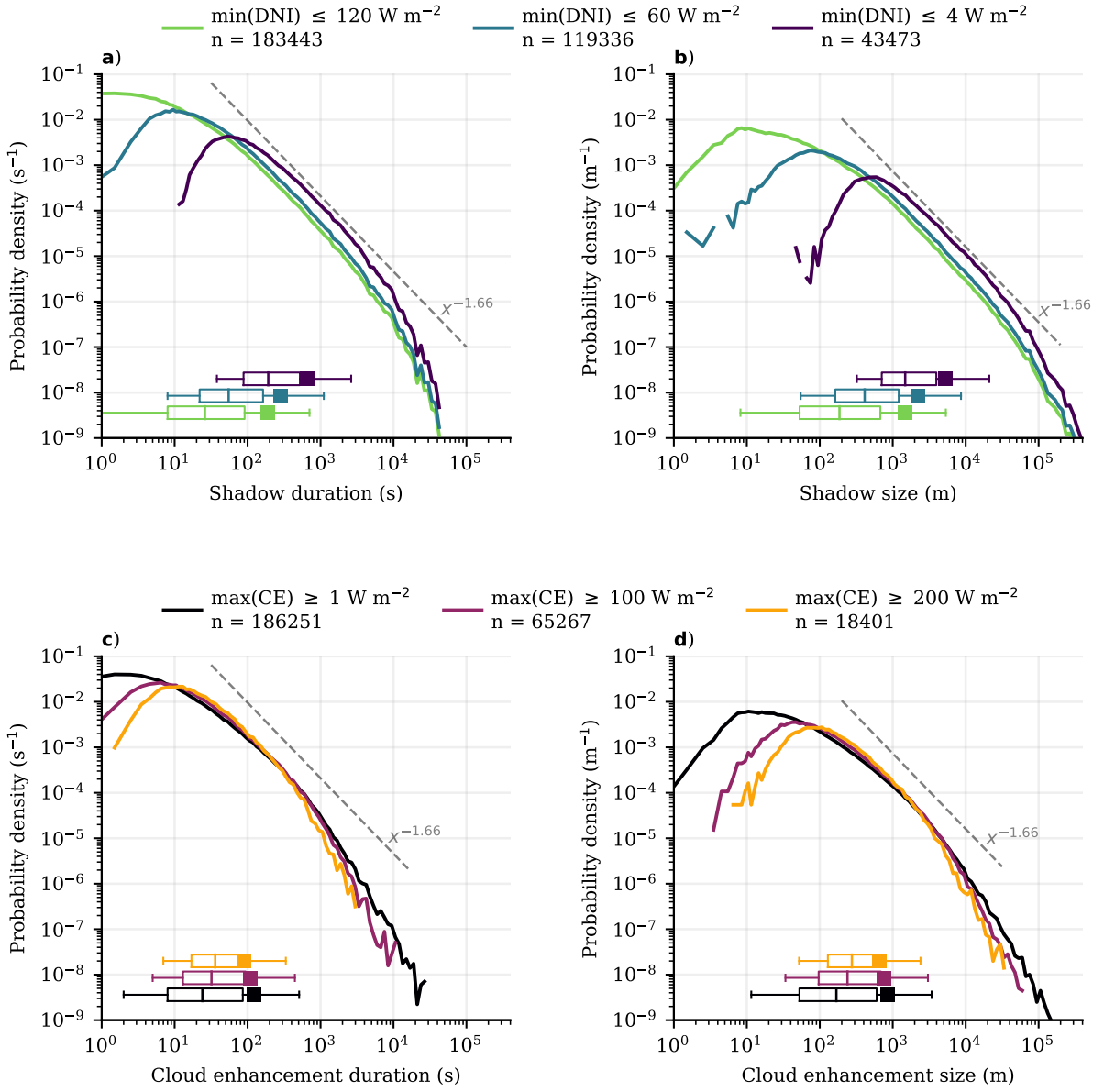

Figure 6.3: Duration and size distributions for cloud shadows and enhancements for three different threshold criteria of minimum or maximum event strength, on a log-log scale. The most strict shadow threshold is set to the event minimum direct normal irradiance 'min(DNI)' $\leq$ 4 W m^{-2}, and indicates near complete blocking of direct irradiance by clouds. Cloud enhancement (CE) events are filtered by the maximum absolute clear-sky exceendance 'max(CE)' for an event. Event duration, shown in **(a, c)** is converted to a length scale using the measured 200 meter wind speed, shown in **(b, d)**. The gray dashed lines show the cloud size distribution best fit for reference (Wood & Field, 2011). The numbers in the labels are the amount of events that make up the distributions, and the box plots at the bottom span the 5 to 95 percentile, with the mean indicated by a square.

6.3 Results and discussion

6.3.1 Distributions of cloud Shadows and enhancements

Probability density functions for the duration of cloud shadow and enhancement events are illustrated in Figure 6.3a,c. Distributions of 1D horizontal sizes, also known as chord lengths (Figure 6.3b,d), are estimated by multiplying event duration by the observed 200 meter wind speed of the tower at the observatory in Cabauw. This wind speed is an approximation of cloud propagation speed (discussed further in Section 6.3.4). The distributions show that cloud shadows and enhancements cover a wide spatiotemporal range, such that there is not one characteristic time or length scale. This behaviour is consistent among different levels of strictness in the classification criteria. 'Dark' shadow events (minimum DNI $\leq$ 4 W m^{-2}, i.e. where clouds block all direct irradiance), make up the right tail of the distribution, meaning they result from larger, optically thick clouds. Conversely, the 10 % strongest cloud enhancement events (maximum CE $\geq$ 200 W m^{-2}) are confined to a more narrow range of scales compared to the weaker ones, though they still cover two orders of magnitude, approximately 5 to 500 seconds and 50 to 5000 meters for the middle 90 % of data. These numbers are in the same range as an analysis using spatial data by (Järvelä et al., 2020), except they found shorter duration and size for the strongest peaks in their dataset, possibly explained by the fast response time of their pyranometers compared to ours. The response time of the instrumentation of the BSRN station we use is in the order of seconds, thus we expect the probability densities in Figure 6.3 to be negatively biased below 10 seconds (discussed further in Section 6.3.3).

Shadows and cloud enhancements occur as frequently and over the same spatiotemporal range for the least strict threshold criteria, 18.4 $\pm$ 1.4 and 18.8 $\pm$ 1.6 thousand times per year respectively. This equals to $\approx$ 50 shadows and cloud enhancements per day, though it will greatly depend on the weather for that day. Shadows and cloud enhancement occurrence being balanced is perhaps not a coincidence, a cloud that casts a shadow also scatters light next to the shadow, resulting in irradiance enhancement. But optically thin clouds like scattered cirrus can create weak enhancement without casting shadows, and a cumulus field underneath cirrus will create shadows but possibly no enhancement due to too much attenuated direct irradiance. There are seasonal differences, where from May to August cloud enhancement events are 10 % more common than shadows, compensated by the winter months such that their total counts converges to within 2 %. The scales over which dark shadows (min(DNI) $\leq$ 4 W m^{-2}) occur, however, are about a factor 10 larger than that of strong cloud enhancements (max(CE) $\geq$ 200 W m^{-2}, see box plots in Figure 6.3). Gu et al. (2001) found this asymmetry too, and reported shadows lasting 3 times longer than cloud enhancemen. Their findings are based on two months of 1-minute resolution observations, which might explain why the mean duration is 5 times longer than what we find. Both their and our results suggest there is an asymmetry in spatiotemporal scales between peaks and shadows. However, the ratio will depend on subjectively chosen thresholds, and also requires high enough resolution to fully resolve the spatiotemporal scales, and is thus not a general rule. Rather,

the true nature of the relationship between the spatiotemporal scales of cloud shadows and enhancements are fully represented by the distributions such as those presented in Figure 6.3.

6.3.2 Cloud types driving variability

Thus far, we have considered irradiance variability by looking at time and length scales of cloud shadows and enhancement. Optical properties of clouds vary greatly, though, and it matters for irradiance variability whether clouds are isolated, close together, or form a continuous cover. We use a geostationary satellite dataset (MSG SEVIRI, Benas et al., 2017) in the following analysis, and combine this with the irradiance dataset by extracting a time series from the spatial data for an area around Cabauw.

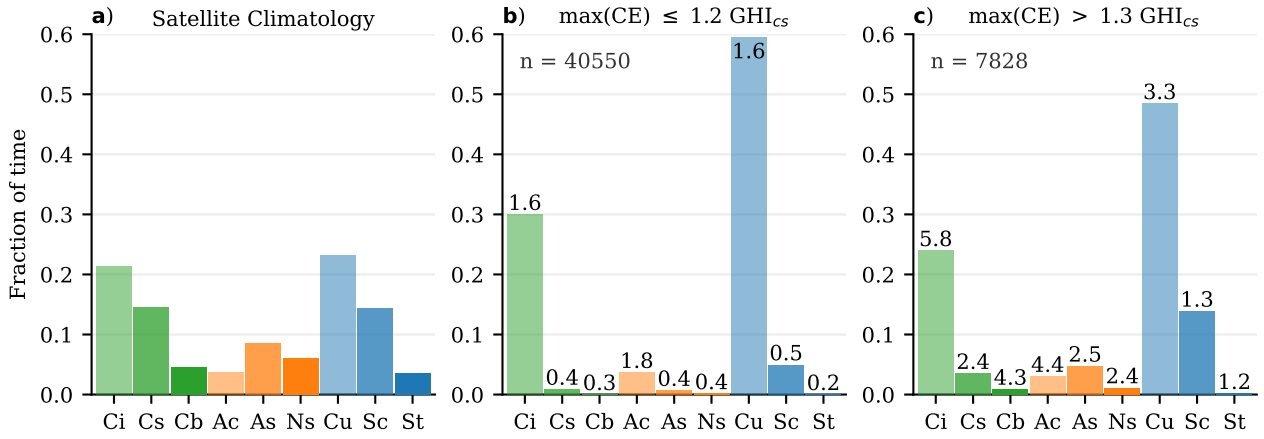

Figure 6.4: Cloud types for weak and strong cloud enhancement based on combining satellite observations (Benas et al., 2017) with irradiance observations for Cabauw, the Netherlands. The figure is based on the dominant cloud type in a 10 km radius around the observational site, for the years 2014, 2015, and 2016. **(a)** shows the cloud type climatology, as probability density under cloudy conditions. **(b, c)** show the same, but for cloud enhancement events that peak up to 20 % of clear-sky irradiance or above 30 %, respectively. The numbers in the top left indicate the amount of events that make up the distributions. Numbers on the bars indicate mean event duration in minutes. Cloud classes, from left to right, are Cirrus, Cirrostratus, Cumulonimbus, Altocumulus, Altostratus, Nimbostratus, Cumulus, Stratocumulus, and Stratus, and are simple classification based on optical depth versus cloud top height (Rossow, 2022).

Relative to cloud climatology, the conditions under which cloud enhancement occur are dominated by high transparent clouds (cirrus) and broken or scattered low clouds, illustrated in Figure 6.4. Cumulus clouds are the main driver of cloud enhancement, both by count and total duration, followed up by cirrus and stratocumulus. Cirrus is not important for generating variability, though, as it creates relatively long lasting, weak enhancements and is often too optically thin for casting shadows. Because the cloud classification algorithm uses pixel cloud top height, it can detect high clouds even if cumulus underneath is actually driving irradiance variability, meaning cirrus is likely over represented in this analysis. Stratocumulus typically has a high cloud cover, but small gaps can cause particularly strong and short cloud

enhancements, shown e.g. by Yordanov (2015), which is likely why it increases in relevance for enhancements exceeding 30 % of clear-sky irradiance (Figure 6.4c). Based on our data they generate the shortest lasting cloud enhancement events, averaging roughly one minute versus three minutes for cumulus. Stratocumulus is in absolute amount of cloud enhancement events almost as common as cumulus for strong cloud enhancement, and together they make up over 70 % of all enhancement events.

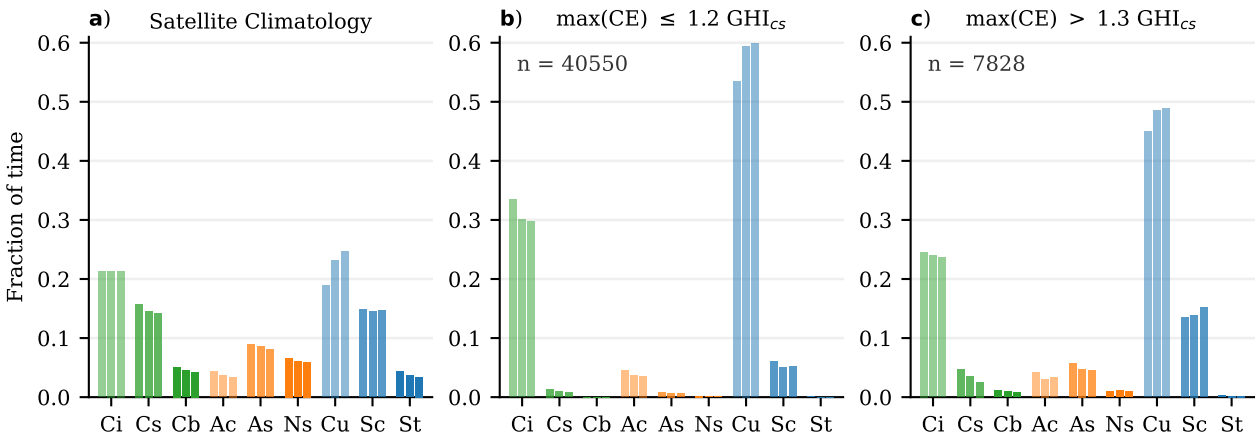

Figure 6.5: Cloud types for weak and strong cloud enhancement method sensitivity analysis. Similar to Figure 6.4, but here the area radii are 5, 10, and 15 km, plotted from left to right for each cloud type in each subplot.

Results are similar for cloud types causing shadows (Figure 6.6), with optically thin and low clouds being the most common until approximately 10 km, and again a likely overestimation of cirrus. As the shadow length increases, the optically thicker clouds increase in dominance, and the contribution from low clouds decreases. This means that both peaks and shadows, and thus intra-day irradiance variability, are generated predominantly by boundary layer cloud fields of varying cloud fraction, and make up the majority of the distributions presented in Figure 6.3.

6.3.3 Power laws and cloud size distributions

Cloud shadow and enhancement distributions in Figure 6.3 exhibit power law scaling over multiple orders of magnitude, most notably for shadow sizes. For the shadow size, a statistical best fit is found for a truncated power law function $f(x) = x^{\alpha}e^{x\lambda}$ for $x \in [0.765, 296]$ km, with parameters α = -1.643 $\pm$ 0.039 and λ^{-1} = 79.4 $\pm$ 13.1 km (Figure 6.7b). The exponential truncation term $e^{x\lambda}$ corrects for the undersampling of the scales that approach the observational limit ($\approx$ 296 km, Section 6.2.3). The uncertainty in α ($\pm$ 0.039) is the year-to-year best fit standard deviation. Our best fit for exponent α = -1.643 falls within the range of the power law exponent that describes the cloud size distribution β = -1.66 $\pm$ 0.04 as reported by Wood & Field (2011). Ten years of data and thus a wide variety of cloud types and weather conditions have produced this scaling exponent, and exceeds the scaling ranges reported in previous studies (Gu et al., 2001; Tabar et al., 2014; Madhavan et al., 2017).

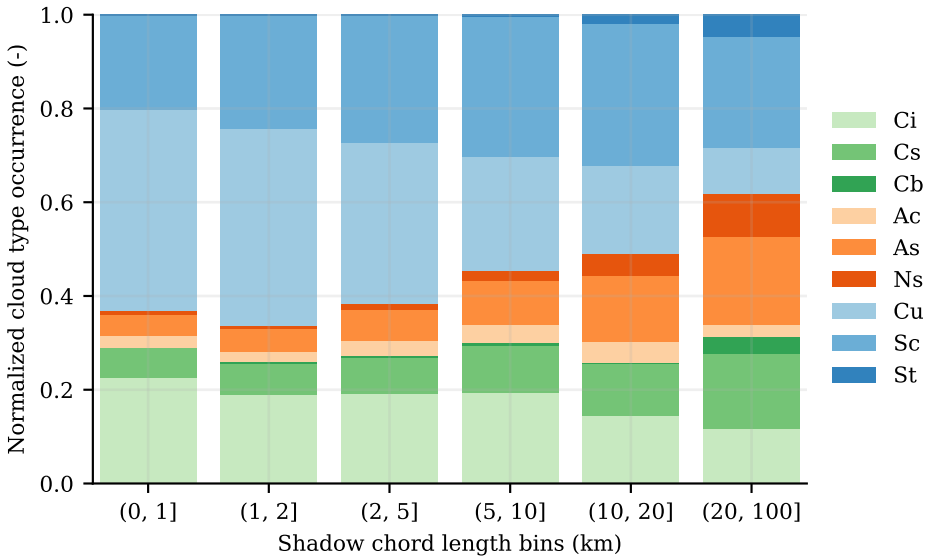

Figure 6.6: Dominant cloud type for shadow events of different sizes for 2014-01 until 2016-12. Histograms are normalized and based on event occurrence count. See Figure 6.4 for the full cloud type names.

Below approximately 765 meters, the observed shadow lengths statistically deviate from the cloud size distribution. Using a simple model, we can conceptually show how shadows down to 10 meters are still linked to cloud size distribution. We introduce length scale L, which represents the size of cloud edge transparency L_{ce} to direct irradiance (Figure 6.7b), plus a sensor response time bias L_{sb} (schematically shown in Figure 6.7c). The effective reduction of shadow length compared to cloud length is because of lower liquid water content at cloud edges (Rodts et al., 2003), making cloud edges more transparent to direct sunlight. I.e., an optical thickness of $\tau < 1.9$ for a typical direct normal irradiance of 750 W m^{-2} already results in more than 120 W m^{-2}. The simple model randomly generates a set of 1D cloud sizes from a prescribed cloud size distribution, and subtracts a fixed length scale L from each cloud sample. Figure 6.7b shows that the resulting distribution for $L = 100$ m exactly matches shadow length observations. The value we find for L may be specific to our location, and is rather a value that works for the total 10 years of cloud conditions combined with solar angles, not one that would work for every individual cloud passage. Higher typical cloud bases would make the shadow to sunshine transitions more spread out at the surface, and some clouds have much sharper edges than others, which could increase or decrease L respectively. Perhaps more importantly for the analysis of this dataset, part of the length scale L is a result of the non-instant response of the thermopile sensor, making $L = 100$ m an upper limit estimate of the true length scale of irradiance transitions (L_{ce}). There are some techniques that attempt to reconstruct the original true 1 Hz signal from the measured slower signal by deconvolution, such as (Ehrlich & Wendisch, 2015). However, we have no accurate 1 Hz observations to validate against, hence disentangling the contribution of sensor response time bias and cloud edge transparency remains a challenge. Instead, we make an estimation of the approximate contribution to the length scale L based on manufacturer's

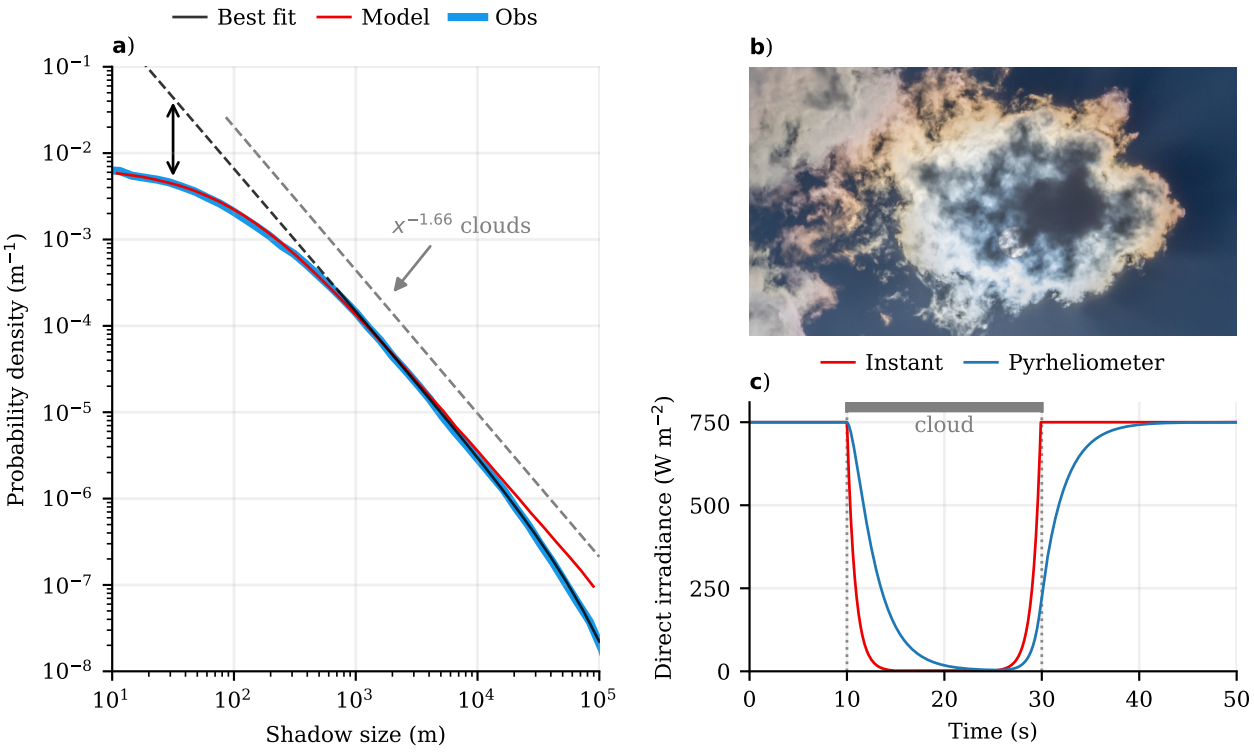

Figure 6.7: Shadow size distribution, power law fit, and its relation to cloud size is illustrated in **(a)**. The best fit is extrapolated to 10 meters to illustrate the deviation from power law scaling at smaller scales. The observed shadow probability distribution integrates to 1, all other distributions are scaled for visual comparison. The reference cloud size distribution of $x^{-1.66}$ is from Wood & Field (2011). **(b)** shows a camera picture of a small cloud to illustrate the transparency of cloud edges to direct irradiance. The cloud is ≈ 175 meters across (10 Sun diameters and cloud base at 2000 meters). For illustration, the effect of an idealized cloud passage on direct (normal) irradiance versus what a pyrheliometer would measure is schematically shown in **(c)**. The response of this simulated measurement is exponential, based on the manufacturers specifications (Kipp & Zonen, 2001)ove. The schematic cloud has smooth edges, inspired by mean profiles of liquid water in cumulus (Rodts et al., 2003) and the picture in **(b)**.

specification of sensor response time and typical cloud movement speeds, assuming the measured response to a signal behaves similar to what is illustrated in 6.7c. Our pyrheliometer sensor bias is ≈ 5 seconds (Section 6.2.1), which for ≈ 10 m s^{-1} wind speed (10-year average 200 meter wind speed from the tower) gives $L_{sb} \approx 50$ meters, which is half of L. The best estimate of the transparency length scale is then $L_{ce} = L - L_{sb} \approx 50$ meters, or 25 meters for each edge. Newer generation thermopiles with reduced response times, or fast responding semi-conductor instruments (e.g., Chapter 3), can improve upon this estimate by taking away the uncertainty of response time and improve the probability density calculations at the shortest scales in Figure 6.3. Having such accurate measurements can also help research into the cloud size distribution at scales below 100 meters by using the irradiance signal as a measurement technique. Based on our analysis of the current 1 Hz dataset we nonetheless conclude that the spatiotemporal scales of cloud enhancements and shadows are set by the

cloud size distribution, a concept we explore further in the next two sections.

6.3.4 Exponent sensitivity

Our exponent α = -1.643 for cloud shadow power law scaling is within a percent of Kolmogorov's scaling exponent of -5/3 for isotropic turbulence, which raises the question of whether irradiance variability stems from something fundamental and universal in fluid mechanics. Although our presented distributions in Figure 6.3 partially exceed the spatiotemporal range of where Kolmogorov's -5/3 scaling is valid, there is evidence supporting an extension of this scaling into the mesoscale (Callies et al., 2014). Power law scaling is also found in the atmosphere for a wide range of scales for properties related to clouds, some examples are wind and temperature (Nastrom & Gage, 1985), total water variability (Schemann et al., 2013), and cloud mass flux (Sakradzija & Hohenegger, 2017).

A lot of complexity is hidden in our observed cloud shadow scaling analysis. Thus far we have taken for granted the complex 3D geometry of clouds, multi layered cloud fields, resulting shadow projections onto the surface as a function of solar elevation angle, decoupled 200 m wind from cloud field propagation velocity, and changing cloud shapes as it passes over the instrument. Sensitivity analyses reveal this complexity to some extent, and help gain some insight into how generally applicable our results are. Constructing shadow size distributions for only winter or summer data shows smaller shadows are more common in summer (α = -1.79) than in winter (α = -1.56), potentially driven by frequent summertime cumulus over land for some regions as suggested by Wood & Field (2011). However, selecting only summer data, and comparing low (5 to 40 degrees) to high ($>$ 45 degrees) solar elevation angles show an effect of similar magnitude. Using satellite data to select only low clouds, such that the 200 m wind speed is a more reasonable assumption, shows largely unchanged size distributions, likely because the majority of clouds are low (Section 6.3.2). By comparing individual years, we find best fit exponents ranging between -1.57 and -1.70, which indicates variability in cloud size distributions and their timing with solar angles play a role. Indeed, the driving cloud size distribution power law exponents are known to vary regionally, yearly, seasonally, and per time of day (Berg & Kassianov, 2008; Wood & Field, 2011; Schemann et al., 2013; Laar et al., 2019), suggesting -5/3 scaling in irradiance variability may not be universal. Power law scaling is nonetheless a robust finding in all our sensitivity tests, and variations on the slope are small enough that the interpretation of its link to cloud size distributions remains unaffected, is likely universal, and finds it origin in the scaling of atmospheric properties. We draw this general conclusion from a single observational given the apparent robustness of power law scaling under variations in solar position and season, and similar scaling found globally for cloud size distributions in other studies. Furthermore, there is evidence of power law scaling in irradiance variability for different geographical and climate regions. Despite different analysis methodologies and limited temporal extent, (Tabar et al., 2014) find -5/3 scaling of irradiance variability in the time domain for Hawaii and Germany, and (Gu et al., 2001) estimate a similar scaling with even fewer temporal data just south of the Amazon region in Brazil.

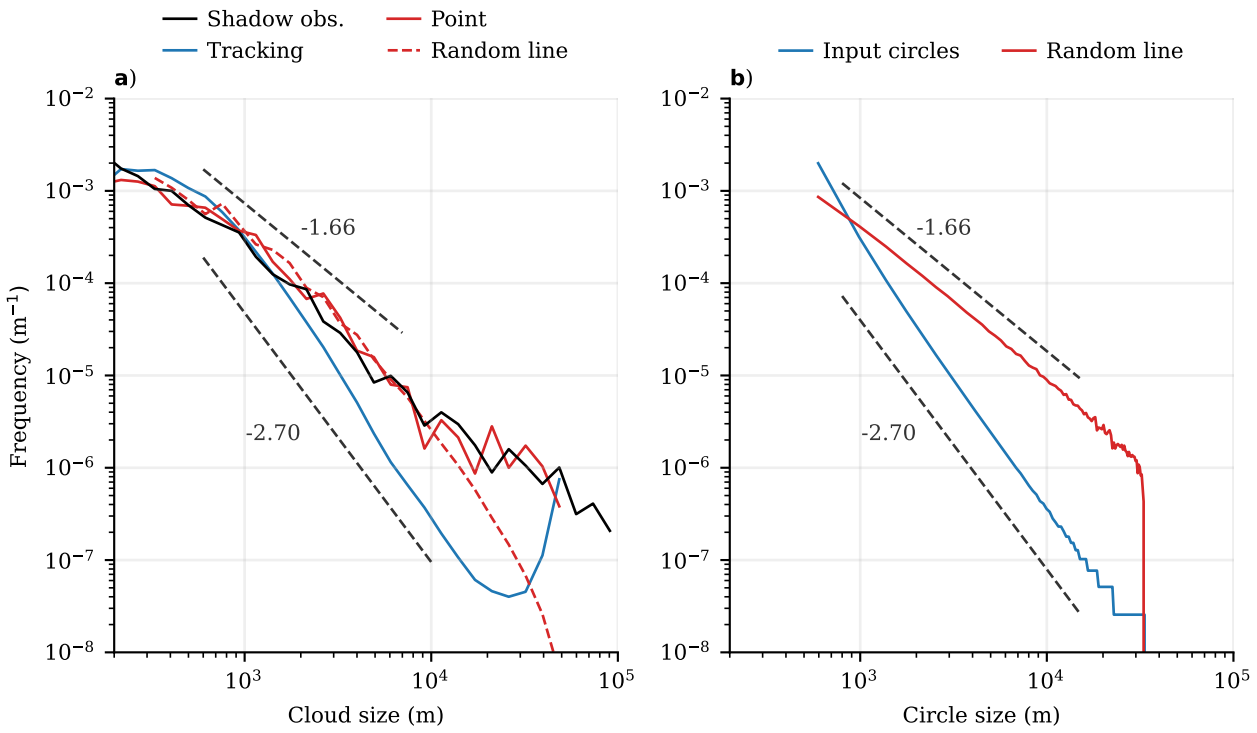

Figure 6.8: Different techniques of measuring cloud or shadow length and their effect on the power law slope. Large-eddy simulation is run for August 2016 for the location of Cabauw, where the irradiance observations are made. The domain size is 51.2 x 51.2 km^2 with a horizontal resolution of 100 m. **(a)** compares observations to point, random line, and cloud tracking techniques based on cloud fields from this model. Gray dashed lines indicate the two power law slopes from 1D and 2D methods over a range where they are largely unaffected by model model resolution and domain size limitations. **(b)** compares the probably distribution of circle chord lengths using the random line technique applied to a 2D field of circles generated from a power law distribution with a slope of -2.7.

6.3.5 Testing measurement technique using a cloud-resolving model

There is a rich body of literature on cloud size distributions which we can relate our results to, including the interpretation of power law slopes and measurement technique sensitivity. One aspect is how a 1D method, i.e. time series or random line transacts through a 2D cloud field, result in different size distributions than a 2D method, such as satellite imagery from which you can derive cloud areas. Cloud cover derived from a 1D method is equivalent to a 2D method, but the cloud size that contributes most to total cloud cover shifts to smaller scales for 1D methods, as shown by Rodts et al. (2003). This has to do with 1D methods underestimating the size of objects, because of the high chance of only slicing part of an irregular shape, but also having a higher chance of detecting a larger object, which Rodts et al. (2003) are able to analytically compensate for. However, Berg & Kassianov (2008) find in their analysis that complicated cloud geometry (shape, tilt, overlap) has a bigger influence than measurement technique.

To test this on our dataset, we have set up a cloud resolving model (LES) to reproduce one month of summer weather conditions at Cabauw, and an idealised circular cloud model similar to Rodts et al. (2003). Figure 6.8a shows that our model is able to reproduce cloud fields that match the observed distribution, with a power law slope close to -1.66 for 1D methods (random line and simulated point measurements). Cloud tracking, i.e. finding the areas of all clouds in the domain and converting to 1D length scales by taking the square root, results in a slope close to -2.7, similar to what Heus & Seifert (2013) found. Constructing a 2D field of circles of which the radii distribution is described by a -2.7 power law slope is shown in Figure 6.8b, and illustrates that if you use a random line sampling technique on this 2D field, the -2.7 slope changes to -1.66, a similar shift in slope as found for cloud resolving model with realistically shaped clouds. Model domain size or horizontal grid resolution affect the upper and lower end of the resulting distributions, but consistently reproduces this change in slope in a sensitivity analysis (Figure 6.9). A power law slope of -2 means all cloud sizes contribute equally to cloud cover, but for steeper slopes ($<$ -2) this shifts the importance to smaller clouds and vice versa for less steep slopes (Wood & Field, 2011). This means the observed characterisation of 1D irradiance variability caused by cloud shadows and enhancement (Figure 6.3) is driven relatively more by larger clouds, whereas the spatial 2D distribution of irradiance variability is relatively rich in smaller clouds.

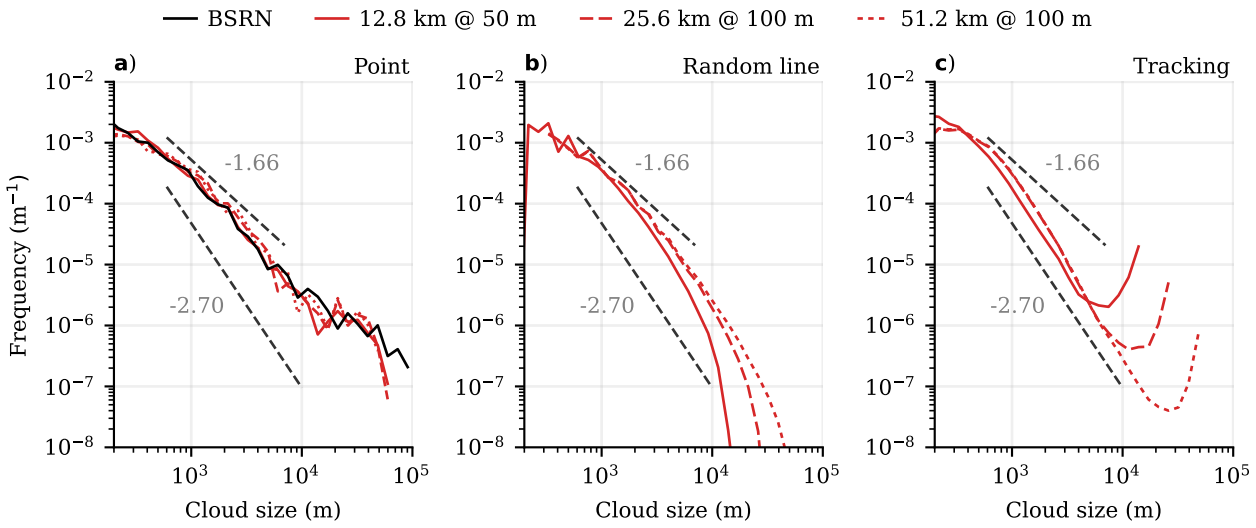

Figure 6.9: Different techniques of measuring cloud or shadow length similar to Figure 6.8a, but for different domain size and resolution.

6.4 Conclusion and implications

Based on a ten-year dataset of high resolution observations of surface solar irradiance variability, complemented with modelling and studies on cloud size distributions, we have shown how the cloud size distributions drive the spatiotemporal scales of irradiance variability. These scales of variability cover multiple orders of magnitude regardless of season, time of day, measurement technique or detection criteria, with the following implications. To model surface irradiance variability to its full extent and reproduce observed distributions of cloud shadows and enhancements, scales down to seconds or tens of meters ($L_{ce} \approx 25$ meters) need to be resolved. Similarly for observational campaigns, we recommend using fast responding instruments with at least 1 Hz sampling to directly observe the scales down to which clouds occur and contribute to irradiance variability. Most variability is driven by scattered or broken boundary layer clouds, so focusing on these weather types in observing and modelling efforts is an effective research strategy, both for time series (1D) and spatial (2D) techniques. Already, though, our presented distribution shapes and how they originate from cloud size distributions provide observational guidance towards an accurate representation of irradiance variability in models. These results thus have implications for weather and climate in general, but also solar energy and the photosynthetic response of vegetation under variable light, where detailed knowledge of surface solar irradiance is essential.

Chapter 7

Observed patterns of surface solar irradiance under cloudy and clear-sky conditions

This chapter is based on:

Mol, W., Heusinkveld, B., Mangan, M. R., Hartogensis, O., Veerman, M., & van Heerwaarden, C. (2024). *Observed patterns of surface solar irradiance under cloudy and clear-sky conditions*. In Quarterly Journal of the Royal Meteorological Society. Wiley. https://doi.org/10.1002/qj.4712

Abstract

Surface solar irradiance varies on scales as small as seconds or meters. This variability is driven mostly by wavelength-dependent scattering by clouds, and to a lesser extent by aerosols and water vapour. The highly variable nature of solar irradiance is not resolved by most atmospheric models, yet it affects, most notably, the land-atmosphere coupling and the quality of solar energy forecasting. Characterising variability, understanding the mechanisms, and developing models capable of accurately resolving it requires spatially and spectrally resolved observational datasets of solar irradiance at high resolution, which are rare. In 2021, we deployed a network of low-cost radiometers at the FESSTVaL (Germany) and LIAISE (Spain) field campaigns to gather data on cloud-driven surface patterns of irradiance, including spectral effects, with the aim to address this gap in observations and understanding. We find in case studies of cumulus, altocumulus, and cirrus clouds that these clouds generate large spatiotemporal variability in irradiance, but through different mechanisms and at different spatial scales, ranging from 50 m to 30 km. Spectral irradiance in the visible range varies at similar scales, with significant blue enrichment in cloud shadows, most strongly for cumulus, and red enrichment in irradiance peaks, particularly in the case of semi-transparent clouds or near cumulus cloud edges. Under clear-sky conditions, solar irradiance varies significantly in water vapour absorption bands at the minute scale, due to variability in atmospheric moisture in the boundary layer. With this study, we show that observing detailed spatiotemporal irradiance patterns is possible using a relatively small, low-cost sensor network, and that such network observations can provide insight and validation for the development of models capable of resolving irradiance variability.

7.1 Introduction

Solar radiation is a fundamental driver of weather and climate, varying in time and space on a wide range of scales. Variations in solar irradiance at the surface, excluding any influence from vegetation or other obstructions, can occur on scales as small as seconds or tens of meters, and are mainly driven by clouds. Cloud fields generate complex, high contrast spatial patterns that range from stationary to dynamically evolving, depending on cloud type, cloud velocity, and cloud shape evolution. The spatiotemporal scales of surface irradiance patterns are directly linked to cloud sizes, meaning scales ranging between seconds (10^1 m) to hours (10^5 m) all contribute significantly to the total variance (Wood & Field, 2011; Tabar et al., 2014, Chapter 6).

Measuring or forecasting these variations is challenging but important to get right, because they influence the coupled land-atmosphere system (i.e., the energy, water, and carbon cycle), atmospheric photochemistry, and solar energy production. For example, heterogeneity in surface heat fluxes driven by cloud-induced irradiance variability can feed back to cloud development (Lohou & Patton, 2014; Jakub & Mayer, 2017; Veerman et al., 2022), and the highly variable nature of solar irradiance negatively impacts electricity grid stability and solar energy yield (Liang, 2017; Kreuwel et al., 2021; Yang et al., 2022). In addition to clouds, light scattering and absorption in the atmosphere by gas molecules and aerosols also result in changes in the light spectrum, which has implications for photosynthesis (Durand et al., 2021) and wavelength-dependant photovoltaic technologies (Dirnberger et al., 2015).

Variability in surface irradiance is amplified by the three-dimensional nature of scattering, and thus redistribution, of solar radiation in the atmosphere. Cloud shadows are caused by the (partial) blocking of direct irradiance and are darker due to part of the light horizontally scattering to an area around the cloud shadow rather than directly in it. When this scattered irradiance locally combines with unobstructed direct irradiance in a cloud-free area, it exceeds clear-sky irradiance, and potentially even extra-terrestrial irradiance (Yordanov et al., 2015; Gueymard, 2017; Cordero et al., 2023). In this study, we refer to such areas as cloud-induced enhancement of irradiance above clear-sky values as simply 'cloud enhancement' (CE), as discussed by Gueymard (2017).

As Earth system modelling moves to higher resolution and complexity, accurately resolving small scale variability in irradiance becomes increasingly important, but also more difficult. While the physics of three-dimensional radiative transfer is well-known, the path light takes through an atmosphere filled with liquid water and ice, aerosols, and gas molecules, and over a partially reflecting surface, is highly complex. To add to the complexity, radiative transfer processes depend on wavelength, in particular in the case of gas absorption (e.g. ozone or water vapour) and Rayleigh scattering, but also clouds become optically more absorbent and sensitive to wavelengths beyond the visible range (O'Hirok & Gautier, 1998; Schmidt et al., 2010). Qualitatively, the spatial patterns of irradiance that a cloudy atmosphere generates can be visible to the eye, for example from an aerial view or on the side of mountains. However, a quantitatively characterising solar spectral irradiance and explaining how exactly

it results from a given atmospheric state remains a challenge, especially at small scales.

Both observations and modelling at these small scales have their limitations. Spatial observations of surface irradiance at the scale of cloud shadow and enhancement patterns (10^1 - 10^4 m, Chapter 6), with an adequate temporal resolution of 1 s or better (Tomson, 2010; Yordanov et al., 2013), are rare. Many high quality solar irradiance observations exist, for example the Baseline Surface Radiation Network (Driemel et al., 2018), but while these adhere to the highest quality standards, they are effectively single point measurements at typically 1 minute resolution. Examples of more dense networks are the 99 pyranometers network deployed during the HOPE campaign (Madhavan et al., 2016), or the 17 photodiode pyranometers used by Weigl et al. (2012); Tabar et al. (2014), both deployed on $\sim$ 1 km^2 scale areas. Photodiode pyranometers are fast responding ($<<$ 1 s) sensors, and thus capture the fastest atmospheric driven fluctuations in irradiance, but they do not provide spectral information. None of these networks provide sufficient temporal, spectral, and spatial resolution to characterise surface irradiance heterogeneity at the scale of clouds, in part due to the high cost and operational burden of performing such measurements.

In terms of using modelling, reproducing observed solar irradiance variability requires a fully resolved and realistic simulation of clouds, information about atmospheric composition and aerosols, and accurate 3D radiative transfer calculations using techniques such as Monte Carlo ray tracing. In practise, the most detailed operational weather models operate at a resolution of approximately 1 km, too coarse to resolve clouds at the necessary scales. Apart from that, the physics of radiative transfer is often simplified to a two-stream approach (up and down) (Hogan & Bozzo, 2018), which by design means it cannot resolve cloud enhancement and will thus underestimate the contrast between shaded and sunlight surfaces. There are ways to improve upon two-stream methods by subgrid parameterisation of clouds and 3D radiative effects, such as SPARTACUS (Schäfer et al., 2016) or ecRAD (Ukkonen & Hogan, 2024) for operational weather models. More accurately resolving 3D radiation is possible in academic setups, where specific mechanisms can be studied in a controlled manner. For example, Veerman et al. (2022) coupled a 3D Monte Carlo ray tracer to a cloud resolving model to study cumulus, Gristey et al. (2022) used a similar technique but in an uncoupled setup to study cumulus with aerosol effects, Villefranque et al. (2023) functionalised a ray tracer to study the effect of surface albedo on irradiance in cumulus fields, and Pincus & Evans (2009) demonstrated an alternative to ray tracing altogether. However, even in the best studied case of boundary layer shallow cumulus, one can question the realism with which large-eddy simulation (LES) can resolve such clouds (Romps et al., 2021). This makes validation of irradiance models non-trivial, where errors in irradiance can originate from unrealistic cloud fields rather than from radiative transfer calculations.

Improving parameterised or optimised 3D radiative transfer calculations for finer scales depend on our understanding of 3D radiative transfer in the atmosphere and validation against observed variability. To gather more observations of variability in total and spectral solar irradiance at cloud-scale, we have developed low-cost radiometers to be deployed in spatial network setups (Chapter 3). The design philosophy is similar to that of the APOLLO (Au-

tonomous cold POoL LOgger) network (Kirsch et al., 2022): autonomously running low-cost instruments optimised to accurately capture fluctuations rather than high accuracy single-point data. With calibration against expensive, high-quality reference stations, these instruments give useful information at a fraction of the cost while also being flexible in their setup, necessary to densely cover and maintain a large area.

In this paper, we describe the deployment and measurement analyses of a network of 20 to 25 radiometers at two field campaigns in 2021, namely FESSTVaL and LIAISE. Both campaigns were organised to observe and understand local meteorology: FESSTVaL is focused on sub-mesoscale variability and cold pools from convective storms, and LIAISE is aimed at observing the land-atmosphere coupling from irrigated crop fields to the regional scale in complex terrain. The detailed observations of the atmosphere gathered by other groups at these campaigns are essential for understanding what we see in our own measurements. Section 7.2 covers the design and limitations of the radiometers, our network measurement strategy at both campaigns including a brief description of the weather, and a technique we use to construct spatial patterns from spatiotemporal data. What follows are three sections of results, each with their own calibration and validation discussion. First, we discuss three spatial patterns of broadband irradiance (Section 7.3), followed by a study of how the visible part of the spectrum changes in these cases (Section 7.4), and thirdly how irradiance varies in clear-sky conditions linked to water vapour variability (Section 7.5). Conclusions and impacts of our results for solar irradiance variability research are discussed in Section 7.6.

7.2 Methodology and campaigns

7.2.1 Solar irradiance sensor design

The sensors we use have been specifically designed to capture the fastest cloud-driven fluctuations of incoming sunlight, and variations in the light spectrum induced by the atmospheric composition, clouds, aerosols, and vegetation. At a sampling frequency of 10 Hz, the Fast Response Optical Spectroscopy Time synchronised instrument (FROST, Chapter 3), measures incoming shortwave irradiance at 18 wavelengths in the visible to near-infrared spectrum (410 to 940 nm). The locations of the 18 bands are detailed in Figure 7.1, which shows the response curves for the factory specification of 20 nm full-width half maximum, combined with a simulated solar spectrum of a mid-latitude summer day around solar noon. The 18 bands are spread over 3 subgroups of 6 bands on the spectrometer chip, which are color-coded in the figure. Since these three subsensors are spatially separated by about a centimetre (in a triad), we use a Teflon diffuser on top to equally distribute incoming sunlight.

Material costs for one sensor are under €200 in total, they are powered by their own small solar panel, and are all time-synchronised using a GPS chip. This makes them scalable and easy to deploy on tripods in field campaigns in flexible setups compared to conventional high quality (10 times or more expensive) pyranometers or spectrometers. The low-cost design philosophy is a trade-off against accuracy compared to high-end instrumentation, but

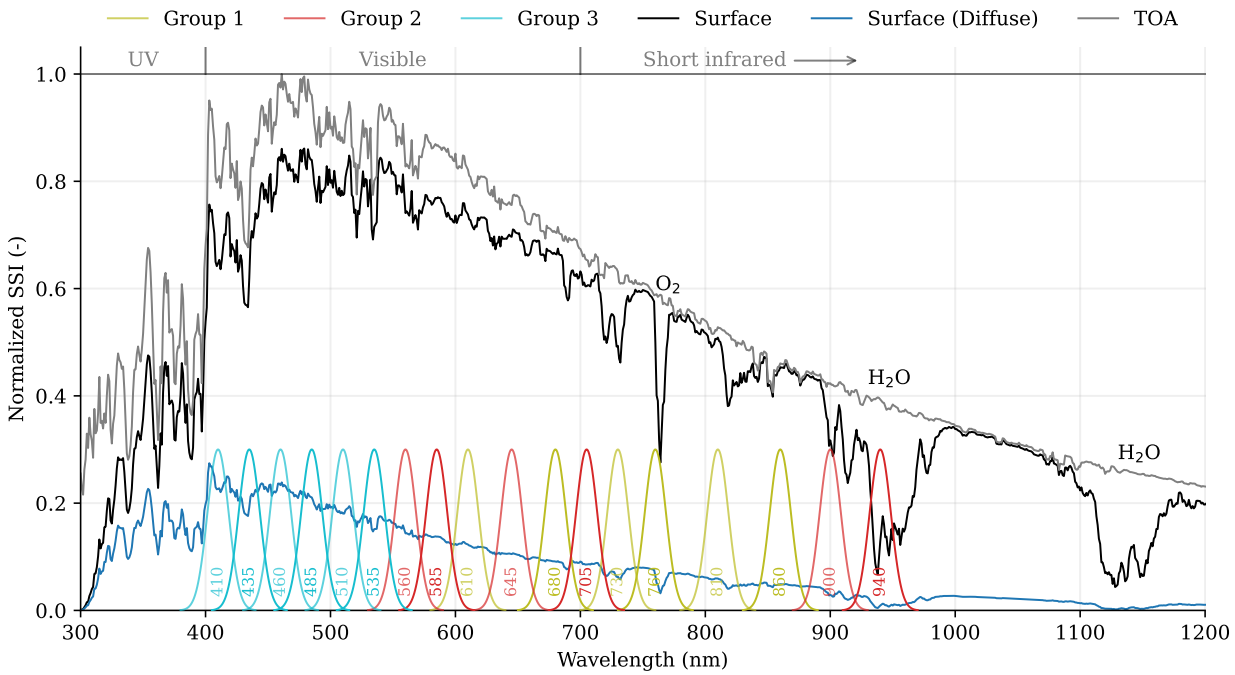

Figure 7.1: Spectral solar irradiance and the radiometer wavelength bands. Each radiometer band is color-coded according sensor subgroup. Normalized top of atmosphere and surface solar spectral irradiance are based on a clear-sky simulation using libRadtran (Emde et al., 2016) for 18 June 2021, 11:30 UTC, FESSTVaL campaign area in Germany (Section 7.2.5). Spectra are smoothed with a 5 nm rolling mean for readability.

performance is good enough to capture and analyse spatial surface irradiance patterns driven by clouds and spectral signals of these variations. We focus on the practical application of the sensor in this work, but a complete and technical reference with more use cases is described in Chapter 3. Important sources of error are discussed next, which we either correct for or take into account in the analysis presented in Sections 7.3 to 7.5.

7.2.2 Sources of measurement error

Cosine response

Given a solar zenith angle θ, the horizontally measured signal strength of a constant light source Q as function of θ would ideally be $\mathrm{Q} \cdot \cos(\theta)$, see also Figure 7.2. In practise, there is an increasing relative underestimation of irradiance for high θ in our instrument (Figure 7.2a), referred to as the cosine response, for which we correct in post processing. While this cosine response correction is in principle a function of $\cos(\theta)$ as well, the triad sensor design results in a unique response curve for each subsensor, despite the diffuser, which is also a function of the orientation of the sensor with respect to the sun. This means that the sensor orientation is important to keep constant throughout a measurement campaign, and ideally all sensors in a network are placed in the same orientation to minimise variations among sensors. The variation in cosine response between subgroups is relevant for the usability of

the ratio between spectral bands, of which we make use in Sections 7.4 and 7.5, as these bands can be on different subgroups. This generally limits the use of spectral analyses to zenith angles of about 65 degrees or below. Relative errors in spectrally integrated irradiance will also become pronounced at zenith angles of 75 or higher.

Build and placement consistency

All instruments are hand-made, which leads to small imperfections or inconsistencies, such as the exact distance and position of the spectrometer from the diffuser. It is also challenging to place and keep all sensors level within a tolerance of 0.5 degrees from day to day. This results in measurable variations among instruments, more noticeable at high zenith angles, and imposes a limit on what is achievable through post processing. While ideally there would be one universal calibration for all instruments, we find the best overall results when calibration is fine-tuned per individual instrument when possible. This ultimately leads to a limitation in accuracy, which we quantify as the spread among sensors in a network.

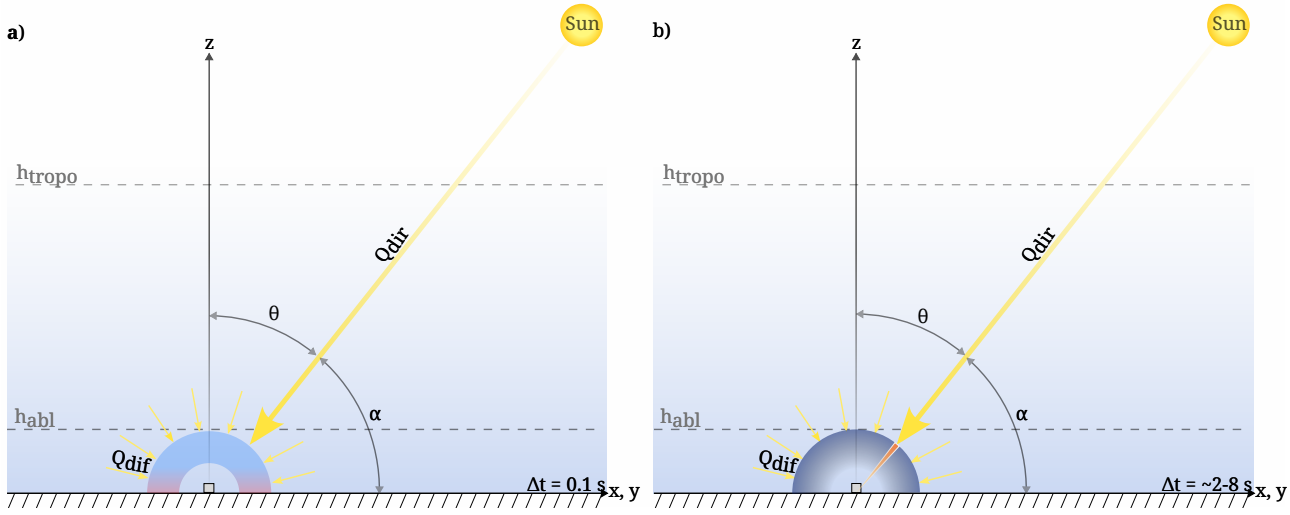

Figure 7.2: Schematic of surface solar irradiance measurements using FROST **(a)** and a suntracker with a pyranometer and pyrheliometer **(b)**, both located at gray square in the axis origin. The solar elevation angle α depicts the origin of direct irradiance Q_{dir}, of which a fraction (typically 10 to 30%, see Figure S7.1) scatters and results into diffuse irradiance Q_{dif}, in this clear-sky example. FROST does not distinguish between Q_{dir} and Q_{dif}, and misses part of the signal originating from low angles α, illustrated by the red part of the semi circle in **(a)**. A suntracker measures Q_{dir} and Q_{dif} separately, illustrated by the 5° degree arc and semi circle in **(b)**, and is less biased for small α. The blue background gradient illustrates decreasing air density with height, h_{tropo} and h_{abl} are the approximate tropopause and atmospheric boundary layer heights. Δt denotes the resolved temporal resolution of each instrument.

Crosstalk

Especially the third group of wavelength bands (Figure 7.1) experiences significant crosstalk, meaning a sensitivity to wavelengths λ_{ct} outside the specified range of the band. Under worst-case conditions (a flat spectrum of light plus a 10.6 mm Teflon diffuser) the 410, 435,

and 460 nm bands derive $\sim$ 70 % of their total signal from $\lambda > 750$ nm. In reality, the solar spectrum is significantly less energetic for λ_{ct} compared to 410 - 465 nm, effectively halving the crosstalk. The bands of group 1 in Figure 7.1 are all affected less than 10 %. The second group between 10 and 20 %, except for 585 nm with $\sim$ 35 % crosstalk. This issue is resolved in a new version of the instrument by using certain wavelength filters over the affected subsensors (Chapter 3), but the sensor version used in this work is still without such filters. Since the crosstalk effectively adds extra signal to be used when integrating spectra to broadband irradiance, we use all 18 bands in Section 7.3. For spectral analyses, we quantify the effect crosstalk has on measured changes in irradiance spectra and choose bands that are least affected. Response curves for each band and diffuser are shown, and available as supplementary material, in Chapter 3.

Temperature sensitivity

There are two components introducing a temperature sensitivity in the instrument, with no significant difference across wavelengths. A small, linear change in signal strength of -0.25 % per +10 K comes from the spectrometer itself. The Teflon diffuser has a +2 % jump in transmittance from 20 to 21 ^{o}C, and slowly declines at a rate of approximately -0.4 % per +10 K afterwards. While 10 cm or 2 m air temperature is known for all measurements, it does not directly translate to Teflon diffuser and spectrometer temperature, making a temperature correction not trivial. We use measured surface temperature $\mathrm{T_s}$ (10 cm) as a proxy for qualitative assessment of measurement quality, while keeping in mind $\mathrm{T_s}$ is still an underestimation. The role of temperature in measurement accuracy is discussed further in Section 7.3.1 on broadband calibration.

Factory calibration

Because of limitations of the spectral quality in the sensor version used in this research, it is not easy to derive accurate measurements in W m^{-2} nm^{-1}. However, ratios between certain bands and changes therein contain valuable information and can be done in native sensor units, i.e., without calibration. Sensor to sensor and wavelength band to band variations in factory calibration accuracy is generally $\pm$ 10 %, with some outliers up to $\pm$ 20 %, which also affects ratios between bands among sensors (Figure S7.2a). Even though each sensor can be treated separately in some cases, it often helps to have homogeneous raw output among sensors for a given light signal. We therefore homogenise the factory calibration as well as possible using a clear-sky periods where all sensors should measure the same, prior to performing any spectral analyses. This reduces the spread to within 2 % (Figure S7.2b), and produces a dataset labelled as 'precalibration', which is the starting point for spectral analyses presented in this study.

Maintenance and quality control

We performed irregular but frequent maintenance on the sensors during the field campaigns, usually early or late in the day, to check whether they were still running, level, and free of

dirt or dust (birds or flies liked to sit on some particular sensors). All data is provided with quality flags that mark data points with bad or unreliable data, which is mostly due to periods of sensor maintenance. In addition, temporary displacement of sensors or the obscuring of direct sunlight by nearby objects at low solar angles (trees, crops, other instrumentation) is flagged.

7.2.3 Measurement strategy at field campaigns

We participated in two major field campaigns aimed at observing local to regional scale atmospheric dynamics and land-atmosphere coupling. Two weeks in June 2021 during FESSTVaL (Field Experiment for Submesoscale Spatio-temporal Variability in Lindenberg, Hohenegger et al. (2023)) in north-east Germany, and two weeks in July 2021 during LIAISE (Land surface Interactions with the Atmosphere over the Iberian Semi-arid Environment, `https://liaise.aeris-data.fr/`) in north-east Spain. Differences between the two campaigns in climate, local atmospheric dynamics, time of year, and geographical location have offered a diverse range of solar irradiance conditions to observe through the network of sensors, resulting in a total of $\sim$ 4 weeks of spatial measurements. The campaigns and sensor network measurement strategy are described next.

FESSTVaL

During the FESSTVaL campaign, we deployed a network of 20 sensors in a simple, equidistant rectangular grid. Our measurements took place between June 14 and June 29, 2021, at the Falkenberg supersite of the Deutscher Wetterdienst, $\sim$ 50 meters above sea level. Figure 7.3a shows the 4 by 5 sensor network layout with a 50 meter horizontal grid spacing. The choice of grid spacing is a combination of aiming for something that resembles the grid of a high resolution cloud resolving model, an a priori estimate of the required resolution to resolve shadow/sunlight transitions, practical constraints of the Falkenberg site, and the number of sensors we had available. Technically, the grid spacing was 49 meters due to the constraints of rolling out the sensor network that is as little as possible obstructed by, or in the way of, other instrumentation on the field.

We deployed two consumer action cameras (with an on-board GPS clock) at the northern two grid corners to take time-lapse photos of the sky at a 5 second interval, so that we can relate the cloud field to surface irradiance. These cameras were oriented up towards the sun in the south-east for the north-western camera, and south-west for the north-eastern camera. Calibration of the sensors is done against the Falkenberg suntracker, equipped with high quality instrumentation and located in the south-east corner of the field. Instrument locations relative to the grid are illustrated in Figure 7.3a.

In addition to this setup, three sensors (1, 22, 23) were located several kilometers to the west, south, and east of the field (Figure 7.3b), to capture part of the larger scale variability in the campaign area. Two other supersites are Lindenberg and Birkholz, and all supersites were equipped with microwave radiometers which measure integrated water vapour, used in this study, among other things. There were many more instruments deployed, see

https://fesstval.de and Hohenegger et al. (2023) for details. Our two weeks at FESSTVaL featured one fully clear-sky day, one rainy day with thick cloud cover, but was otherwise characterised by many different (broken) cloud covers (Figure 7.4a).

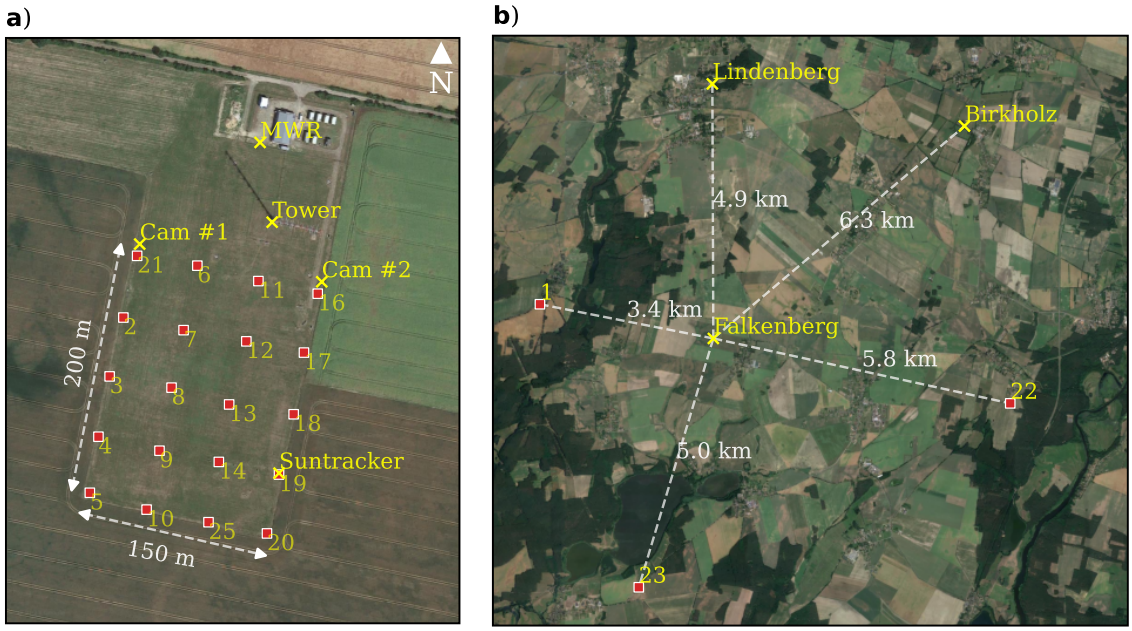

Figure 7.3: Radiometer network measurement layout at FESSTVaL. The 4 by 5 sensor grid at Falkenberg with a horizontal spacing of ∼50 meters is shown in **(a)**, together with the 98 meter tower, suntracker, two cloud cameras, and microwave radiometer (MWR) locations. Number labels are sensor IDs. Additional sensors set up in the FESSTVaL campaign area around Falkenberg are shown in **(b)**, and includes the location of the FESSTVaL supersites Lindenberg and Birkholz. Background satellite data: Google © 2023.

LIAISE

Between 14 and 30 July 2021, we set up a network of sensors at the La Cendrosa site of the LIAISE campaign (https://liaise.aeris-data.fr/). La Cendrosa is located within an irrigated part of an otherwise semi-arid region, with complex local, regional, and mesoscale dynamics (Mangan et al., 2023). The typical expected, and observed (see Figure 7.4b), summertime weather in this region in north-eastern Spain is cloud-free, dry, and hot. Specifically at La Cendrosa, due to local topography and sea breeze dynamics (locally called 'Marinada'), prevailing day time winds are westerly, shifting via a southern sea breeze to easterly night time winds. While the goal is primarily to observe cloud-driven irradiance variability, frequent clear-sky days offer a good calibration opportunity and analyses in spectral variations due to day-to-day variations in aerosol and water vapour content. We had a bit more space to set up the network compared to Falkenberg, so in an attempt to capture larger patterns, we decided on a grid spacing of 100 meters. With the prevailing westerly daytime winds, we oriented the grid in a similar direction, in hopes of tracking cloud shadows and enhancements over a length of 400 meters, illustrated in Figure 7.5a. An additional group of radiometers

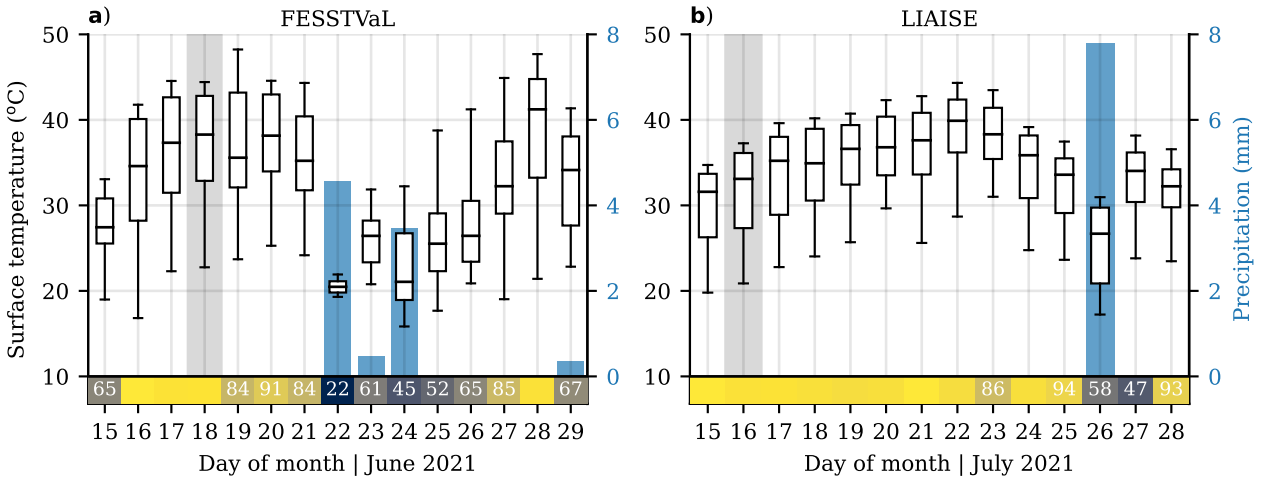

Figure 7.4: Overview of weather variables most relevant for irradiance measurements at FESSTVaL and LIAISE. All data is during day time (solar elevation angle $> 15^{o}$). Box plots are the surface temperatures at **(a)** Falkenberg and **(b)** Els Plans. The blue bars are accumulated precipitation during day time at the sensor network. The color shading at the bottom is the observed percentage of clear-sky irradiance (CAMS McClear), where darker colors indicate more cloudiness, labelled with numbers for values $< 95\%$. Vertical gray bars at June 18 and July 16 are the reference cloud-free calibration dates used in Section 7.3.

was set up in footprint of the scintillometer, which in the context of this study gives additional resolution in the grid center, but makes the total network non-equidistant.

Two action cameras were mounted on the energy balance station (EBS), west and east oriented, but pointed straight ahead rather than at the sun to include a visual record of the vegetation growth and irrigation during the campaign period. The EBS measures incoming broadband irradiance as part of the radiation balance measurements, which is used in this study as a calibration reference. Hourly boundary layer soundings were deployed at La Cendrosa during Intensive Observation Periods (IOPs), which we combine with hourly full troposphere soundings at the non-irrigated site Els Plans (Figure 7.5b), located 14.1 km to the south east. There are many more observations and sites within the campaign area, which can be found on `https://liaise.aeris-data.fr/`.

7.2.4 Visualising spatial patterns

We find, as will be shown shortly, that cloud shadow and enhancement patterns often both exceed the network size and have details finer than the network resolution. It is furthermore challenging to visualise a high amount of spatiotemporal data in a concise way without applying statistics. For some figures, we therefore apply a data processing technique that makes use of the high temporal resolution and an estimate of the cloud velocity in order to increase the effective network size and spatial resolution. Essentially, the following technique transforms temporal data to spatial data. The technique assumes clouds retain their shape (analogous to Taylor's hypothesis of frozen turbulence) when moving over the measurement

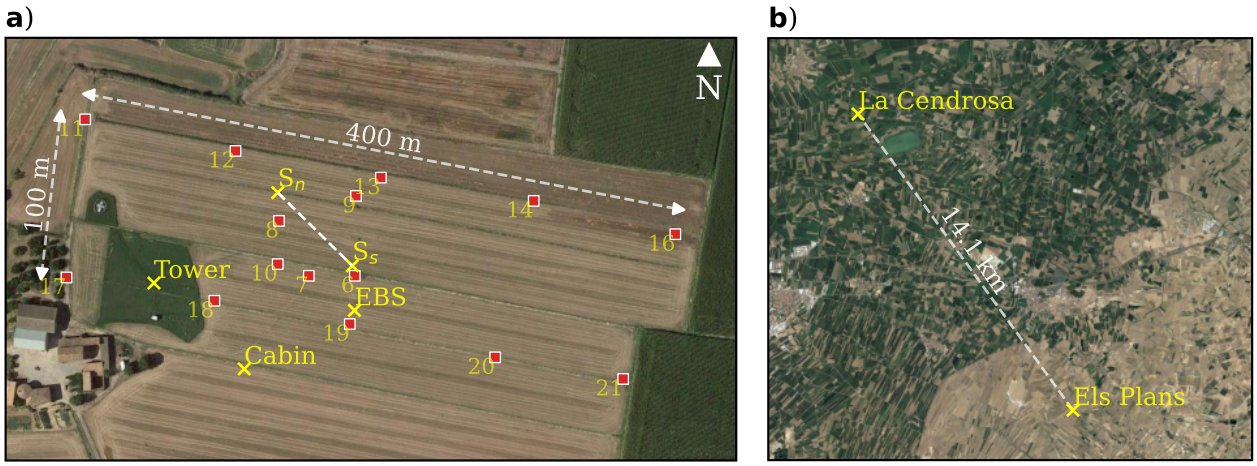

Figure 7.5: Sensor network measurement layout at LIAISE. The west-east oriented 5 by 2 sensor grid at La Cendrosa has a horizontal spacing of ∼100 meters, with an additional set of 5 sensors within the footprint of the scintillometer (S_n to S_s), shown in **(a)**. The reference pyranometer is mounted on the EBS (energy balance station). La Cendrosa and Els Plans are shown in **(b)**, which illustrates the irrigated (green) versus non-irrigated (beige) area. Background satellite data: Google © 2023.

network (a schematic example is available in Figure S7.3). For example, we can 'advect' the Falkenberg network (Figure 7.3a) in space with a time step of 5 s and 5 m s^{-1} cloud velocity for 10 steps, resulting in effectively a spatial network of 200 points (20 sensors × 10 steps) that spans ∼ 450 m (5 s × 5 m s^{-1} × 10 steps + original network length of 200 m) in the advection direction and has approximately double the resolution (one step is 25 m). The virtual 200 points can then be interpolated to a new equidistant grid for easier comparison and visualisation.

The main challenge with this technique is the determination of the cloud velocity vector, which we initially base on wind speed at cloud level from nearby soundings and ceilometer data, and then manually fine-tune to produce an as smooth as possible result. Small changes in direction or speed quickly result in noisy results with artefacts from incorrectly placed data points reporting contradicting values. Keeping the total integration time short minimises our violation of the static cloud shapes assumption, though some artefacts can remain. The cloud velocity step fine-tuning needs to be repeated frequently, every 10 to 30 minutes or so, due to wind and cloud velocity (subtly) changing or simply varying among clouds. Results are consistent when this exercise is repeated with selective omission of sensors, with mean absolute errors and root mean square errors between 0 to 5 % of the total variation in irradiance (see Figures S7.4 and S7.5 for examples). We apply this technique to three distinct cases, first shown in Section 7.3.

7.2.5 Simulated solar position, clear-sky irradiance, and irradiance spectra

In addition to observations, we require extra information about solar irradiance, mostly for the interpretation of measurements. An estimate of clear-sky irradiance is required for iden-

tifying cloud enhancement events in the measurements, which we base on the globally available CAMS McClear product (Gschwind et al., 2019). This product is based on a radiative transfer model that calculates, for a cloud-free atmosphere, global horizontal (and diffuse) irradiance, given a geographical location, time of year, and time of day. Included in these calculations is the atmospheric composition based on 3-hourly CAMS analyses (aerosols, water vapour, and various other gases). Accuracy of global horizontal irradiance is within several percent (Gschwind et al., 2019), enough for our purposes in this study as we will look at measurements of significantly larger variations. It is available at a 1 minute resolution, which we linearly interpolate to 1 second when necessary.

For both context and independent validation of measured spectral irradiance, we calculate clear-sky shortwave irradiance spectra using libRadtran (Emde et al., 2016). Aerosols are set to default (rural-type boundary layer aerosol), total column water vapour is taken from microwave radiometer (FESSTVaL) or sounding (LIAISE) measurements, surface albedo is set to "cropland", and other atmospheric profiles are set to the "mid-latitude summer" default. Other relevant settings are the coordinates and time of day, which are case-specific. Validation of the setup is done using four clear-sky moments of the FESSTVaL campaign: 8:00 UTC on June 17, 18, 27, and 11:30 UTC on June 18. Values of clear-sky irradiance overestimate the Falkenberg sun tracker observations by 0.8 to 1.0 % (5.5 - 7 W m^{-2}) for the 8:00 UTC cases, and by 1.3 % (11 W m^{-2}) for 11:30 UTC on June 18. Performance for diffuse irradiance is significantly worse, likely due to using prescribed default aerosols, and is overestimated in all cases between 25 and 34 %, except for 8:00 UTC June 17 with 9 %. The impact of this bias is small in the context of this study, but will be taken into account when results are discussed. An overview of all simulations with validation statistics is available in Table S7.1. The spectrum of June 18 at 11:30 UTC is illustrated in Figure 7.1.

Finally, for sensor cosine response corrections and calibration, we need accurate solar zenith and azimuth angles, which we calculate using PySolar (Pingswept, 2022).

7.3 Spatial patterns of surface solar irradiance

7.3.1 Deriving global horizontal irradiance

Broadband solar irradiance is the total shortwave surface solar irradiance, often called global horizontal irradiance (GHI). GHI is measured using pyranometers, or in combination with pyrheliometers (Figure 7.2b), and typically has a spectral range encompassing most or all of the shortwave irradiance spectrum (e.g. 200 to 3600 nm for the CMP22, Kipp & Zonen (2004)). This range exceeds the spectral range covered by the 18 wavelength bands of our sensor (410 to 940 nm, a bit more including the crosstalk sensitivity), but these bands cover the most energetic part of the spectrum (410 to 940 nm $\approx$ 68 % of total irradiance based on data in Figure 7.1). We derive the GHI by first taking the mean of all spectral bands (Figure 7.1), correcting for the cosine response, and converting raw measurement units, counts $\mathrm{bin}^{-1}\,\Delta t^{-1}$, to W m^{-2}. This calibration generalises under the assumption that the spectrum shape of short-wave irradiance remains constant.

For both FESSTVaL and LIAISE, we have at least one clear-sky day with high quality reference GHI measurements available from pyranometers to calibrate against. The cosine response is a function of solar zenith angle, so we take the ratio between the spectral average of our instrument and the reference GHI measurement as a function of this angle. Figure 7.6a shows the resulting ratio curve relative to the suntracker reference for a single radiometer at FESSTVaL for a clear-sky day (June 18, 2021). The best curve fit extrapolated from 15 to 10 degrees, and kept constant for any value below, because here the absolute signal gets too low and relative measurement errors, including that of the pyranometer cosine response, negatively impact the curve fit. Especially differences between the cosine response of each subgroup become more pronounced at such low angles.

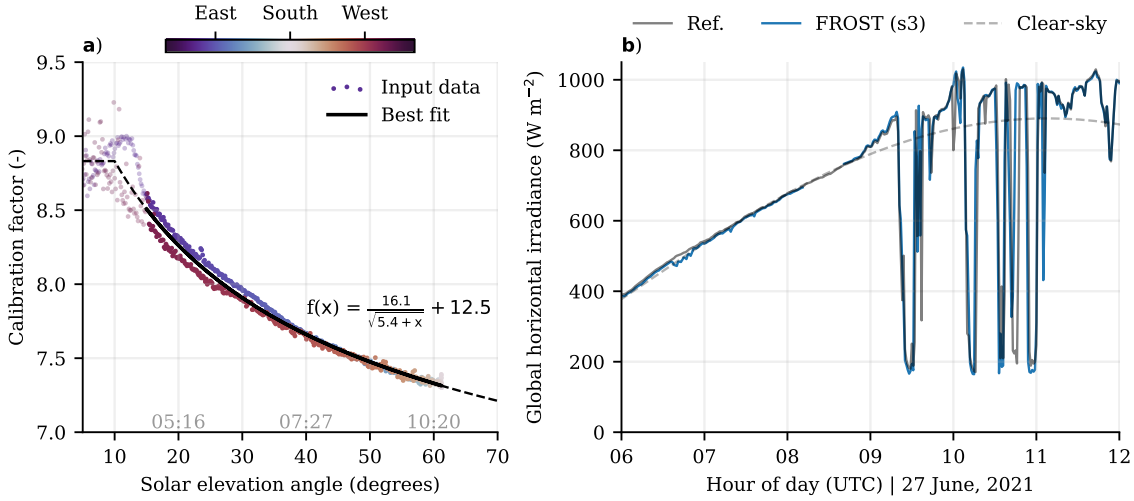

Figure 7.6: Broadband global horizontal irradiance calibration example. Calibration factor as function of solar elevation angle between raw instrument data and the irradiance data from the Falkenberg suntracker for June 18 is shown in **(a)**. The best fit curve is manually extended at the lower and upper end of the data range (dashed line), and follows the function with best fit coefficients between 15 and 60 degrees elevation angle. Time at the bottom is in UTC for morning until noon. The scatter colors indicate the solar azimuth angle. In **(b)**, the best fit calibration from **(a)** is applied to measurements of June 27, and compared again to the Falkenberg suntracker reference. All FROST data shown is for sensor 3, resampled to 1 minute.

Furthermore, when the sensor is not perfectly level, measured incoming irradiance between morning and evening for the same solar elevation angle introduces an asymmetry, which explains part of the hysteresis effect visible in Figure 7.6a. We find that a fitting technique that takes the solar azimuth angle into account and fits on subgroups separately does not generalise beyond the calibration data, and thus does not improve data accuracy for days with clouds. This is likely due to slight variations (less than 0.5 degrees) in sensor orientation that may occur from day to day, the exact reasons of which we do not know, and different combinations of solar elevation and azimuth angle as the Earth's orbit around the Sun progresses. Figure 7.6b illustrates the resulting time series when the reference date best fit is applied to a different day (June 27, 2021). This examples shows sensor 3 captures both the daily cycle and cloud driven fluctuations.

We apply this calibration routine to all data for each sensor individually, for both campaigns separately. Figures 7.7 give an overview of the performance of all grid sensors across all campaign days for FESSTVaL and LIAISE, compared to their respective reference station. Overall, the bias is within 2 %, and mean absolute error (MAE) between 5 to 15 W m^{-2} for most days and sensors. Notable outliers, June 22 or July 26 and 27, are explained by overcast and rainy weather (Figure 7.4), which leads to increased absorption in mostly near-infrared wavelength bands that our instrument does not sample, but is part of the shortwave spectrum. GHI is thus overestimated, because clear-sky conditions with less relative absorption in the near-infrared are the basis for calibration, violating our assumption that the solar spectrum shape is constant under all conditions (see Chapter 3.3 for more details). Sensor to sensor variations are typically smaller or equal to the error with respect to the reference station, and likely originate from variations in construction and minor day to day changes in sensor orientation. Changes in calibration quality due to the sensors' temperature sensitivity are small, as for most days the measured 10 cm temperature, and therefore the Teflon diffuser temperature, was well above the 2% signal jump at 20 degrees Celsius (Figure 7.4).

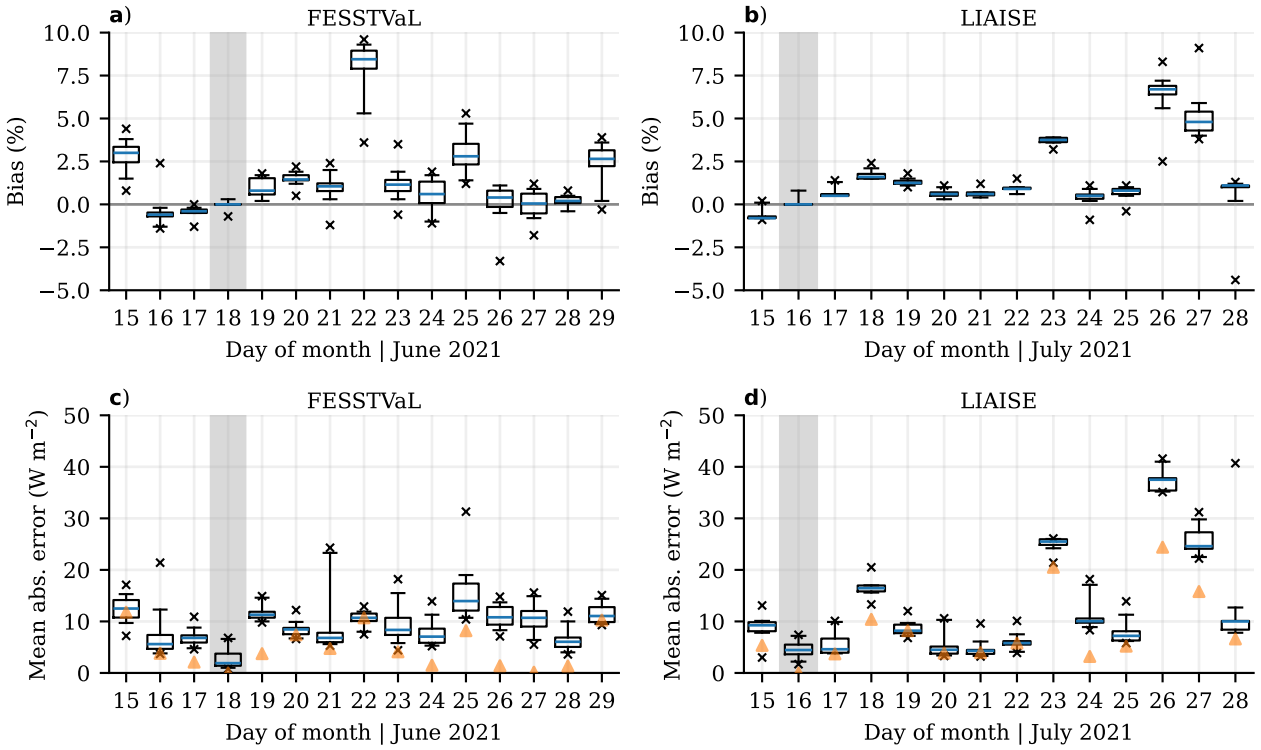

Figure 7.7: Global horizontal irradiance calibration performance of all sensors for FESSTVaL and LIAISE. Panels **(a, b)** show the mean bias of daily sums of irradiance compared to a reference pyranometer for all sensors, and panels **(c, d)** the mean absolute error. Vertical shading indicates the reference clear-sky calibration date for FESSTVaL in **(a, c)** and LIAISE in **(b, d)**. Box plots span the 5-95th percentile range of the spread among sensors. The orange triangle markers in **(b, d)** indicate the absolute median bias in W m^{-2}. Only data with solar elevation angle above 15 degrees is used for verification.

7.3.2 First impression and video

To get a first impression of cloud-driven patterns of surface solar irradiance, we plot the sensor network directly on a map combined with the cloud camera images, and render frames for each time step to create a video. For June 27, 2021, a day with cumulus clouds at FESSTVaL, such a video is available on `https://vimeo.com/827602111` (or supplementary material). One frame is displayed here in Figure 7.8, but in particular the video shows how the sensor network captures irradiance patterns made by the dynamic cumulus field. An interesting feature is how some cloud passages show a clear temporary increase in diffuse irradiance, whereas for others the diffuse irradiance remains constant, but always higher than clear-sky irradiance. The example shown in Figure 7.8 shows a fractured cloud passage (a-b) with a local increase in diffuse irradiance leading to relatively stronger enhancements or irradiance (c-e) compared to other cloud passages. There is an extra step of complexity once cirrus fields pass over, superimposing their effect onto that of the boundary layer cumuli. It is also clear that the spatial scale of cumulus shadows and enhancements is well above that of the network size and transitions between shaded and sunlit areas occur at scales smaller than the network sensor spacing.

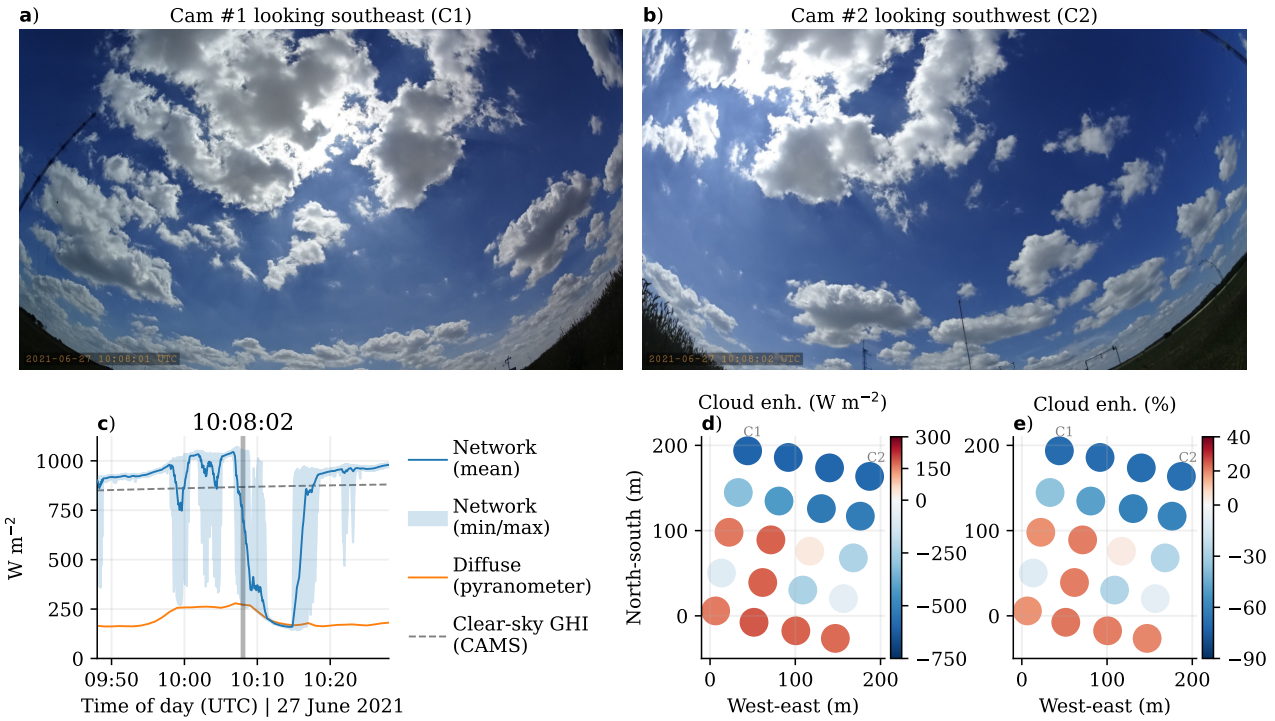

Figure 7.8: Network measurements of GHI combined with cloud imagery for June 27, 2021, at Falkenberg (FESSTVaL campaign). The time series **(c)** are centered around the 11:00 UTC snapshot, and features diffuse irradiance from the Falkenberg sun tracker, clear-sky GHI, and the FROST network measurements (spatial mean and min/max range). The network measurements are plotted relative to clear-sky GHI (CAMS McClear) in an absolute **(d)** and relative way **(e)**. For an animated version, see supplementary material or `https://vimeo.com/827602111`.

As an illustration of overall observed variability throughout both field campaigns, we construct a power density spectrum of all time series in FESSTVaL, LIAISE, and for three cases separately, illustrated in Figure 7.9. The campaign averaged spectra follow approximately $f^{-5/3}$ scaling between 10^{-4} and 10^{-1} s^{-1}, before a scale brake between 10^{-1} and 10^{0} and an apparent continuation of weaker power law scaling thereafter. Similar $f^{-5/3}$ scaling is shown by Tabar et al. (2014) until $\sim 10^{-1}$ s^{-1}, after which it similarly deviates. The scale break between 10^{-1} and 10^{0} s^{-1} is expected, at least for broken cloud conditions, due to the smallest clouds becoming transparent to solar irradiance (Chapter 6), making the biggest source of variability disappear. Other studies using spatial pyranometer networks find clearly different spatiotemporal scales and magnitude of variability for different sky types, and identify 'broken clouds' as the most potent for generating variability at the smallest scales (Lohmann et al., 2016; Madhavan et al., 2017). Power density spectra for single sensor time series of clear-sky (June 18), overcast (June 22), and cumulus (June 27) show differences in power law scaling in the 10 to 3600 s range, the variance in cumulus dominating over other sky types across all scales, and overcast conditions having the lowest variance of all sky types at scales shorter than 10 s, all consistent with spatial wavelet variance presented in Madhavan et al. (2017) (their Figure 5). Grid-averaged spectra start to deviate from single point measurements at scales shorter than 10 minutes. The spectral power of Falkenberg grid average is an order of magnitude below that of a single sensor at these small scales, relatively consistent between the three sky types.

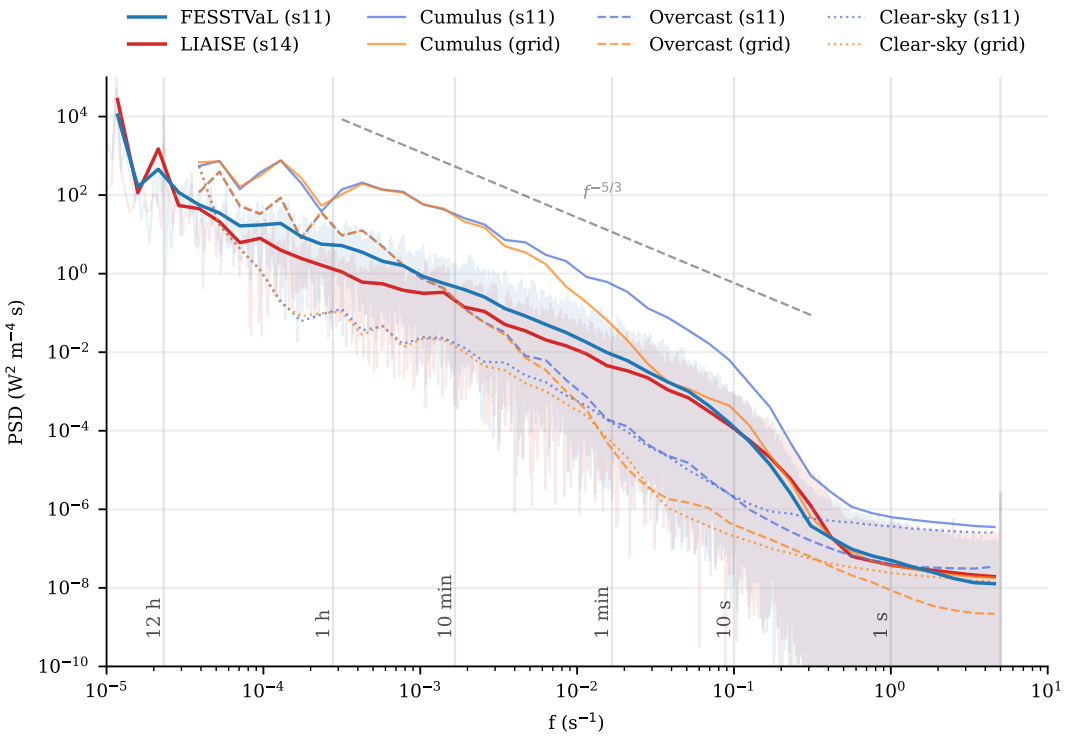

Figure 7.9: Power density spectra for global horizontal irradiance time series of the whole FESSTVaL and LIAISE campaigns. A cumulus (June 27), overcast (June 22), and clear-sky day (June 18) are illustrated separately for both a single sensor and the average of the Falkenberg grid.

7.3.3 Three types of patterns

Often during the campaign, a combination of cloud types are present with varying degrees of total cloud cover and optical thickness, for example a mix of cumulus (passive to deep convective), multiple layers of altocumulus, and/or cirrus. To demonstrate the diversity of observed surface irradiance variability during the campaigns, we select three cases. These selected cases are of cloud types that occur in isolation, making the interpretation easier, and are frequently present in the campaign period: 1) boundary level cumulus, 2) mid level altocumulus, and 3) high level cirrus, illustrated in Figure 7.10. The patterns are visualised using the technique explained in Section 7.2.4, and are robust to sensor exclusion tests (shown in Figures S7.4 and S7.5, for the first two cases).

The first case (Figure 7.10a-c) is from the same date as Figure 7.8 (June 27, 2021), and features slow-moving (4.5 ± 1 m s^{-1}) fair weather cumuli with cloud bases at $\sim$ 1750 m, and a relatively clean atmosphere (deep blue sky). Cloud enhancement to shadow transitions are very sharp, about 40 to 60 m as estimated from Figure 7.10b, making cumulus cloud shadows slightly smaller than their size with a length scale similar to what we found in Chapter 6 based on long-term time series. Diffuse irradiance does not vary significantly on the spatiotemporal scales of this example, suggesting the total light scattering off of clouds in this case has a very wide horizontal range without much contribution to the total enhancement from local forward scattering at transparent cloud edges. Around the smaller cloud fragments (11:00 to 11:05 UTC, bottom pattern in Figure 7.10b), we do observe an increases in cloud enhancement of $\sim$ 30 to 40 W m^{-2} (4 % of clear-sky), and overall the diffuse is lower after the passage (11:10 UTC) than before (10:50 UTC). We think the absence of diffuse peaks close to transitions in this case may be due to the relatively high cloud base, where forward scattering through cloud edges is spread out over a large surface area rather than more locally focused. However, the suntracker measurements are 1 minute averages, so it may miss local peaks in diffuse irradiance, and changes in the sources of scattered light (overall cloud field vs. local cloud edge) could coincidentally be counteracting. The contrast between cloud enhancement and shadow is large, approximately 750 W m^{-2}, or 80 % of clear-sky irradiance. Some of the artefacts arise from small biases between sensors, such as the horizontal stripes at 10:50 and 11:10 UTC, or likely changing cloud shape, such as the noisy pattern around 11:06 UTC. Section 7.4 introduces a few more cumulus passages of this case, including spectral effects, to further investigate what is going on.

The second case (Figure 7.10d-f) is of an altocumulus field at 5 km altitude (estimated using the ceilometer of Falkenberg), moving at 14.3 m s^{-1}, and under overall hazier conditions than the first case. Individual altocumulus clouds are about 1 to 5 times the area of the sensor network based on the distance between cloud enhancement peaks, whereas these peaks are up to $\sim$ 200 m in diameter and thus mostly fit within the network area. Apart from the spatial scales being significantly smaller than the cumulus case, the shadow patterns are weak (250 W m^{-2} or 35 % below clear-sky), and cloud enhancements very strong, locally more than 300 W m^{-2} or 40 % above clear-sky.

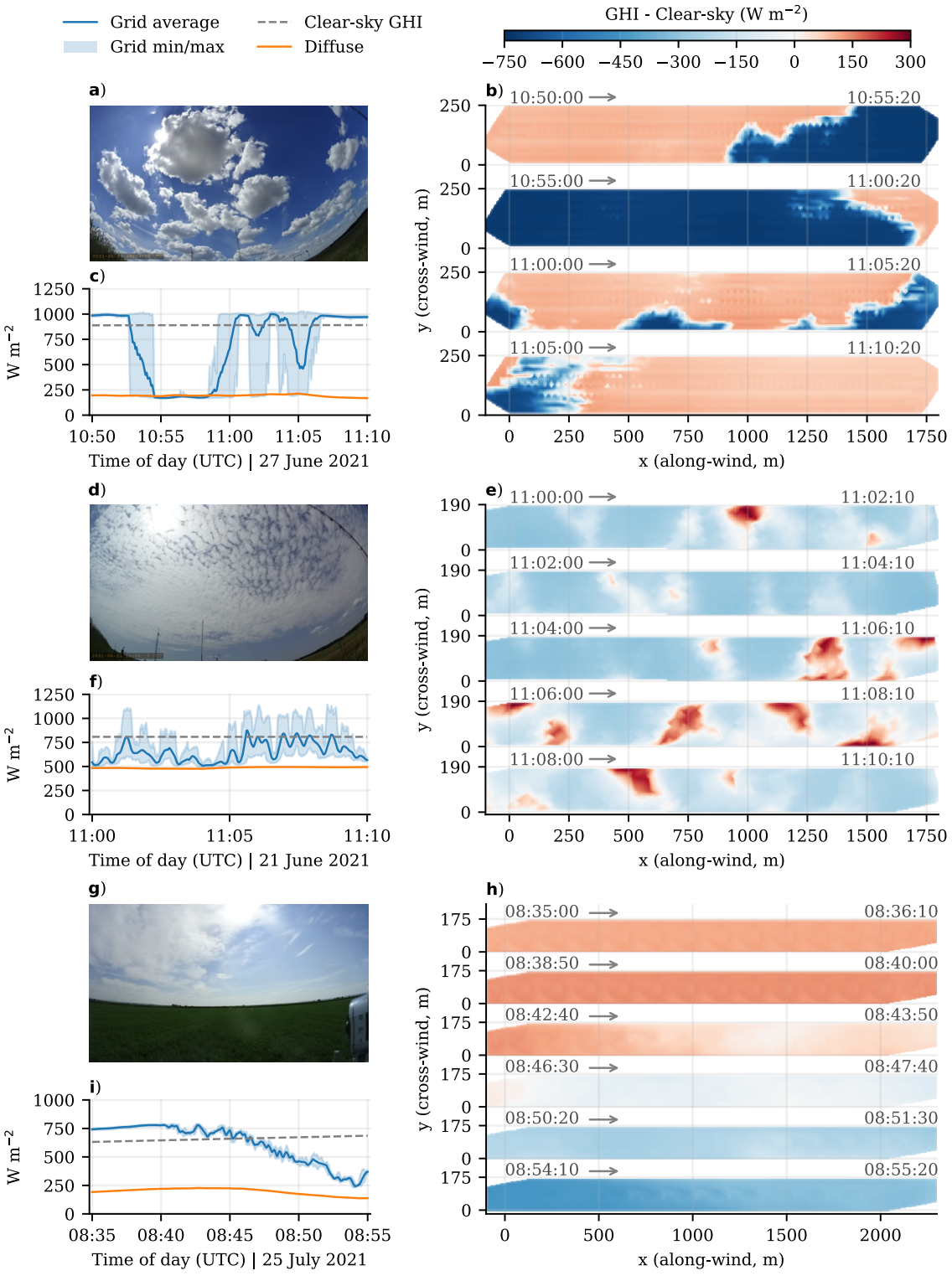

Figure 7.10: Spatial patterns of cloud enhancements and shadows for three cases: cumulus **(a-c)**, altocumulus **(d-f)**, and cirrus **(g-i)**. **(a, d, g)** show a representative photo. The time series include grid measurements (FROST network at $\Delta t = 1$ s), clear-sky GHI (CAMS McClear at $\Delta t = 60$ s), and diffuse irradiance (Falkenberg sun tracker **(c, f)** at $\Delta t = 60$ s or La Cendrosa energy balance station at $\Delta t = 5$ s **(i)**). Data in **(b, e, h)** are plotted relative to clear-sky irradiance. The temporal range of each pattern segment is labeled in HH:MM:SS on top.

The mechanism appears to be a consistently high diffuse irradiance (500 W m^{-2}, two-thirds of clear-sky) generated by forward scattering in the semi-transparent altocumulus field as a whole, with superimposed gaps in the clouds that let up to 650 W m^{-2} of direct irradiance locally pass through. These are thus particularly extreme variations at small spatiotemporal scales, with a similar relative magnitude (cloud shadow to enhancement contrast) to that of the previous example with cumulus clouds.

The third and last case (Figure 7.10g-i) is features an optically thick cirrus field moving over the LIAISE network setup at 35 m s^{-1} (July 25, 2021), and is notably different from the other two cases. Only weak spatial patterns of about 500 meters in length are visible in some parts of the cirrus (8:43 and 8:46 UTC for example, Figure 7.10h). Despite the high cloud velocity, it takes 15 minutes to go from a 120 W m^{-2} or 18 % of cloud enhancement (8:39 UTC) to a near complete blocking of direct irradiance (8:54 UTC). The area of influence of this patch of cirrus far exceeds the radiometer grid size, with the transition from cloud enhancement to shadow minimum covering 35 m s^{-1} $\times$ 900 s = 31.5 km.

7.3.4 Broadband patterns in summary

The scales of patterns caused by these three cloud types suggest errors made by radiative transfer models using the independent column approximation (i.e., without 3D radiative effects) will be apparent in all cases. This is not only true for the smaller scales of broken boundary layer clouds, but also for cirrus in coarser resolution medium range numerical weather prediction (e.g., ECMWF's IFS at $\sim 9\times9$ km^2). The characteristics of spatial surface irradiance patterns within the category of 'broken cloud', here extended beyond boundary layer clouds, is large. Altocumulus clouds appear to be particularly effective in generating small scale but large enhancements in surface irradiance (up to $\sim$ 200 m in diameter, 40 % above clear-sky). This effectiveness did not clearly show up in a multi-year analysis of cloud enhancements as function of cloud type (Chapter 6), possibly due to limitations of satellite resolution and pyranometer response time, but also Schade et al. (2007) identified altocumulus as very effective drivers of large peaks in surface solar irradiance. We therefore believe these (broken) mid and high level clouds are worth more attention given that their global occurrence is similar to that of cumulus (e.g. Sassen & Wang (2008)) and their (potential) effect on surface irradiance is large.

7.4 Spectral signature of cloud-driven irradiance patterns

7.4.1 Identifying changes in 'blue' versus 'red' light

Clear-sky conditions are famously characterised by blue skies (diffuse irradiance enriched in shorter wavelengths) and a yellow sun (direct irradiance depleted of those same wavelengths), owing to the λ^{-4} dependency of Rayleigh scattering. An example of this spectral signature is illustrated in Figure 7.1. As clouds interact with both components of irradiance, we expect to see changes in the ratio between short and long wavelengths in our surface measurements. Such changes can help point to where the irradiance originates from and help understand how a cloud field modifies surface irradiance. For example, if a single cumulus cloud in an otherwise clear sky blocks direct (blue-depleted) irradiance, we expect the spectrum of remaining light to have a larger share of short wavelengths relative to clear-sky conditions. In this section, we expand upon the three cases of Section 7.3 by analysing observed changes in the ratio of these short and long wavelengths, firstly to quantify spectral effects of clouds, and secondly to help further understand these cases.

Relating observed changes in short and long wavelengths to a different mix of clear-sky diffuse and direct sunlight means we assume no other factors influence the spectrum, and therefore requires scattering and absorbing of light by clouds to be constant with wavelength. This assumption holds for the visible (and most energetic) part of the solar spectrum (Ackerman & Stephens, 1987; O'Hirok & Gautier, 1998; Key et al., 2002; Schmidt et al., 2010), all other conditions kept equal (aerosol amount, spectral surface albedo, gas concentrations). An exception may be the effects of hygroscopic growth of aerosols in air with high relatively humidity, often found near cloud edges or recently dissipated clouds. Hygroscopic growth causes aerosols to scatter more despite constant aerosol amount, and more so for shorter wavelengths. This was found by Gristey et al. (2022), in cases of shallow cumuli, to be an important contribution to enhanced diffuse irradiance in cloud shadows from extra scattered light around the cloud. Given its wavelength dependence, it may in our analysis contribute to more 'blue' cloud shadows. This contribution is not within our ability to quantify in this study, but we take it into account when interpreting the results.

Ratio calculation

In order to quantify changes in the wavelength ratio, we need to choose a set of bands in FROST and determine a reference value for clear-sky conditions. For the observed ratio, we combine multiple bands of the radiometer to get a stronger signal, and further limit our choice by excluding bands of $\lambda < 485$ nm (too high crosstalk, Section 7.2.2) and $\lambda > 700$ nm (growing contribution of spectral effects of water). Specifically, we choose the bands λ_s = (485, 510, 530 nm) and λ_l = (645, 680, 705 nm) and define the ratio $r = \lambda_s/\lambda_l$ to represent 'blue' versus 'red' light. We define changes in r due to clouds as $\Delta r = r - r_{cs}$.

The clear-sky reference values r_{cs}, which depend on the solar zenith angle, can be derived in

two ways. One involves extrapolating an observed r at a time before clouds form to a later time with cloudy conditions, based on how r changes in a cloud-free day. The drawback of this method is that is requires at least some part of the day to be cloud-free, which is often not the case, and assumes changes in r with solar zenith angle in a cloud-free day to generalise to other days. Alternatively, we therefore also simulate clear-sky spectra for each analysed case (see Section 7.2.5), which provides independent estimates of r_{cs} and helps validate the first approach. For the cases of June 17 and 27, we can use both methods (with June 18 as the clear-sky observed reference), which shows that observed and modelled r in clear-sky conditions at 08:00 UTC are consistent. Furthermore, the modelled change in r between 08:00 and 11:30 UTC is nearly the same as in the observations of June 18 (+1.16 % and +1.05 %, respectively). For cases where we can not use the first approach (June 21, July 25), we test the sensitivity of modelled r_{cs} for June 18 by, somewhat dramatically, doubling the total column water vapour or excluding aerosols. This results in a change of +1.5 % and +1.2 %, respectively, so we deem the sensitivity to either factor to be small and therefore the simulated r_{cs} to be accurate enough for our purposes. An overview of all simulations and ratios calculated from them is given in Table S7.1.

Crosstalk correction

A caveat to estimating r using FROST is its crosstalk (Section 7.2.2). Under a flat spectrum, the crosstalks (ct) for the chosen bands are $ct_s \approx 45\,\%$, $ct_l \approx 14\,\%$ for λ_s, λ_l, respectively. Crosstalk is roughly halved for a more typical clear-sky spectrum (as in Figure 7.1). We can not a priori correct for crosstalk, because it would require knowing the spectrum of irradiance and how it changes, whereas this is what we want to measure and characterise. However, we can simulate how measured changes in r, Δr_m, relate to true changes Δr_t. Taking the clear-sky diffuse illustrated in Figure 7.1 and mixing in direct irradiance from 0 to 1.6 times the clear-sky value, we find a linear relationship $\Delta r_m = \gamma \Delta r_t$ and $\gamma \approx 0.5$, i.e., measured changes are underestimated due to crosstalk (Figure S7.6). Both observations by Durand et al. (2021) (their Figure 2) and a simulation with a homogeneous water cloud ('fval_j18_wc', Table S7.1) show that r would indeed decrease in overcast conditions compared to clear-sky, but that changes in the λ_{ct} range are insignificant. Furthermore, Figure 3.17 in Chapter 3 shows that the sensor version without crosstalk has qualitatively the same effect of overcast compared to clear conditions. We are therefore confident that the sign of change we observe is correct and that the magnitude of change is underestimated. Quantitative results will nonetheless be interpreted with caution. Because the measured spectral data are in raw sensors units, we apply a one-time calibration factor of 1.4, such that $r = 1.4 r_m$, based on consistent results from four simulated and measured clear-sky spectra.

7.4.2 A time series of spectral changes

Figure 7.11 shows how r varies in relation to multiple cloud shading and enhancement events of cumulus clouds on June 27 (FESSTVaL). The time series underlines that the fairly constant diffuse irradiance seen in the first case of cumulus is not representative of all cumulus passages, as most others show local distinctly enhanced diffuse irradiance. As for r, most notice-

able are the large shifts ($\Delta r_m \approx 0.3$) towards blue-enriched light in fully shaded conditions, e.g. at 09:26 or 10:13 UTC. Further away from transitions, e.g. 09:10 and 09:50 UTC, there is enhanced irradiance, but no clear deviations from estimated clear-sky ratios. Interestingly, every shading event is flanked by brief reductions in r, typically 0.01-0.02 below r_{cs}, for example at 09:19 and 09:32 UTC, just as the sun illuminates the local cloud edge as seen from the surface. Furthermore, it appears not every cloud enhancement has the same proportions of λ_s and λ_l, as there are different combinations of cloud enhancement magnitude and Δr_m (e.g. 09:19 vs 09:32 UTC).

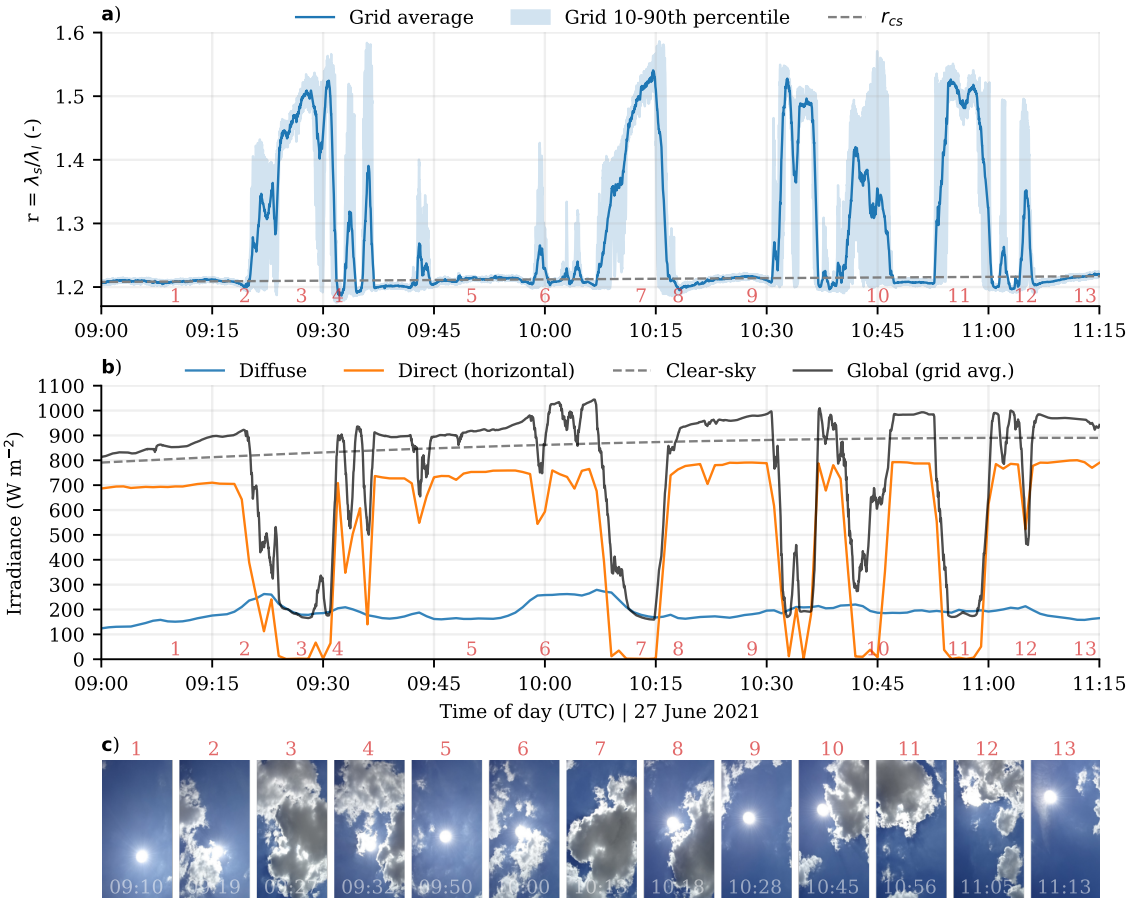

Figure 7.11: Time series of r as measured by the network at FESSTVaL on 27 June 2021 in **(a)**, combined with broadband irradiance to illustrate the total effect of cloud passages in **(b)**. Direct and diffuse irradiance are 1-minute averages of the Falkenberg suntracker, clear-sky is based on CAMS McClear. Global horizontal irradiance is 1 Hz data based on the mean values in the FROST network at Falkenberg. In **(c)**, cropped images of one of the cloud cameras are shown for 13 manually chosen points in the time series to illustrate degrees of direct light obstruction of cumulus clouds.

This puts some value to the idea that the lack of extra local irradiance enhancement around shadows observed in the first case of Section 7.3 is due to counteracting local and non-local scattering sources. We speculate that the horizontal distribution of light scattered off (or escaping from, Várnai & Davies (1999)) cloud sides is approximately a clear-sky mix of diffuse and direct light ($r = r_{cs}$, $\Delta r_m = 0$) and acts over a larger area further away from the cloud(s), whereas localised forward scattering right at cloud edges is mostly direct light with lower r ($\Delta r_m \approx$ -0.01 to -0.02). We will take a closer look at this phenomenon spatially using the cumulus, altocumulus, and cirrus cases of Section 7.3.

7.4.3 Spatial patterns of spectral changes

Figure 7.12 shows Δr_m, now expressed in percent-points, for the cumulus, altocumulus, and cirrus case, previously described in Section 7.3. Data is plotted relative to r_{cs}, partially estimated from observations and simulations for the cumulus case, or entirely from simulated spectra in the other two. The result is another diverse set of patterns, albeit more noisy than for broadband irradiance due to reduced signal strength.

Cumulus and mixing irradiance components

We first zoom in on four areas in the cumulus case (Figure 7.12a-c): 10:51, 10:56, 11:01, and 11:10 UTC. For the three enhanced areas, the shift in the middle one (11:01 UTC) is about twice as strong (Δr_m = -1.8 %) compared to before (10:51 UTC, Δr_m = -1.1 %) and after (11:10 UTC, Δr_m = -0.8 %), whereas the cloud enhancement in broadband irradiance only varies between 9 (11:10 UTC) and 12 % (10:51 UTC). In the shadow at 10:56 UTC, Δr_m = 30.4 %.

To help understand these numbers, we can hypothetically 'mix' different amounts of clear-sky diffuse and direct irradiance together and calculate the resulting Δr_m. Assuming all 170 W m^{-2} of irradiance in the shadow at 10:56 UTC comes from a clear-sky diffuse source, Δr would be 74.7 %. Adding 26 W m^{-2} of clear-sky direct irradiance to the simulated 144 W m^{-2} of clear-sky diffuse to match the observed 170 W m^{-2} of (non clear-sky) diffuse irradiance gives Δr = 60.0 %. If we first correct for a $\sim$ 25 % bias in the simulated clear-sky diffuse, based on observed clear-sky conditions at 08:00 UTC, and then add enough clear-sky direct irradiance to match observed values, we find Δr = 45.0 % . The first and last approximation are an under and over-estimation of the amount of blue-enriched irradiance in the shadow: the observed diffuse irradiance cannot be purely clear-sky diffuse given the presence of a scattering cloud field, nor would all of the enhanced diffuse relative to clear-sky originate from clear-sky direct irradiance alone. The middle estimate (60.0 %) is nearly the same value as Δr_m if we apply the crosstalk correction γ (60.8 %). It may be such a close match for the wrong reasons, but at least it represents a case where a significant portion of irradiance is coming from horizontally scattered direct or total irradiance mixed in with clear-sky diffuse.

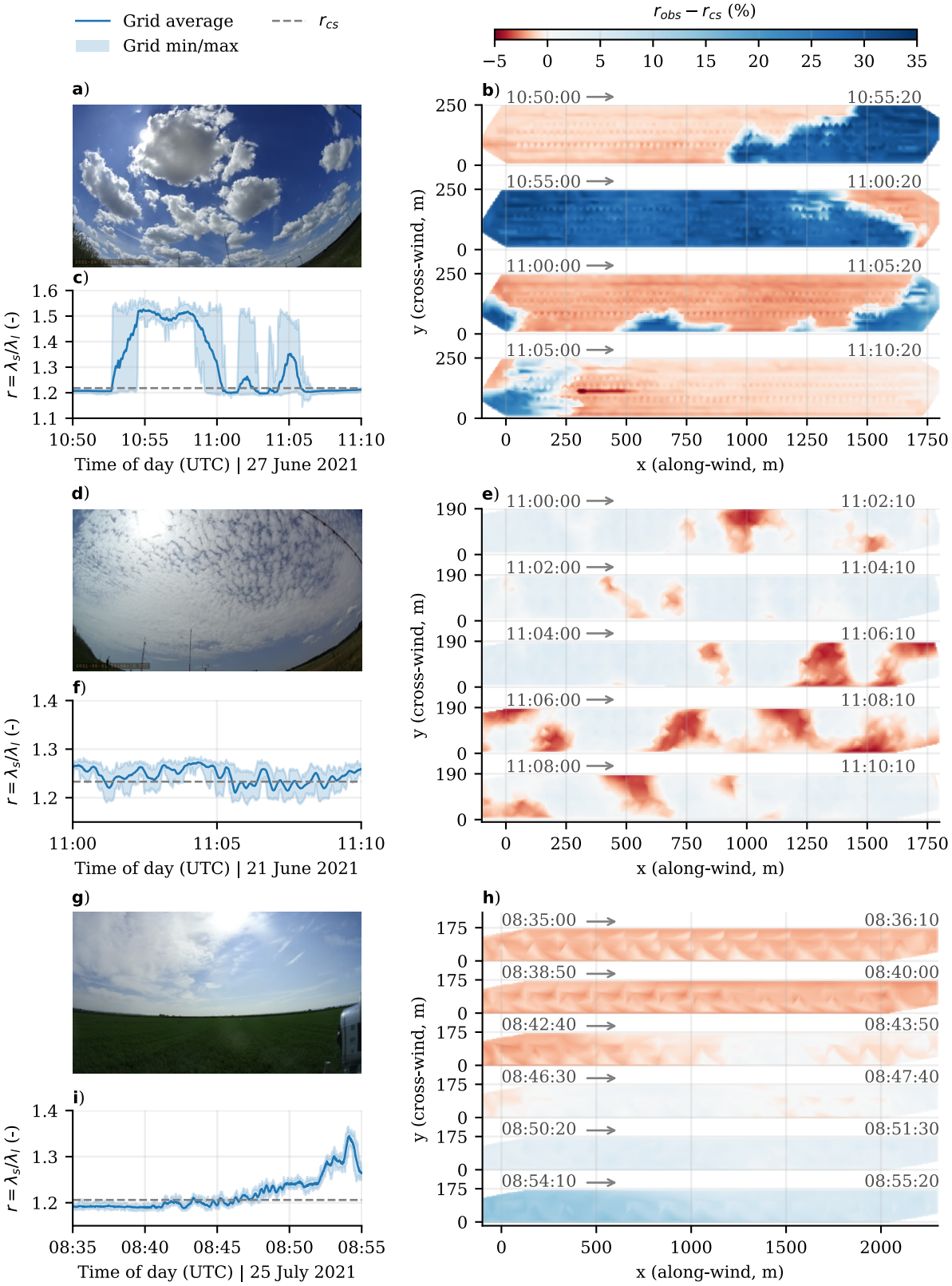

Figure 7.12: Spatial patterns of changes in r compared to clear-sky. Lower values indicate red-enrichment, higher values blue-enrichment. Values for r_{cs} are based on simulated clear-sky spectra. Note the asymmetric colormap scaling. Similar layout as Figure 7.10

Similarly, attributing all cloud enhancement to direct irradiance gives Δr = -2.8 % and -2.5 % for 10:51 and 11:10 UTC, an overestimation even after a γ correction, suggesting the extra irradiance is mix of spectral irradiance closer to that of clear-sky conditions. For 11:01 UTC, however, the estimate of Δr = -2.7 % more closely matches the observed Δr_m = -1.8 % (or $\gamma \Delta r_m \approx$ -3.6 %), and coincides with a higher degree of fragmented semi-transparent clouds that can effectively scatter direct irradiance forward. Alternatively, optically thick cumulus may also reduce r by blocking part of diffuse clear-sky irradiance, though we expect this to be of secondary importance and more non-local due to the approximately isotropic nature of diffuse irradiance. Hygroscopic growth of aerosols in regions near cloud edges may also contribute to subtle changes in r and make the regions near cloud edges more potent in forward scattering.

Another cumulus case with notably lower cloud cover, higher cloud base, and high apparent haziness (June 17 at FESSTVaL, not shown), has qualitatively similar patterns around cloud shadows, but perturbations Δr_m are significantly larger. Thus, an analysis beyond two cumulus case studies and controlling for cloud and aerosol optical properties is necessary before drawing more general conclusions.

Altocumulus and cirrus

The altocumulus (Figure 7.12d-f) and cirrus cases (Figure 7.12g-i) are more tricky to analyse, as here the clouds are all semi-transparent and at higher altitude, thus making assumptions about the origin of light and its spectral signature more questionable. The relative spread in r_m is also larger in both, for altocumulus because the patterns are similar to the network scale, and for the cirrus because it is earlier in the day with a weaker signal, visible in a noisier time series (Figure 7.12f) or pattern (Figure 7.12h). Values for Δr_m are nonetheless significant larger than the noise in both cases, and although the hypothetical mixing of clear-sky spectra will not help to identify the scattering mechanisms, they can put the numbers in context.

For the darkest shadow in the altocumulus case, at 11:04:15 UTC, Δr_m = 3.8 %. Assuming the increase of diffuse irradiance compared to clear-sky is all attributable to the clear-sky direct irradiance gives Δr = 8.8 %. This is an expected overestimation of blue-enrichment (even after a factor γ), given that direct irradiance is $>$ 0 W m^{-2}. For one of the stronger cloud enhancements (30.0 % at 11:05:40), Δr_m = -4.0 %. Attributing all enhancement to direct irradiance gives Δr = -4.0 %, likely an underestimation given the transparency of the altocumulus to direct irradiance, suggesting part of the strongly enhanced diffuse irradiance may be more enriched in λ_l. Averaged over the network, the differences between minima and maxima in r are small ($\approx$ 5 %), about 6 to 7 times smaller than those of the cumulus case.

Lastly, for the cirrus case the cloud enhancement is 20.9 % at 08:39 UTC, with Δr_m -1.5 %. Assuming all enhancement is from clear-sky direct irradiance gives Δr = -4.6 %, resulting this time in a clear overestimation compared to what is measured. For the partially shaded area at 08:50 UTC we find Δr_m = 3.1 %, and attributing the increase in observed diffuse to clear-

sky direct irradiance gives $\Delta r = 6.3\,\% \approx \gamma \Delta r_m$. This matches, except it does not account for the fact that over half of the observed irradiance is of a direct origin (Figure 7.10g). The most optically thick part of the cirrus at 08:54 UTC causes a significant shift towards shorter wavelengths as this contribution of direct irradiance reduces. Qualitative behaviour of cirrus, at least in this case, is thus the same: cloud enhancements are characterised by reductions in r, and (partial) shadings by increases. Variations in r for this cirrus case are in between those of the cumulus and altocumulus ($\approx 15\,\%$), with the spatiotemporal scale two orders of magnitude larger.

7.4.4 Spectral patterns in summary

In all presented cases, both the cloud enhancement and shadow patterns show significant deviations from clear-sky spectral irradiance, which are particularly large in magnitude and spatiotemporal scale for the cumulus clouds. The fact various combinations of diffuse and direct irradiance can create cloud enhancements of the same magnitude is well known (e.g. Gueymard (2017)), and so is the fact clouds have spectral effects (e.g. O'Hirok et al. (2000)). What we demonstrated in this section highlights that there are variations in part of the spectrum linked to where irradiance originates from, in a situation where otherwise the optical properties, on the scale of these variations, are mostly wavelength-independent. In particular, the spectral signature of low and optically thick cumulus passages give some weight to our speculation that various light scattering mechanisms affect different areas relative to the cloud.

7.5 Temporal patterns driven by water vapour variability

One other significant spectral signature is that of water vapour. In this section, we will look at two examples of variability in atmospheric moisture as measured by the FROST network at FESSTVaL and LIAISE. These examples have a scope that is more towards regional scale (campaign area) land-atmosphere coupling and atmospheric dynamics under clear-sky conditions, rather than cloud-driven irradiance variability. The variations in water vapour are not large enough to affect broadband irradiance in the way clouds do, but they may help explain observed variations in GHI in clear-sky conditions.

7.5.1 Deriving total column water vapour

Total column water vapour (TCWV) in the atmosphere is indirectly measurable using water vapour absorption bands, where heightened levels of water vapour result in significantly reduced signal within absorption bands compared to other wavelengths. Figure 7.1 highlights two of such bands for water, at 940 and 1130 nm. A strong absorption band is captured by the 940 nm channel of FROST, which in theory means we are able to detect changes in atmospheric moisture when comparing the 940 nm signal to a reference band outside the absorption band. Choosing a reference channel is limited by some sensor design and performance limitations. The cosine response varies between the three subgroups, such that changes in the ratio between two channels (e.g. 940 vs. 860 nm) are partially a result of instrument imperfections (see also Section 7.2.2) rather than changes in absorption strength. The choice of suitable channels is further limited by crosstalk at the shorter wavelengths of the subsensor with 940 nm, making the 900 and 940 nm channels the best options, despite 900 nm also partially being in a (weak) absorption band. Figure 7.13 illustrates the signal at 900 and 940 nm, where early in the day the ratio under clear-sky conditions is lower (more absorption) than noon due to the longer path length of irradiance. Shading from (semi-transparent) cumuli also gives distinct absorption signals, though seemingly only for the most optically thick cumulus passages in this example. This might be due to the change in diffuse/direct partitioning, with a longer path length and thus absorption of diffuse irradiance, but any stronger statement requires a more careful analysis. But this underlines why only clear-sky conditions are suitable for estimating TCWV, as we currently can not separate the effect of liquid water (or ice) from that of water vapour. One more limitation is the signal strength for the individual bands being low compared to the signal of water vapour variations, even at high solar elevation angles. For a clear signal we therefore take a moving average of 120 seconds or more, thereby effectively reducing the temporal resolution. In a new version of FROST, the crosstalk and weak signal issues have been addressed.

In Figure 7.14a we show we can derive an absorption signal that is highly correlated to accurate reference measurements of TCWV. Higher values in the 940 nm / 900 nm ratio indicate less TCWV, so by flipping the y-axis this correlation (r^2 = 0.75) is more clearly visible. The reference TCWV measurement comes from a co-located microwave radiometer

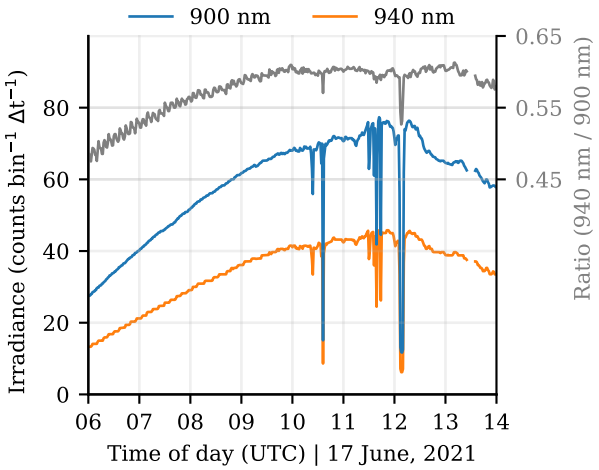

Figure 7.13: Spectral signature of water vapour measured by the 900 and 940 nm bands of FROST. The time series shows part of a daily cycle for a single sensor in the Falkenberg network, which is clear-sky until 10 UTC, but features brief cumulus passages thereafter. The ratio of the 940 nm / 900 nm bands is shown in grey on the right axis.

(Löhnert et al., 2022), with a 5 minute moving average applied to both time series to get a comparable signal. The microwave radiometer measures along a single straight vertical path (Figure S7.7a), but the signal our sensors measure is a function of the path that light travels through the atmosphere, mostly from direct irradiance (Figure 7.2a). For fitting a model to the data we therefore include the atmospheric mass fraction (AMF), i.e. the path length light travels through the atmosphere given a solar elevation angle α. This also means that the light our instruments measure has a horizontal footprint of several kilometres, whereas the microwave radiometer is a vertical integral measurement at one fixed horizontal point. Furthermore, under clear-sky conditions, diffuse irradiance still typically constitutes about 10 to 30% of GHI (see Figure S7.1), and would have travelled a longer distance through the atmosphere (by definition, as it is scattered light compared to direct light). This effect is implicitly taken into account, as the diffuse fraction is also a function of solar elevation angle, and thus the atmospheric mass fraction. We expect some bias in our model fit for extremely clear or hazy days, but we have no clear signal or quantification of its effect within our observational dataset.

The relationship between TCWV, AMF, and measured water vapour absorption (WVA) is captured by a function of the form $f(x, y) = a\,x + b + c\,y^2 + d\,y + e\,x\,y$, where x = WVA and y = AMF. Figure 7.14b illustrates the best fit of this model, based on 30-minute averages of all available clear-sky data during FESSTVaL for sensor 11 at Falkenberg compared to the microwave radiometer. Measurement uncertainties are based on the standard deviation within the 30-minute windows.

Since there is a limitation to the accuracy of the spectra from sensor to sensor and within sensors (Section 7.2.2), we find no gain by training the model from data of all sensors together, or calibrating sensors individually as we do for GHI, likely to due over-fitting. Instead, we

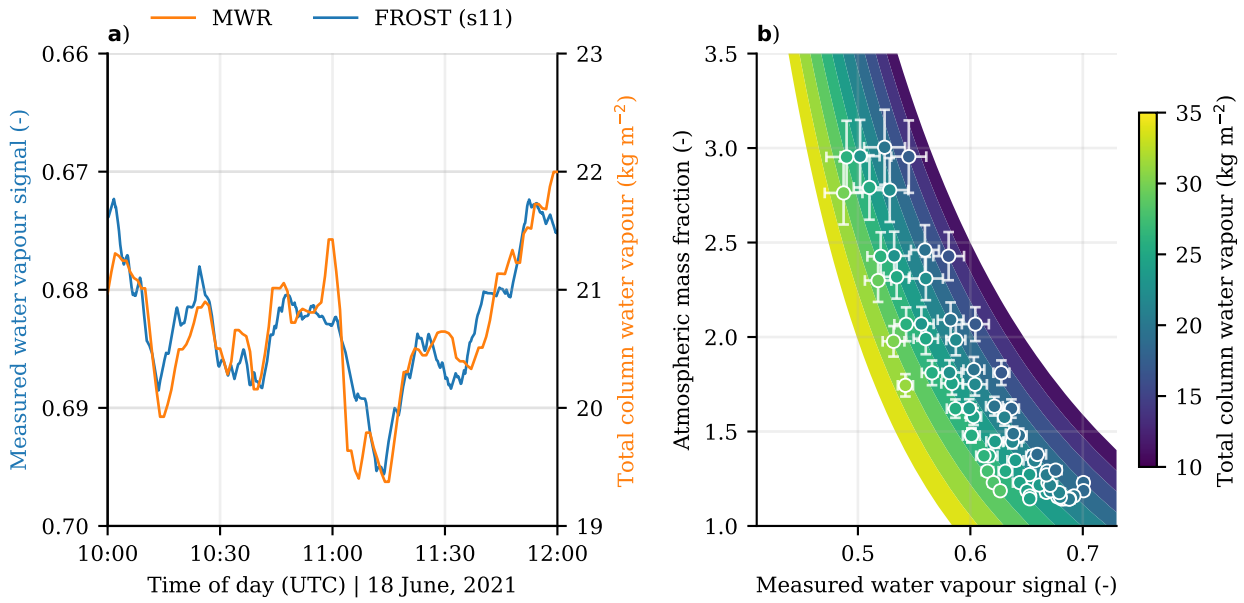

Figure 7.14: Total column water vapour (TCWV) derived from the radiometer water vapour signal. In **(a)**, an example time series of the signal (940 / 900 nm band ratio) compared to TCWV from the microwave radiometer (Löhnert et al., 2022) is shown for June 18 at Falkenberg (FESST-VaL). In **(b)**, the scatters represent 30-minute averages and standard deviations of the measured water vapour signal and atmospheric mass fraction, coloured by the TCWV from the microwave radiometer. The results from the model best-fit are shown in the curved shading.

apply the best fit based on sensor 11 at FESSTVaL, and use the uncertainty in the ratio between spectral bands as an error estimation. Similar to broadband irradiance estimates, one could fine-tune the calibration on a case-specific basis if a high quality reference is available. We estimate uncertainty by taking the standard deviation between all sensors in a network, which results in $\pm$ 0.5 kg m^{-2} for sufficiently high solar elevation angles ($\alpha > 30^{o}$), and increases towards sunset and sunrise.

7.5.2 Sub-mesoscale water vapour variability at FESSTVaL

June 18 at FESSTVaL was a clear-sky, warm summer day (maximum 2 m temperature of 31 °C). There are intra-hourly variations in TCWV of 1-3 kg m^{-2}, as illustrated in Figure 7.15 for various locations within the larger campaign area (Figure 7.3b). With a predominantly southerly wind of $\approx$ 9 m s^{-1} average over the lower troposphere, we tried to track moisture patterns across a 10 km south-north transect in the FESSTVaL domain (Figure 7.3b), south of Falkenberg to Lindenberg, at a 10 and 20 minute time lag respectively. The southern and Falkenberg measurements are based on the TCWV derived from our instruments, with at Falkenberg and Lindenberg two high quality measurements taken from the microwave radiometers. While our instruments and the microwave radiometers at Falkenberg are in agreement on the local variations (despite a bias of $\sim$ 0.5 kg m^{-2}), there appears to be no correlation between the southern (s23) and northern (Lindenberg) location (Figure 7.15).

We therefore think that the temporal variability in TCWV is more locally driven by turbulence structures in the convective boundary layer rather than the advection of (sub)-mesoscale horizontal patterns in moisture. In support of this, observed variations in GHI relative to clear-sky at Falkenberg show an anti-correlation with TCWV (r = -0.79), where +1 mm TCWV $\simeq$ -1 % GHI (Figure 7.15). These changes in GHI can not be explained by the direct effect of TCWV variations alone, which would be closer to -0.1 % GHI for +1 mm of water vapour, and might instead point to buoyant plumes in the boundary layer that carry extra aerosols from the surface. The more subtle differences in variability between FROST and microwave radiometer based measurements may be explained by the different footprint of FROST sampling different moisture structures, given its horizontal component in the diagonal cross-section through the atmosphere (Figure 7.2a).

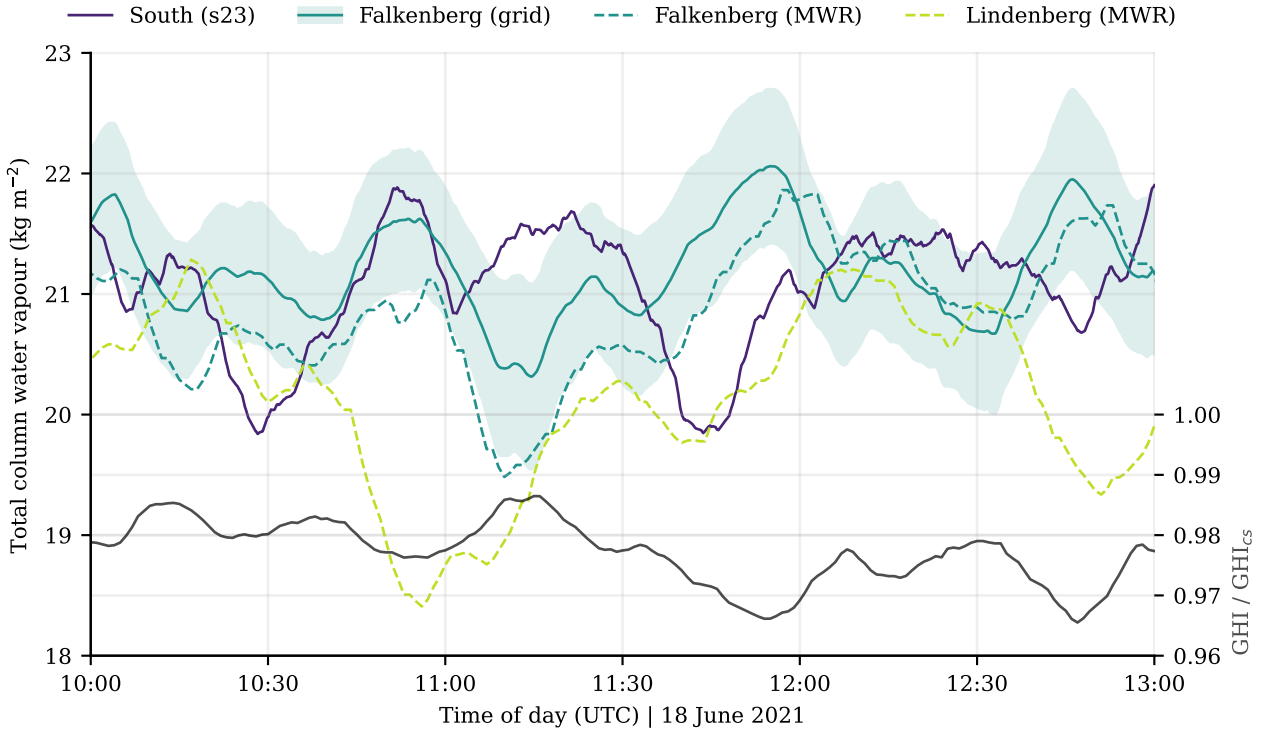

Figure 7.15: Time series of total column water vapour (TCWV) from a south to north transact in the FESSTVaL campaign area. FROST-derived TCWV is compared to high quality microwave radiometer measurements, both resampled to 10 minute moving averages. The shading is the FROST grid standard deviation. The south to north transact (south - Falkenberg - Lindenberg) is approximately 10 km, with Falkenberg in the middle (see also Figure 7.3b), and the wind is $\approx$ 10 m s^{-1} from the south. The black line is the Falkenberg global horizontal irradiance relative to clear-sky, also with a 10 minute moving average.

7.5.3 Variability in water vapour at LIAISE

During the LIAISE campaign, most days were clear-sky (Figure 7.4), which gives ample data to study intra-day variability in atmospheric moisture. The campaign area is characterized by complex meteorology due to a combination of topography, strong heterogeneity in sur-

face fluxes at various scales due to irrigation (Bowen ratio between 0.01 and 30, Mangan et al. (2023)), and late afternoon south-eastern sea breeze dynamics with varying timing and strength. This collection of complex factors affecting local weather is not captured by high resolution weather models, and even less so by the one ERA5 grid cell covering the campaign area. Measuring TCWV helps to identify internal boundary layers and moisture plumes at the local scale to synoptic scale advection, that both contribute to variability. We apply the best fit derived from FESSTVaL (Figure 7.14) to the sensor network at the irrigated La Cendrosa site. Figure 7.16 shows the resulting time series for four (clear-sky) IOP days compared against ERA5 and hourly radiosondes, using a 3 minute moving average to get a clear signal. FROST-derived TCWV time series and soundings do not at all agree with the magnitude and trends of ERA5, which highlights the difficulty (coarse) models have with the complex meteorology in the LIAISE domain. Radiosondes and our spectrally derived TCWV time series are in much better agreement overall, and provides a good validation of our calibration methodology. Derivation of TCWV from radiosondes is precarious, though, since the hourly boundary layer radiosondes at La Cendrosa (Price, 2023) only reach to about 1.5 - 4 km and need to be supplemented with hourly tropospheric radiosondes from Els Plans (Canut & Garrouste, 2022), a non-irrigated location 14.1 km to the south-east. The atmospheric conditions in Els Plans and La Cendrosa converge above their respective local boundary layers to a regional atmospheric profile, described by a blending height of approximately 1.5 km (Mangan et al., 2023). For each sounding in La Cendrosa, we supplement its information with the mid to upper tropospheric data gathered from the closest (in time) Els Plans sounding (schematically illustrated in Figure S7.7b). Timing and footprint differences between instantaneous spectrum-derived TCWV and hourly combined soundings are, we believe, the main reason for differences between their measurements.

In terms of variability, there seem to be multiple time scales at play. On hourly time scales, trends in TCWV can be up to 5 kg m^{-2} h^{-1}, whereas at the minute time scales the constant fluctuations do not exceed 1 kg m^{-2}. The latter we believe to be driven by moist boundary layer thermals and subsequent dry air entrainment. Daily cycles of boundary layer drying through local advection (Mangan et al., 2023) and synoptic scale advection of air masses (captured by ERA5) respectively explain the multi-hour and day to day variations.

To explain the sub-hourly variability in water vapour, we correlate variability of measured specific humidity at 45 meters (q_{45m}) in the well mixed boundary layer to variation in TCWV. Both time series are re-sampled to a common resolution of 2 minutes, the lowest we can go with our TCWV measurements for a usable signal to noise ratio. To exclude hourly or daily trends, we define variations in TCWV or q_{45m} as the deviations with respect to their 60 minute centred moving average. The boundary layer contains a significant portion of the total vertical moisture, but we find the resulting correlation between variations at q_{45m} and the TCWV to be very weak, with an r^2 of 0.17. Rather, the TCWV from FROST has larger scale variations due to its diagonal cross-sectional footprint through turbulence structures in the whole boundary layer, as compared to a single point measurement close to the surface. For an illustration of this difference, and the poor correlation between the two time series, please refer to Figure S7.8.

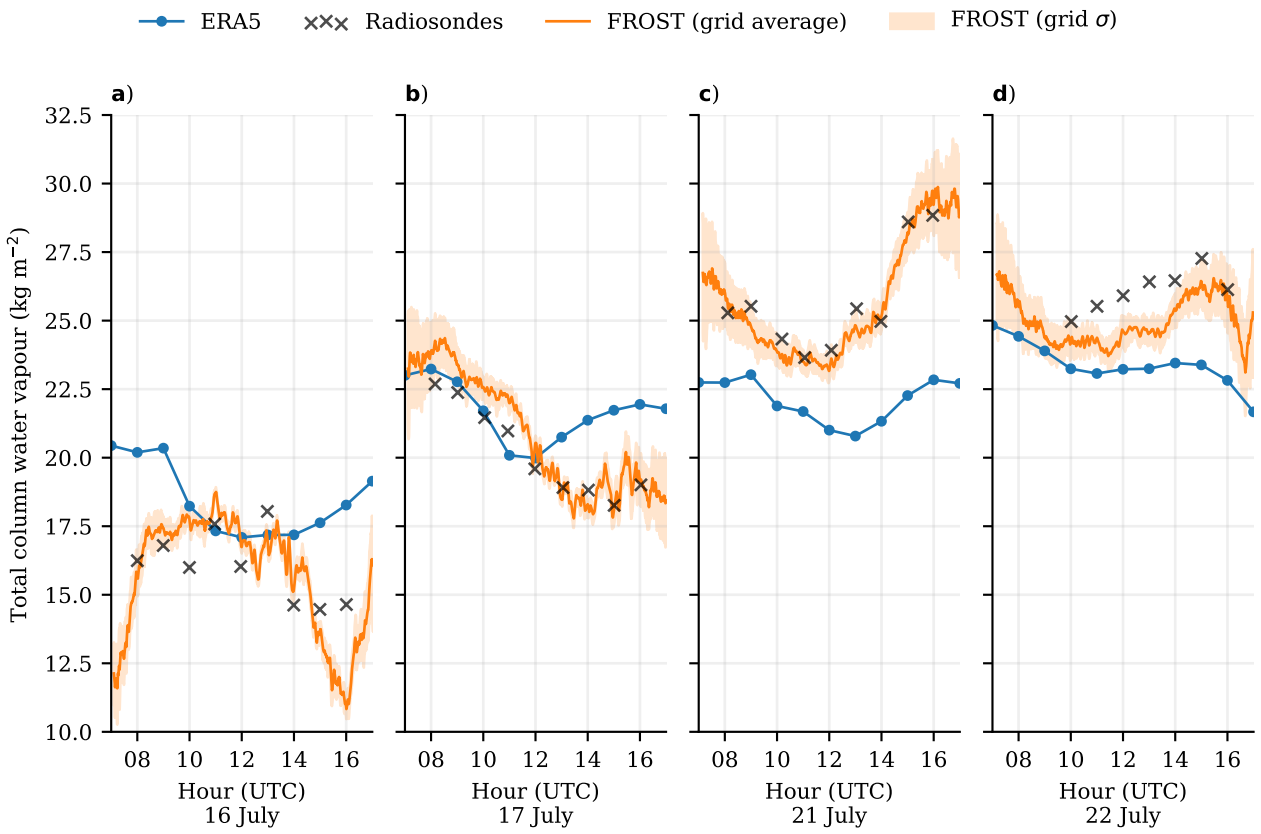

Figure 7.16: Time series of total column water vapour (TCWV) at La Cendrosa during LIAISE. Irradiance based measurements are compared to ERA5 (interpolated to La Cendrosa), and hourly soundings of La Cendrosa combined with Els Plans. The uncertainty range of the FROST measurements is the standard deviation among sensors in the network. The four dates are ideal clear-sky days and official Intensive Observation Periods.

In summary, we find FROST is able to capture moisture variability that is representative for the kilometre scale and above, rather than at individual field level. In an newer version of FROST, we have an improved signal to noise ratio and thus require shorter time averaging, which may enable the ability to capture variations at shorter time scales than 2 minutes. This could offer a flexible, low-cost alternative to a microwave radiometer or soundings, if absolute accuracy is of lesser importance.

7.6 Conclusions and outlook

Using low-cost radiometers calibrated against high-quality reference stations, we have gathered two high-resolution and spectrally resolved datasets of surface solar irradiance at cloud-scale. In combination with supplementary observations and simulations, such as cloud cameras at FESSTVaL, soundings at LIAISE, and simulated clear-sky spectra, we have derived insights into spatial patterns of surface irradiance caused by three types of clouds and by cloud-free atmospheric moisture variability. This work demonstrates how low-cost instru-

ments can provide accurate and detailed spatial measurements, making them an effective addition to field campaigns. This is particularly the case for campaigns in areas where deployment of expensive, heavy, and high-maintenance equipment is difficult.

We have analysed cases of boundary layer cumulus, mid level altocumulus, and high level cirrus. All three of the cases have distinctly different surface irradiance patterns, spatial scales of variability (50 m to 30 km), cloud types, direct/diffuse partitioning, spectral irradiance, and mechanisms through which these patterns are formed. The contribution of individual scattering mechanisms to the total variability remains difficult to quantify, due to the complexity of real-world measurements. However, by comparing changes between visible blue and red wavelengths, we think the enhanced irradiance next to the shadow of a cumulus has a large contribution of forward-scattered light from the local cloud edge. This contrasts with further away from a shadow, where the enhanced radiation originates mostly from the sides of cloud in the overall cloud field. For the mid and high level cloud cases, conditions of reduced irradiance are more blue and enhanced irradiance more red compared to clear-sky, similar to cumulus. However, the cause of changes in spectral irradiance in these cases is inconclusive in our analysis. The calculations we do to explain the changes don't quantitatively match the observations, probably because the assumptions underlying this method break down for higher altitude clouds.

None of the three commonly occurring cases we have discuss are well-represented by state-of-the-art numerical weather prediction, nor by most cloud-resolving models in academic setups, due to simplifications in radiative transfer calculations. In particular altocumulus appears to be potent in creating strong, localised peaks, and may be underrepresented in the field of 3D radiative transfer research. We have only focused on cloud cases that occur in isolation, to make interpretation easier, but often clouds of varying type occur simultaneously and the effects may not simply be additive. This proves a real challenge in both observational and modelling studies.

We are also able to capture variability in the irradiance spectrum that arises from significant changes in atmospheric water vapour in clear-sky conditions, despite some limitations on sensor quality for spectral irradiance. These local variations are often larger than synoptic scale moisture advection, but correlate with variations in GHI in the order of a percent, and thus illustrate heterogeneity in moisture fluxes and optical properties of a cloud-free boundary layer.

The presented datasets provide observations of cloud- and moisture-driven irradiance variability that can guide the development of radiative transfer variability parameterisations. The datasets can furthermore help constrain the input for land-surface, photosynthesis, or dynamic vegetation models that are currently driven by incorrect (spectral) irradiance distributions. A more comprehensive understanding of cloud-driven irradiance variability will, however, require analyses of many more clouds and irradiance patterns in datasets such as these. We believe the analyses of complex real-world data can improved by using idealised cloud resolving models with 3D radiative transfer to quantitatively characterise mechanisms.

7.7 Open data

All data measured with FROST sensors at FESSTVaL and LIAISE are published open-access datasets. These include ready to use calibrated quality controlled data and the raw instrument data, which requires pyranometer calibration references:

- Radiometer data FESSTVaL (Mol et al., 2023a): https://doi.org/10.25592/uhhfdm.10272
- Radiometer data LIAISE (Mol et al., 2023b): https://doi.org/10.5281/zenodo.7966437

The code for calibration of raw data and analyses presented in this work, the video of Section 7.3.2, and the libRadtran input files, are available at https://zenodo.org/records/10159129. La Cendrosa solar irradiance is not yet available at the time of writing, but will be available on the LIAISE database: https://liaise.aeris-data.fr/page-catalogue/?uuid=d9608a55-b836-427b-a186-e007462012b9.

Supporting information

S7.1 Sensor calibration

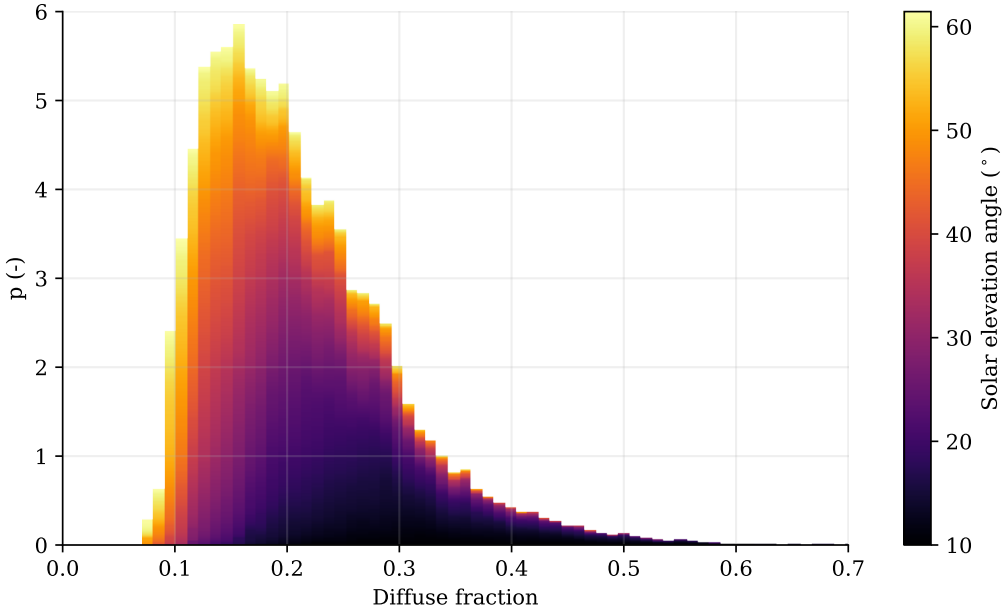

Figure S7.1: Observed diffuse fraction during clear-sky conditions for BSRN Cabauw 1 Hz dataset (Chapter 2), as function of solar elevation angle. 2011-2022 average. Clear-sky defined as in the dataset.

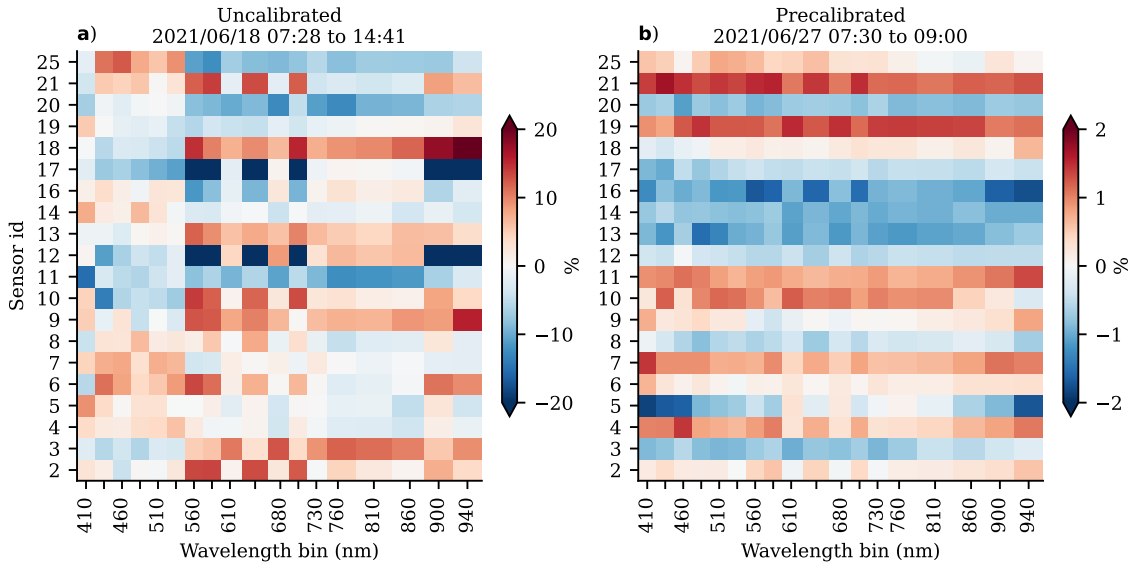

Figure S7.2: Improving the factory calibration of FROST spectra. Factory calibrated wavelength spread among sensors shown in **(a)**, as the deviation from the mean value per wavelength of all sensors. Improved calibration coefficients are derived from the training data (June 18, 7:28 to 14:48 UTC) in **(a)**. The application to test data (June 27 data 7:30 - 9:00 UTC) is shown in **(b)**. Both training and test data are under clear-sky conditions with a solar elevation angle above 40 degrees, at FESSTVaL. Note the values in **(b)** are an order of magnitude smaller.

S7.2 Constructing spatial patterns from temporal data

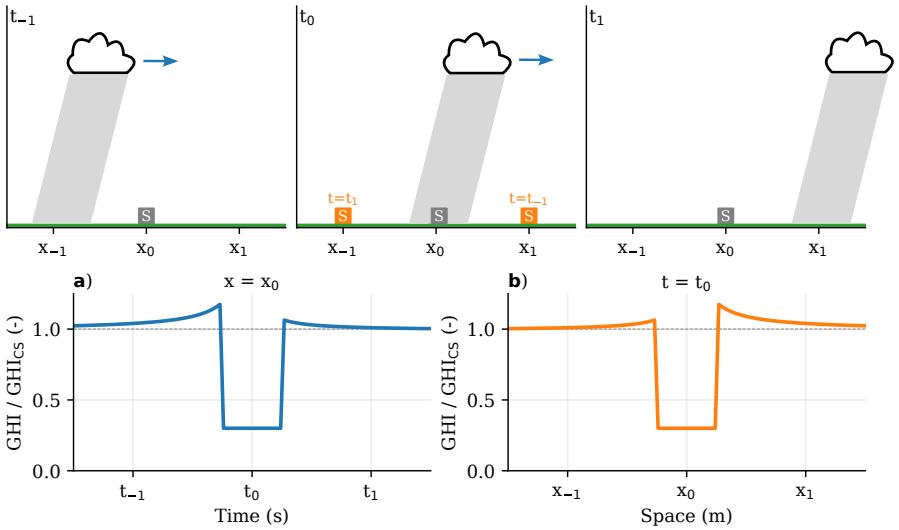

Figure S7.3: Schematic illustration of a 1D translation from a single point time series (a) to a spatial pattern (b), assuming the cloud velocity is known and the cloud's shape is constant in time. At t_0, a sensor is underneath a cloud shadow, preceded by cloud enhancement at the front side of the cloud at t_{-1}, and followed up by a (weaker) cloud enhancement after the passage at t_1. The asymmetry in enhancement is commonly, but not always, seen in reality, and used here for illustrative purposes. The reconstructed spatial pattern in **(b)** has effectively transformed a single point measurement into a three point measurement (x_{-1}, x_0, x_1) using the temporal information.

S7.3 Clear-sky spectra simulations

We use libRadtran (Emde et al., 2016) for clear-sky irradiance spectra modelling to support the interpretation of spectral measurements. Table S7.1 contains an overview of all simulations, validation if possible, and $\lambda_{s,l}$ values. Runfiles (.INP) are included in `https://zenodo.org/records/10159129`. Most settings are kept to standard values, or modified where it is straightforward to do so. Since integrated water vapour has an influence on the ratio λ_s/λ_l, as evident from the 'fval_j18_moist' where we double the observed value, we prescribe these values directly derived from a co-located microwave radiometer (FESSTVaL) or sounding data (LIAISE). Surface albedo is set to the IGBP library type 12 'cropland'. These two parameter changes resulted in simulations very close to observed GHI values, albeit with consistently too much diffuse irradiance. Prescribed standard aerosols is likely the main cause, and deviations from the standard mid-latitude summer atmosphere as a second factor. Turning off aerosols or doubling integrated water vapour leads to larger errors.

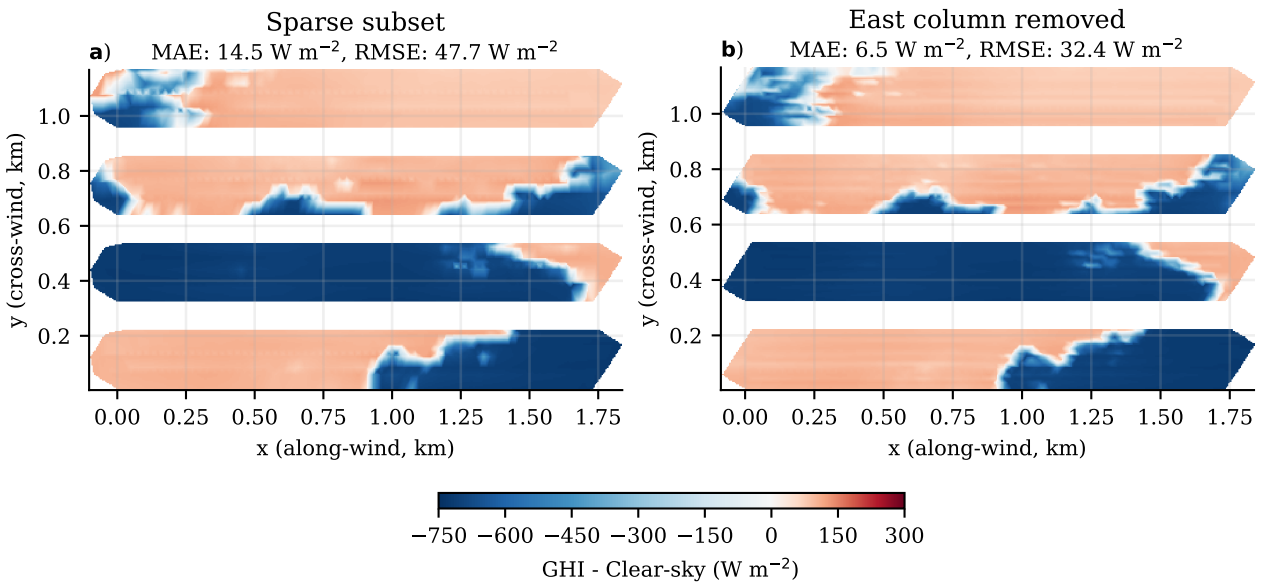

Figure S7.4: Same as the first case as Figure 10a, but with **(a)** every other sensor removed (all even numbers), or **(b)** the eastern column removed. All other settings unchanged. Mean absolute error (MAE) and root mean square error (RMSE) are calculated with respect to the full dataset.

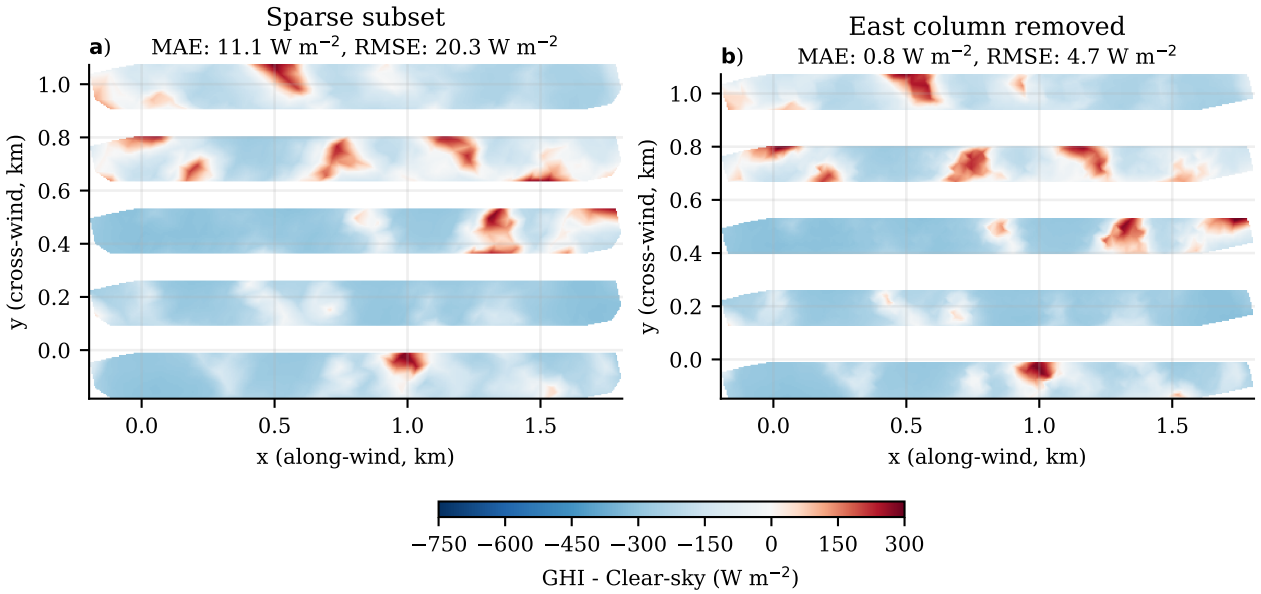

Figure S7.5: Similar to Figure S7.4, but for the second case.

Table S7.1: Overview of all model simulations with libRadtran for FESSTVaL (fval) and LIAISE cases. Compared to the baseline 'fval_j18' simulation, '_no_aero' has aerosols disabled and '_wc' has an additional default water cloud. Numbers in the run name indicate day of the month June for FESSTVaL, July for LIAISE. GHI is global horizontal irradiance, DIF is the diffuse irradiance. Numbers in brackets for GHI and DIF are observed values from a reference station, only in available in clear-sky conditions. $\lambda_{s,l}$ are the mean spectral irradiances for two chosen bands as described in Section 4 in W m^{-2} nm^{-1}, and r their ratio.

Case name	Time (UTC)	IWV (mm)	GHI (W m^{-2})	DIF (W m^{-2})	λ_s	λ_l	r
'fval_j18_morn'	08:00	19	690 (684)	131 (99)	1.116	0.927	1.204
'fval_j18'	11:30	20.5	884 (873)	144 (116)	1.435	1.178	1.218
'fval_j18_no_aero'	11:30	20.5	905	53	1.484	1.203	1.233
'fval_j18_moist'	11:30	41	856	147	1.445	1.169	1.236
'fval_j18_wc'	11:30	20.5	145	145	0.263	0.218	1.207
'fval_j17_morn'	08:00	25	680 (673)	130 (120)	1.117	0.923	1.209
'fval_j17'	11:30	24	877	143	1.435	1.175	1.221
'fval_j27_morn'	08:00	19	684 (678)	131 (103)	1.106	0.920	1.203
'fval_j27_11utc'	11:00	18.5	889	144	1.438	1.181	1.217
'fval_j27'	11:30	17	891	144	1.433	1.179	1.215
'fval_j21_11utc'	11:00	24	863	146	1.448	1.174	1.233
'liaise_j25'	08:45	23	658	129	1.074	0.891	1.206

S7.4 Simulated sensitivity to crosstalk

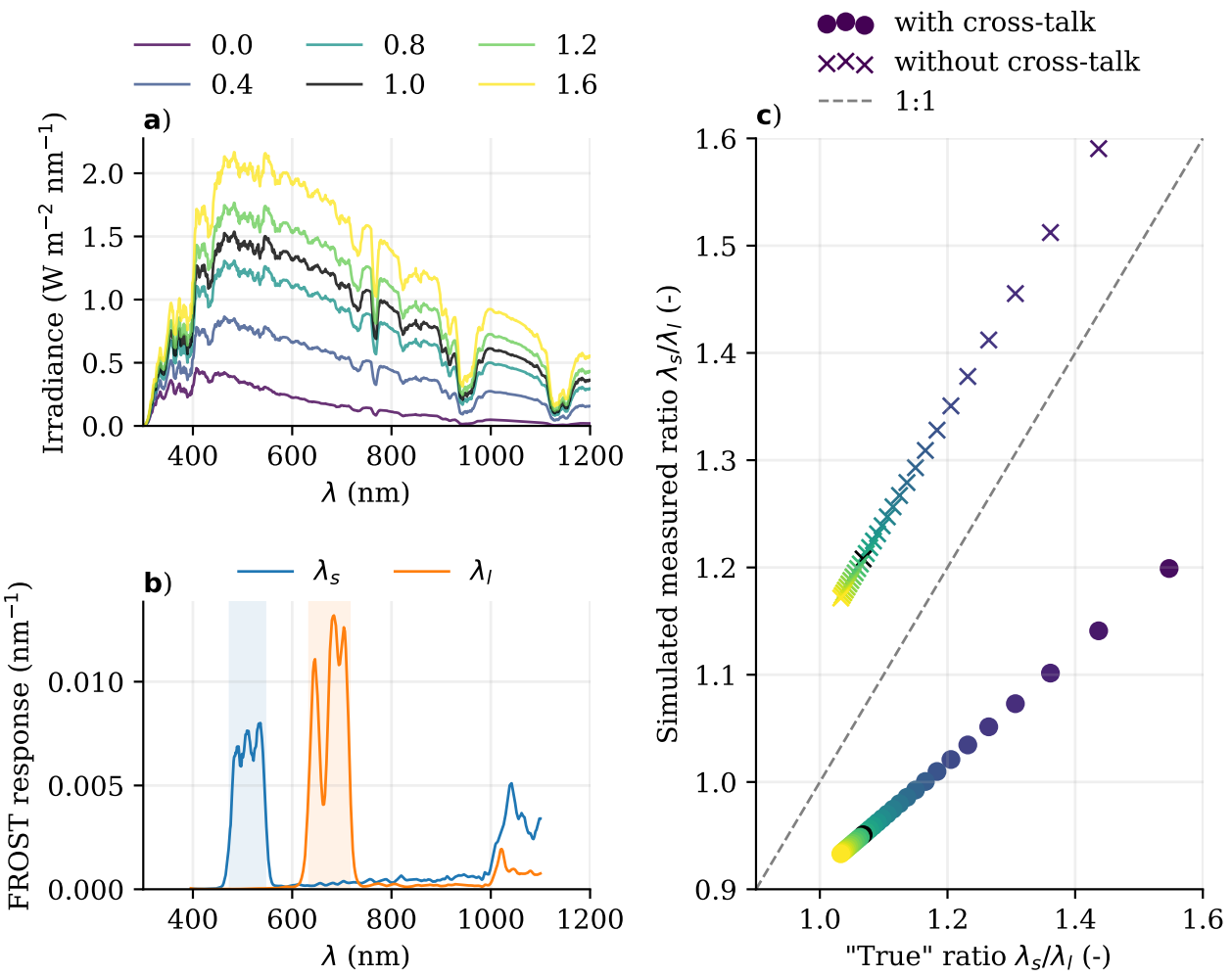

Figure S7.6: Simulated effect of crosstalk to Δr_m. **(a)** shows a range of clear-sky irradiance spectra, varying between 0 and 1.6 times the clear-sky direct horizontal irradiance value. In **(b)**, the true response curves are shown with lines, and the shading area is the approximation used to calculate the ratio from simulated spectra. In **(c)**, the simulated measured ratio using the response curves is shown as function of the true ratio. The dashed line is the 1:1 ratio. With crosstalk included, the response is underestimated, and without crosstalk the simulated response follows the true ratio.

S7.5 Water vapour measurements

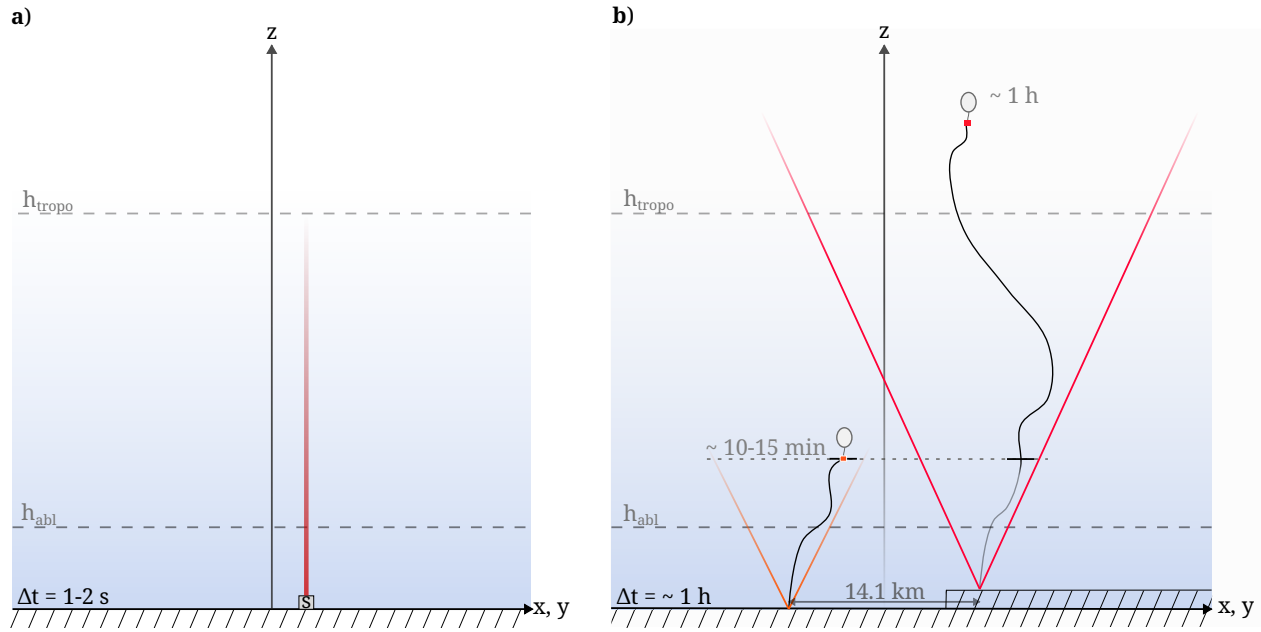

Figure S7.7: Schematic of total column water vapour measurements using a microwave radiometer (MWR) **(a)** and radiosondes **(b)**. The MWR is a passive instrument that measures humidity through microwave emissions from water vapour or liquid water, retrieved along a narrow vertical beam. To get the same measurement from soundings at La Cendrosa, shown in **(b)**, the boundary layer soundings (left, orange) are extended with tropospheric soundings (right, red) of Els Plans, 14.1 km apart and at slightly higher elevation. The coloured cones illustrate the potential horizontal displacement with respect to the initial position, with the solid curved lines an example path a sounding could take. Measurement duration is approximately 10 to 15 minutes or 1 hour, respectively. The remainder of this plot is similar to Figure 2.

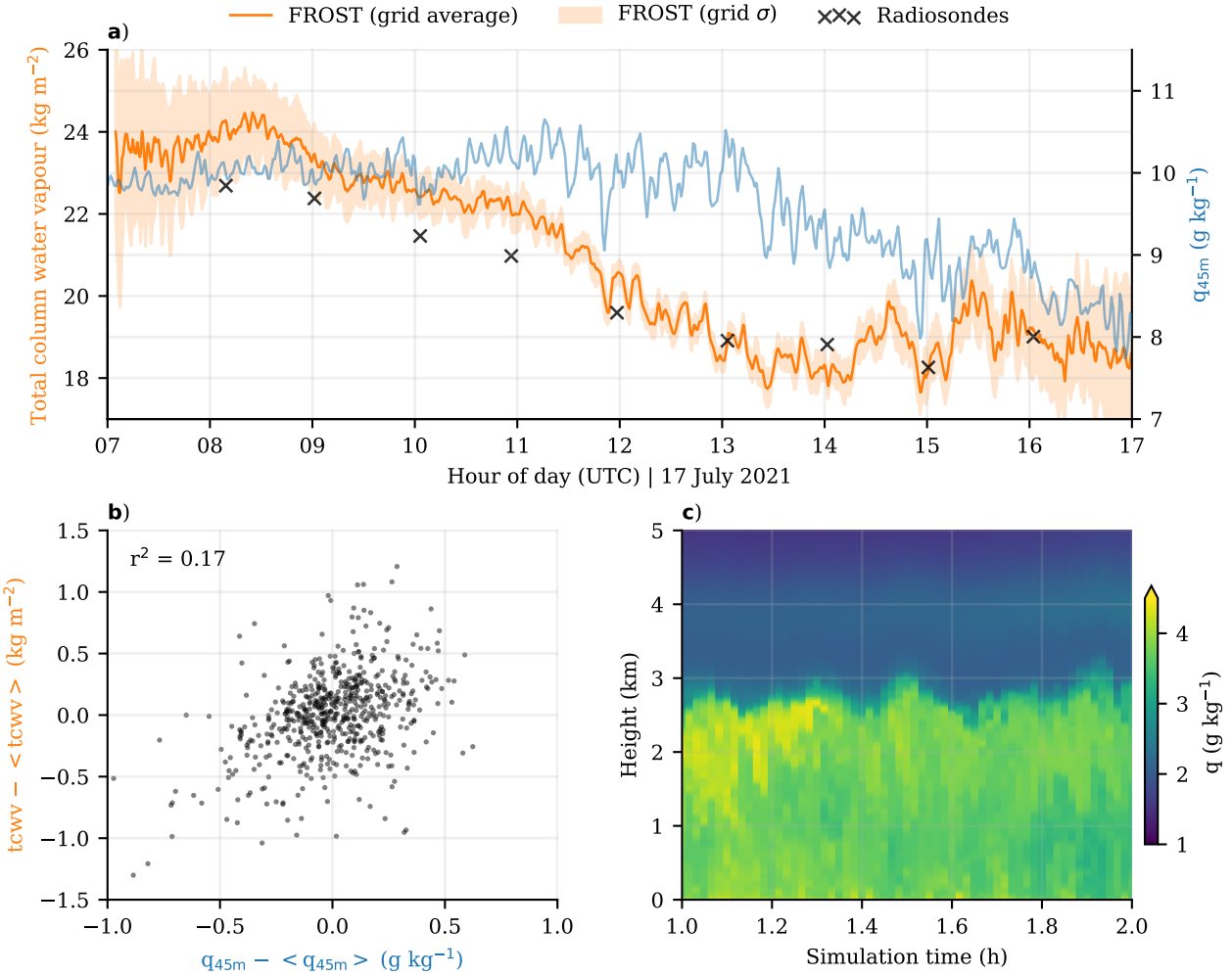

Figure S7.8: Moisture variability of total column compared to 45 meters at La Cendrosa. (a) shows a detailed time series of the same data as Figure 16b, combined with specific humidity at 45 meters above ground level. The correlation between deviations from hourly mean values for both total column water vapour and specific humidity at 45 meters are shown in **(b)**. To illustrate the difference between total column and single point moisture, **(c)** shows a (time, height) cross section of a convective boundary layer from large eddy simulation.

Chapter 8

Mechanisms of surface solar irradiance variability under broken cloud cover

This chapter is based on:

Wouter B. Mol & Chiel C. van Heerwaarden, 2024, *Mechanisms of surface solar irradiance variability under broken cloud cover*. **In review** in Atmospheric Chemistry and Physics. Copernicus.

Abstract

Surface solar irradiance variability is present under all broken clouds, but the patterns, magnitude of variability, and mechanisms behind it vary greatly with cloud type. In this study, we performed numerical experiments to understand which main mechanisms drive surface solar irradiance extremes across a diverse set of cloud conditions based on observations. The results show that we can capture the essence in four mechanisms. We find that for optically thin ($\tau < 6$) and clouds, scattering in the forward direction (*forward escape*) is the dominant mechanism. In cloud types such as altocumulus, it is able to produce irradiance enhancements of up to 50 % of clear-sky values due to small gaps in the cloud field. For flat, optically thick clouds ($\tau > 6$) like stratus, *downward escape* becomes the dominant mechanism, and the irradiance extremes are found underneath the cloud edge or gaps. Albedo has a significant effect under optically thick cloud cover, contributing 10 to 60 % of the total irradiance enhancement for low (0.2) to high (0.8) albedo. For deep convective clouds, *side escape* is the dominant mechanism enhancing domain-averaged diffuse irradiance. This effect has a large area of influence, extending over 20 km from the sunlit side of the cloud. Extreme irradiance enhancement, however, comes from *downward escape* and *forward escape* just underneath the cloud edge on the sunlit side, not from *side escape*. These results provide a framework for understanding the vast diversity and complexity found in surface solar irradiance and cloudiness. A next step is to apply this analysis to multi-layered cloud fields and non-isolated deep convective clouds.

8.1 Introduction

In this chapter, we aim to determine the main mechanisms that drive the spatial and temporal patterns of surface solar irradiance in the presence of clouds that we have observed throughout the work in this thesis. The motivation for this is to understand how different clouds and cloud fields create irradiance variability, which should help to simplify the vast diversity and complexity found in surface irradiance and cloudiness. In this introduction, we will first define what we mean by variability in surface solar irradiance (SSI) and demonstrate this with a diverse selection of (extreme) SSI variability from observations. This selection consists of prototype examples based on the 1 Hz BSRN data of Chapter 2 or on 1-minute data of the Veenkampen station (`https://maq-observations.nl/veenkampen/`). Additionally, we include a selection of spatially observed SSI extremes from the fieldwork described in Chapter 7.

Then, we formulate our hypothesis that SSI variability can be explained by four mechanisms. These mechanisms are based on prior research and theory (Section 8.1.2). From the prototype examples we design idealised numerical experiments, both to qualitatively reproduce the set of examples of observations, and demonstrate how the four mechanisms work and when they are effective. Once the basics are established, we introduce more realistically simulated cloud fields to see how the hypothesis holds up when the complexity of clouds and cloud fields increases. The tools we use to simulate the cloud fields and calculate radiative transfer are introduced in Section 8.2, followed by an overview of all experiments in Section 8.3.

8.1.1 Conditions of extreme variability

SSI variability at cloud-scale expresses itself in diverse ways, as will be shown shortly, and the choice of any definition is subjective and perhaps arbitrary. Here, we focus on conditions in which SSI is able to exceed clear-sky SSI, referred to as cloud-induced irradiance enhancement, or *irradiance enhancement* (IE). We further characterise SSI variability by having frequent and rapid fluctuations between (partial) shading and IE of at least 10 %, spatiotemporal SSI patterns with IE and shading in excess of minutes or kilometres, or simply by a single, large peak in SSI (IE $>$ 30 %). This loose definition purposefully excludes some common but less pronounced SSI variability conditions, as the impact is lower, and we assume conditions are easier to understand when SSI variability is more pronounced. Furthermore, we will mostly present SSI normalised with clear-sky SSI to be able to compare across cases with varying solar zenith angles. As small absolute changes in SSI can result in relatively large irradiance enhancement at high solar zenith angles, we only consider solar zenith angles of 75° or below.

Shallow cumulus

The shortwave radiative effects of shallow cumulus are the best described and studied among cloud types in the field of solar irradiance variability research. Key features are the fast and

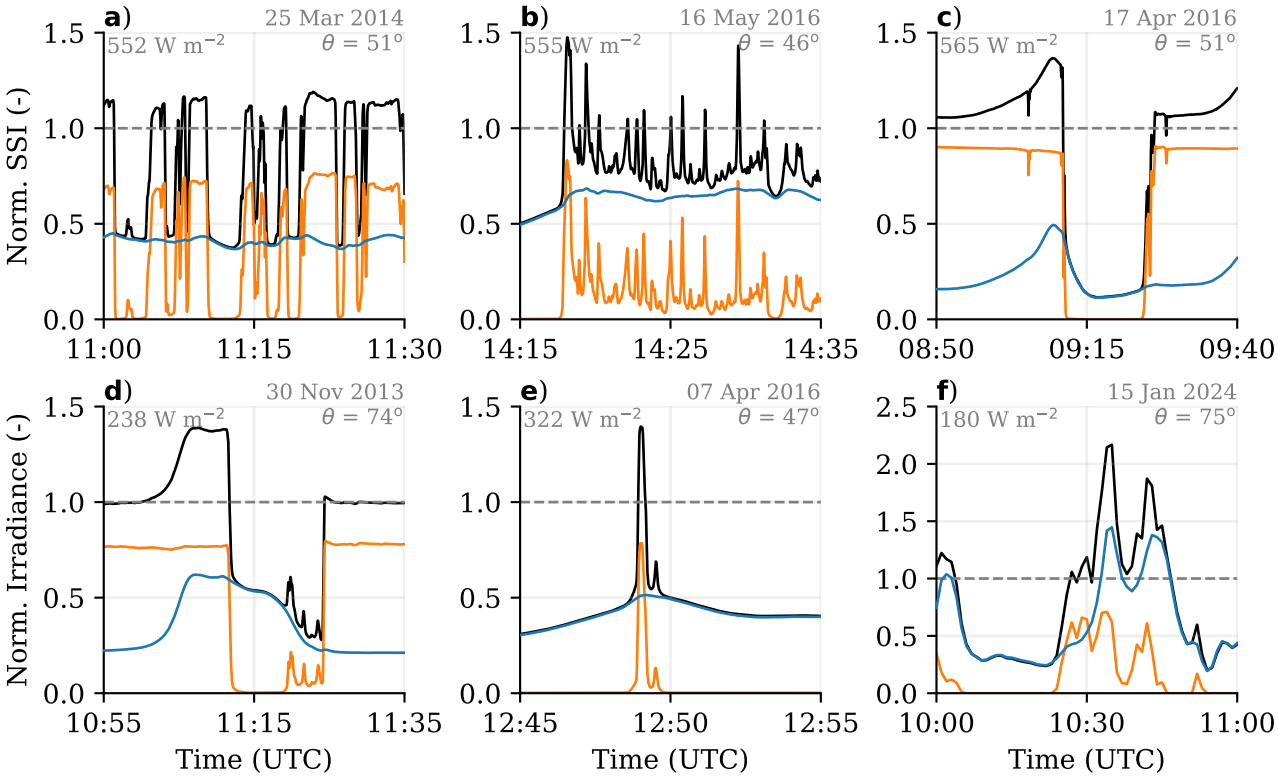

Figure 8.1: A collection of observed time series featuring irradiance variability under different conditions. The conditions are **(a)** shallow cumulus, **(b)** altocumulus, **(c)** cumulonimbus, **(d)** stratus field passage, **(e)** gap in stratocumulus, and **(f)** convective snow shower passage. All data is normalised with clear-sky SSI based on CAMS McClear (Gschwind et al., 2019). Average clear-sky SSI, solar zenith angle, and date are given in grey in the top of each subplot. Note that **(f)** has a larger y-axis.

frequent transitions between shade and sunshine (Figure 8.1a), and the bimodal distribution of global horizontal irradiance (e.g., Gristey et al., 2020a; Tijhuis et al., 2023). In the distribution, one peak is centred around the typical value of diffuse irradiance in cloud shadows where no direct irradiance is able to penetrate, the other peak resembles the irradiance enhancement in directly sunlit areas. The shadows are typically dark and the transitions to sunlit areas are sharp, illustrated by examples of spatial SSI patterns of cumulus in Figure 8.2.

Altocumulus

Altocumulus cloud fields result in a bimodal SSI distribution too, but increased cloud cover fraction reduces how frequently irradiance enhancement occurs. Diffuse irradiance is generally higher than seen in most other conditions of SSI variability and remains relatively constant on the spatiotemporal scale of individual irradiance enhancement peaks. Direct irradiance is often not completely attenuated, meaning the clouds are optically thin. Brief openings between individual altocumuli allow for direct irradiance to fully pass through and combine with the enhanced diffuse irradiance at the surface, thereby producing some of the

most extreme observed IE peaks. Figure 8.1b shows all of these features in a time series, with one peak reaching nearly 50 % above clear-sky SSI. Fields of altocumuli were frequently observed while we did spatial SSI measurements during the FESSTVaL campaign (Chapter 7). Figure 8.2 shows five different SSI patterns as a result of altocumulus, and one that includes cumulus as well. Peak irradiance enhancement varies between 30 and 60 % in these patterns. There are not many studies on altocumulus, but at least Schade et al. (2007) and Yordanov et al. (2015) also identified specifically altocumulus as being highly potent in creating such significant irradiance enhancement.

Cumulonimbus

Deep convective clouds with a vertically developed structure and anvil at the tropopause have the largest area of influence of the cloud types we consider in this study. The sheer size and scattering surface area of a single cumulonimbus cloud make it an ideal candidate for casting long shadows and enhancing diffuse irradiance on the sunlit side. Segal & Davis (1992) identified some of these features in observations, in particular the long-lasting irradiance enhancement at the sunlit side of the cumulonimbus clouds. Figure 8.1c shows the passage of a relatively isolated cumulonimbus moving from north to south over the sensor location with the Sun in the south, from our own observations. The key SSI pattern features for this cloud-type are the slow ramping up of SSI on the sunlit side of the vertically developed cloud, subsequent rapid reduction to SSI values below even clear-sky diffuse irradiance, and the return to clear-sky SSI after the Sun reappears. In the observational example, this pattern is superimposed on a 5 % background enhancement of SSI that likely arises from other clouds in the vicinity. A fast rising cloud top of a cumulus congestus caused the shadow in the bottom right pattern of Figure 8.2, which is similar to the reappearance part in the time series pattern.

Stratus and stratocumulus

Stratus and stratocumulus are generally optically thick cloud types that result in little SSI variability, unless they dissolve (or form), have gaps in them, or otherwise advect into or away from clear-sky region. Irradiance enhancement is not commonly associated with these cloud types, because the areas in which such variability can occur is small compared to the total cloud size, or brief compared to the total cloud lifetime. However, clear-sky to overcast conditions, or cloud gaps within overcast cloud fields, are associated with extreme irradiance peaks. Example are respectively illustrated in Figures 8.1d and 8.1e, and specifically for the cloud gap case in the study of Yordanov (2015). There is also a spatial SSI pattern caused by a small cumulus that formed in a cloud gap shown in the top left of Figure 8.2.

High albedo with broken cloud cover

A high albedo can enhance cloud-induced SSI variability by a significant amount, sometimes leading to extreme irradiance enhancement beyond what is normally observed under broken cloud cover. In Figure 8.1f, we show an example of a convective snow shower bringing a fresh

layer of snow cover, which pushed the diffuse irradiance above clear-sky SSI values for multiple minutes. Such a measurement seems unrealistic, but has been observed before, see for example Gueymard (2017), their Figure 4. Villefranque et al. (2023) furthermore identified that surface albedo plays a significant role in SSI variability under cumulus clouds.

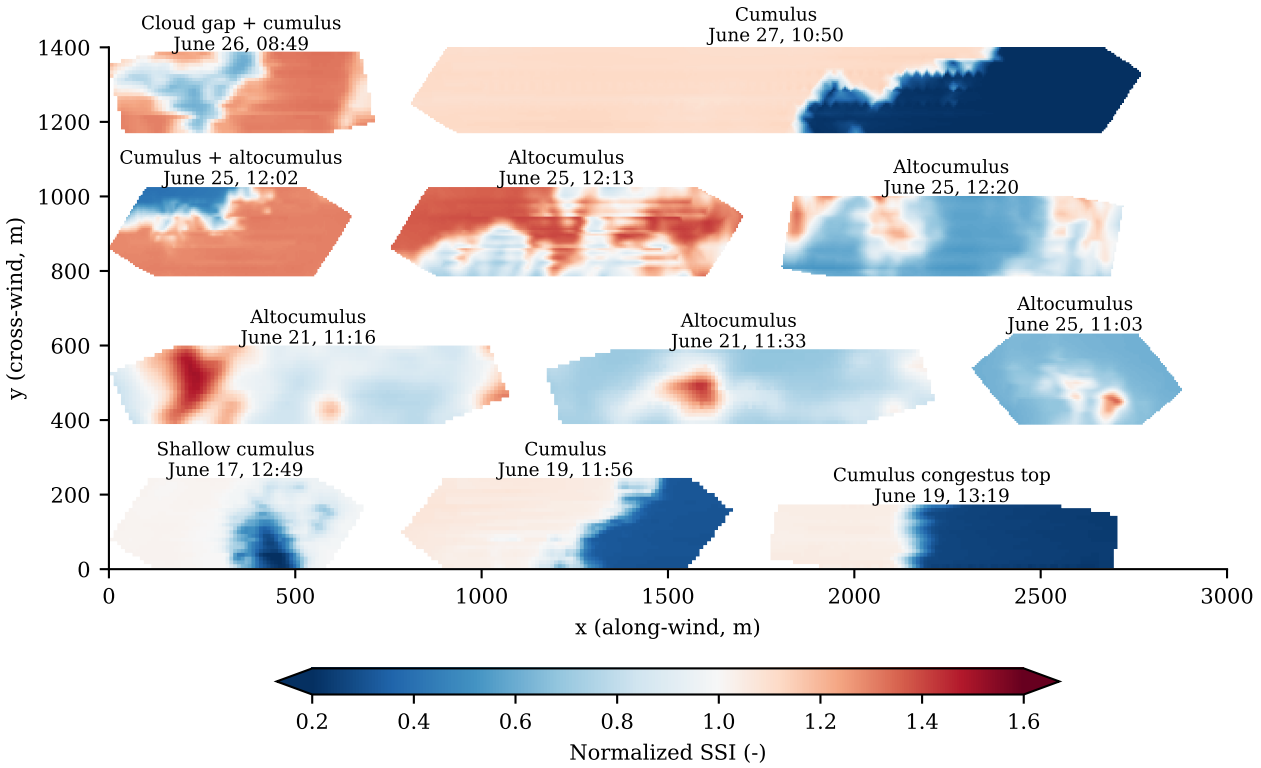

Figure 8.2: A collection of observed spatial patterns of surface solar irradiance. The patterns are spatially interpolated using temporal data as described in Chapter 7. The labels indicate cloud type and date and time of occurrence (UTC), all in the year 2021. SSI is normalised with clear-sky SSI from McClear.

8.1.2 Proposed mechanisms

Cloud fields can manifest in a countless number of different configurations, each resulting in a unique surface irradiance field. It all cases, however, it starts with scattering of direct irradiance that is horizontally and diffusely redistributed onto the surface. We hypothesise that four key mechanisms by which solar radiation is horizontally redistributed can explain all the previously described prototype examples of SSI variability and irradiance enhancement peaks. These mechanisms are in part based on prior research and may be known under different names, hence we will review and (re)define the terminology. Figure 8.3 schematically shows the four mechanisms.

1. Forward escape

Between transparent and opaque clouds, there is a region of optical thickness where direct irradiance is scattered mostly only once or twice, if at all. In the case of cloud droplets,

we are in the regime of Mie scattering. Thus, 90-99 % of scattering occurs within 5° of the forward direction (calculated using `miepython`, Prahl, 2023), depending on droplet radius and photon wavelength. Consequently, part of the direct irradiance is scattered to an area just besides the direct beam path, leading to irradiance enhancement if the direct path to this area is sufficiently cloud-free. Small isolated cumulus clouds, for example, were found by Robinson (1977) to affect an area of approximately 5 to 15° off the direct beam centre. This type of scattering occurs at cloud edges, where optical thickness approaches zero, and in other optically thin (parts of) clouds. Although scattering by individual cloud edges or transparent sections is limited, we expect this can become substantial for clouds or cloud fields with a significant amount of optically thin area. Altocumulus as shown in Figure 8.1b is an example of such an optically thin cloud field, indicated by the fact that direct irradiance is not fully attenuated.

2. Downward escape

Towards the upper limit of optical thickness, scattered radiation loses its forward component due to multiple scattering. While radiation then increasingly gets scattered back up, the large remaining part that does not get absorbed by the cloud is highly diffusely transmitted downward through the cloud, thereby create irradiance enhancements as it lands in adjacent cloud-free areas. We call this mechanism *downward escape*, a term introduced by Várnai & Davies (1999) (although their definition is expressed in terms of the horizontal photon transport bias in the 1D radiative transfer approximation).

Downward escape differs from *forward escape* in the location where the diffuse irradiance lands and how the diffuse irradiance coincides with direct to create extremes in SSI. Pecenak et al. (2016) show the transition between *forward escape* and *downward escape* clearly in 2D simulation experiments of rectangular clouds, with the peak of enhanced irradiance moving from near the projected shadow location to underneath the cloud as optical thickness increases. Optically thick but flat clouds, like the stratus and stratocumulus of Figure 8.1, are likely candidates for where this mechanism is a dominant factor in creation of SSI variability. Solar zenith angle will play an important role in the effectiveness of *downward escape* as a mechanism, as it determines to what extent direct irradiance can coincide with the peak in diffuse enhancement near or underneath the cloud.

3. Side escape

Optically thick clouds scatter a large part of the solar irradiance back to space. Similarly, under solar zenith angles higher than 0°, the sides of vertically structured clouds have the same effect, except due to the vertical orientation the scattering is partially directed towards the surface. Segal & Davis (1992) described these effects of deep convective clouds as reflections, but Várnai & Davies (1999) refer to this phenomenon more accurately as backscattering. We will call it *side escape*, where cloud sides act as a region where photons diffusely escape after multiple scattering events, rather than reflecting radiation like a mirror.

We expect this mechanism to become effective as the total vertically oriented surface area

increases compared to the horizontal size of the cloud, typical in cases of deep moist convection. In such cases, optical thickness will generally be high and thus *forward escape* will be ineffective and most radiation escapes on the sunlit side. We thus also expect strongly asymmetric surface patterns of irradiance with vertically structured clouds due to diffuse irradiance being enhanced primarily on the sunlit side, as we find in the example in Figure 8.1c.

4. Albedo enhancement

Surface albedo can enhance the cloud-enhanced surface irradiance by multiple iterations of scattering between surface and cloud base. This mechanism may explain the extreme irradiance peaks observed during snow cover (high albedo) combined with broken cloud cover as reported by Gueymard (2017), or shown in Figure 8.1f. In a more general sense, this mechanism is known as *entrapment*, which can occur between any two scattering surfaces (Schäfer et al., 2016; Hogan et al., 2019). In this study, we focus on the entrapment of radiation between a surface (land or ocean) and a cloud (field). The effectiveness of this mechanism, aside from higher surface albedo, will increase with cloud cover and optical thickness, required to scatter back reflected surface irradiance, up to the point where too little irradiance is available. Areas at the edge of stratus, gaps in stratocumulus, and perhaps large cumulus clouds are therefore candidates for significant *albedo enhancement*.

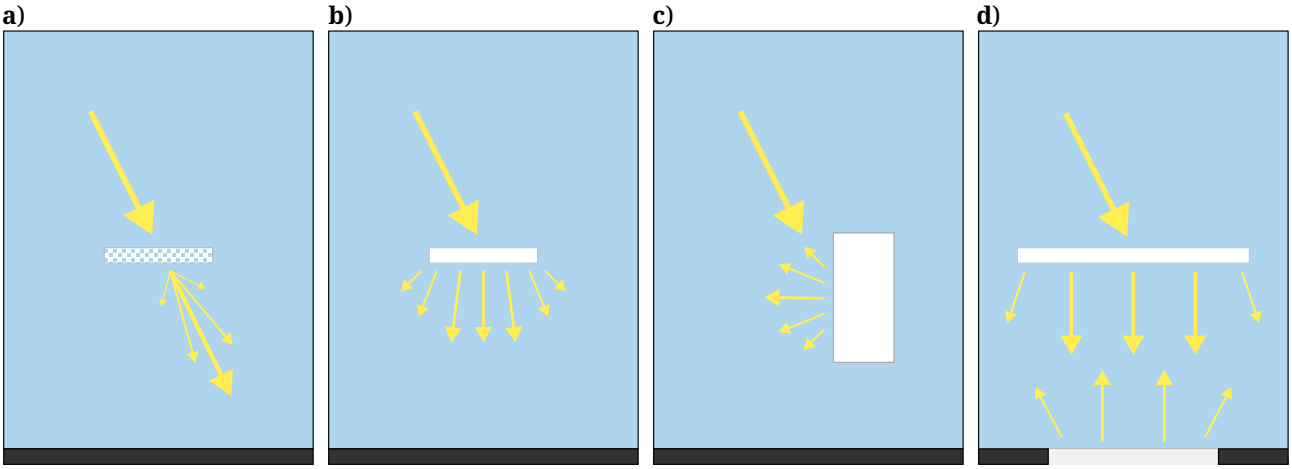

Figure 8.3: Schematic representation of the four proposed mechanisms that drive surface solar irradiance variability. From **(a)** to **(d)**, these are *forward escape*, *downward escape*, *side escape*, and *albedo enhancement*. Incident solar radiation is indicated by the large downward arrow, the other arrows indicate approximated average direction and intensity of scattered radiation. Surface albedo is indicated by the lightness of the surface. Only the arrows relevant to each mechanism are drawn.

8.2 Simulation tools

We use a Monte Carlo ray tracer (MCRT) to simulate 3D radiative transfer within cloud fields overlying a surface. These cloud fields either come from case studies run using large-eddy

simulation (LES) where we simulate specific cloud types, or the cloud fields are manually created. The combination of the MCRT with these cloud fields allows us to isolate, to some extent, the contribution of the four mechanisms to the total surface irradiance variability. Information on creating the cloud fields and the ray tracer setup in general is given below. The details of each experiment are demonstrated in the next section. All model code, input data, and case setups are freely available, see our open data Section 8.6.

8.2.1 3D radiative transfer

For simulating 3D radiative transfer, we use the GPU-accelerated version of the Monte Carlo ray tracer as introduced by Veerman et al. (2022). This model is based on the RTE+RRTMGP solver and is fast enough to run coupled to the LES, although in this study we use it in offline mode. One of the optimisations is a reduced spectral resolution, via smaller sets of so-called g-points, chosen in such a way as to have minimal impact on accuracy (Veerman et al., 2024). We use the 112 set for shortwave and the 128 set for longwave, halving the calculation time. This time is spent on spatial resolution, amount of rays, and the use look-up tables for an accurate Mie scattering phase function. The latter is important to resolve the narrow but dominant forward peak in scattering direction in the case of cloud particles.

For some cases, we solve radiative transfer online (i.e., coupled to the model) in order to simulate more realistic clouds that are radiation driven, such as altocumulus. We then use the standard RRTMGP solver with the independent-column approximation, which is much faster and good enough to create the cloud fields we want. Any analysis of irradiance we do only with the 3D MCRT.

We sample optical thickness τ from the MCRT, which gives a 3D field of τ per grid cell and wavelength band. τ is typically higher for longer wavelengths, but in this study we use the band centred in the visible spectrum, which contains the most energy. For a given amount of condensate, τ also varies with the effective droplet radius, which in turn depends on the droplet number concentration. We keep that number fixed at 2.5×10^8 m^{-3} for all cases, therefore an increase in τ with total liquid (or ice) mixing ratio is slightly offset by an increased effective radius. This will have no influence on the interpretation of our results.

8.2.2 Simulated and synthetic cloud fields

We use MicroHH in LES-mode as our cloud-resolving atmospheric model (van Heerwaarden et al., 2017). The model is initialised with vertical profiles of temperature, moisture, and wind, either from observed soundings, reanalysis data, or from idealised experiments based on literature. The lateral boundaries are periodic, and domain size and spatial resolution are case-dependant. For the synthetic cloud fields, we start by initialising the model and then manually modify the cloud fields, either by changing the temperature in a layer and letting the model condense water vapour, or by directly modifying the liquid (q_l) or ice (q_i) fields.

We can manually move any cloud field up and down to test effects of cloud height, or test a range of optical thickness by increasing or decreasing the amount of condensate while keeping the cloud geometry and location fixed. The surface is flat in all simulations. Albedo is spatially homogeneous, wavelength-independent, and kept the same for direct and diffuse radiation. In some simulations we prescribe homogeneous surface fluxes or run with online radiation and an interactive surface layer.

8.3 Experiments

What now follows is an overview of all cloud fields that we create. We run the 3D radiative transfer model on these cloud fields and vary a set of parameters across a range of values, depending on the specifics of the experiment. These parameters are surface albedo α, solar zenith angle θ, solar azimuth angle ϕ, cloud optical thickness τ, cloud altitude h, and cloud depth d. For all configurations we run the radiative transfer model also once without clouds to estimate clear-sky irradiance (GHI_{cs}).

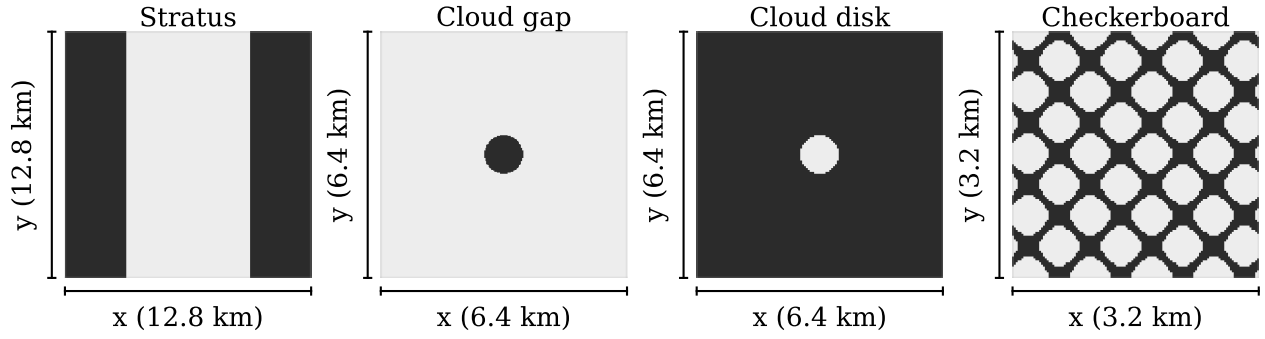

Figure 8.4: Top view of the synthetic cloud fields. Light greys indicate clouds, dark grays are the cloud-free areas. These clouds are thin relative to their horizontal size (cloud depth varies between 25 m and 150 m). Cloud depth, altitude, and optical thickness depend on the case and experiment. Note that the horizontal domains vary in size per case.

8.3.1 Synthetic cloud fields

Flat clouds

The horizontal geometry of four synthetic clouds fields are shown in Figure 8.4. The `stratus` case cloud is infinite in the y-direction, is 3 grid-points thick (150 m), and sits at an altitude centred around 450 m above ground level (AGL). Vertically integrated liquid water is 0.158 kg m^{-2} ($\tau \sim 19$). This is an idealisation of a case of stratus to clear-sky transition (and vice versa), such as the example in Figure 8.1d.

For the `cloud gap`, we use the same configuration as in the `stratus` case, but now it stretches across the whole domain and has a circular gap of 1 km in diameter in the centre. This resembles the cloud gap study by Yordanov (2015) and the stratocumulus with a gap shown in Figure 8.1e.

The `cloud disk` case is the inverse of `cloud gap`, as can be seen in Figure 8.4, but only has a thickness of 1 grid-point (50 m). That is unrealistically thin, but minimises the effect of *side escape*, as we manually vary its total condensate manually to control optical thickness. Cloud disk altitude and diameter are also varied. This cloud is for testing the effect of a singular patch of optically thin cloud, which may resemble a small cumulus, a transparent cloud edge, a single patch of altocumulus or a piece of cirrus.

The `checkerboard` case features a checkerboard-like pattern of 100 m thick patches that are 500 m in diameter, with at most a 150 m spacing in between patches, and sits centred around an altitude of 2850 m above ground level. This idealisation is inspired by an observed case of altocumulus in FESSTVaL (see Section 8.3.2), with similar properties as shown in Figure 8.1b.

Vertical clouds

For studying the effect of cloud sides in the most simple way, we take the `cloud disk` and extend it vertically, effectively creating a perfectly homogeneous and smooth cylinder. The cloud base is at 1000 m above ground level and cloud top varies from 1500 to 12000 m. This case is an idealisation of a growing deep convective cloud (cumulus congestus) in an environment free of wind shear, and therefore called `towering cumulus`. Figure 8.1c shows the passage of such a deeply developed cloud, although there is also an anvil cloud present in this observation.

8.3.2 Simulated altocumulus

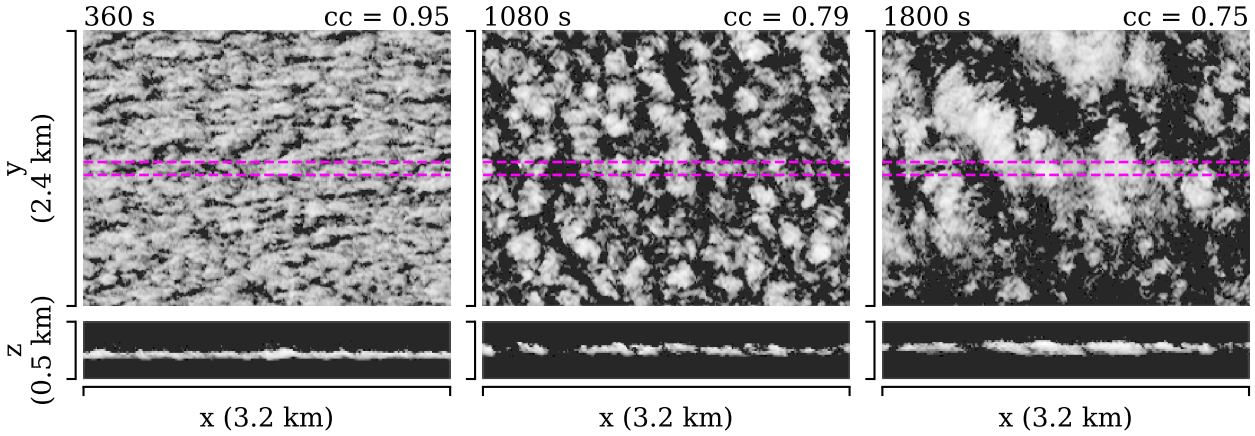

Figure 8.5: Simulated altocumulus evolution. The top row shows a top view of vertically integrated liquid water (q_l), the bottom row shows a side view of horizontally integrated q_l over a 200 m slice in the y-direction (marked by the dashed magenta lines). Cloud altitude is $\sim$ 2800 m. The full domain is 6.4 $\times$ 6.4 km^2, only a subset is shown. Time step and cloud cover are labelled at the top.

In this case, we simulate an altocumulus cloud field observed during the FESSTVaL campaign on June 21 (shown in Chapter 7 or partly in Figure 8.2). The model is initialised from a

radiosonde at the observatory, which has a small layer of nearly condensed air at approximately 2850 m and drier air above and below that layer. By increasing the relative humidity beyond 100 % in this layer at the first time step, we force the creation of a thin layer of condensation. With small noise in the vertical velocity field at initialisation, the model runs freely with coupled 1D radiative transfer, which develops the layer of condensation into a thin field of dynamic altocumulus, as illustrated in Figure 8.5. Altocumulus requires a high simulation resolution in order to resolve the altocumulus, as the vertical depth and horizontal cell structures are small. Domain size is therefore on the small side for an LES, with 6.4 $\times$ 6.4 km^2 (Δx, Δy = 12.5 m) and a vertical domain of 4.2 km (Δz = 16 m). After 1800 s, we get unrealistic wave growth in our periodic domain, which explains the large structures that emerge at this time step.

8.3.3 Simulated cumulonimbus

To extend `towering cumulus` to something more realistic, we run two versions of an isolated cumulonimbus. These are adaptions of the idealised supercell simulation setup introduced by Weisman & Klemp (1982). In one simulation, we disable vertical wind shear, in the other we set it to 25 m s^{-1}, resulting in a straight vertical cloud and a tilted one, respectively. The horizontal domain is 153.6 $\times$ 153.6 km^2 (Δx, Δy = 200 m), with the domain top at 19.2 km (Δz = 150 m). A large domain is necessary to keep the cumulonimbus from scattering onto itself, due to periodic boundary conditions in the MCRT. Vertically and horizontally integrated liquid and ice water mixing ratios are shown in Figure 8.6 for three time steps during the growing stage.

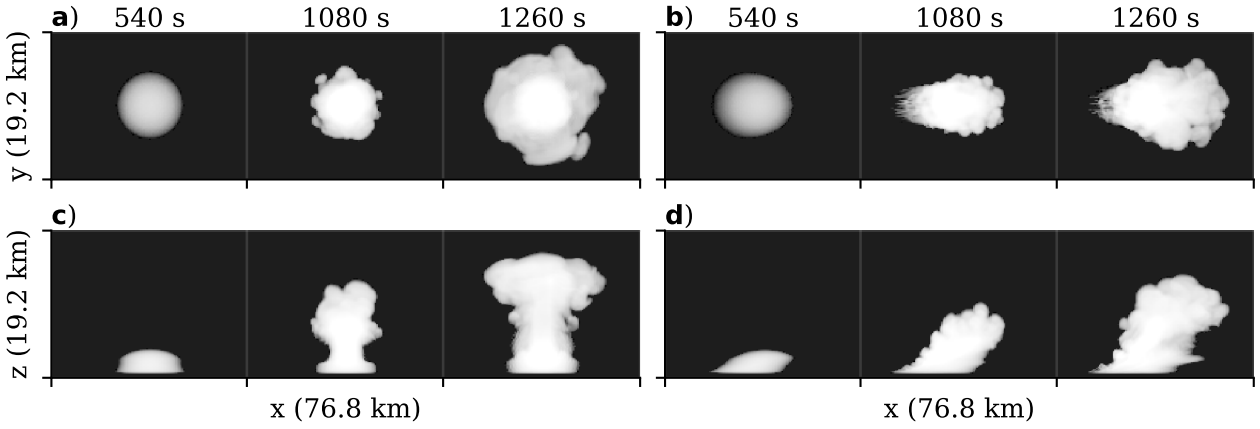

Figure 8.6: Two simulated deep convective updrafts. **(a, c)** show the updraft in shear-free conditions, **(b, d)** show the same updraft but with 25 m s^{-1} vertical wind shear. White colours indicate high values of liquid and ice water mixing ratios ($q_l + q_i$) integrated along the z or y-axis.

8.3.4 Simulated free convection

With the final simulation, called `free convection`, we aim to demonstrate what happens in a cloud field that is on the high-end of possible complexity, in contrast to the other experiments

in this study. This simulation has a horizontal domain of 102.4 $\times$ 102.4 km^2 (Δx, Δy = 200 m), with the domain top at 19.2 km (Δz = 100 m). We initialise the simulation using an observed conditionally unstable thermodynamic profile with low wind shear. We include online 1D radiative transfer to heat up an interactive land surface which will thermodynamically trigger convection. Figure 8.7 shows this evolution of `free convection` in three stages, from cumulus towards deep convection. After one hour, as the convective inhibition diminishes with daytime heating, widespread cumulus and cumulus congestus forms randomly, as there is no other forcing or form of organisation. In subsequent hours, convection consolidates in a smaller number of strong deep convective clouds with large anvils.

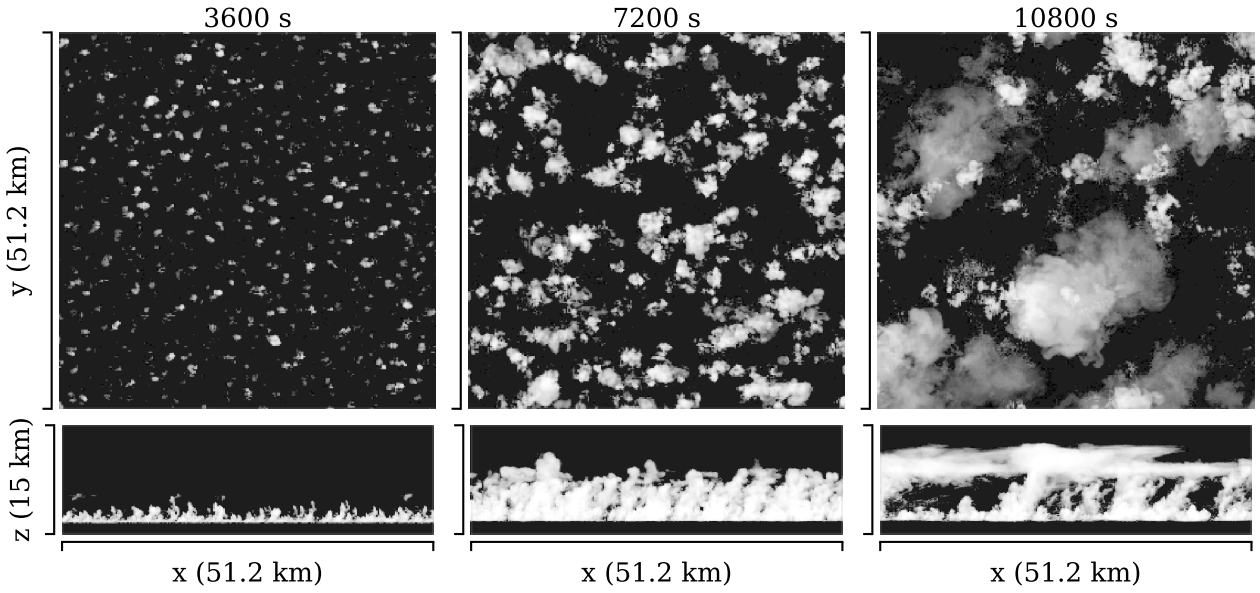

Figure 8.7: Simulated free convection. The top row shows the vertically integrated liquid and ice content ($q_l + q_i$), bottom row shows the same integral along the y-axis. Only a quarter of the full horizontal domain is shown.

8.4 Results

8.4.1 Cloud optical thickness controls which mechanism dominates

We will first demonstrate the relationship between the mechanisms of *forward escape*, *downward escape*, and *albedo enhancement*. The interplay between these three mechanisms using the `cloud disk` case is illustrated in Figure 8.8.

For low optical thickness ($\tau \approx 0.2$), radiation is primarily scattered into the projected cloud shadow at the surface. At high optical thickness ($\tau \approx 44.2$), the forward projection disappears, and instead a wide area centred underneath the cloud is diffusely enhanced. Albedo has no effect on the low end of the optical depth range, whereas it contributes significantly at the high end (~ 4 times more than *downward escape* at $\alpha = 0.8$). Intermediate values of τ show a transition from predominantly *forward escape* without *albedo enhancement* to *downward escape* with *albedo enhancement*.

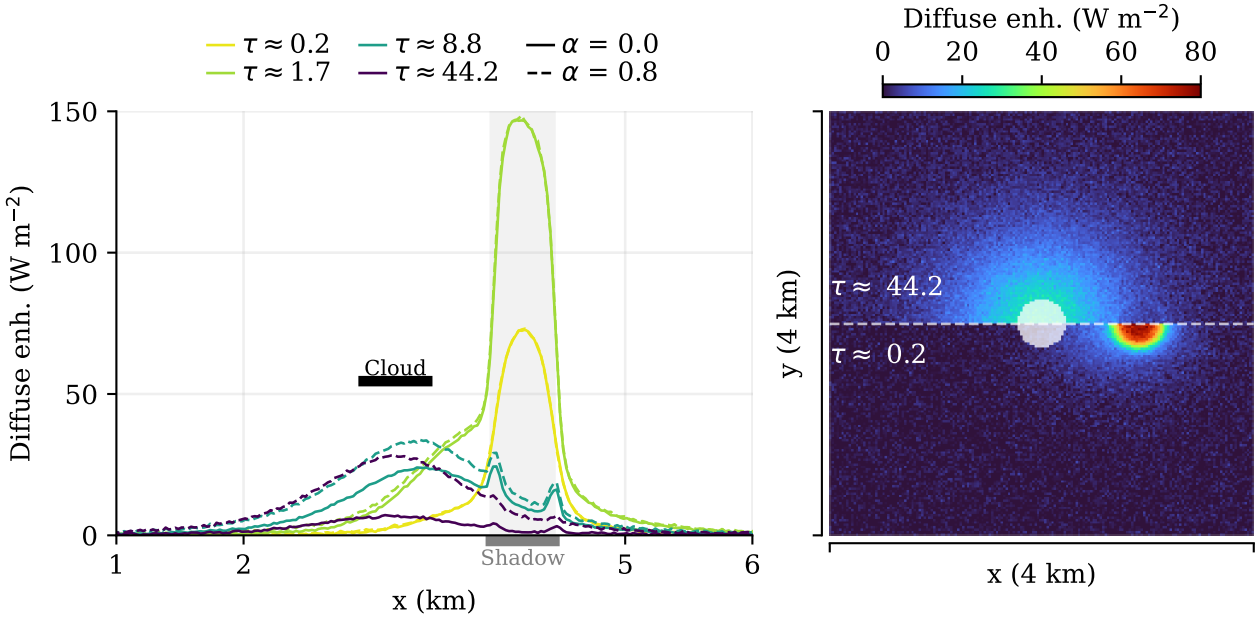

Figure 8.8: From *forward escape* to *downward escape*. A cloud disk at 1 km altitude with 25 meter depth and a 500 meter diameter scatters radiation coming in at a zenith angle of 45°. Diffuse SSI enhancement is calculated relative to clear-sky values. The lines in the left plot are averaged over the middle 400 m in the y-direction, whereas the right plot shows the 2D surface field.

For this experiment, we can estimate a value for τ where the transition occurs as the point where the diffuse enhancement underneath the cloud exceeds that of within the projected shadow location. Estimated from Figure 8.8, this transition occurs between $\tau = 1.7$ and 8.8. Numerically, by simulating the values of τ in this transition range, we find *downward escape* takes over at $\tau > 6.3$, or $\tau > 5.4$ when *albedo enhancement* is included ($\alpha = 0.8$). We keep these numbers for τ in mind for the next sections as an estimate for the scattering regime we are in terms of mechanism.

What this experiment illustrates is that when *forward escape* dominates in a cloud field, *albedo enhancement* is negligible. Furthermore, for a uniform cloud, *downward escape* and *forward escape* only co-occur in the intermediate range of optical thickness. In more complex clouds or cloud fields, in which low and high optical thickness are common and close together, these mechanisms may still co-occur.

8.4.2 How the mechanisms work in stratus, cloud gap, and checkerboard

We will now further describe the *albedo enhancement* and *forward escape* mechanisms using the synthetic cloud fields. In Figure 8.9a-c, we show the resulting SSI pattern for the `stratus`, `cloud gap`, and `checkerboard` cases. All three resemble the patterns of diffuse, direct, and total SSI from the observations in Figure 8.1b,d, and e, respectively.

Given the optical thickness regimes we estimated in the previous section, the patterns for `stratus` and `cloud gap` are driven exclusively by *downward escape* in the absence of albedo. Diffuse irradiance is primarily enhanced underneath the cloud, with the largest enhancement found just at the transition where direct irradiance appears. Increasing the zenith angle in the `stratus` case further shifts the direct irradiance underneath the cloud on the sunlit side where diffuse irradiance is enhanced the most, which maximises the possible irradiance enhancement in this configuration.

For a 100 m diameter cloud gap, diffuse irradiance is uniformly enhanced below the cloud field, and any direct irradiance would coincide with the peak enhanced diffuse (Figure 8.5). Widening the gap would reduce the diffuse enhancement underneath that gap, as we are in the *downward escape* regime, and thereby make the irradiance enhancement more dependent on having a high enough solar zenith angle to optimally position the direct irradiance with respect to peak diffuse enhancement. For a gap diameter that is close to the cloud vertical depth, direct irradiance will be unable to pass through and create any irradiance enhancement at higher solar zenith angles, as is the case for $\theta = 60^\circ$ in Figure 8.9h.

The `checkerboard` case is different, as the cloud field is optically thin, which results in a pattern that is dominated by *forward escape*, ignoring potential *albedo enhancement* for now. Diffuse irradiance is enhanced almost uniformly underneath the cloud field despite dominant *forward escape*. This is due to the high altitude of the cloud (2850 m), which allows the forward diffuse peaks of individual cloud patches to be spread over a larger surface area and merge together. As a result, irradiance enhancement is approximately 45 % in the sunlit gaps between the cloud patches with only slight variations. We will now further investigate the *albedo enhancement* and *forward escape* mechanisms in these cloud fields.

8.4.3 Albedo significantly enhances SSI under optically thick clouds

We quantify the *albedo enhancement* (AE) in the presence of a cloud for a specific surface albedo (α) as $\mathrm{AE}_\alpha = \mathrm{IE}_\alpha - \mathrm{IE}_{\alpha_0}$. Here, IE_α is the cloud-enhanced surface irradiance for a given albedo α, i.e., $\mathrm{SSI}_\alpha - \mathrm{SSI}_{\alpha,cs}$. α_0 is the reference albedo of 0, representing the cloud-enhanced irradiance without any *albedo enhancement*. AE_α is shown in Figure 8.9 for the

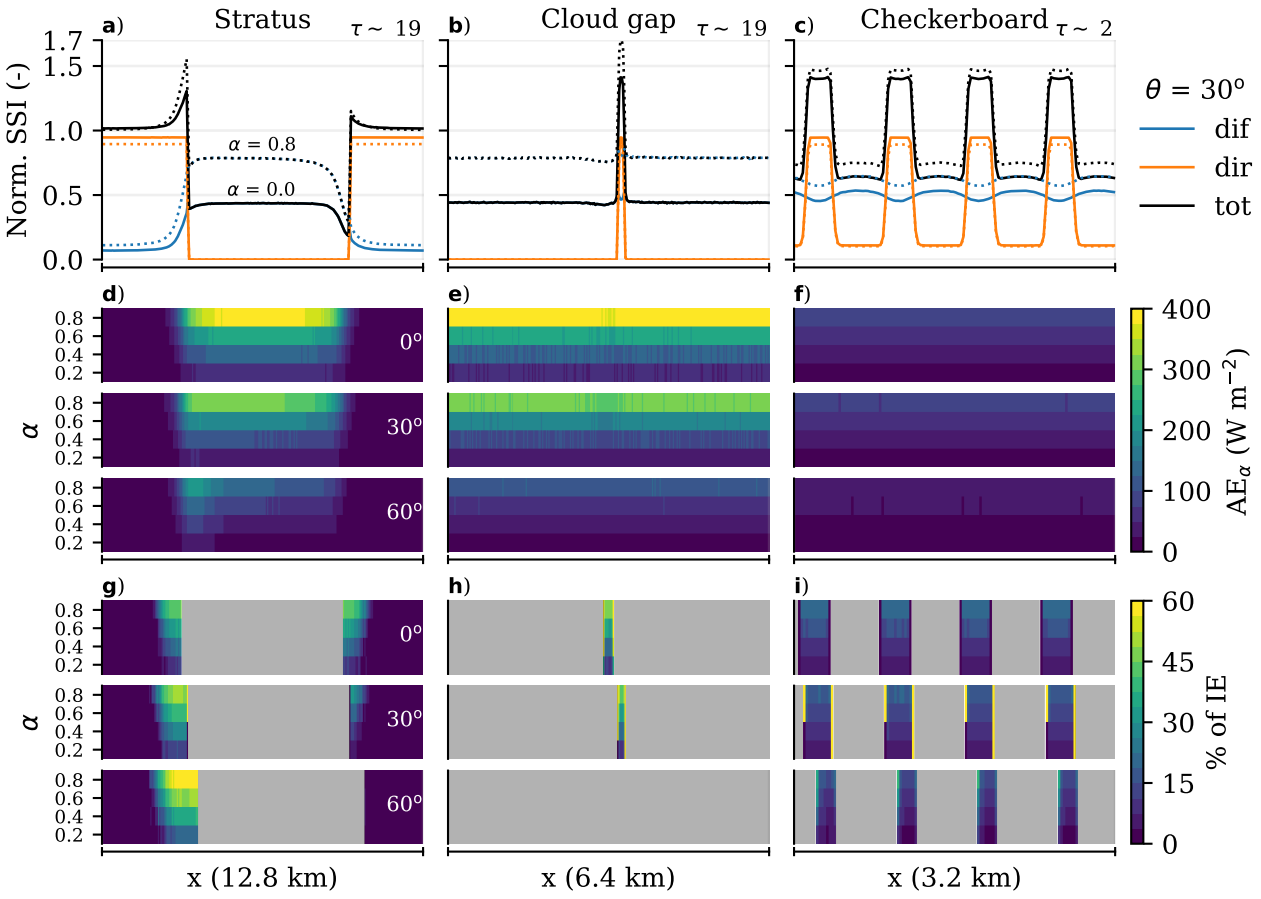

Figure 8.9: Surface patterns for the stratus, cloud gap, and checkerboard cloud fields. The top row shows the diffuse, direct, and total surface solar irradiance along the x-axis and averaged over (a part of) the y-axis. The middle row shows *albedo enhancement* for a given albedo (AE_α) as the irradiance enhancement relative to $\alpha = 0$ for $\alpha \in [0.2, 0.8]$. The bottom row shows the relative contribution of AE_α to the total enhancement of irradiance IE_α. Solar zenith angle is 30° for the top row, or 0, 30, and 60° for the other subplots.

`stratus`, `cloud gap`, and `checkerboard` cases.

The simplest effect can be seen in the patterns in Figure 8.9a-c, where the dotted lines are $\alpha = 0.8$, which all show a significant increase in diffuse irradiance and minor reduction in direct irradiance (normalised by their respective clear-sky values). The high cloud cover and optical thickness of the stratus cloud in the `stratus` and `cloud gap` cases result in significant *albedo enhancement*. Firstly, albedo enhances the diffuse irradiance most where local cloud cover is highest, which explains the patterns in Figure 8.9d and e. Once again, this shows that low cloud optical thickness renders *albedo enhancement* negligible, as shown by the weak diffuse enhancement in the `checkerboard` case (even for $\alpha = 0.8$).

Figures 8.9g-i show the relative contribution of *albedo enhancement* to the total IE, with shaded areas greyed out. This shows that at a modest albedo of 0.2, the albedo accounts for 10 % of the total IE in the stratus and cloud gap cases. For high albedo, this can increase to

as much as 60 % ($\alpha = 0.8$) for the `stratus` case at $\theta = 60°$. Under such conditions, direct irradiance lands further underneath the stratus cloud on the sunlit side, and thereby adds a significant amount of radiation that gets trapped between the cloud and the surface.

In the `cloud gap` case, *albedo enhancement* is similar to stratus. While the cloud gap case would have a higher potential for *albedo enhancement*, given that direct irradiance nearly always lands underneath the peak diffuse enhancement, the gap limits the amount of direct irradiance available for multiple scattering. Still, while the relative contribution of *albedo enhancement* to IE is approximately 10 to 45 %, the total IE is larger in this case, reaching 70 % for $\alpha = 0.8$ at $\theta = 30°$.

For optically thick clouds and high cloud cover, *albedo enhancement* can thus be significant, already contributing ~ 10 % to the total IE at a modest albedo of 0.2. The `checkerboard` case shows only a 10 to 15 % contribution of *albedo enhancement* to IE for the most extreme case of $\alpha = 0.8$. This is consistent with the low optical thickness of the cloud field and thus limited entrapment. At lower albedo, the contribution of *albedo enhancement* is negligible, meaning the extremes in SSI in this case are nearly exclusively driven by *forward escape*.

8.4.4 Forward escape enhances SSI for low clouds or high cloud area

As previously discussed in Section 8.4.1, *forward escape* results in scattered irradiance that closely follows the direct beam, of which a fraction lands next to the partially shaded area, creating irradiance enhancement. Hence, peak irradiance enhancement is low, as most scattered radiation falls within the projected shadow of the cloud (see Figure 8.8). We think this is why SSI is barely, or not at all, enhanced near the edges of cumulus clouds, as can be seen in the spatial patterns in Figure 8.2. The areas of low optical thickness in cumulus clouds, found at the edges or for the whole of the smallest shallow cumuli, are so small compared to the whole hemisphere from which radiation originates, that *forward escape* contributes little to irradiance enhancement or SSI variability. So how can *forward escape* still be effective in creating (extreme) SSI variability?

How forward escape effectiveness varies with cloud altitude and area

To further understand *forward escape*, we will study its relationship with cloud altitude and area. For this, we create `cloud disks` of 100 and 1000 m in diameter with an optical thickness of $\tau \approx 2$. Figure 8.10 illustrates the effect of both cloud altitude and area. First, for the 1000 m diameter `cloud disk`, the peak diffuse enhancement or total irradiance enhancement is increased by at least a factor of 2 compared to the 100 m diameter one. Second, by lowering the altitude of the cloud disk, the forward scattered irradiance is spread out over a smaller area and thus peak enhancement in both diffuse and total irradiance increases. The total irradiance enhancement is always lower than diffuse enhancement, because for low optical thickness most scattered irradiance still falls within the projected shadow of the cloud.

A small area of optically thin cloud at low altitude is still not very effective, as the peak in irradiance enhancement is only able to exceed 5 % with respect to clear-sky at an altitude below 500 m. Conversely, the larger cloud disk already exceeds clear-sky SSI by 10 % at 6 km, and peaks at 25 % around 500 m altitude. The small decrease below 500 m is likely due to the cloud disk being so close to the surface that scattered radiation can not spread out horizontally enough to maximally combine diffuse and direct irradiance. To create more extreme SSI values, we can further increase the cloud area and place it at a higher altitude to maximise the combination of all scattered irradiance. Essentially, this is what we think happens in altocumulus, which we will now demonstrate.

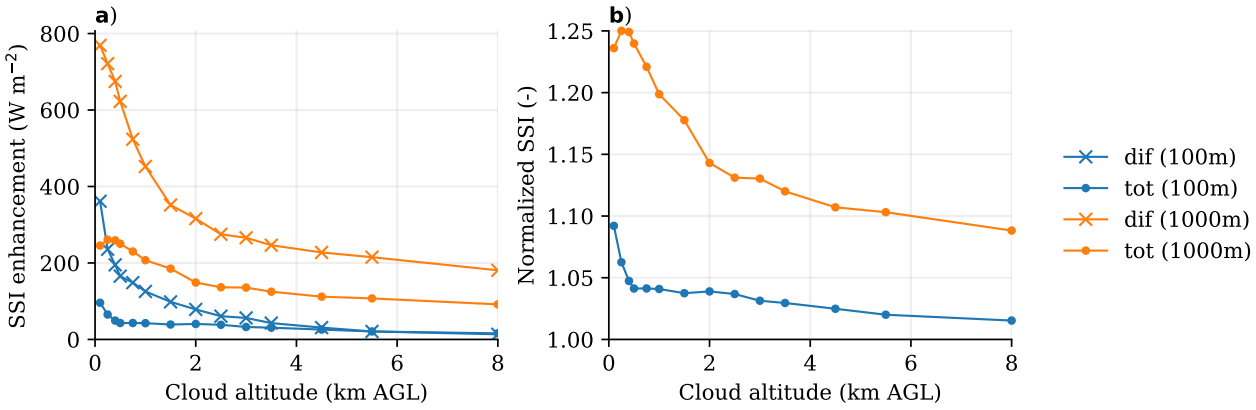

Figure 8.10: Effects of *forward escape* with varying cloud altitude and cloud diameter. Domain maxima for cloud diameters 100 m and 1000 m are shown here. In **(a)** the absolute surface solar irradiance (SSI) enhancement with respect to clear-sky (total or diffuse), and in **(b)** the total SSI enhancement normalised by clear-sky values. Solar zenith angle is 0°, surface albedo is 0, and cloud optical thickness $\tau \approx 2$.

Why altocumulus fields create extreme SSI peaks

The simulated altocumulus fields affect the surface solar irradiance fields very similar to that of the `checkerboard` cloud field. Figure 8.11 illustrates the general patterns and dependence on solar zenith angle. Diffuse irradiance is relatively constant throughout the domain, with strong irradiance enhancements in the gaps between cloud patches. Higher total cloud cover (0.71 to 0.94), all of which has low optical depth ($\tau \sim 0.4$ to 0.6 on average), increases the total enhancement of diffuse and thereby increases the magnitude of the irradiance peaks. Higher cloud cover reduces the probability of these peaks occurring, however. Solar zenith angle affects the results primarily through reducing the effective size of the cloud-free areas, while increasing the relative magnitude of the enhancement.

The effect of albedo is also very small in for the simulated altocumulus, despite high cloud cover. At an albedo of 0.8, the contribution to the irradiance peaks is only $\sim$ 15 % (varying slightly with cloud cover and zenith angle). This means that the altocumulus field we simulate is nearly exclusively generating extreme irradiance variability by *forward escape*, even in high-albedo conditions. The 3D radiative effects should therefore be relatively simple to

reproduce by a diffuse forward projection of the clouds combined with attenuated direct irradiance, and may not require an expensive model like we are using.

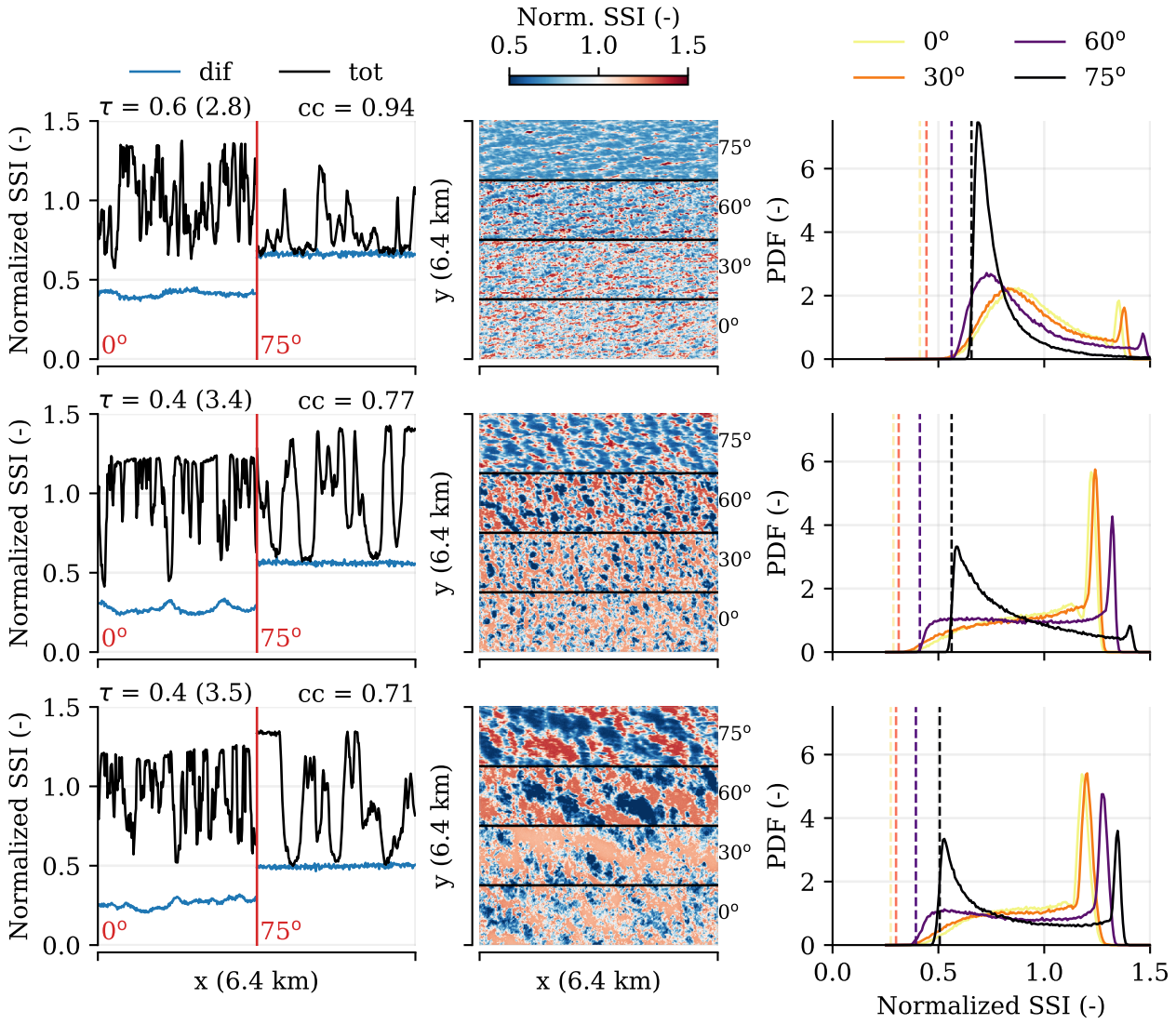

Figure 8.11: Surface irradiance effects of simulated altocumulus. The first column shows a section through the centre of the domain along the x-axis for a solar zenith angle of 0° and 75°. The centre column shows for all simulated zenith angles the total surface irradiance field. The right column shows the probability density functions of these fields, and adds the locations of the diffuse peak probability with the dashed lines. The rows are individual time steps (360, 1080, and 1800 s), accompanied by decreasing cloud cover (see also Figure 8.5). Surface albedo is 0.

8.4.5 How cloud depth enhances SSI

We will now introduce the fourth mechanism, *side escape*, by analysing vertically developed clouds, starting with the synthetic towering cumulus and followed by two types of simulated and isolated cumulonimbus. For all experimental results that follow, the Sun is located in the west (azimuth angle of 270 degrees), with a variable zenith angle θ, and albedo set to 0. Furthermore, integrated optical thickness is, for the most part, well beyond the *forward escape* regime in all experiments (typically $\tau > 50$), even when considering horizontally integrated optical thickness. There are two exceptions where *forward escape* still occurs. The first is at non-zero zenith angles, where direct irradiance passes through the corners of an (optically thick) cloud. The second is for the edges of the simulated cumulonimbus, which are in or near the *forward escape* regime ($\tau < 10$), even when vertically integrating τ. Before we further discuss these effects, we describe the general patterns of SSI for the simpler case of `towering cumulus` and the role of cloud depth in these patterns.

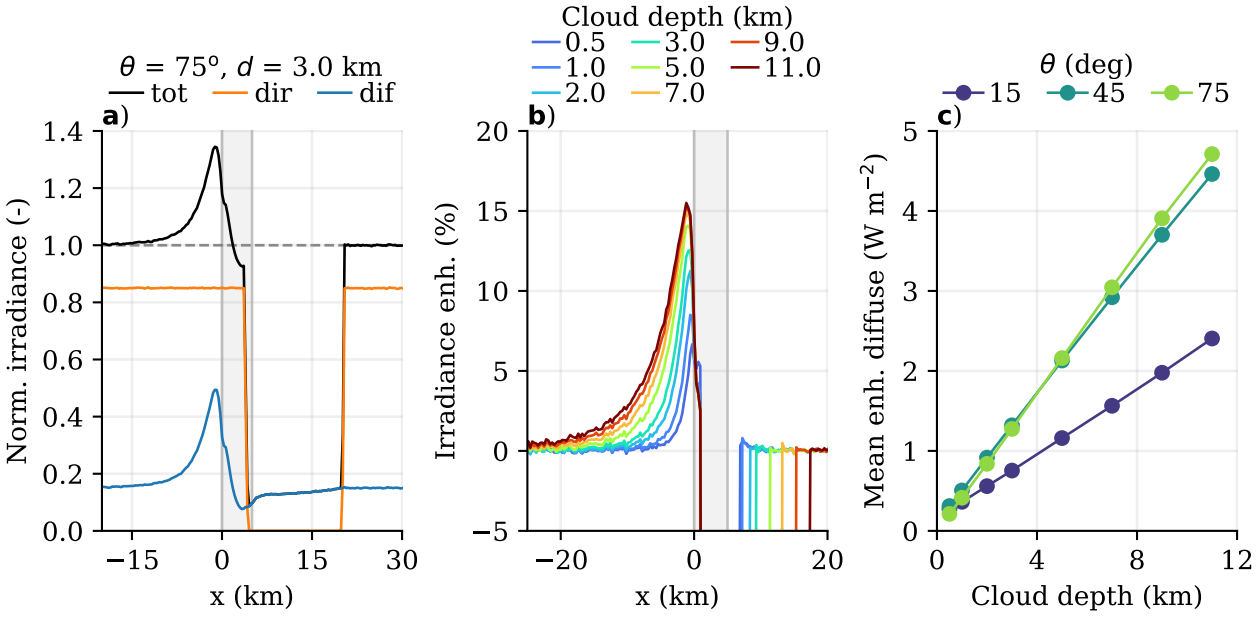

Figure 8.12: SSI pattern for an idealised towering cumulus. An example surface irradiance pattern is shown in **(a)**. The effect of increasing cloud depth on this pattern is shown in **(b)** for a solar zenith angle of 45°. Mean diffuse enhancement on the sunlit side of the cloud is shown in **(c)** for varying cloud depths and zenith angles. Cloud base is at 1000 m, surface albedo is 0. The x-axis is relative to the location of the sunlit cloud side.

Synthetic towering cumulus

A key feature of the SSI pattern in the presence of a vertically structured cloud is the significant irradiance enhancement on the sunlit side and (near) absence of enhancement on the shaded side. Figure 8.12a illustrates this for a `towering cumulus` 3 km in depth, 5 km diameter, and a 75° solar zenith angle. The SSI pattern is similar to the observed time series of a cumulonimbus passage in Figure 8.1c, with a peak of enhanced diffuse irradiance on the

sunlit side, a reduction underneath the cloud, and a return to (almost) clear-sky levels of SSI afterwards. As the `towering cumulus` increases in vertical depth, the rate of increase of the peak enhancement diminishes progressively, converging to a maximum of 15 % (for $\theta = 45°$, Figure 8.12b).

However, while the peak enhancement levels off, the area of influence extends further out, with IE still being a quarter of peak levels 10 km west of the sunlit side for the 11 km deep cloud. The total amount of diffuse enhancement in the domain scales linearly with cloud depth ($r^2 \approx 0.99$, Figure 8.12c). Both the levelling off of the peak irradiance enhancement and increased horizontal extent of the surface pattern is explained by additional scattering occurring at increasingly higher altitude, which result in additional scattered diffuse radiation being spread out over a larger horizontal area on the surface.

Total scattered irradiance on the half of the domain that is on the sunlit side of the cloud, including increased top of domain outgoing radiation, is close to 100 % of the scattered direct irradiance intercepted by the cloud side. Scattering off of cloud sides appears to be symmetrical in the vertical, at least for a perfectly straight and smooth cloud side, as half the radiation lands on the surface and half is radiated upwards out of the domain.

Simulated cumulonimbus

In the cumulonimbus simulations, the updraft cloud is more turbulent and textured than the perfectly smooth `towering cumulus`. The SSI patterns remain largely the same, with significant enhancement only on the sunlit side close to the cloud and increased enhancement over a large area with increased cloud depth (Figure 8.13a). However, the peak irradiance enhancement in the shear-free case is $\sim$ 30 % and remains fairly constant with increased cloud depth, unlike the `towering cumulus`. Once the anvil cloud reaches far enough out to completely shade the updraft from direct irradiance, peak irradiance enhancement reduces from 30 to 10 %, visible in the last two simulation snapshots in Figure 8.13a (18.4 and 17.2 km).

The dynamic evolution of the simulated cumulonimbus also alters the relationship of total diffuse enhancement we observe in the domain. We identify with three distinct parts, illustrated in Figure 8.13b. Initially, in part 1, the warm bubble that triggers the convection is wider than it is tall, and therefore diffuse enhancement is driven by *forward escape* and *downward escape*. During updraft growth, in part 2, the relationship between cloud depth and diffuse enhancement returns to the linear relationship observed for the `towering cumulus`. For higher zenith angles, diffuse irradiance is enhanced relatively more with cloud depth than for conditions with near overhead Sun ($\theta = 15°$). Finally, in part 3, the anvil growth takes over and accelerates the domain mean diffuse enhancement, whereas peak irradiance enhancement decreases as the updraft itself becomes shaded.

The disappearance of the peak irradiance enhancement due to anvil shading hints to *downward escape* and *forward escape* being the mechanisms driving the irradiance extremes, not *side escape*. In support of this, Figure 8.14 illustrates the relative position of the diffuse and

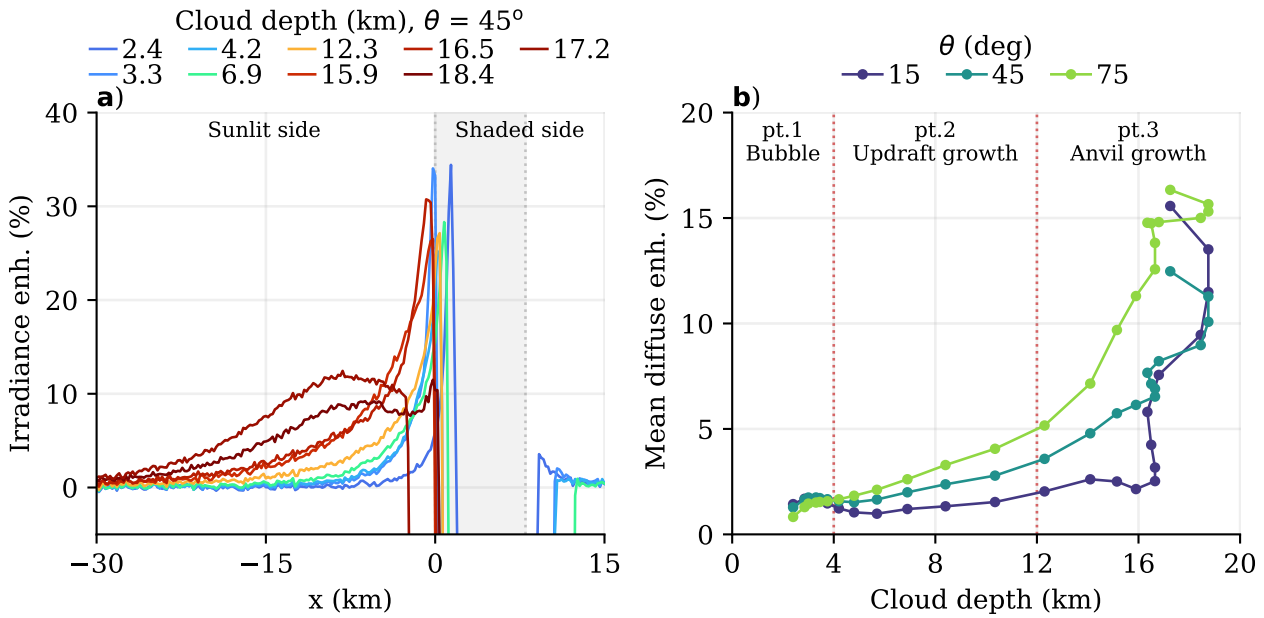

Figure 8.13: SSI patterns for a cumulonimbus in a shear-free environment. The pattern in **(a)** is an average over the updraft width in the y-direction. The grey shading marks the approximate position and width of the updraft. Domain-mean surface diffuse enhancement on sunlit half is shown in **(b)** as function of cloud depth. Simulation evolution is marked by three phases (further explained in the text). Surface albedo is 0.

total enhancement with respect to the cloud and direct irradiance path, with and without anvil shading. Without anvil shading, the peak diffuse enhancement lies directly underneath, and not in front of, the cloud edge at the sunlit side. Here, only *forward escape* and *downward escape* can occur, and thus these mechanisms drive peak enhancement. Most diffuse enhancement in front of the cloud comes from *side escape* before the anvil forms, as this scales with cloud depth. Once the anvil spreads out, it takes over the *side escape* mechanism and further enhances diffuse SSI by *forward escape* and *downward escape*, stretching out for $>$ 20 km relative to the cloud centre.

Tilting the updraft (with vertical wind shear) does not qualitatively change the SSI pattern with respect to the shear-free simulation, as illustrated in Figure 8.15. However, the relationship of domain averaged diffuse enhancement with cloud depth is not linear anymore during the updraft growth. Likely, the tilt results in a non-linear relationship between total sunlit cloud area as function of cloud depth, unlike the shear-free and idealised versions of this experiment.

Solar azimuth angle becomes important in this simulation, since the simulated cumulonimbus is not rotationally symmetric anymore, especially once the anvil develops and gets advected downwind, away from the updraft base. With the Sun in the west (upwind), there is no interference from the anvil cloud, and thus the peak irradiance enhancement underneath the cloud edge on the sunlit side remains. Illumination on the eastern (downwind) side of the cloud is quickly obscured by anvil shading. With the Sun in the south, the updraft base stays

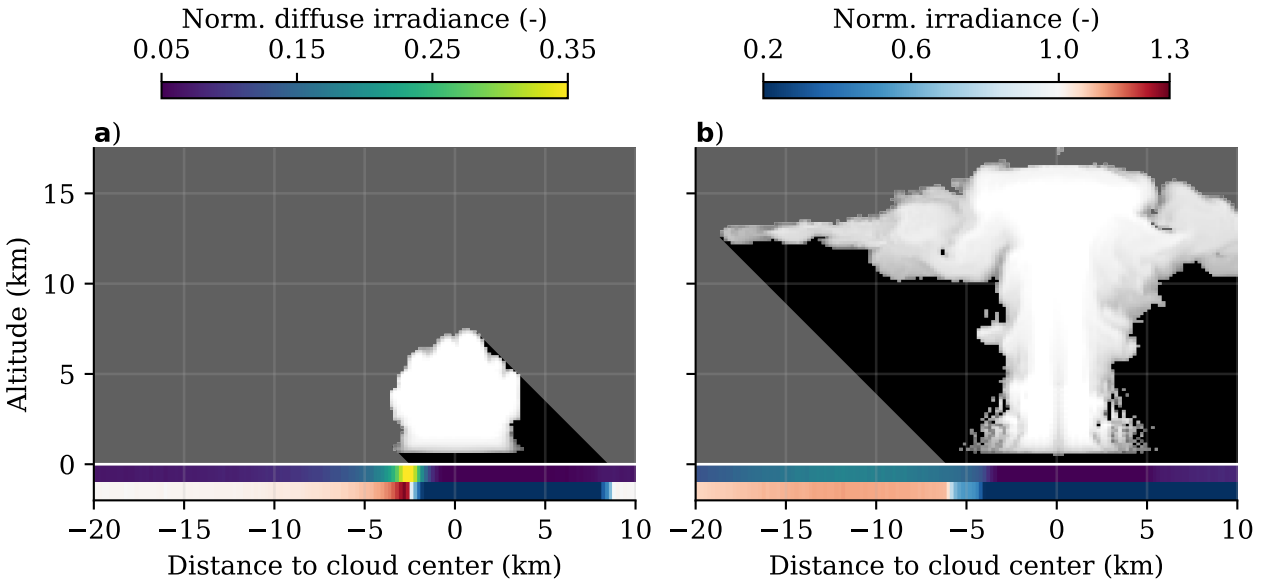

Figure 8.14: SSI peak location and the effect of anvil shading. An example surface irradiance pattern from the shear-free cumulonimbus simulation is shown at two time steps, one with and one without anvil shading. Solar zenith angle is 45°, surface albedo is 0. The cloud is visualised by a liquid and ice-water cross-section, taken exactly halfway through the cloud in the y-direction. Dark grey shading illustrates the area where direct irradiance is 0. Normalised with clear-sky surface solar irradiance.

sunlit with a slight extension of the anvil, and so peak and total irradiance enhancement on the sunlit side is among the highest. There is no clear relationship between solar azimuth angle and total diffuse enhancement, however. We think any differences will relate to the specific shape of the cloud and its orientation with respect to the solar angle, and hence will not generalise beyond this case.

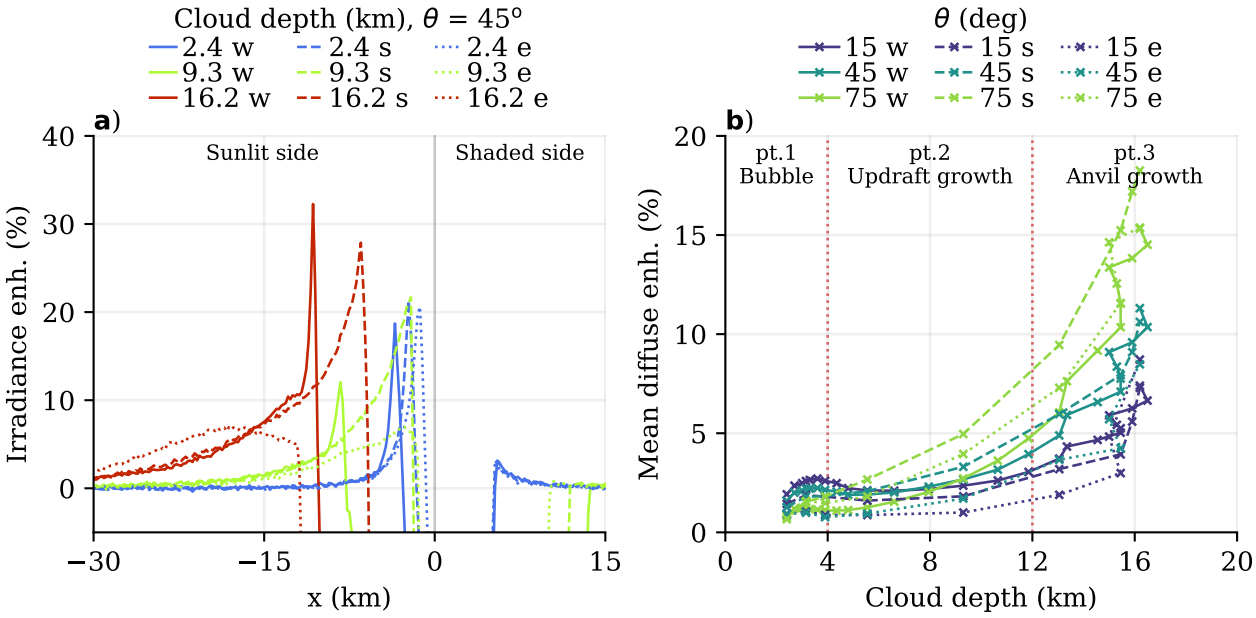

Figure 8.15: The effect of wind shear and solar azimuth angle on SSI in a simulated cumulonimbus. The surface diffuse enhancement is shown in **(a)**, similar to Figure 8.13. Now, the x-coordinate is centred in the middle of the domain rather than the cloud centre or side, so the pattern shifts as the cloud moves or dynamically evolves, and as the solar azimuth angle changes. The sun shines from the west, south, or east, labelled with w, s, and e, respectively. Data is rotated such that the x-coordinate follows the solar azimuth angle.

8.4.6 Free convection integrates all mechanisms

All clouds presented so far are either flat and horizontally structured, or vertically structured but isolated. In the last experiment, we want to give a first look at what happens under highly complex cloud fields, for which we use the simulated `free convection` case. After three hours of simulation time, the cloud field features a handful of deep convective clouds with large anvils, about as many newly developing cumulus congestus, and numerous cloud remnants of previous convection distributed throughout the domain. This cloud field and resulting SSI field for an intermediate solar zenith angle of 45° is shown in Figure 8.16.

One similarity with the cases of isolated deep convection is that peak irradiance enhancement occurs on the sunlit side of deep convective clouds, but in this case only when there is no shading from other nearby clouds. In regions furthest away from clouds, the enhancement decreases to a local minimum of $\sim 10\,\%$ (e.g., x = 25 km, y = 80 km). Regions with the highest irradiance enhancement are enclosed by an optically thick updraft to the east and a high degree of cloudiness in the other directions (e.g., x = 20 km, y = 20 km). *Forward escape* plays a partial role in this, but it can originate from multiple clouds and cloud layers. To mark these parts of the cloud field, we show areas where $\tau < 6$ at an altitude above 7 km in blue, and in red when below 7 km in Figure 8.16b. These cover 20 % and 10 % of the domain, respectively, and can overlap. Other cloud areas have high enough optical thickness for *albedo enhancement* to contribute.

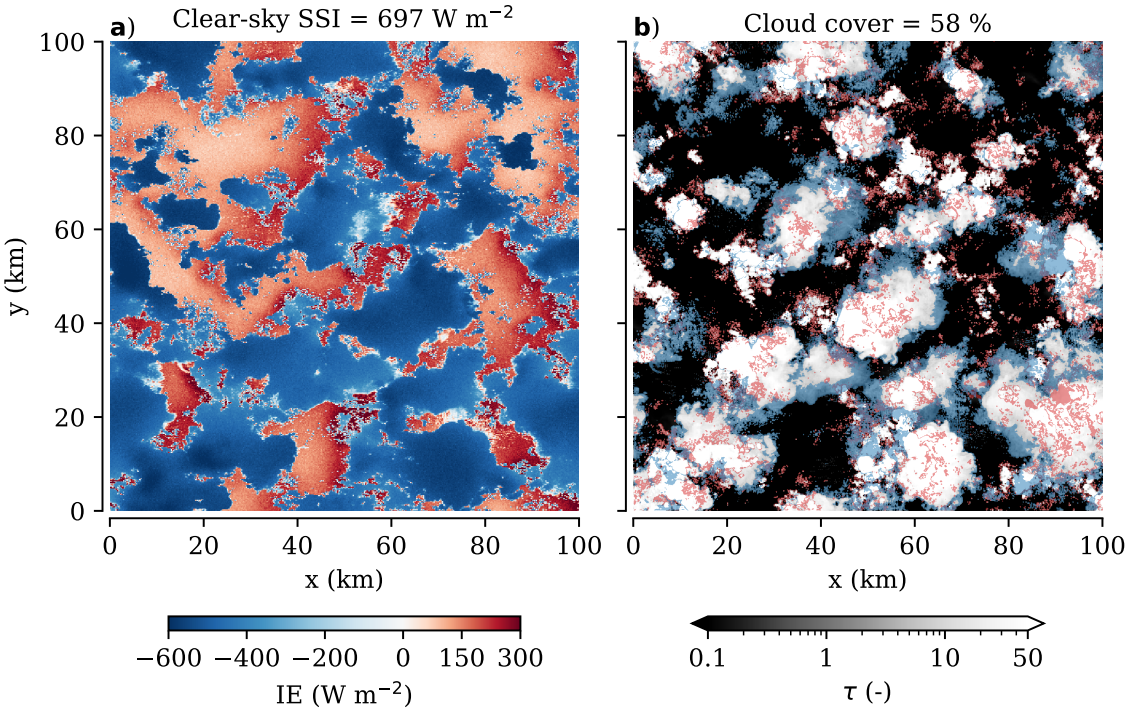

Figure 8.16: Irradiance enhancement in free, deep convection. Total surface solar irradiance relative to clear-sky is shown in **(a)**, for a solar zenith angle of 45°. Vertically integrated cloud optical thickness τ is shown in **(b)**. Clouds with $\tau < 6$ at an altitude above 7 km are marked in blue, or in red when below 7 km, to indicate regions where *forward escape* occurs.

What this simulation shows is that all four mechanisms can be active at once and be further complicated by having multiple deep convective clouds. The latter can be destructive to peak irradiance enhancement by anvil shading, or shading of other clouds, but also constructive by providing additional diffuse irradiance from multiple cloud edges towards areas already strongly enhanced by a sunlit cloud base. Finding an analogue in observations is unfortunately difficult, with the cloud field being this complex and the SSI patterns this large.

8.5 Synthesis and outlook

In this study, we performed numerical experiments to understand which main mechanisms drive surface solar irradiance extremes across a diverse set of prototype cases based on observations. We formulated four mechanisms, based on observations and prior research, that can explain the observed irradiance extremes: *forward escape*, *downward escape*, *side escape*, and *albedo enhancement*. First, we will synthesise the results of all the experiments. Then, we will discuss some limitations and potential future research directions, with a first look at what happens in the complex, multi-layered cloud field of unorganised deep convection.

8.5.1 Synthesis of results

For clouds or cloud fields that are much wider than tall, such as stratus or altocumulus, we find that the mechanisms driving SSI variability depend on cloud optical thickness τ. The transition zone between *forward escape* and *downward escape* is estimated to be between $\tau = 5.4$ and 6.3, for high and low surface albedo, respectively. In the presence of optically thin clouds ($\tau < 6$), *forward escape* drives enhancement of diffuse irradiance, which largely follows the path of direct irradiance. Cloud altitude determines the extent of horizontal smoothing of the forward scattered irradiance. It leads to smaller areas of higher extremes at lower altitude compared to more uniform diffuse irradiance from scattering at higher altitude. Increasing the cloud area increases the total amount of scattering, which explains the extremes observed and simulated in cloud fields with gaps like altocumulus.

For optically thick clouds ($\tau > 6$), irradiance is scattered uniformly downward, leading to irradiance extremes near cloud edges or cloud gaps. In the transition zone ($\tau \sim 6$), both *forward escape* and *downward escape* contribute to the irradiance extremes.

Once *downward escape* starts to play a role in SSI variability, the clouds are optically thick enough to produce multiple scattering events between the surface and cloud. Under high albedo conditions and optically thick cloud cover, diffuse irradiance is then further enhanced by surface albedo, and accounts for 10 to 60 % of the total irradiance enhancement depending on low (0.2) or high (0.8) albedo conditions, respectively. The `checkerboard` case shows little contribution of *downward escape*, thus *albedo enhancement* is negligible and only contribute to a further 10 % increase in diffuse irradiance for the highest surface albedo conditions (0.8).

For isolated deep convective clouds, the sides of the cloud act as a region where photons

diffusely escape, leading to large areas ($\sim$ 20 km) of relatively weak irradiance enhancements ($\sim$ 5 %) on the sunlit side of the cloud. Underneath the cloud edge, at non-zero solar zenith angles, the peak enhancement is 10 to 30 %, and is driven by *downward escape* and *forward escape* rather than *side escape*. Anvil shading onto the updraft of the cloud removes the local irradiance extreme found near the sunlit cloud edge.

8.5.2 Outlook

We have purposefully focused the majority of this study on understanding prototype cases of SSI variability that occur in single-layer horizontal or isolated vertical cloud fields. One reason for this is that observing the 3D structure of more complex cloud fields is very difficult, as ground-based observation typically can not see beyond the bottom of the first layer, and satellite observations not beyond the top of the highest layer. Reconstructing a prototype case to then numerically simulate brings too much uncertainty with it to disentangle the extra complexity that such a 3D cloud field provides. This is another way of saying that we do not have the observations to validate the case of simulated `free convection`, contrary to all other simulations in this study.

However, a next step would indeed be to expand this research to multi-layered cloud fields and non-isolated deep convective clouds. Multi-layer cloud fraction is estimated to be between 10 and 50 % globally (Li et al., 2015), highest around the equator and mid-latitudes, and mostly because of high clouds. It would be interesting to find out whether multi-layered cloud fields are additive in their effect on SSI, or if entrapment between layers results in significant non-linearity. As for non-isolated deep convection, a first analysis we did into this direction suggests such cloud fields produces irradiance extremes from a combination of all mechanisms formulated in this study. Furthermore, there is the additional effect of multiple clouds constructively or destructively combining their effects on SSI.

To better quantify how much each mechanism contributes to the total SSI variability, it would help to keep statistics of scattering events and direction of travel of photons. This is possible with ray tracing, but simply is not implemented in our model. Instead, we estimated the transition between *forward escape* and *downward escape* by sampling the diffuse SSI field given a cloud. With the extra statistics, however, this transition between mechanisms can be more precisely defined.

We have not separated out the effects of liquid and ice phase condensate in our analyses, but the contribution of each scattering mechanism may depend on cloud droplet phase as well. For example, this may be relevant for the cloud tops and anvils of cumulonimbus clouds in the upper troposphere, or in mixed-phase clouds, as is often the case in altocumulus (Barrett et al., 2017). The simulations with deep convection do not suggest there is a significant change in how the mechanisms behave once ice appears, however. Primarily, it is the overall 3D cloud geometry and optical thickness that determine how the SSI is affected.

In summary, the findings of our experiments provide a foundation to understand which mechanisms are at play for any given cloud or cloud field that is either flat and horizontally struc-

tured or isolated and vertically structured. We believe this is a good starting point for future analyses of surface solar irradiance under cloudy conditions, whether those are simple but more observationally constrained conditions than our prototypes, or perhaps maximum complexity like unorganized deep convection. In any case, the diversity of SSI patterns and extremes with the set of cloud fields we have demonstrated should motivate others to consider cloud fields beyond a single type, and likely include effects of surface albedo.

8.6 Open data

BSRN time series data is described in Chapter 2, and is available in Knap & Mol (2022) and Mol et al. (2022). Spatial SSI data of FESSTVaL is described in Chapter 7, and is available in Mol et al. (2023a). Model code, setup files, output data, Veenkampen time series data, spatial SSI patterns, and python scripts to analyse and visualise the data are available at `https://doi.org/10.5281/zenodo.11503609`.

Chapter 9

General discussion

Introduction

This marks a good moment to take a step back and discuss where we now stand in relation to the motivation, questions, and methodology laid out in the general introduction, and where to go next. A summary of all results can be found in the very beginning of this thesis, but some of them I want to reflect on further in this discussion.

In the previous chapter, I developed theory to consolidate the insights gathered throughout doing the research presented in this thesis. The analysis revealed that four key mechanisms answer the overarching research question of this research: *How do clouds drive surface solar irradiance variability?* The mechanisms are *forward escape*, *downward escape*, *side escape*, and *albedo enhancement*, and their relative importance depend on cloud properties and surface albedo. Although these mechanisms are not sufficiently quantified to directly build a model from, they provide a foundational understanding to explain surface irradiance variations for any cloud field.

The foundational understanding presented in Chapter 8 forms the basis of this discussion, which I organise in four themes. Firstly, in Section 9.1 I reflect on the diversity of clouds and variability in surface solar irradiance (SSI). Next, I discuss our experiences with model validation using the new spatial observations in Section 9.2. Based on these experiences and other findings in this thesis, I suggest improvements to future fieldwork campaigns in Section 9.3. Lastly, where cloud-scale SSI variability occurs most and how it affects the global and climate scale is an open question. In Section 9.4, I share my ideas on how to best proceed in answering this question. I offer a final reflection on the motivation of this work in Section 9.5

9.1 Diversity in clouds and their 3D radiative effects

9.1.1 Clarifying variability in surface solar irradiance

This thesis deals with variability in the atmosphere, and in particular with cloud-driven variability in surface solar irradiance (SSI). Yet, the term *variability* sometimes obscures what we are really studying: the way clouds intercept and distribute incoming solar radiation on the Earth's surface. These cloud effects are most pronounced in the presence of variability and thereby have the most impact. Variability at cloud-scale is also where models are most likely to fail, either due to oversimplifying radiative transfer or by not resolving clouds in the first place. Most of the work in this thesis therefore focuses on variability.

But it is not just about *variability* in the sense of *not being constant*. High amounts of diffuse irradiance and enhancement of irradiance above clear-sky values are also 3D radiative effects that can have significant implications of their own. To name two, photosynthesis is higher if radiation is relatively diffuse (Gu et al., 2003; Mercado et al., 2009), and satellite retrieval algorithm accuracy is affected by horizontally scattered radiation (Wagner et al., 2023). These 3D effects only loosely correlate with variability. Cumulus and altocumulus cloud fields can

both create significant variability, even when only considering the attenuation of direct irradiance. Yet, it is the horizontal distribution of scattered radiation that sets the two cloud fields apart. In this discussion, I refer to the full range of 3D radiative effects with the term *variability* and explicitly mention nuances therein when relevant.

9.1.2 Cloud effects differ per type, but classification is prone to error

Cumulus clouds emerged as the primary driver of irradiance variability from 10 years of 1 Hz measurements, accounting for over half of irradiance peaks and shadows (Chapter 6). These cumulus clouds are studied by many due to their pronounced effects on surface irradiance and frequent occurrence (e.g., Tomson & Hansen, 2011; Madhavan et al., 2017; Jakub & Mayer, 2017; Lohmann, 2018; Gristey et al., 2019; He et al., 2024). In contrast, observations and simulations from Chapters 7 and 8 have shown altocumulus and various other mid- and high-level cloud fields to have a high potential in driving surface irradiance variability, often with irradiance extremes exceeding those typically observed with cumuli. This potential other cloud types have is not new information, given for example the work of Falconer (1965) and Ylivinkka et al. (2020) who linked patterns of surface irradiance variability to many (combinations of) cloud types, or the relevance of altocumulus identified by Schade et al. (2007) and Yordanov et al. (2015).

Why, given the potential for variability of other cloud types, do cumulus clouds account for most shadows and irradiance enhancement peaks based on the analysis in Chapter 6? And, surprisingly, why do clouds categorised as *altocumulus* or *cumulonimbus* not show any potential in driving irradiance enhancements, based on Figure 6.4?

Likely, this can be explained by limitations of the methodology used to classify clouds, which already made us careful in drawing conclusions about specific cloud types. In altocumulus, the size of gaps or of individual altocumuli is in the order of 100 meters, far below the resolution of the satellite pixel we used (4×4 km^2, see also Figure 9.1). Second, the cloud top pressure used to distinguish between cumulus and altocumulus is fixed at 680 hPa. But the distinction between cumulus and altocumulus should be whether they are coupled to surface heat fluxes in the atmospheric boundary layer (cumulus) or are uncoupled from these fluxes and exist in the free troposphere (altocumulus). The altocumulus we describe in Chapter 7 would be incorrectly classified as cumulus if we followed the methodology in Chapter 2.

While cumulus clouds are undeniably a significant and common driver of radiation variability, their overall importance may thus be overestimated at the expense of other cloud types. Coming back to the definition of *variability*, using peak irradiance enhancement as a proxy for all 3D radiative effects may also downplay cloud types that cause high amounts of diffuse irradiance or have a large area of influence. This motivated us to study a broad spectrum of clouds types in the final Chapter 8 and move away from the focus on cumulus.

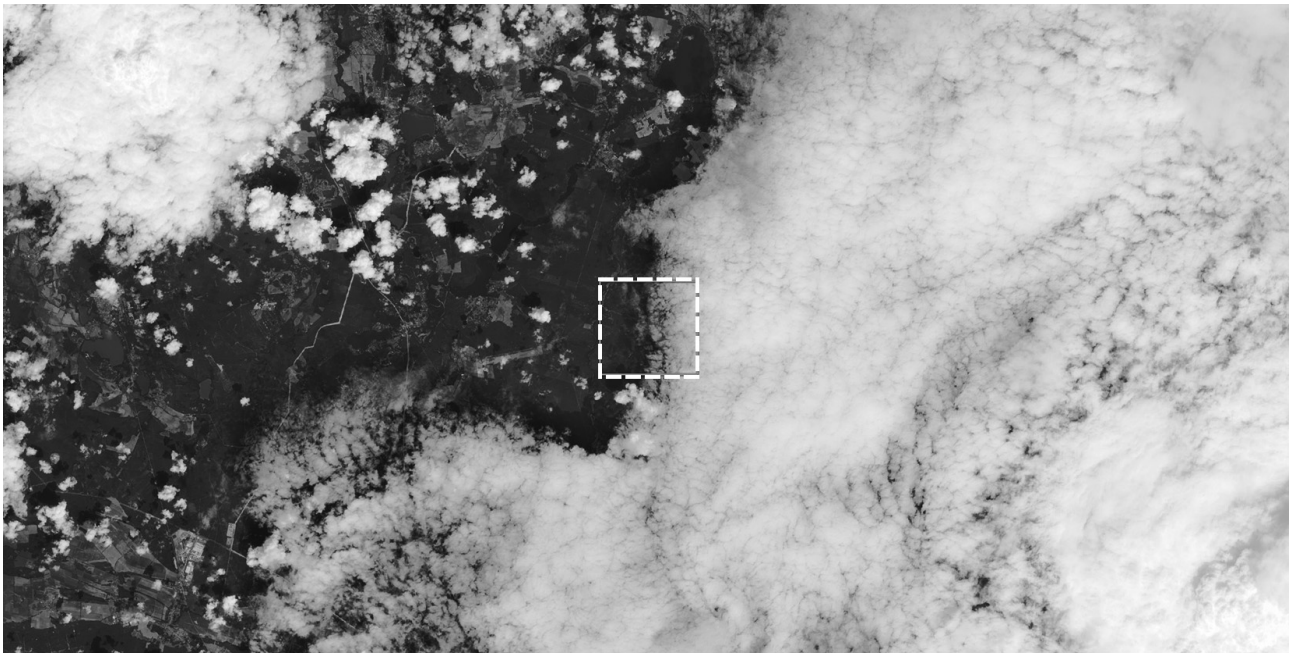

Figure 9.1: Cumulus and altocumulus during FESSTVaL. Satellite image taken by Sentinel 2 (10 $\times$ 10 m^2 resolution) taken at 10:26 UTC on June 25, 2021 of part of the FESSTVaL campaign area. The 4 $\times$ 4 km^2 box in the centre represents a single Meteosat Second Generation pixel. Copernicus Sentinal-2 L2A image retrieved with `https://apps.sentinel-hub.com/`.

9.1.3 Variability beyond single cloud types

Categorising clouds in specific types helps to communicate and identify broad regimes of 3D radiative effects that are often linked to specific meteorological conditions. However, the spread of cloud properties within a cloud type and even the definition and classification of these types, as just discussed, can vary greatly. Furthermore, clouds of various types frequently co-occur, illustrated in Figure 9.1, and cloud fields may also be multi-layered and vertically overlapping. Li et al. (2015) found the zonal average of multi-layered cloud cover to be between 10 and 50 %, depending on season and latitude. In the FESSTVaL campaign, most cloud fields were multi-layered and contained multiple cloud types — too complex for use in our initial analyses.

Perhaps it is more productive to study 3D radiative effects of clouds not per type, but as a function of cloud (field) characteristics that are important to generating variability (I will discuss which characteristics shortly). In fact, any cloud field with a high coverage and some degree of brokenness is all that is necessary to create a strongly enhanced diffuse irradiance field with superimposed intermittent direct irradiance. This is irrespective of optical thickness, that is, cloud fields do not need to be able to cast shadows to cause high variability in solar irradiance at the surface.

9.1.4 Outlook

Future research into cloud-scale SSI variability should respect the full spectrum of optical properties and configurations in which clouds occur. Results from Chapter 8 take a first step in that direction by reducing the complexity of variability generated by clouds to four mechanisms which are agnostic to cloud type. That is, the mechanisms depend on cloud geometry, cloud water (liquid + ice), and cloud altitude, or essentially the 3D distribution of cloud water in the atmosphere. I think this provides enough information in terms of clouds for a simplified radiative transfer model to resolve 3D solar irradiance variability.

However, the work in Chapter 8 has barely started to cover the full range of possible cloud field configurations. More quantitative results and inclusion of more complex cloud fields are obvious next steps towards building such a simplified 3D model of radiative transfer. It is also still unknown which conditions, categorised in cloud types or not, drive most of the variability in SSI globally. More on the unknowns in Section 9.4. First, I will discuss the model validation and fieldwork in light of the findings in this thesis.

9.2 Model validation with cloud-scale observations

The spatial observations of SSI we gathered during the FESSTVaL and LIAISE campaigns have been essential to characterise cloud-scale SSI variability (Chapter 7). In the Introduction of this thesis, I discussed that a motivation for gathering specifically spatial observations was to validate SSI in cloud resolving models. I also suggested modelling as a way to enrich observations and thereby get a more process-based understanding. Spatial observations were therefore initially gathered in an equidistant rectangular grid with a 50 m spacing, which mimics the grid of a cloud resolving model, enabling a direct comparison between the two.

Ultimately, this direct comparison has not proven to be useful, and yet we have been able to learn a lot about how clouds drive SSI variability. In this section, I will discuss the limitations of direct model validation we encountered and how we circumvented these limitations to validate and learn from a model anyway.

9.2.1 Challenges in comparing models with observations

Observations do not capture enough of the surface solar irradiance field

During fieldwork, it quickly became apparent that a rectangular grid with 50 m spacing was neither large enough to capture the size of patterns made by most cumuli, nor dense enough to resolve the finer structures made by cloud edges or fractured clouds. We could mimic these observations in the model by sampling simulated SSI fields in an identical grid layout. This allowed for a direct comparison with the same limitations, and fine scale structures did not matter as the model did not resolve scales below the observed resolution anyway.

The real problem, however, is the lack of statistical convergence of the observations in case

studies. Only a handful of cloud passages are partially captured within an hour, whereas the entire cloud field, which already covers a range of different clouds, is dynamically evolving throughout the day. Partially observed patterns of single clouds are not representative of the whole cloud field, and so statistics of SSI can show agreement or disagreement between model and observations for no other reason than random chance, illustrated for two cumulus cases in Figure 9.2.

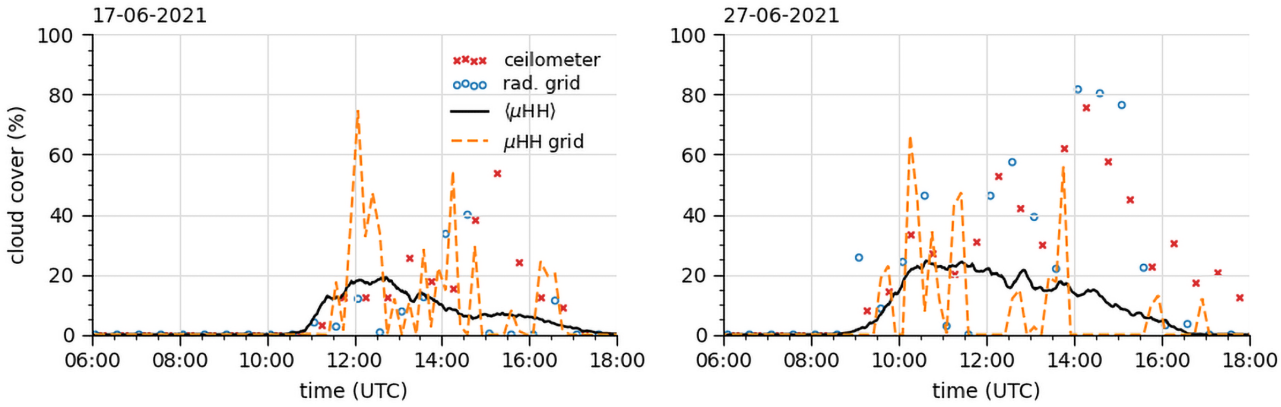

Figure 9.2: Cloud resolving model and spatial observations in disagreement? Two case study large-eddy simulations using MicroHH compared to observed estimates of cloud cover at Falkenberg, during the FESSTVaL campaign. Cloud cover is derived from radiation measurements based on a 50 % threshold reduction in SSI compared to clear-sky at 30-minute intervals. A simulated observation grid (50 m horizontal resolution) shows how representative the observations are for the whole simulated cloud field. *(Figure courtesy of Menno Veerman and Bart van Stratum)*.

Simulated clouds do not match observations

How to distinguish between modelling errors in radiative transfer calculations and errors caused by incorrectly resolved clouds? There are many aspects to get right in resolving clouds, depending on the level of accuracy that is expected in terms of SSI, assuming perfect radiative transfer calculations. As mentioned before, SSI at one given time is primarily controlled by the 3D distribution of cloud water. A mismatch between observation and simulation in typical cloud horizontal size can already lead to differences in SSI distributions beyond errors due to simplifications in radiative transfer calculations.

In some cases, differences in SSI distributions actually cause cloud properties (such as total liquid water) to change (e.g., Jakub & Mayer, 2017; Veerman et al., 2022). We may see such sensitivity to radiative transfer calculation errors in other radiation-driven clouds as well, such as altocumulus (see Figure 8.5). Another example is the under-resolved variability at the hourly scale in observation-driven large-eddy simulation (van Stratum et al., 2023). Incorrectly simulated clouds and their impact on surface properties may explain part of the mismatch between model and observation in Figure 9.2.

9.2.2 Indirect validation through mechanism and process understanding

How, then, can we validate models and still derive something useful from them? I have found an indirect, process-based method productive, and will illustrate this method by three examples.

Resolve irradiance enhancement patterns

A fundamental aspect for a radiative transfer model to include is the horizontal transport of radiation. Is irradiance enhancement resolved? Is the order of magnitude of the enhancements and the position relative to the cloud (field) correct?

Time series and spatial observations have been essential is characterising how these patterns should look for many cloud fields. High quality time series with separate diffuse and direct irradiance measurements show how variability in SSI can be formed by different combinations of constant or variable direct and diffuse irradiance. Spatial patterns of individual small clouds or passages of larger ones provide a unique view of SSI at cloud-scale, some of which are shown in Figures 7.10, 7.12, and 8.2.

Consistency between cloud field and SSI variability

There is robust evidence of power law scaling in SSI variability and a causal link to cloud size distributions, as we have shown in Chapter 6. If a model is externally forced with radiation, it should thus include this range and distribution of scales in SSI variability (matched to scales of the process being simulated). If the model is supposed to resolve this variability by itself, then, similarly, it should reproduce power law scaling and cover a wide range of spatiotemporal scales. However, if it fails to produce a cloud field with the correct scales, the resulting SSI variability should still be internally consistent, which can be checked.

Mechanisms of variability

The previous two examples have given me confidence in the model I have used in Chapter 8. Variability did not need to be fully resolved as long as it was consistent within the model, and spatial patterns of SSI closely matched the magnitude, location with respect to the cloud(s), and partitioning of diffuse and direct irradiance of the diverse set of observations. Using the model has resulted in a better understanding of how the observed patterns are formed, which suggests there are specific regimes of scattering. You can now validate whether your model is correctly responding to a change in surface albedo given the cloud cover and optical thickness of the cloud field and if cloud sides scatter radiation proportional to the cloud depth, for example.

9.2.3 Limitations of indirect validation

The given examples of indirect validations are on the qualitative side, but if the model behaves as expected for a wide range of cloud fields, then I consider this as evidence of the model being able to accurately resolve SSI variability. However, the higher the demands for

accuracy are, the more quantitative validation needs to become. Details influencing radiative transfer, such as cloud droplet size distributions, will start to play a more significant role in modelling accuracy. Spatially resolved observations of surface solar irradiance will continue to be necessary. In the next section, I will share my thoughts on how to do future fieldwork of this kind.

9.3 Fieldwork recommendations

There are two main reasons for gathering more spatial observations of SSI. First, more conditions need to be sampled to have validation data that is representative of the full range of possible clouds. Second, quantitative validation requires much more spatial data to get representative and robust statistics for a single cloud (field). Both reasons are important as we are trying to understand and resolve SSI with more realistic and complex cloud fields.

Given the effort involved in gathering such observations, I have four suggestions to improve upon our fieldwork strategy. These are based on lessons learned in model validation and more broadly the insights from this thesis. In short, these are improving the spatial network layout, partitioning diffuse and direct irradiance, observing clouds better, and capturing the whole spectral range of solar radiation.

One thing that does not need to be improved is the temporal sampling resolution of 10 Hz. We found 10 Hz enough, and for many purposes (above vegetation) it may already be enough to sample at a frequency of 1 Hz − as long as the instrument responds at least as fast.

9.3.1 Optimize observational network layout

Apart from deploying more sensors for longer, which is challenging due to the practical constraints of fieldwork, the network layout can be optimized to observe more SSI variability and spatial patterns with a similar amount of sensors. Knowing that a direct model comparison is not necessarily useful, we can make two changes to the standard rectangular grid layout. One change is to move to a variable grid spacing, combining a larger total domain size with locally higher resolution in an effort to capture both large and small structures. The second change is to use a triangular grid layout, since three points are enough to determine the direction and speed of passing patterns.

Concretely, a starting point of a new layout would be an equilateral triangle divided up 5 times in the centre, as illustrated in Figure 9.3. This only requires 18 sensors. Setting the long side to 1 km would give $1 / 2^5 = 31.25$ m resolution in the centre, while covering an area that is 144 times larger than the rectangular grid with a 50 m spacing. Of course, resolution is lost in the outer triangles, but dividing these up once would only require an additional 6 sensors for a total of 24, illustrated with the additional orange points in Figure 9.3b.

It is worthwhile to test beforehand what a more optimal layout would be, given the effort involved in planning fieldwork and deploying the network. The network we deployed in LIAISE had a non-equidistant layout, with an arrangement of sensor in the scintillometer

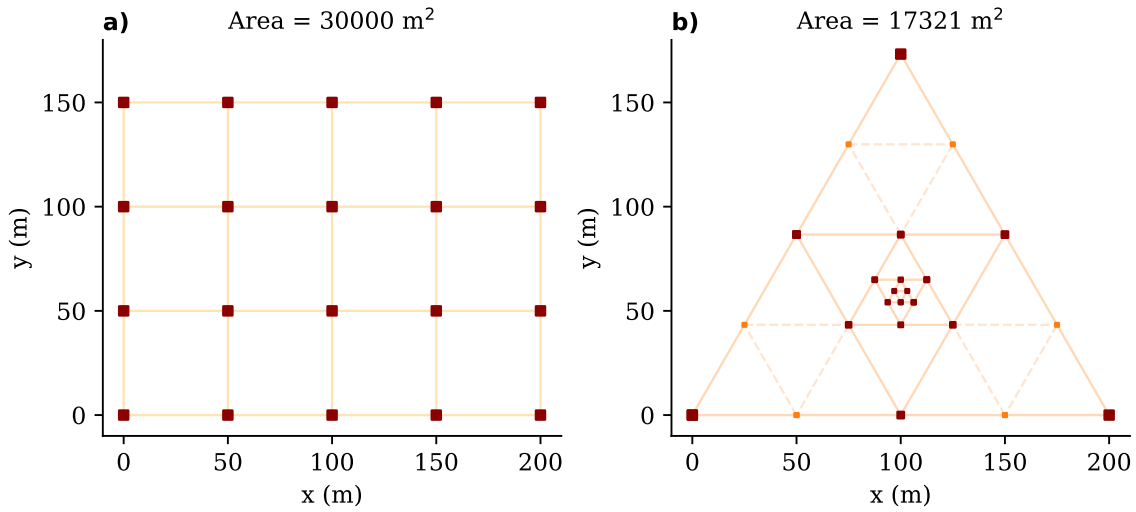

Figure 9.3: Rectangular versus triangular. Keeping the long side the same (200 m), for easier visual comparison, the triangular layout in **(b)** encapsulates approximately half the area, but reaches a resolution of 6.25 m in the centre with 18 compared to 20 sensors. Red points mark the sensor locations, which in a numerical model would mark grid cell centres. Orange points are extra sensors to increase the resolution in the outer triangles.

footprint within the rectangular grid. Unfortunately, most days were clear-sky or otherwise lacking in broken cloud cover to get an idea of the benefits of this other layout. Testing how much of the total variability a specific grid layout resolves could instead be estimated by performing synthetic measurements with high resolution simulation, similar to the validation attempt shown in Figure 9.2. It does not necessarily matter if the simulation resolves the full variability accurately. Rather, it can give a good first estimate based on how much of this resolved variability would be captured with a specific observational network layout.

9.3.2 Capture diffuse irradiance

Diffuse irradiance contains the essence of 3D radiative effects of clouds. Because the spatiotemporal variability of diffuse radiation is much lower, a similar amount of sensors as in Figure 9.3 would capture more of the spatial variability if put in a layout optimised for the scales of diffuse irradiance. It would be interesting to compare how such a layout differs from a standard one, which can also be tested with simulated measurements.

If a diffuse measurement network is indeed effective and easier to deploy, it would be worth designing solutions for blocking direct irradiance. 3D printed shadow rings are a low-cost option to keep the instruments such as FROST scalable, as long as the reliability and operability of the sensors is not affected. A few unmodified sensors in combination with cloud cameras would be enough to estimate direct irradiance, as this radiation component is a relatively straightforward projection of cloud optical thickness. Such a modification to our instrument would in any case be highly interesting, as it allows to sample the spectral composition of scattered and unscattered solar radiation separately.

9.3.3 Observe clouds in detail

Having information about the cloud field is essential for understanding the observed SSI and for reproducing and validating simulations of observed cloud fields. Information from simple camera imagery has proven invaluable for the work in Chapter 7. The two consumer-grade action cameras we used in the FESSTVaL and LIAISE campaigns gave a first impression of the relationship between surface irradiance measurements and the overlying cloud field and served as validation for the derived surface patterns of SSI (e.g. Figure 8.2). Hence, these inexpensive cameras were foundational for the hypotheses in Chapter 8.

One problem, however, was the limited field of view of the southward directed cameras. This lead to guesswork about potentially important clouds that were outside the field of view. Depending on the budget and practical constraints, a third camera pointing upwards and to the north would largely fill in the gap that our two-camera setup had. With waterproof casings and expandable battery packs, these cameras are flexible, low-cost, and easy to deploy.

More advanced and expensive options are skyview cameras, these capture the whole hemisphere, or a stereographic camera system from which 3D cloud geometry evolving over time can be reconstructed (Romps & Öktem, 2018). The latter system, while limited to shallow cumulus, is also a great way to validate if a model correctly simulates cloud geometry. In addition to visual data, ceilometers, lidars, and microwave radiometers are great instruments for estimating vertical atmospheric properties, such as cloud base height, integrated liquid water, temperature, and humidity. Radiosondes can also be helpful in estimating the altitude of cloud layers, which for example gave the estimate of 2850 m for the June 21 altocumulus height in Chapter 7, consistent with the ceilometer.

The sampling frequency for any cloud-observing instrument is ideally similar to that of the irradiance observations (1 Hz). For cloud type and cover classification, 1-minute resolution may be enough, but for more in-depth studies or intensive field campaigns, I recommend going to 1-second resolution. This allows for a more exact matching of the cloud field with surface irradiance observations, which, as shown throughout this thesis, can be dynamic and rapidly evolving.

9.3.4 Measure the whole wavelength spectrum

More complete spectral measurements will reduce errors made in total SSI derived from incomplete spectra, and provide more detail of wavelength-dependant radiative transfer. In our measurements, there were two key parts of the solar spectral radiation missing: ultraviolet ($\lambda < 410$ nm) and near-infrared ($\lambda > 940$ nm), which account for respectively ~ 10 % and ~ 30 % of the total spectral irradiance. UV radiation is known to vary differently than total irradiance with cloudiness (Calbó et al., 2005), and near-infrared features multiple H_2O-related absorption bands. We have found significant shifts in the spectral properties in direct and diffuse radiation under different cloud conditions, and it would thus be interesting to see how these shifts extend to the full spectrum at cloud-scale.

Covering the full spectrum reduces error in total SSI estimates. We found missing information

in the near-infrared spectrum leads to positive biases up to 10 % in estimated total SSI in overcast conditions, as we assume longer wavelengths change similar to the average of the range we measure (410 to 940 nm), whereas they are relatively more absorbed. Similarly, we make assumptions about changes in near-infrared to explain shifts in spectra under broken cloud conditions (Chapter 7), although these did not concern fully overcast conditions and thus involved smaller errors.

9.4 Global impact of cloud-scale SSI variability

9.4.1 Deriving a global potential for surface solar irradiance variability

Which cloud configurations, through cloud cover, optical thickness, altitude, and their geometry, are most important for surface irradiance variability? While we identified and explained diverse conditions highly conducive to variability in SSI in Chapter 8, we did not quantify the relative frequency with which they occur in reality, on a global scale. This largely remains an open question, and answering it will focus efforts in resolving SSI variability where it matters most.

Single location or local case studies play a role in identifying the specific conditions under which irradiance variability and high amounts of diffuse irradiance occurs, as done throughout this thesis. These conditions can then be looked for elsewhere, globally and year-round. For example, cumulus clouds and deep convection over land may be more linked to locations and times of year with high surface heating, whereas altocumulus and other mid-level clouds may be more linked to specific synoptic conditions found in the mid- and high latitudes. Here, we can integrate observations from the domain of remote sensing and meteorological surface-based cloud climatology and combine them with (re)analyses data of surface albedo and calculated solar zenith angles.

The answer may very well be that nothing concrete or certain emerges from this exercise, which would only underline the need to acknowledge the full diversity of cloud fields in any study of 3D cloud-radiative effects. Concrete answer or not, it gives a clear direction for where efforts of fieldwork and model development should be focused.

9.4.2 Geographical diversity: complex terrain and open water

There are some caveats to deriving the global potential of SSI variability based on studies that may be biased towards their own geographical location and cloud (+ aerosol) climatology. I will discuss two areas that require specific attention.

Complex terrain

In complex terrain, there is the direct effect of shading caused by hills or mountains and subsequent scattering of intercepted radiation. Furthermore, at higher altitude the air is typically cleaner and drier, resulting in increased total solar irradiance with a relatively low fraction of diffuse. When accounting for factors such as slope angle, elevation, and albedo,

surface irradiance in complex terrain under clear-sky conditions can be modelled reasonably well (e.g., Oliphant et al., 2003).

However, how complex terrain and higher altitudes affects overall surface irradiance variability, and specifically how the link between cloud and surface irradiance patterns change, is not at all trivial. Albedo alone can have a quite dramatic effect already, as shown in Figure 9.4. And the highest known value of SSI in literature, a 2177 W m^{-2} peak in SSI, occurred at 5148 m above sea level in the Altiplano, Chile (Cordero et al., 2023). Based on MODIS satellite data, this peak occurred in the presence of optically thick convective clouds, some with anvil cirrus, suggesting the peak is driven by a non-trivial combinations of all four mechanisms we identified in Chapter 8.

Figure 9.4: Not so shaded mountain valley. Fresh snow on the sunlit side scatters part of the sunlight back and brightens up the shaded side of a valley in the Alps (Austria).

Open water

Studies of surface solar irradiance variability are nearly exclusively performed over land, whereas the Earth's surface is for $\sim$ 70 % covered by water surfaces. Aside from directly absorbing solar radiation, the ocean takes up a significant amount of carbon through photosynthesis (Keeling & Manning, 2014), primarily by algae, and is full of complex life depending on sunlight (DeLong & Karl, 2005). In addition, floating photovoltaics on open water bodies is being considered as a way to expand solar energy production

(Hooper et al., 2021; Jin et al., 2023). In deriving global SSI variability potential, it is thus important to consider the differences between land and sea.

Findings in this thesis are largely applicable to the open sea, accounting for two key differences between land and sea: surface albedo and cloud climatology. Effects of surface albedo can be readily accounted for, water namely has a near-zero albedo (~ 0.06), reducing the complexity of solar irradiance variability by one potential mechanism. Less trivial to account for is the potential difference in cloud properties, as most observations are biased towards clouds that are formed over a land surface or indirectly influenced by it. To the best of my knowledge, there are no spatial measurements or time series of SSI at cloud-scale over the ocean.

9.4.3 Longwave radiation variability

Because many clouds are driven by a net radiation imbalance at the surface (cumulus) or cloud layer itself (e.g., altocumulus), there must be some discussion of the role of longwave radiation. Surface longwave irradiance variability is closely tied to clouds and is inherently diffuse and 3D in nature, thus sharing some familiar themes with (shortwave) solar irradiance. Capturing the full extent of longwave variability is likely possible with standard observational techniques, such as the Baseline Surface Radiation Network (BSRN) stations, similar to how diffuse solar irradiance does not require a spatial network as dense as one for total irradiance. In fact, the BSRN station we used in Chapters 2 and 6 has logged the full radiation balance at a 1-second resolution.

Figure 9.5 shows some of this longwave radiation data in a time series compared to net radiation under variable conditions of cloudiness of the BSRN station in Cabauw. Here, you can see the anti-correlation between net longwave and shortwave radiation, which dampens the SSI variability in the net surface radiation balance. The magnitude of variability is an order of magnitude lower, however, with tens of W m^{-2} compared to hundreds of W m^{-2} for SSI. Whether the anti-correlations holds for other conditions than this 2-hour example, and when or why not, remains to be seen.

9.4.4 In-canopy spectral irradiance and diffuse fertilisation

In the back of this thesis, you will find a list of publications, among which is a dataset of a network of spectral measurements of SSI in the Amazon rain forest. Rather than just a horizontal network above canopy, a set of FROST sensors was deployed in a vertical profile in the canopy to measure the extinction of spectral solar radiation with height. We measured this because cloud-driven SSI variability does not just stop at the surface, but often extends into vegetation, which in turns greatly enhances the variability and modifies the spectrum through absorption and scattering. How vegetation influences in-canopy radiative transfer and how photosynthesis (including carbon uptake), evapotranspiration, and land-atmosphere coupling as a whole responds to this variability remains largely unknown (Vilà-Guerau de Arellano et al., 2023). One factor is more efficient photosynthesis under diffuse irradiance

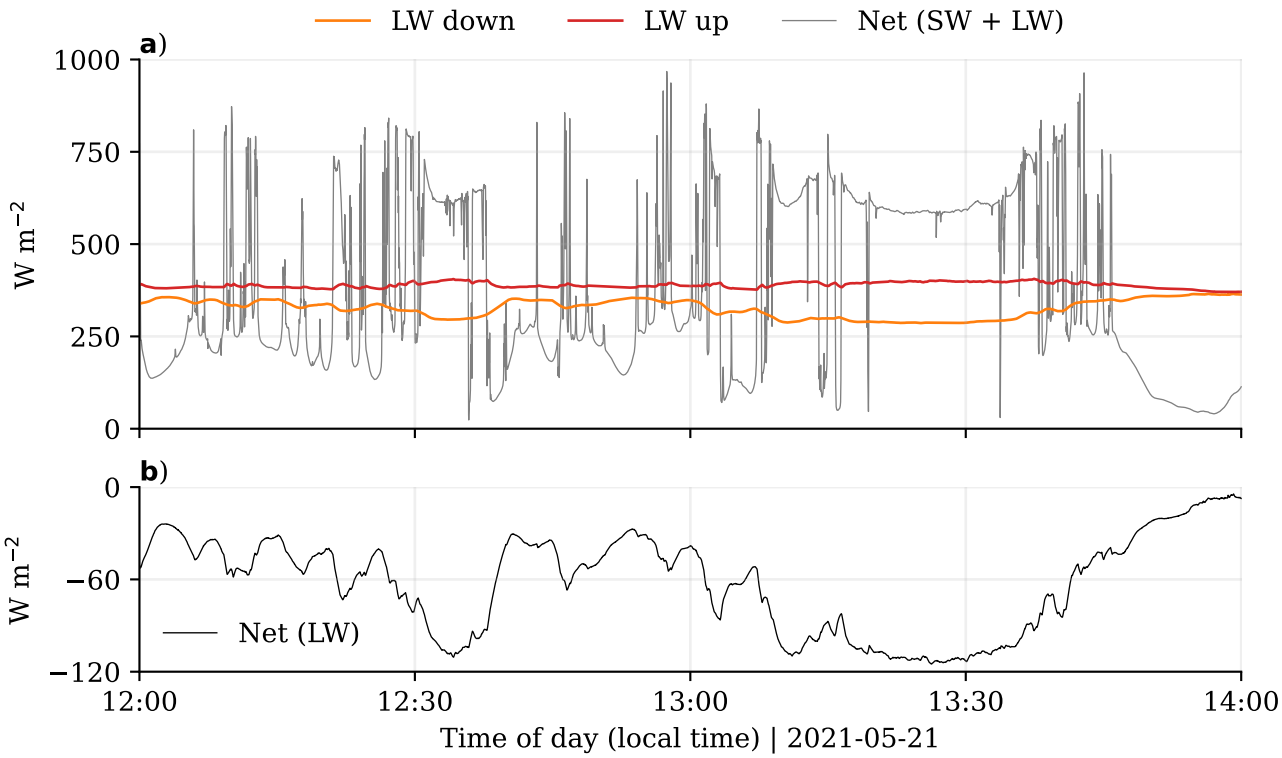

Figure 9.5: Longwave variability is also connected to clouds. Time series of surface solar and thermal radiation, both up and down, measured by the BSRN station in Cabauw (Chapter 2). In **(a)**, the net surface radiation balance is shown, with the two longwave components separately. Most variability comes from shortwave irradiance. Net longwave radiation variability is shown in **(b)**, note the longer time scales and lower amplitude.

conditions, another is a secondary photosynthesis pathway in response to enrichment of far-red wavelengths (700 to 800 nm, Huber et al., 2024).

In the introduction of this thesis, I have already mentioned the distinction between diffuse and scattered radiation, namely that not all scattered radiation is necessarily very diffuse. My belief in this is reinforced by the results in Chapters 7 and 8, which clearly presents conditions in which the origin of scattered radiation differs, i.e. *forward escape* and *side escape* being directional in contrast to *downward escape* (and *albedo enhancement*). How the direction of solar irradiance affects the diffuse fertilisation effect at canopy level and how it scales up to forest level or the global carbon cycle is an unknown in which clouds play a central role.

9.5 Final reflection on motivation

Addressing the complexities and uncertainties in radiation at cloud-scale remains a central challenge in weather and climate research. I do not think we understand these uncertainties enough to know how much they impact our ability to resolve weather and project future climate.

Societal factors have a larger influence on radiative forcing, however, and thereby contribute significantly to the uncertainties in climate projections. Consider the transition to renewable energy sources away from fossil fuel burning. Projections for oil demand by 2050 vary widely. The Organization of the Petroleum Exporting Countries (OPEC) expects a slight increase from current levels, while the International Energy Agency forecasts a significant decline of nearly 80 %, with other estimates spanning the entire range in between. Historically, such projections have often failed to predict actual outcomes accurately (Economist, 2024).

Despite these societal uncertainties, the importance of solar radiation as a renewable energy source in the near future is undeniable. And, as noted in the general introduction of this thesis, solar radiation touches nearly every part of weather and climate. Accurately resolved solar irradiance in models play an essential role here. Not only for optimising solar energy production, but also for improving the physical realism of weather and climate models that are running at increasingly high resolution. Even if alternative renewable energy sources surpass solar energy, advancements in solar radiation research will strengthen the foundation of atmospheric and climate science.

'Museum of the Future' in Berlin.

References

Ackerman, S. A., & Stephens, G. L. (1987). *The Absorption of Solar Radiation by Cloud Droplets: An Application of Anomalous Diffraction Theory*. https://doi.org/10.1175/1520-0469(1987)044<1574:TAOSRB>2.0.CO;2

Alados-Arboledas, L., Batlles, F. J., & Olmo, F. J. (1995). *Solar radiation resource assessment by means of silicon cells*. https://doi.org/10.1016/0038-092X(94)00116-U

Alstott, J., Bullmore, E., & Plenz, D. (2014). *Powerlaw: a Python package for analysis of heavy-tailed distributions*. https://doi.org/10.1371/journal.pone.0085777

Balsamo, G., Beljaars, A., Scipal, K. et al. (2009). *A revised hydrology for the ECMWF model: Verification from field site to terrestrial water storage and impact in the Integrated Forecast System*. https://doi.org/10.21957/yzyeh0vlw

Barrett, A. I., Hogan, R. J., & Forbes, R. M. (2017). *Why are mixed-phase altocumulus clouds poorly predicted by large-scale models? Part 1. Physical processes*. https://doi.org/10.1002/2016JD026321

Bauwens, M., Compernolle, S., Stavrakou, T. et al. (2020). *Impact of coronavirus outbreak on NO_2 pollution assessed using TROPOMI and OMI observations*. https://doi.org/10.1029/2020GL087978

Beljaars, A. C. M. (1995). *The parametrization of surface fluxes in large-scale models under free convection*. https://doi.org/10.1002/qj.49712152203

Benas, N., Finkensieper, S., Stengel, M. et al. (2017). *The MSG-SEVIRI-based cloud property data record CLAAS-2*. https://doi.org/10.5194/essd-9-415-2017

Berg, L. K., & Kassianov, E. I. (2008). *Temporal Variability of Fair-Weather Cumulus Statistics at the ACRF SGP Site*. https://doi.org/10.1175/2007JCLI2266.1

Bissolli, P., & Dittmann, E. (2001). *The objective weather type classification of the German Weather Service and its possibilities of application to environmental and meteorological investigations*. https://doi.org/10.1127/0941-2948/2001/0010-0253

Blanc, P., Espinar, B., Geuder, N. et al. (2014). *Direct normal irradiance related definitions and applications: The circumsolar issue*. https://doi.org/10.1016/j.solener.2014.10.001

Bony, S., Stevens, B., Frierson, D. M. et al. (2015). *Clouds, circulation and climate sensitivity*. https://doi.org/10.1038/ngeo2398

Bosveld, F. (2020). *Meteo profiles - validated tower profiles of wind, dew point, temperature and visibility at 10 minute interval at cabauw*. https://dataplatform.knmi.nl/dataset/cesar-tower-meteo-lb1-t10-v1-2. Accessed 06-Jul-2022.

Bretherton, C. S., Blossey, P. N., & Khairoutdinov, M. (2005). *An Energy-Balance Analysis of Deep*

Convective Self-Aggregation above Uniform SST. https://doi.org/10.1175/JAS3614.1

Brunner, L., Hegerl, G. C., & Steiner, A. K. (2017). *Connecting atmospheric blocking to European temperature extremes in spring*. https://doi.org/10.1175/JCLI-D-16-0518.1

Burkhardt, U., & Kärcher, B. (2011). *Global radiative forcing from contrail cirrus*. https://doi.org/10.1038/nclimate1068

Cahalan, R. F., Oreopoulos, L., Marshak, A. et al. (2005). *THE I3RC: Bringing Together the Most Advanced Radiative Transfer Tools for Cloudy Atmospheres*. https://doi.org/10.1175/BAMS-86-9-1275

Calbó, J., Pagès, D., & González, J.-A. (2005). *Empirical studies of cloud effects on UV radiation: A review*. https://doi.org/10.1029/2004RG000155

Callies, J., Ferrari, R., & Bühler, O. (2014). *Transition from geostrophic turbulence to inertia–gravity waves in the atmospheric energy spectrum*. https://doi.org/10.1073/pnas.1410772111

Canut, G., & Garrouste, O. (2022). *Liaise_la-cendrosa_cnrm_rs_l2*. [dataset]. https://doi.org/10.25326/322

Chew, B. N., Campbell, J. R., Reid, J. S. et al. (2011). *Tropical cirrus cloud contamination in sun photometer data*. https://doi.org/10.1016/j.atmosenv.2011.08.017

Clarke, L., Wei, Y.-M., De La Vega Navarro, A. et al. (2022). *Mitigation of Climate Change: Energy Systems (in IPCC, Climate Change 2022)*. https://doi.org/10.1017/9781009157926.008

Coddington, O., Lean, J. L., Pilewskie, P. et al. (2016). *A Solar Irradiance Climate Data Record*. https://doi.org/10.1175/BAMS-D-14-00265.1

Coppin, D., & Bony, S. (2015). *Physical mechanisms controlling the initiation of convective self-aggregation in a General Circulation Model*. https://doi.org/10.1002/2015MS000571

Cordero, R. R., Feron, S., Damiani, A. et al. (2023). *Surface Solar Extremes in the Most Irradiated Region on Earth, Altiplano*. https://doi.org/10.1175/BAMS-D-22-0215.1

Coumou, D., Capua, G. D., Vavrus, S. et al. (2018). *The influence of arctic amplification on mid-latitude summer circulation*. https://doi.org/10.1038/s41467-018-05256-8

Cronin, T. W., & Emanuel, K. A. (2013). *The climate time scale in the approach to radiative-convective equilibrium*. https://doi.org/10.1002/jame.20049

DeLong, E. F., & Karl, D. M. (2005). *Genomic perspectives in microbial oceanography*. https://doi.org/10.1038/nature04157

Dirnberger, D., Blackburn, G., Müller, B., & Reise, C. (2015). *On the impact of solar spectral irradiance on the yield of different PV technologies*. https://doi.org/10.1016/j.solmat.2014.09.034

Driemel, A., Augustine, J., Behrens, K. et al. (2018). *Baseline Surface Radiation Network (BSRN): structure and data description (1992–2017)*. https://doi.org/10.5194/essd-10-1491-2018

Durand, M., Murchie, E. H., Lindfors, A. V. et al. (2021). *Diffuse solar radiation and canopy photosynthesis in a changing environment*. https://doi.org/10.1016/j.agrformet.2021.108684

DWD (2020). *German weather in spring 2020*. https://www.dwd.de/DE/presse/pressemitteilungen/DE/2020/20200529_deutschlandwetter_fruehjahr2020_news.html

ECDW (2020). *European Centre for Disease Prevention and Control, COVID-19 pandemic*. Accessed:

2020-07-21.
https://www.ecdc.europa.eu/en/covid-19-pandemic

Economist (2024). *The end of oil, then and now*. https://www.economist.com/special-report/2024/03/11/the-end-of-oil-then-and-now

Ehrlich, A., & Wendisch, M. (2015). *Reconstruction of high-resolution time series from slow-response broadband terrestrial irradiance measurements by deconvolution*. https://doi.org/10.5194/amt-8-3671-2015

Emde, C., Buras-Schnell, R., Kylling, A. et al. (2016). *The libRadtran software package for radiative transfer calculations (version 2.0.1)*. https://doi.org/10.5194/gmd-9-1647-2016

Falconer, R. E. (1965). *A simple method for obtaining a continuous record of the presence and type of clouds in the sky during the day*. https://doi.org/10.1007/BF00874827

Feingold, G., Ghate, V. P., Russell, L. M. et al. (2024). *Physical science research needed to evaluate the viability and risks of marine cloud brightening*. https://doi.org/10.1126/sciadv.adi8594

Feister, U., & Shields, J. (2005). *Cloud and radiance measurements with the VIS/NIR Daylight Whole Sky Imager at Lindenberg (Germany)*. https://doi.org/10.1127/0941-2948/2005/0066

Fiedler, S., & Putrasahan, D. A. (2020). *Circulation response to aerosol forcing of the 1970s and 2000s - the case of the North Atlantic warming hole*. https://doi.org/10.1002/essoar.10504502.1

Fiedler, S., Stevens, B., Gidden, M. et al. (2019). *First forcinxg estimates from the future CMIP6 scenarios of anthropogenic aerosol optical properties and an associated Twomey effect*. https://doi.org/10.5194/gmd-12-989-2019

Folland, C. K., Knight, J., Linderholm, H. W. et al. (2009). *The summer North Atlantic Oscillation: Past, present, and future*. https://doi.org/10.1175/2008JCLI2459.1

Forster, P. M., Forster, H. I., Evans, M. J. et al. (2020). *Current and future global climate impacts resulting from COVID-19*. https://doi.org/10.1038/s41558-020-0883-0

Francis, J. A., & Vavrus, S. J. (2012). *Evidence linking arctic amplification to extreme weather in mid-latitudes*. https://doi.org/10.1029/2012gl051000

Gristey, J. J., Chiu, J. C., Gurney, R. J. et al. (2019). *Shortwave Spectral Radiative Signatures and Their Physical Controls*. https://doi.org/10.1175/JCLI-D-18-0815.1

Gristey, J. J., Feingold, G., Glenn, I. B. et al. (2020a). *On the Relationship Between Shallow Cumulus Cloud Field Properties and Surface Solar Irradiance*. https://doi.org/10.1029/2020GL090152

Gristey, J. J., Feingold, G., Glenn, I. B. et al. (2020b). *Surface Solar Irradiance in Continental Shallow Cumulus Fields: Observations and Large-Eddy Simulation*. https://doi.org/10.1175/JAS-D-19-0261.1

Gristey, J. J., Feingold, G., Schmidt, K. S., & Chen, H. (2022). *Influence of Aerosol Embedded in Shallow Cumulus Cloud Fields on the Surface Solar Irradiance*. https://doi.org/10.1029/2022JD036822

Gschwind, B., Wald, L., Blanc, P. et al. (2019). *Improving the McClear model estimating the downwelling solar radiation at ground level in cloud-free conditions – McClear-v3*. https://doi.org/10.1127/metz/2019/0946

Gu, L., Baldocchi, D. D., Wofsy, S. C. et al. (2003). *Response of a Deciduous Forest to the Mount Pinatubo*

Eruption: Enhanced Photosynthesis. https://doi.org/10.1126/science.1078366

Gu, L., Fuentes, J. D., Garstang, M. et al. (2001). *Cloud modulation of surface solar irradiance at a pasture site in southern Brazil*. https://doi.org/10.1016/S0168-1923(00)00209-4

Gueymard, C. A. (2012). *Temporal variability in direct and global irradiance at various time scales as affected by aerosols*. https://doi.org/10.1016/j.solener.2012.01.013

Gueymard, C. A. (2017). *Cloud and albedo enhancement impacts on solar irradiance using high-frequency measurements from thermopile and photodiode radiometers. Part 1: Impacts on global horizontal irradiance*. https://doi.org/10.1016/j.solener.2017.05.004

Gueymard, C. A., & Yang, D. (2020). *Worldwide validation of cams and merra-2 reanalysis aerosol optical depth products using 15 years of aeronet observations*. https://doi.org/10.1016/j.atmosenv.2019.117216

Guichard, F., & Couvreux, F. (2017). *A short review of numerical cloud-resolving models*. https://doi.org/10.1080/16000870.2017.1373578

Hahn, C. J., Rossow, W. B., & Warren, S. G. (2001). *ISCCP Cloud Properties Associated with Standard Cloud Types Identified in Individual Surface Observations*. https://doi.org/10.1175/1520-0442(2001)014<0011:ICPAWS>2.0.CO;2

He, Z., Libois, Q., Villefranque, N. et al. (2024). *How to observe the small-scale spatial distribution of surface solar irradiance, and how is it influenced by cumulus clouds?*. https://doi.org/10.5194/egusphere-2024-1064

Heerwaarden, C. C. v., & Mellado, J. P. (2016). *Growth and Decay of a Convective Boundary Layer over a Surface with a Constant Temperature*. https://doi.org/10.1175/JAS-D-15-0315.1

Heinze, R., Moseley, C., Böske, L. N. et al. (2017). *Evaluation of large-eddy simulations forced with mesoscale model output for a multi-week period during a measurement campaign*. https://doi.org/10.5194/acp-17-7083-2017

Helbig, M., Gerken, T., Beamesderfer, E. R. et al. (2021). *Integrating continuous atmospheric boundary layer and tower-based flux measurements to advance understanding of land-atmosphere interactions*. https://doi.org/10.1016/j.agrformet.2021.108509

Held, I. M., Hemler, R. S., & Ramaswamy, V. (1993). *Radiative-Convective Equilibrium with Explicit Two-Dimensional Moist Convection*. https://doi.org/10.1175/1520-0469(1993)050<3909:RCEWET>2.0.CO;2

Hersbach, H., Bell, B., Berrisford, P. et al. (2020). *The ERA5 global reanalysis*. https://doi.org/10.1002/qj.3803

Heus, T., & Seifert, A. (2013). *Automated tracking of shallow cumulus clouds in large domain, long duration large eddy simulations*. https://doi.org/10.5194/gmd-6-1261-2013

Heusinkveld, B. G., Mol, W. B., & van Heerwaarden, C. C. (2023). *A new accurate low-cost instrument for fast synchronized spatial measurements of light spectra*. https://doi.org/10.5194/amt-16-3767-2023

Hogan, R. J., & Bozzo, A. (2018). *A Flexible and Efficient Radiation Scheme for the ECMWF Model*. https://doi.org/10.1029/2018MS001364

Hogan, R. J., Fielding, M. D., Barker, H. W. et al. (2019). *Entrapment: An Important Mechanism to*

Explain the Shortwave 3D Radiative Effect of Clouds. https://doi.org/10.1175/JAS-D-18-0366.1

Hohenegger, C., Ament, F., Beyrich, F. et al. (2023). *FESSTVaL: The Field Experiment on Submesoscale Spatio-Temporal Variability in Lindenberg*. https://doi.org/10.1175/BAMS-D-21-0330.1

Hohenegger, C., & Stevens, B. (2016). *Coupled radiative convective equilibrium simulations with explicit and parameterized convection*. https://doi.org/10.1002/2016MS000666

Holloway, C. E., & Woolnough, S. J. (2016). *The sensitivity of convective aggregation to diabatic processes in idealized radiative-convective equilibrium simulations*. https://doi.org/10.1002/2015MS000511

Hooper, T., Armstrong, A., & Vlaswinkel, B. (2021). *Environmental impacts and benefits of marine floating solar*. https://doi.org/10.1016/j.solener.2020.10.010

Huber, M., de Boer, H. J., Romanowski, A. et al. (2024). *Far-red light enrichment affects gene expression and architecture as well as growth and photosynthesis in rice*. https://doi.org/10.1111/pce.14909

Huguenin, M. F., Fischer, E. M., Kotlarski, S. et al. (2020). *Lack of change in the projected frequency and persistence of atmospheric circulation types over central Europe*. https://doi.org/10.1029/2019GL086132

Humphrey, V., Berg, A., Ciais, P. et al. (2021). *Soil moisture–atmosphere feedback dominates land carbon uptake variability*. https://doi.org/10.1038/s41586-021-03325-5

Högström, U. (1988). *Non-dimensional wind and temperature profiles in the atmospheric surface layer: A re-evaluation*. https://doi.org/10.1007/BF00119875

Jakub, F., & Mayer, B. (2015). *A three-dimensional parallel radiative transfer model for atmospheric heating rates for use in cloud resolving models—The TenStream solver*. https://doi.org/10.1016/j.jqsrt.2015.05.003

Jakub, F., & Mayer, B. (2017). *The role of 1-D and 3-D radiative heating in the organization of shallow cumulus convection and the formation of cloud streets*. https://doi.org/10.5194/acp-17-13317-2017

Jensen, E. J., Toon, O. B., Kinne, S. et al. (1998). *Environmental conditions required for contrail formation and persistence*. https://doi.org/10.1029/97jd02808

JHU (2020). *COVID-19 dashboard by the Center for Systems Science and Engineering (CSSE) at Johns Hopkins University (JHU)*. Accessed: 2020-07-21. https://coronavirus.jhu.edu/map.html

Jin, Y., Hu, S., Ziegler, A. D. et al. (2023). *Energy production and water savings from floating solar photovoltaics on global reservoirs*. https://doi.org/10.1038/s41893-023-01089-6

Järvelä, M., Lappalainen, K., & Valkealahti, S. (2020). *Characteristics of the cloud enhancement phenomenon and PV power plants*. https://doi.org/10.1016/j.solener.2019.11.090

Kaufman, Y. J., Remer, L. A., Tanre, D. et al. (2005). *A critical examination of the residual cloud contamination and diurnal sampling effects on modis estimates of aerosol over ocean*. https://doi.org/10.1109/TGRS.2005.858430

Kazadzis, S., Kouremeti, N., Nyeki, S. et al. (2018). *The world optical depth research and calibration center (WORCC) quality assurance and quality control of GAW-PFR AOD measurements*. https://doi.org/10.5194/gi-7-39-2018

Keeling, R. F., & Manning, A. C. (2014). *Studies of Recent Changes in Atmospheric O2 Content*. https://doi.org/10.1016/B978-0-08-095975-7.00420-4

Keenan, T. F., Migliavacca, M., Papale, D. et al. (2019). *Widespread inhibition of daytime ecosystem respiration*. https://doi.org/10.1038/s41559-019-0809-2

Key, J. R., Yang, P., Baum, B. A., & Nasiri, S. L. (2002). *Parameterization of shortwave ice cloud optical properties for various particle habits*. https://doi.org/10.1029/2001JD000742

Khairoutdinov, M. F., & Randall, D. A. (2003). *Cloud Resolving Modeling of the ARM Summer 1997 IOP: Model Formulation, Results, Uncertainties, and Sensitivities*. https://doi.org/10.1175/1520-0469(2003)060<0607:CRMOTA>2.0.CO;2

Kipp & Zonen (2001). *CH1 pyrheliometer instruction manual*. Retrieved 26-07-2022 from https://www.kippzonen.com/Download/42/CH-1-Pyrheliometer-Manual-English.

Kipp & Zonen (2004). *CM22 precision pyranometer instruction manual*. Retrieved 26-07-2022 from https://www.kippzonen.com/Download/55/CM-22-Pyranometer-Manual.

Kirsch, B., Hohenegger, C., Klocke, D. et al. (2022). *Sub-mesoscale observations of convective cold pools with a dense station network in Hamburg, Germany*. https://doi.org/10.5194/essd-14-3531-2022

Kivalov, S. N., & Fitzjarrald, D. R. (2018). *Quantifying and Modelling the Effect of Cloud Shadows on the Surface Irradiance at Tropical and Midlatitude Forests*. https://doi.org/10.1007/s10546-017-0301-y

KMI (2020). *A dry and exceptionally sunny spring*. https://www.meteo.be/nl/klimaat/klimatologisch-overzicht/2020/lente

Knap, W. (2022). *Basic and other measurements of radiation at station cabauw (2005-02 et seq)*. https://doi.pangaea.de/10.1594/PANGAEA.940531

Knap, W., & Meirink, J. F. (2020). *Uitzonderlijk blauwe voorjaarsluchten*. https://www.knmi.nl/over-het-knmi/nieuws/uitzonderlijk-blauwe-voorjaarsluchten

Knap, W. H., & Mol, W. B. (2022). *High resolution solar irradiance variability climatology dataset part 1: direct, diffuse, and global irradiance*. [dataset]. https://doi.org/10.5281/zenodo.7093164

KNMI (2020). *Sunniest spring since start of measurements*. https://www.knmi.nl/over-het-knmi/nieuws/zonnigste-lente-sinds-het-begin-van-de-metingen

KNMI (2024). *KNMI climatology overviews*. Accessed: 2024-06-10. https://www.knmi.nl/nederland-nu/klimatologie/geografische-overzichten/archief/maand/sq

Kreuwel, F. P. M., Knap, W. H., Visser, L. R. et al. (2020). *Analysis of high frequency photovoltaic solar energy fluctuations*. https://doi.org/10.1016/j.solener.2020.05.093

Kreuwel, F. P. M., Mol, W. B., Vilà-Guerau de Arellano, J., & van Heerwaarden, C. C. (2021). *Characterizing solar PV grid overvoltages by data blending advanced metering infrastructure with meteorology*. https://doi.org/10.1016/j.solener.2021.09.009

Kroll, J. H., Heald, C. L., Cappa, C. D. et al. (2020). *The complex chemical effects of COVID-19 shutdowns on air quality*. https://doi.org/10.1038/s41557-020-0535-z

Kučerová, M., Beck, C., Philipp, A., & Huth, R. (2017). *Trends in frequency and persistence of atmospheric circulation types over europe derived from a multitude of classifications*. https://doi.org/10.1002/joc.4861

Laar, T. W. v., Schemann, V., & Neggers, R. A. J. (2019). *Investigating the Diurnal Evolution of the Cloud Size Distribution of Continental Cumulus Convection Using Multiday LES*. https://doi.org/10.1175/JAS-D-18-0084.1

Lappalainen, K., & Valkealahti, S. (2016a). *Analysis of shading periods caused by moving clouds*. https://doi.org/10.1016/j.solener.2016.05.050

Lappalainen, K., & Valkealahti, S. (2016b). *Apparent velocity of shadow edges caused by moving clouds*. https://doi.org/10.1016/j.solener.2016.09.008

Le, T., Wang, Y., Liu, L. et al. (2020). *Unexpected air pollution with marked emission reductions during the COVID-19 outbreak in china*. https://doi.org/10.1126/science.abb7431

Lee, D. S., Fahey, D. W., Forster, P. M. et al. (2009). *Aviation and global climate change in the 21st century*. https://doi.org/10.1016/j.atmosenv.2009.04.024

Li, J., Huang, J., Stamnes, K. et al. (2015). *A global survey of cloud overlap based on CALIPSO and CloudSat measurements*. https://doi.org/10.5194/acp-15-519-2015

Liang, X. (2017). *Emerging Power Quality Challenges Due to Integration of Renewable Energy Sources*. https://doi.org/10.1109/TIA.2016.2626253

Liepert, B. G., Feichter, J., Lohmann, U., & Roeckner, E. (2004). *Can aerosols spin down the water cycle in a warmer and moister world?*. https://doi.org/10.1029/2003gl019060

Lindsay, N., Libois, Q., Badosa, J. et al. (2020). *Errors in PV power modelling due to the lack of spectral and angular details of solar irradiance inputs*. https://doi.org/10.1016/j.solener.2019.12.042

Liu, Z., Ming, Y., Wang, L. et al. (2019). *A model investigation of aerosol-induced changes in the east asian winter monsoon*. https://doi.org/10.1029/2019gl084228

Lohmann, G. M. (2018). *Irradiance Variability Quantification and Small-Scale Averaging in Space and Time: A Short Review*. https://doi.org/10.3390/atmos9070264

Lohmann, G. M., Monahan, A. H., & Heinemann, D. (2016). *Local short-term variability in solar irradiance*. https://doi.org/10.5194/acp-16-6365-2016

Löhnert, U., Knist, C., Böck, T., & Pospichal, B. (2022). *Microwave radiometer observations during fesstval 2021*. [dataset]. https://doi.org/10.25592/UHHFDM.10197

Lohou, F., & Patton, E. G. (2014). *Surface Energy Balance and Buoyancy Response to Shallow Cumulus Shading*. https://doi.org/10.1175/JAS-D-13-0145.1

Lopes Pereira, R., Trindade, J., Gonçalves, F. et al. (2014). *A wireless sensor network for monitoring volcano-seismic signals*. https://doi.org/10.5194/nhess-14-3123-2014

Madge, G. (2020). *May 2020 becomes the sunniest calendar month on record*. https://www.metoffice.gov.uk/about-us/press-office/news/weather-and-climate/2020/2020-spring-and-may-stats

Madhavan, B. L., Deneke, H., Witthuhn, J., & Macke, A. (2017). *Multiresolution analysis of the spatiotemporal variability in global radiation observed by a dense network of 99 pyranometers*.

https://doi.org/10.5194/acp-17-3317-2017

Madhavan, B. L., Kalisch, J., & Macke, A. (2016). *Shortwave surface radiation network for observing small-scale cloud inhomogeneity fields*. https://doi.org/10.5194/amt-9-1153-2016

Manabe, S., & Strickler, R. F. (1964). *Thermal Equilibrium of the Atmosphere with a Convective Adjustment*. https://doi.org/10.1175/1520-0469(1964)021<0361:TEOTAW>2.0.CO;2

Mangan, M. R., Hartogensis, O., Boone, A. et al. (2023). *The surface-boundary layer connection across spatial scales of irrigation-driven thermal heterogeneity: An integrated data and modeling study of the LIAISE field campaign*. https://doi.org/10.1016/j.agrformet.2023.109452

Martínez, M. A., Andújar, J. M., & Enrique, J. M. (2009). *A New and Inexpensive Pyranometer for the Visible Spectral Range*. https://doi.org/10.3390/s90604615

Mayer, B. (2009). *Radiative transfer in the cloudy atmosphere*. https://doi.org/10.1140/epjconf/e2009-00912-1

Meirink, J. F., Knap, W. H., & Stammes, P. (in press). *Uitzonderlijk blauwe voorjaarsluchten in 2020*. https://www.knmi.nl/research/publications/uitzonderlijk-blauwe-voorjaarsluchten-in-2020

Mercado, L. M., Bellouin, N., Sitch, S. et al. (2009). *Impact of changes in diffuse radiation on the global land carbon sink*. https://doi.org/10.1038/nature07949

Michalsky, J. J., Perez, R., Harrison, L., & LeBaron, B. A. (1991). *Spectral and temperature correction of silicon photovoltaic solar radiation detectors*. https://doi.org/10.1016/0038-092X(91)90121-C

Mol, W., Heusinkveld, B., & van Heerwaarden, C. (2023a). *Radiometer grid at falkenberg and surroundings, downwelling shortwave radiation, fesstval campaign*. [dataset]. https://doi.org/10.25592/uhhfdm.12548

Mol, W., Heusinkveld, B., & Van Heerwaarden, C. (2023b). *Radiometer network dataset of 10 hz spectral irradiance and derived variables (liaise campaign)*. [dataset]. https://doi.org/10.5281/ZENODO.7966437

Mol, W. B., Knap, W. H., & van Heerwaarden, C. C. (2022). *High resolution solar irradiance variability climatology dataset part 2: classifications, supplementary data, and statistics*. [dataset]. https://doi.org/10.5281/zenodo.7092058

Muhammad, S., Long, X., & Salman, M. (2020). *COVID-19 pandemic and environmental pollution: A blessing in disguise?*. https://doi.org/10.1016/j.scitotenv.2020.138820

Muller, C., & Bony, S. (2015). *What favors convective aggregation and why?*. https://doi.org/10.1002/2015GL064260

Muller, C. J., & Held, I. M. (2012). *Detailed Investigation of the Self-Aggregation of Convection in Cloud-Resolving Simulations*. https://doi.org/10.1175/JAS-D-11-0257.1

NASA (2024). *NASA Worldview*. Accessed: 2024-06-10. https://worldview.earthdata.nasa.gov

Nastrom, G. D., & Gage, K. S. (1985). *A Climatology of Atmospheric Wavenumber Spectra of Wind and Temperature Observed by Commercial Aircraft*. https://doi.org/10.1175/1520-0469(1985)042<0950:ACOAWS>2.0.CO;2

Naumann, A. K., Stevens, B., & Hohenegger, C. (2019). *A Moist Conceptual Model for the Boundary Layer Structure and Radiatively Driven Shallow Circulations in the Trades*. https://doi.org/10.1175/JAS-D-18-0226.1

Naumann, A. K., Stevens, B., Hohenegger, C., & Mellado, J. P. (2017). *A Conceptual Model of a Shallow Circulation Induced by Prescribed Low-Level Radiative Cooling*. https://doi.org/10.1175/JAS-D-17-0030.1

Neggers, R. A., Siebesma, A., & Heus, T. (2012). *Continuous single-column model evaluation at a permanent meteorological supersite*. https://doi.org/10.1175/BAMS-D-11-00162.1

O'Hirok, W., Gautier, C., & Ricchiazzi, P. (2000). *Spectral signature of column solar radiation absorption during the Atmospheric Radiation Measurement Enhanced Shortwave Experiment (ARESE)*. https://doi.org/10.1029/2000JD900190

Oliphant, A. J., Spronken-Smith, R. A., Sturman, A. P., & Owens, I. F. (2003). *Spatial Variability of Surface Radiation Fluxes in Mountainous Terrain*. https://doi.org/10.1175/1520-0450(2003)042<0113:SVOSRF>2.0.CO;2

O'Hirok, W., & Gautier, C. (1998). *A Three-Dimensional Radiative Transfer Model to Investigate the Solar Radiation within a Cloudy Atmosphere. Part II: Spectral Effects*. https://doi.org/10.1175/1520-0469(1998)055<3065:ATDRTM>2.0.CO;2

Parding, K. M., Liepert, B. G., Hinkelman, L. M. et al. (2016). *Influence of synoptic weather patterns on solar irradiance variability in northern europe*. https://doi.org/10.1175/JCLI-D-15-0476.1

Pearcy, R. W., & Way, D. A. (2012). *Two decades of sunfleck research: looking back to move forward*. https://doi.org/10.1093/treephys/tps084

Pecenak, Z. K., Mejia, F. A., Kurtz, B. et al. (2016). *Simulating irradiance enhancement dependence on cloud optical depth and solar zenith angle*. https://doi.org/10.1016/j.solener.2016.07.045

Peters, I. M., Brabec, C., Buonassisi, T. et al. (2020). *The impact of COVID-19-related measures on the solar resource in areas with high levels of air pollution*. https://doi.org/10.1016/j.joule.2020.06.009

Pfahl, S., & Wernli, H. (2012). *Quantifying the relevance of atmospheric blocking for co-located temperature extremes in the Northern Hemisphere on (sub-) daily time scales*. https://doi.org/10.1029/2012GL052261

Philipp, A., Della-Marta, P. M., Jacobeit, J. et al. (2007). *Long-term variability of daily North Atlantic–European pressure patterns since 1850 classified by simulated annealing clustering*. https://doi.org/10.1175/JCLI4175.1

Pincus, R., & Evans, K. F. (2009). *Computational Cost and Accuracy in Calculating Three-Dimensional Radiative Transfer: Results for New Implementations of Monte Carlo and SHDOM*. https://doi.org/10.1175/2009JAS3137.1

Pincus, R., Mlawer, E. J., & Delamere, J. S. (2019). *Balancing accuracy, efficiency, and flexibility in radiation calculations for dynamical models*. https://doi.org/10.1029/2019MS001621

Pingswept (2022). *Pysolar is a collection of Python libraries for simulating the irradiation of any point on earth by the sun*. https://github.com/pingswept/pysolar. Accessed 06-Jul-2022.

Popke, D., Stevens, B., & Voigt, A. (2013). *Climate and climate change in a radiative-convective equilib-*

rium version of ECHAM6. https://doi.org/10.1029/2012MS000191

Prahl, S. (2023). *miepython: Pure python implementation of Mie scattering*. [software]. https://doi.org/10.5281/zenodo.8218010

Price, J. (2023). *Liaise_els-plans_ukmo_radiosondes_l1*. [dataset]. https://doi.org/10.25326/429

Quéré, C. L., Jackson, R. B., Jones, M. W. et al. (2020). *Temporary reduction in daily global CO2 emissions during the COVID-19 forced confinement*. https://doi.org/10.1038/s41558-020-0797-x

Reed, K. A., Medeiros, B., Bacmeister, J. T., & Lauritzen, P. H. (2015). *Global Radiative–Convective Equilibrium in the Community Atmosphere Model, Version 5*. https://doi.org/10.1175/JAS-D-14-0268.1

Ritchie, H., Rosado, P., & Roser, M. (2024). *Energy production and consumption*. https://ourworldindata.org/energy-production-consumption

Robinson, P. J. (1977). *Measurements of Downward Scattered Solar Radiation from Isolated Cumulus Clouds*. https://doi.org/10.1175/1520-0450(1977)016<0620:MODSSR>2.0.CO;2

Rodts, S. M. A., Duynkerke, P. G., & Jonker, H. J. J. (2003). *Size Distributions and Dynamical Properties of Shallow Cumulus Clouds from Aircraft Observations and Satellite Data*. https://doi.org/10.1175/1520-0469(2003)060<1895:SDADPO>2.0.CO;2

Romps, D. M., & Öktem, R. (2018). *Observing Clouds in 4D with Multiview Stereophotogrammetry*. https://doi.org/10.1175/BAMS-D-18-0029.1

Romps, D. M., Öktem, R., Endo, S., & Vogelmann, A. M. (2021). *On the Life Cycle of a Shallow Cumulus Cloud: Is It a Bubble or Plume, Active or Forced?*. https://doi.org/10.1175/JAS-D-20-0361.1

Rossow, W. B. (2022). *Climate data record (cdr) program - climate algorithm theoretical basis document (c-atbd)*. https://ncei.noaa.gov/pub/data/sds/cdr/CDRs/Cloud_Properties-ISCCP/AlgorithmDescription_01B-29.pdf

Sakradzija, M., & Hohenegger, C. (2017). *What Determines the Distribution of Shallow Convective Mass Flux through a Cloud Base?*. https://doi.org/10.1175/JAS-D-16-0326.1

Sassen, K., & Wang, Z. (2008). *Classifying clouds around the globe with the CloudSat radar: 1-year of results*. https://doi.org/10.1029/2007GL032591

Schade, N. H., Macke, A., Sandmann, H., & Stick, C. (2007). *Enhanced solar global irradiance during cloudy sky conditions*. https://doi.org/10.1127/0941-2948/2007/0206

Schafer, M., Strohmeier, M., Lenders, V. et al. (2014). Bringing up OpenSky: A large-scale ADS-b sensor network for research. In *IPSN-14 Proceedings of the 13th International Symposium on Information Processing in Sensor Networks*. IEEE.

Schalkwijk, J., Jonker, H. J., Siebesma, A. P., & Bosveld, F. C. (2015). *A year-long large-eddy simulation of the weather over cabauw: An overview*. https://doi.org/10.1175/MWR-D-14-00293.1

Schemann, V., Stevens, B., Grützun, V., & Quaas, J. (2013). *Scale Dependency of Total Water Variance and Its Implication for Cloud Parameterizations*. https://doi.org/10.1175/JAS-D-13-09.1

Schlemmer, L., & Hohenegger, C. (2014). *The Formation of Wider and Deeper Clouds as a Result of Cold-Pool Dynamics*. https://doi.org/10.1175/JAS-D-13-0170.1

Schlemmer, L., & Hohenegger, C. (2016). *Modifications of the atmospheric moisture field as a result of*

cold-pool dynamics. https://doi.org/10.1002/qj.2625

Schmidt, K. S., Pilewskie, P., Mayer, B. et al. (2010). *Apparent absorption of solar spectral irradiance in heterogeneous ice clouds*. https://doi.org/10.1029/2009JD013124

Schäfer, S. A. K., Hogan, R. J., Klinger, C. et al. (2016). *Representing 3-D cloud radiation effects in two-stream schemes: 1. Longwave considerations and effective cloud edge length*. https://doi.org/10.1002/2016JD024876

Segal, M., & Davis, J. (1992). *The Impact of Deep Cumulus Reflection on the Ground-Level Global Irradiance*. https://doi.org/10.1175/1520-0450(1992)031<0217:TIODCR>2.0.CO;2

Seifert, A., & Beheng, K. D. (2006). *A two-moment cloud microphysics parameterization for mixed-phase clouds. Part 1: Model description*. https://doi.org/10.1007/s00703-005-0112-4

Stuber, N., Forster, P., Rädel, G., & Shine, K. (2006). *The importance of the diurnal and annual cycle of air traffic for contrail radiative forcing*. https://doi.org/10.1038/nature04877

Tabar, M. R. R., Anvari, M., Lohmann, G. et al. (2014). *Kolmogorov spectrum of renewable wind and solar power fluctuations*. https://doi.org/10.1140/epjst/e2014-02217-8

Tijhuis, M., van Stratum, B. J. H., Veerman, M. A., & van Heerwaarden, C. C. (2023). *An Efficient Parameterization for Surface Shortwave 3D Radiative Effects in Large-Eddy Simulations of Shallow Cumulus Clouds*. https://doi.org/10.1029/2022MS003262

Tobin, I., Bony, S., Holloway, C. E. et al. (2013). *Does convective aggregation need to be represented in cumulus parameterizations?*. https://doi.org/10.1002/jame.20047

Tomita, H. (2008). *New microphysical schemes with five and six categories by diagnostic generation of cloud ice*. https://doi.org/10.2151/jmsj.86A.121

Tompkins, A. M., & Craig, G. C. (1998a). *Radiative–convective equilibrium in a three-dimensional cloud-ensemble model*. https://doi.org/10.1002/qj.49712455013

Tompkins, A. M., & Craig, G. C. (1998b). *Time-scales of adjustment to radiative-convective equilibrium in the tropical atmosphere*. https://doi.org/10.1002/qj.49712455208

Tomson, T. (2010). *Fast dynamic processes of solar radiation*. https://doi.org/10.1016/j.solener.2009.11.013

Tomson, T., & Hansen, M. (2011). *Dynamic properties of clouds Cumulus humilis and Cumulus fractus extracted by solar radiation measurements*. https://doi.org/10.1007/s00704-011-0434-8

Tran, N.-T., & Fukuzawa, M. (2020). *A Portable Spectrometric System for Quantitative Prediction of the Soluble Solids Content of Apples with a Pre-calibrated Multispectral Sensor Chipset*. https://doi.org/10.3390/s20205883

Twomey, S. (1974). *Pollution and the planetary albedo*. https://doi.org/10.1016/0004-6981(74)90004-3

Ukkonen, P., & Hogan, R. J. (2024). *Twelve Times Faster yet Accurate: A New State-Of-The-Art in Radiation Schemes via Performance and Spectral Optimization*. https://doi.org/10.1029/2023MS003932

van Heerwaarden, C. C., van Stratum, B. J. H., Heus, T. et al. (2017). *MicroHH 1.0: a computational fluid dynamics code for direct numerical simulation and large-eddy simulation of atmospheric boundary layer flows*. https://doi.org/10.5194/gmd-10-3145-2017

van Stratum, B. J. H., van Heerwaarden, C. C., & Vilà-Guerau de Arellano, J. (2023). *The Benefits and Challenges of Downscaling a Global Reanalysis With Doubly-Periodic Large-Eddy Simulations*. https://doi.org/10.1029/2023MS003750

Veerman, M. A., Pedruzo-Bagazgoitia, X., Jakub, F. et al. (2020). *Three-Dimensional Radiative Effects By Shallow Cumulus Clouds on Dynamic Heterogeneities Over a Vegetated Surface*. https://doi.org/10.1029/2019MS001990

Veerman, M. A., Pincus, R., Mlawer, E. J., & van Heerwaarden, C. C. (2024). *The Impact of Radiative Transfer at Reduced Spectral Resolution in Large-Eddy Simulations of Convective Clouds*. https://doi.org/10.1029/2023MS003699

Veerman, M. A., van Stratum, B. J. H., & van Heerwaarden, C. C. (2022). *A case study of cumulus convection over land in cloud-resolving simulations with a coupled ray tracer*. https://doi.org/10.1029/2022GL100808

Villefranque, N., Barker, H. W., Cole, J. N. S., & Qu, Z. (2023). *A Functionalized Monte Carlo 3D Radiative Transfer Model: Radiative Effects of Clouds Over Reflecting Surfaces*. https://doi.org/10.1029/2023MS003674

Vilà-Guerau de Arellano, J., Hartogensis, O., Benedict, I. et al. (2023). *Advancing understanding of land–atmosphere interactions by breaking discipline and scale barriers*. https://doi.org/10.1111/nyas.14956

Vilà-Guerau de Arellano, J., Hartogensis, O. K., de Boer, H. et al. (2024). *CloudRoots-Amazon22: Integrating clouds with photosynthesis by crossing scales*. https://doi.org/10.1175/BAMS-D-23-0333.1

Várnai, T., & Davies, R. (1999). *Effects of Cloud Heterogeneities on Shortwave Radiation: Comparison of Cloud-Top Variability and Internal Heterogeneity*. https://doi.org/10.1175/1520-0469(1999)056<4206:EOCHOS>2.0.CO;2

Wagner, T., Warnach, S., Beirle, S. et al. (2023). *Investigation of three-dimensional radiative transfer effects for UV–Vis satellite and ground-based observations of volcanic plumes*. https://doi.org/10.5194/amt-16-1609-2023

Wauben, W., Bosveld, F., & Baltink, H. K. (2010). *Laboratory and field evaluation of the nubiscope*. https://cdn.knmi.nl/knmi/pdf/bibliotheek/knmipubTR/TR334.pdf

Way, D. A., & Pearcy, R. W. (2012). *Sunflecks in trees and forests: from photosynthetic physiology to global change biology*. https://doi.org/10.1093/treephys/tps064

Weigl, T., Nagl, L., Weizenbeck, J. et al. (2012). *Modelling and validation of spatial irradiance characteristics for localised irradiance fluctuations and enhancements*. https://www.researchgate.net/publication/237353116_Modelling_and_Validation_of_Spatial_Irradiance_Characteristics_for_Localised_Irradiance_Fluctuations_and_Enhancements

Weihs, P., Rennhofer, M., Baumgartner, D. J. et al. (2015). *Potential impact of contrails on solar energy gain*. https://doi.org/10.5194/amt-8-1089-2015

Weisman, M. L., & Klemp, J. B. (1982). *The Dependence of Numerically Simulated Convective Storms on Vertical Wind Shear and Buoyancy*. https://doi.org/10.1175/1520-0493(1982)110<0504:TDONSC>2.0.CO;2

Wilcox, L. J., Dunstone, N., Lewinschal, A. et al. (2019). *Mechanisms for a remote response to asian anthropogenic aerosol in boreal winter*. https://doi.org/10.5194/acp-19-9081-2019

Wild, M. (2012). *Enlightening global dimming and brightening*. https://doi.org/10.1175/BAMS-D-11-00074.1

Wild, M., Gilgen, H., Roesch, A. et al. (2005). *From dimming to brightening: decadal changes in solar radiation at earth's surface*. https://doi.org/10.1126/science.1103215

Wild, M., Ohmura, A., Gilgen, H., & Rosenfeld, D. (2004). *On the consistency of trends in radiation and temperature records and implications for the global hydrological cycle*. https://doi.org/10.1029/2003GL019188

Wilson, D. K. (2001). *An Alternative Function For The Wind And Temperature Gradients In Unstable Surface Layers*. https://doi.org/10.1023/A:1018718707419

Wing, A. A., & Cronin, T. W. (2016). *Self-aggregation of convection in long channel geometry*. https://doi.org/10.1002/qj.2628

Wing, A. A., Emanuel, K., Holloway, C. E., & Muller, C. (2017). *Convective Self-Aggregation in Numerical Simulations: A Review*. https://doi.org/10.1007/s10712-017-9408-4

Wing, A. A., & Emanuel, K. A. (2014). *Physical mechanisms controlling self-aggregation of convection in idealized numerical modeling simulations*. https://doi.org/10.1002/2013MS000269

Wing, A. A., Reed, K. A., Satoh, M. et al. (2018). *Radiative–convective equilibrium model intercomparison project*. https://doi.org/10.5194/gmd-11-793-2018

WMO (2014). *Chapter 8 - measurement of sunshine duration*. https://library.wmo.int/index.php?lvl=notice_display&id=19664. Accessed 06-Jul-2022.

Wood, R., & Field, P. R. (2011). *The Distribution of Cloud Horizontal Sizes*. https://doi.org/10.1175/2011JCLI4056.1

Woollings, T., Barriopedro, D., Methven, J. et al. (2018). *Blocking and its response to climate change*. https://doi.org/10.1007/s40641-018-0108-z

Wyngaard, J. C. (2010). *Turbulence in the Atmosphere*. Cambridge University Press.

Yang, D., Wang, W., Gueymard, C. A. et al. (2022). *A review of solar forecasting, its dependence on atmospheric sciences and implications for grid integration: Towards carbon neutrality*. https://doi.org/10.1016/j.rser.2022.112348

Ylianttila, L., & Schreder, J. (2005). *Temperature effects of PTFE diffusers*. https://doi.org/10.1016/j.optmat.2004.11.008

Ylivinkka, I., Kaupinmäki, S., Virman, M. et al. (2020). *Clouds over Hyytiälä, Finland: an algorithm to classify clouds based on solar radiation and cloud base height measurements*. https://doi.org/10.5194/amt-13-5595-2020

Yordanov, G. H. (2015). *A study of extreme overirradiance events for solar energy applications using NASA's I3RC Monte Carlo radiative transfer model*. https://doi.org/10.1016/j.solener.2015.10.014

Yordanov, G. H., Saetre, T. O., & Midtgård, O. (2013). *100-millisecond Resolution for Accurate Overirradiance Measurements*. https://doi.org/10.1109/JPHOTOV.2013.2264621

Yordanov, G. H., Saetre, T. O., & Midtgård, O.-M. (2015). *Extreme overirradiance events in Norway: 1.6 suns measured close to 60°N*. https://doi.org/10.1016/j.solener.2015.02.020

Zuidema, P., Torri, G., Muller, C., & Chandra, A. (2017). *A Survey of Precipitation-Induced Atmospheric Cold Pools over Oceans and Their Interactions with the Larger-Scale Environment*. https://doi.org/10.1007/s10712-017-9447-x

Acknowledgements

In many ways, March 2020 was not the best time to start, with society in a general state of surprise and denial about the pandemic. Thus, in week two of this PhD adventure, I collected my first ”decide for yourself if it is OK to go” conference, which ended up getting cancelled two days later anyway. Now, well over four years later, I get to express my gratitude to those who helped me stay sane in the first phase of my PhD and those who made the rest of my time as a PhDer so enjoyable, in what is one of the most fun sections to write.

Thank you Antonija and Chiel, for welcoming me into your home during the lockdowns, whether for work or otherwise. Jordi, for allowing those who needed it to come to the office, favouring well-being over government and university rules. Anja, for introducing me to a new city that went into lockdown just after I had moved there. And Yoni, Jonas, and Reier, thanks for the landmark kowa's in Utrecht or elsewhere.

Despite a tumultuous start, by early 2021 campaign preparations were in full swing. Bert, it was a joy to help (or watch) you design, build, test, and re-design the measurement instruments, with your endless source of inspiration and creative solutions to any problem we encountered. In the week before the first big campaign (FESSTVaL), we had to repair half the instruments due to rain damage, but ultimately we got a more complete dataset than we had hoped for. The data from these instruments have been essential to this thesis, and the fact we had time left for some (relatively timid, by your standards) outdoor sports together during the campaign was a welcome bonus in the most stressful period of my PhD.

It's hard to express how much effort people put into organising these field campaign. My thanks therefore also goes out to Frank Beyrich, Cathy Hohenegger, Stefan Wacker, and many others involved in the FESSTVaL campaign for their help and collaboration on and off the field. In the same theme, thank you Mary Rose, Oscar, and Jordi for organising and running the LIAISE campaign in Spain, and in addition everyone of the Dutch team for being such great company in Cal Menut. I'm grateful to have shared with you what I remember as easily the best food I've eaten to date.

Imme, assisting you with Atmospheric Practical was a privilige. I still don't quite know how we managed to pull off teaching a practical course fully remote. Luckily we got to enjoy even the excursions in last years, thanks for making such a demanding course so enjoyable. Jordi, whether it was during these excursions, the field campaigns, or any other context, I always enjoy our discussions and highly value your ability to bring people together. Your positivity when it comes to real science (rather than politics) is contagious.

Chiel, given your love for concise text: you have been as close to perfect a supervisor for me as is humanly possible, for which I am very grateful.

I feel priviliged to have done my PhD in a group as vibrant and social as MAQ. I'll attempt to give some highlights at the risk of not doing everyone justice.

Martin, Menno, Mirjam, Robin, Frank, Job, Bart, and Raquel, our (quasi-periodic) Friday afternoon meetings is where I often felt science *happened*. Thanks for the challenging, in-depth, and above all, fun discussions. Wiebke, Sarah, Sreehari, Tristan, Bernard, and Vincent, I'm glad you are part of a new season of these meetings.

To the many people involved in the Veluweloop of 2021 and 2022 and the triathlons in 2023 and (soon) 2024: it's been so much fun to do all this together. Thank you Ingrid, Remco, Anne-Wil, Kim, Marnix, Michiel, and many more. The races themselves are one thing, but mostly I enjoyed the training together, learning to swim, bike, and run better, whether before work, during lunch, or in the weekends.

Christoph, thanks for challenging my (unnuanced) opinions on basically any topic, and I'm glad we got to be office mates in the end. I wish, whenever you and Sanne you read this, that your van is still serving you well. Thomas, I always enjoy our conversations, whether about running, weather, politics, or life in general. Farhan, thank you for sharing your photography and incredible cooking skills with me. Raquel, muchas gracias for joining me on this long drive to the campaign in Spain, and for showing me around your beautiful home island the year after.

As these acknowledgements draw to a close, I'd like to thank the people who build Obsidian, my 'second brain', and `xarray`, my first import into any python script.

Jesse, Kevin, en Thom, dat COVID onze jaarlijkse avonturen niet heeft kunnen stoppen zegt genoeg. En nogmaals Yoni, Jonas, en Reier, bedankt voor de dagelijkse avonturen.

Tot slot, bedankt aan mijn lieve ouders, waar ik altijd en voor alles terecht kan. En mijn broertje, dat je nog altijd meer volwassen bent dan ik. En Theresa, ik ben zo blij je ontmoet te hebben. Bedankt voor jou support tijdens de laatste fase van mijn PhD, en ik kijk uit naar de toekomst.

List of publications

Author lists of project reference articles are shortened to *[First author] et al.*, refer to the online article for a full list. Shared first-authorship is marked with an asterisk (*). For an up-to-date overview, current projects, and some more weather photography, you can visit: `https://woutermol.com`.

Articles

Mol, W. B. & Chiel van Heerwaarden (2024), *Mechanism of surface solar irradiance variability extremes under broken cloud conditions*. **In review** in Atmospheric Chemistry and Physics. Copernicus.

Vilà-Guerau de Arellano, J. et al. (2024). *CloudRoots-Amazon22: Integrating clouds with photosynthesis by crossing scales*. Bulletin of the American Meteorological Society. `https://doi.org/10.1175/bams-d-23-0333.1`

Mol, W. B., Heusinkveld, B. G., Mangan, M. R., Hartogensis, O., Veerman, M., & van Heerwaarden, C. C. (2024). *Observed patterns of surface solar irradiance under cloudy and clear-sky conditions*. Quarterly Journal of the Royal Meteorological Society. `https://doi.org/10.1002/qj.4712`

Hohenegger, C. et al. (2023). *FESSTVaL: The Field Experiment on Submesoscale Spatio-Temporal Variability in Lindenberg*. Bulletin of the American Meteorological Society. `https://doi.org/10.1175/bams-d-21-0330.1`

Heusinkveld, B. G., **Mol, W. B.**, & van Heerwaarden, C. C. (2023). *A new accurate low-cost instrument for fast synchronized spatial measurements of light spectra*. Atmospheric Measurement Techniques. `https://doi.org/10.5194/amt-16-3767-2023`

Mol, W. B., Knap, W. H., & van Heerwaarden, C. C. (2023). *Ten years of 1 Hz solar irradiance observations at Cabauw, the Netherlands, with cloud observations, variability classifications, and statistics*. Earth System Science Data. `https://doi.org/10.5194/essd-15-2139-2023`

Mol, W. B., van Stratum, B. J. H., Knap, W. H., & van Heerwaarden, C. C. (2023). *Reconciling Observations of Solar Irradiance Variability With Cloud Size Distributions*. Journal of Geophysical Research: Atmospheres. `https://doi.org/10.1029/2022jd037894`

Vilà-Guerau de Arellano, J., et al. (2023). *Advancing understanding of land-atmosphere interactions by breaking discipline and scale barriers*. Annals of the New York Academy of Sciences. `https://doi.org/10.1111/nyas.14956`

Jelle A., Bosveld, F., Meirink, J. F., Selten, F., & **Mol, W. B.** (2022). *Drukgolven in Nederland na de eruptie in Tonga op 15 januari 2022*. Meteorologica. https://www.nvbm.nl/meteorologica/archief/2022/maart-2022.

Kreuwel, F. P. M., **Mol, W. B.**, Vilà-Guerau de Arellano, J., & van Heerwaarden, C. C. (2021). *Characterizing solar PV grid overvoltages by data blending advanced metering infrastructure with meteorology*. Solar Energy. https://doi.org/10.1016/j.solener.2021.09.009

van Heerwaarden, C. C.*, **Mol, W. B.***, Veerman, M. A.*, Benedict, I., Heusinkveld, B. G., Knap, W. H., Kazadzis, S., Kouremeti, N., & Fiedler, S. (2021). *Record high solar irradiance in Western Europe during first COVID-19 lockdown largely due to unusual weather*. Communications Earth & Environment. https://doi.org/10.1038/s43247-021-00110-0

Mol, W. B., van Heerwaarden, C. C., & Schlemmer, L. (2019). Surface Moisture Exchange Under Vanishing Wind in Simulations of Idealized Tropical Convection. Geophysical Research Letters. https://doi.org/10.1029/2019gl085047

Datasets

Mol, W. B., Janssens, M., Hartogensis, O., Heusinkveld, B. G., Snellen, H., & van Heerwaarden, C. C. (2024). *Solar spectral irradiance measurements above and in-canopy (SLOCS and CloudRoots Amazonia, 2022) (v0.1.0)*. Zenodo. https://doi.org/10.5281/ZENODO.10554477

Mol, W. B., Heusinkveld, B. G., & van Heerwaarden, C. C. (2023). *Radiometer grid at Falkenberg and surroundings, spectral solar irradiance and cloud imagery, FESSTVaL campaign (v2)*. Universität Hamburg. https://doi.org/10.25592/UHHFDM.12548

Mol, W. B., Heusinkveld, B. G., & van Heerwaarden, C. C. (2023). *Radiometer network dataset of 10 Hz spectral irradiance and derived variables (LIAISE campaign) (v1.2)*.
Zenodo. https://doi.org/10.5281/ZENODO.7966437

Mol, W. B., Knap, W. H., & van Heerwaarden, C. C. (2022). *High resolution solar irradiance variability climatology dataset part 2: classifications, supplementary data, and statistics (v1.1)*. Zenodo. https://doi.org/10.5281/ZENODO.7462362

Knap, W. H. & **Mol, W. B.** (2022). *High resolution solar irradiance variability climatology dataset part 1: direct, diffuse, and global irradiance (v1)*. Zenodo. https://doi.org/10.5281/ZENODO.7093164

Netherlands Research School for the
Socio-Economic and Natural Sciences of the Environment

D I P L O M A

for specialised PhD training

The Netherlands research school for the
Socio-Economic and Natural Sciences of the Environment
(SENSE) declares that

Wouter Bastiaan Mol

born on 17 November 1994 in Soest, The Netherlands

has successfully fulfilled all requirements of the
educational PhD programme of SENSE.

Wageningen, 27 September 2024

SENSE coordinator PhD education

Dr Ir Peter Vermeulen

The SENSE Director

Dr Jampel Dell'Angelo

The SENSE Research School declares that **Wouter Bastiaan Mol** has successfully fulfilled all requirements of the educational PhD programme of SENSE with a work load of 37.5 EC, including the following activities:

SENSE PhD Courses

- Environmental research in context (2020)
- Research in context activity: Initiating cohesion in the world of solar energy (2022-2023)

Other PhD and Advanced MSc Courses

- Un-box your PhD, Wageningen University (2021)
- Solar radiation training, TRANSVALOR + Mines ParisTech, Online (2021)
- Scientific writing, Wageningen University / In'to languages (2023-2024)

Management and Didactic Skills Training

- MAQ Social Committee (social events for staff & students) (2020-2023)
- Assisting practicals of the BSc course 'Atmospheric Practical' (2021-2024)
- Supervising two MSc students with thesis (2021) and (2023)

Selection of Oral Presentations

- *Quantification of the Lockdown Contribution to Record Solar Irradiance in Spring 2020.* NACGEO, 8-9 April 2021, Online
- *Observing Cloud-Driven Surface Irradiance Patterns.* EMS22, 4-9 September 2022, Bonn, Germany
- *High resolution spatiotemporal variability of solar irradiance and water vapour at La Cendros.* LIAISE conference, 27-29 March 2023, Lleida, Spain
- *Cloud-driven patterns of surface solar irradiance as seen by a spatial network of radiometers.* EGU23, 23-28 April 2023, Vienna, Austria

This research received funding from the Dutch Research Council (NWO) VIDI project *Shedding Light On Cloud Shadows* (project no. VI.Vidi.192.068)

Cover design by Wouter Mol
Printed by ProefschriftMaken